Engineered Nanoparticle Systems to Overcome Biological Barriers for Nanomedicine

by

Nahal Habibi

A dissertation submitted in partial fulfillment
of the requirements for the degree of
Doctor of Philosophy
(Chemical Engineering)
in the University of Michigan
2021

Doctoral Committee:

Professor Joerg Lahann, Chair
Professor Lola Eniola-Adefeso
Professor Susan Mallery, Ohio State University
Professor James Moon
Professor Michael Solomon

Nahal Habibi

nahali@umich.edu

ORCID iD: 0000-0001-7736-0168

Dedication

To my grandparents, Aziz and Babai

To my Maman and Baba, Zahra Mahmoudian and Mohammadreza Habibi

Acknowledgements

On January 12th, 2015, at 5:40 p.m., my whole life changed. I received an email that I had been selected for admission to the doctoral program in Chemical Engineering at the University of Michigan. I was thrilled to embark on this journey, but apprehensive about what lay ahead. It was surreal, nerve-racking, scary, and exciting!

Throughout these years, many people have encouraged and supported me but to none do I owe a greater debt of gratitude than to my parents. One never knows how life will unfold. For me, my life in the U.S. began with a travel ban for my country, leaving me unable to see my parents for the last six years. Technology has mitigated distance, however, allowing me to feel their presence here with me. Their constant dedication throughout my life has paved the path for all my successes – from my admission to the prestigious undergraduate institution, Sharif University of Technology, in Iran, to the doctoral program at the University of Michigan. Their faith in me has given me confidence when I was lacking it. Their unconditional love has nurtured, comforted, and fueled my growth. My parents have always encouraged me to persevere through every setback and discouragement. They have challenged me to make my life meaningful, and they have made numerous sacrifices so that I can pursue my dream. They have been my moral compass; they continue to be my idols. I pray that God enables me to give my best daily effort, personally and professionally, to take advantage of the opportunities that their sacrifices have given me. May I emulate my parents' expansive love. May I bring them smiles and happiness every day.

My beloved grandparents, Aziz and Babai, who both succumbed to cancer, were also a source of inspiration. My grandmother has a special place in my heart. When I lost her, the travel ban and restrictions on my visa status prevented me from returning home to mourn her loss and pay my respects. I found solace in resolving to focus my research on drug delivery and cancer treatment. I wish to make my grandparents proud by continuing my career in this field; I hope to contribute as much as I can to the efforts to bring therapies that improve lives and hope to people suffering from terminal diseases.

My uncle, Hamid Habibi, has been my constant source of support and inspiration during these years. When I was still in Iran, he brought me a University of Michigan hoodie to encourage me when applying to Michigan, and it was he who picked me up from the airport and helped me settle down in Ann Arbor. His wife, Lynn Kobes, and her amazing, loving family have made me feel at home in their house filled with love and warmth.

My husband, Ramin Ranjbar, is my best friend, my life-partner. I am grateful for his unending love and patience. Ramin brings magic to our lives every day and finds creative way to surprise me or find a way to make me smile even when life gets hard. His support has been ever present, unwavering, unconditional. He helps me see the bright side of everything, to never let hardships get in the way of following my dreams and to dream big.

At 11:59 p.m. on October 13, 2015, I received an email that Professor Joerg Lahann had officially accepted me to join his lab and he would be my research advisor for the Ph.D. program in the University of Michigan's Chemical Engineering department. I will always remain grateful to him for believing in me and accepting me as his student despite the fact that I had had no prior experience in nanomedicine and drug delivery research. Describing his approach to research and mentorship, he told us that he wanted to see passion in his students' eyes. The rest, he said, one

can learn. He places a greater emphasis on the student's desire to learn and passion for research than a student's pedigree or prior accomplishments. He sets high standards for research performance and, by empowering his students to take ownership of their own projects and to set their own goals and deadlines, he is able to bring out their very best. "Scientists are brave people," he once told me. "It needs courage to discover the unknown." He does not get discouraged with setbacks. In the face of failures, his patience, optimism, and insightful guidance inspire his students to tackle greater challenges. I am always inspired by how he treats failures in research as merely opportunities for learning and growth.

Our lab has a proud history of recruiting a vibrant and diverse group of people from all over the world with varied life experiences and backgrounds. These cultural differences have been a source of personal growth and learning primarily because Professor Lahann has cultivated a nurturing environment where all of us felt like we belonged. Some of us have had to deal with personal challenges and crises outside the confines of science and research. Professor Lahann has always helped us manage many personal issues while continuing to guide our dissertation research. In my case, it was the travel ban and the challenges I faced not being able to see my family. When I lost my grandmother, Aziz, Professor Lahann and his kind wife, Dr. Bita Lahann, invited me to their house to comfort and support me. However, Professor Lahann has supported not only me but many other students as well through challenges so that we could bounce back and continue to thrive as researchers.

His exceptional guidance and thoughtful insights throughout these years allowed me to develop critical scientific skills. I am honored to have been his student and have the opportunity to work in his lab. His mentorship has not only shaped my scientific identity but also my growth as a human being.

Many professors have given me their time and dedication. I would like to thank my Ph.D. committee: Professor Lola Eniola-Adefeso has always been very approachable and kind when I needed help or sought advice; Professor James Moon has provided insightful suggestions and guidance throughout our collaboration; Professor Mike Solomon has taken the time to meet with me one-on-one despite his duties and busy schedule as the Dean of Rackham Graduate School, and Professor Susan Mallery has given me the opportunity to visit her lab and learn new skills. Whether through the classes they offered, our interdisciplinary collaborations, or insightful conversations, they have supported me extensively along the way and have shaped my dissertation. I would also like to thank our collaborators especially Professor Samir Mitragotri, Professor Vladimir Muzykantov, Professor Susan Mallery, and Professor James Moon's groups. I was privileged to have had opportunities to conduct research for a few months in Professor Samir Mitragotri's lab as a research fellow and to visit the labs of Professors Muzykantov, Mallery, and Moon for our collaborative work. I would also like to thank Dr. Tyler Brown and Dr. Daniel Pan who made my time at Harvard University very memorable and fruitful.

It has been an honor and pleasure to work with every member of the Lahann lab, both alum and current. I am indebted to Dr. Divya Varadharajan for her immense support and friendship whether it was getting breakfast or putting lunch on my desk so I would not starve, or working together until late in the lab. Dr. Stephanie Christau brought an extra level of joy, fun and excitement to our collaboration and hard work in the lab. While I was still Iran and without having met me, Sahar Rahmani responded to my emails with warmth and encouragement. This helped me feel part of the University of Michigan community even before I reached the United States, and her friendship continues. Stacy Ramcharan, Ramya Kumar, Kenneth Cheng, and Jake Jordahl went out of their

way to help me in my first steps. I would like to specially thank Stacy and Ramya for their continued generous help, mentorship, and friendship.

I thank Jason Gregory for his scientific advice and help throughout these years. Daniel Quevedo and Dylan Neale started their Ph.D. with me and have been there throughout these years. Ayse Muniz made our journey to the Ph.D. more enjoyable, especially during these last challenging months. I would like to thank Dr. Anne Juggernauth for her mentorship while she was in our lab, and for her friendship and mentorship following lab. Her unconditional support these past years has helped immeasurably. Dr. Jeff Raymond has been a huge source of support and insight in his role as a remarkable mentor and he has taught me so much during the past year.

The members of the Lahann group have always generously provided support and advice during these years. I am proud to have worked with current lab mates: Dr. Yeongun Ko, Albert Chang, Anthony Berardi, Laura Saunders, Fjorela Xhyliu, John Kim, Arit Patra, Zane Zhang, Xiaoyang Zhong, Chris Kim. I am also thankful to our lab members at Karlsruhe Institute of Technology in Germany: Katharina Cu, Marvin Klaiber, and Dr. Mirella Wawryszyn. I would especially like to thank Ava Mauser for her friendship and fun spirit. She inspired me to be a good mentor. I would also like to thank the undergraduate students I have had the opportunity to work with during these past few years: Zixing Fan, Agnieszka Jachimska, Kyle Cameron, and Neha Ray.

I would like to thank the staff members in the Chemical Engineering Department, and the Biointerfaces Institute for all of their help. I would like to extend my gratitude to the staff at core facilities and NCRC for all the training sessions, measurements, and their willingness to always help researchers and answer their questions. I would like to especially thank Dr. Nadine Wong, Lisa Moran, MaryBeth Westin, Karl Oslen, Susan Hamlin, Rhonda Jent, and Kelly Raickovich for all their hard work behind the scenes. I am so thankful for their patience and kindness as there have

been times that I have bothered them on a daily basis and they have always been nothing but kind and helpful.

I would like to thank Saghar Farrehi for her unending support throughout these years. I am forever indebted for her kindness and patience with me. She has helped me navigate toward light when I had lost sight of it, she has patiently listened to me when I felt unheard, she has helped me find solace during troubling times, and brought me back to my senses. I would also like to thank Professors Susan Montgomery and Elyse Vigiletti for their guidance and support through the Ph.D. program. I would like to thank my aunt, Uranus Mahmoudian, for her endless support and love. I am grateful to my friends and "sisters", Niloufar Salehi and Mahshid Chekini. I would like to thank two very special people in my life: my American family, Dr. Joan Gaughan and Maria Guion. I am so lucky to have crossed paths with them in my life. Their presence brings joy and happiness to everyone around them. Their friendship has been a gift and I continue to learn from their wisdom and passion. I thank Joan for her kindness, compassion and caring; and Maria, for always being there for me and being like a family member, providing me with a source of love and peace.

I would like to thank the Ph.D. regimen itself as a transformative process that taught me patience and resilience, and taught me also to accept failure and to learn from it, to not give up, and to always have hope. It was in this process that I realized the excitement of discovering, understanding, explaining, and influencing our world.

Finally, I am thankful to beautiful Ann Arbor with its amazing explosion of colors of trees in different seasons, the lakes, the deer and groundhogs of Northwood apartments. This city embraced me in this new chapter of my life and somewhere along the way gave me another meaning of "my home".

Table of Contents

List of Tables

List of Figures

Abstract

Biological barriers in the body impede the transport of nanotherapeutics to a target site leading to unfavorable biodistribution profiles and inadequate accumulation of drugs, thus limiting the efficacious responses in diseases. Reimagining nanoparticle-based design strategies to navigate extracellular and intracellular biological barriers is therefore needed for efficient therapeutics. This dissertation focuses on the use of electrohydrodynamic (EHD) co-jetting to engineer novel protein- and biopolymer-based nanoparticle systems to address three major biological transport barriers: the immune system barrier, the blood-brain barrier (BBB), and the oral mucosal barrier. A selection of synthetic protein nanoparticles (SPNPs) prepared from (i) single proteins including human serum albumin (HSA), bovine serum albumin, ovalbumin (OVA), human transferrin (TF), hemoglobin, mucin, insulin, and lysozyme, (ii) blend of different proteins, and (iii) compartmentalization of different proteins in the same nanoparticle are used to target the immune system and BBB. Bicompartmental poly(lactide-co-glycolide) (PLGA)-chitosan nanoparticles as the biopolymer-based system are used to overcome the oral mucosal barrier. Tunable physicochemical properties and biological responses of SPNPs are achieved by altering the protein composition, macromere type, macromer-to-protein ratio, solvent system, and by compartmentalization. A systematic study of SPNPs with various protein compositions led to nanoparticles with low polydispersity indices (0.11-0.19), high circularity (0.82 – 0.90), low anisotropy (< 1.45), and high roundness (0.76 – 0.89). Specific SPNPs are then chosen to overcome each of the biological barriers. To target the immune system interface, antigen-based particles (OVA SPNPs) are fabricated with varying physicochemical properties to improve antigen delivery and immunological responses for cancer immunotherapy. When prepared from a macromer-to-protein ratio of 10%, 266 nm sized particles with an elasticity of 42 kPa showed enhanced uptake by dendritic cells, T cell activation, draining lymph nodes delivery, antibody production and anti-tumor efficacy. To cross the BBB, HSA SPNPs owing to the endogenous property of albumin proteins to mediate endothelium transcytosis are chosen and hitchhiked on RBCs due to their

innate vascular mobility and long circulation times. IgG-modified HSA SPNPs showed an average binding of 126 nanoparticles per RBC with no adverse effects on the cells, resulting in a 19-fold and 113-fold increase in brain uptake and in the brain-to-(liver and spleen) ratio, respectively in a mouse model of acute brain inflammation. In another approach, monocytes due to their natural recruitment to the inflamed brain and ability to cross the BBB are used to hitchhike 200 and 500 nm protein-based (HSA and TF) and polymer-based (polystyrene and poly(methyl methacrylate)) nanoparticles to investigate the effect of their physicochemical properties on monocytes. While 500 nm PMMA nanoparticles showed the highest uptake, the migration of 200 nm HSA and TF SPNPs-loaded monocytes were 3.4 and 3.7-fold higher, respectively. These results show that SPNPs delivered by a cell-mediated approach using RBCs or monocytes hold great promise for brain drug delivery. For targeting the oral mucosal barrier, PLGA-chitosan nanoparticles enable different adhesion interactions with mucus layer for oral cancer chemoprevention. The nanoparticles were readily internalized by human oral keratinocytes and penetrated through human oral mucosal explants, with 41% of them reaching the basilar third of the epithelium. PLGA-chitosan nanoparticle-mediated delivery of tocilizumab as a chemopreventive agent resulted in significant oral squamous cell carcinoma tumor-regressive effects. The approaches described in this thesis hence provide new perspectives on transport-driven in vivo mechanisms to enhance the therapeutic efficacy of nanoparticles in the context of biological barriers.

Chapter 1
Introduction

1.1 Nanotechnology-based Drug Delivery Systems

Positive patient outcomes across a wide range of diseases is highly dependent on site-specific delivery of an adequate amount of drugs.[1] Pharmaceutical chemistry has advanced to produce highly potent drugs, but the successful delivery of these therapeutics to the target sites in the body with desired pharmacokinetics is not yet optimal.[1,2] In cancer treatment, for example, optimal delivery of highly potent, yet toxic, chemotherapeutics to only cancerous cells defines the line between efficacious response and severe morbidity. However, current cancer treatments such as surgical intervention, radiation, and chemotherapeutic agents kill healthy cells alongside cancer cells, leading to severe toxicities to the patients.[3,4] Similarly, with brain disease, both neurological and neurodegenerative, clinical failure of many potentially effective drugs are not usually due to the lack of drug potency but rather the inability of the drug to reach the brain through the brain capillary endothelial cells.[5]

Present-day formulations lack the ability to localize the drug to the targeted site with desired pharmacokinetics.[1] Therefore, drug molecules diffuse and distribute throughout the body in a non-targeted manner, leading to undesirable side effects and inefficient site-specific bioavailability.[1] Nanotechnology could help mitigate the limitation of conventional delivery: nanoparticle-based drug delivery systems are an emerging targeted drug class growing towards the development of Ehrlich's concept of the "magic bullet," wherein drugs directly and selectively

attack the targeted cells, while sparing healthy cells.[6,7] This has resulted in the development of various platforms by scientists trying to realize site-specific therapy.[7,8] Nanotechnology refers to structures with 1-100 nm size in at least one dimension, according to its strict definition from the National Nanotechnology Initiative. However, despite this definition, nanotechnology commonly includes structures up to several hundred nanometers and are developed by top-down or bottom-up engineering and manufacturing materials.[9] The application of nanotechnology to drug delivery has widely advanced the field of medicine and greatly improved the living conditions of patients suffering from a myriad of devastating diseases.[10,11]

The fuel to the excitement over nanomedicine is multifaceted, because nanoparticle-based drug delivery systems promise to provide several advantages over their traditional free-drug counterparts.[12–16] Nanoscale carriers can enable the delivery of a wide range of therapeutics, including hydrophobic or hydrophilic small molecules, peptides, and nucleic acids.[17,18] By encapsulating these molecules in nanoparticles, their solubility, stability, and bioavailability can be enhanced.[17,18] When a drug of interest is packaged in a "smart" nanocarrier delivery system, it can be protected from degradation or deactivation in the biological environment.[17] Once the nanoparticles are administered to the body, the blood circulation half-time and bioavailability of the drug cargo can be augmented by engineering nanocarriers with stealth moieties or targeting ligands leading to delivering drugs in a cell- or a tissue-specific manner.[19] Lastly, the drug release profile from nanoparticles can be fine-tuned to maintain the optimal drug concentration over a prolonged period of time, decrease dosing frequency, and increase patient convenience.[11,20] Ultimately, these nanoparticle-mediated drug delivery features can allow for an increase in the amount of the drug in the target cells while minimizing systemic toxicity.

There has been extensive research in the development of nanoparticles to facilitate the realization of their potential and clinical translation. Early efforts in this field led to the development of lipid-based vesicles that are now known as liposomes.[11] Subsequently, nanoparticles composition has expanded to include organic and inorganic biomaterials.[21] Modulating the bulk composition of nanoparticles enabled the design of the first polymer-based system with controlled release modality in 1976.[22] Tuning the surface composition of nanoparticles by incorporating polyethylene glycol (PEG) as "stealth" moieties increased the circulation times of nanoparticles.[23] Building upon these considerable technological successes, the extensive research in this field resulted in the approval of Doxil (doxorubicin liposome) in 1995.[24] Doxil marks one of the major milestones in this field, when the first class of therapeutic nanoparticles received clinical approval for the treatment of AIDS-associated Kaposi's sarcoma. Whether it is the delivery of synergistic ratios of two drugs (VYXEOS) in 2017 or the RNAi therapy by lipid-based nanoparticles (Patisiran/ONPATTRO) in 2018, nanoparticles have been fundamentally transforming how therapeutics are being delivered and enabling novel treatment modalities.[10] However, despite the wide range of tangible efforts and impressive progress in this field, a limited number of nanoparticles have had significant clinical impacts; fewer than 50 nanomedicines have achieved FDA approval during the 20 years following the FDA approval of Doxil.[25]

The limitations in broad clinical translation of nanoparticle-based delivery systems lie in the fact that these platforms face a complex series of biological barriers that need to be addressed to achieve site-specific drug delivery and proper therapeutic outcomes.[6] Nanoparticles have an array of challenges emerging from their biological and technological limitations that hinder their clinical translation. Nanoparticles suffer from rapid clearance from circulation, inefficient permeation across the endothelium into target tissue, and penetration through the tissue interstitium leading to

overall inefficient delivery to target cells.[26] These can be collectively summarized as the limited ability of engineered nanoparticles to cross challenging biological barriers such as the immune system barrier, the blood-brain barrier and the mucosal barrier.[1,27,28]

A meta-analysis of 232 data sets revealed that only a median of 0.7% of the administrated nanoparticle dose was able to reach a solid tumor.[29] These data sets included particles with organic and inorganic materials, various hydrodynamic diameters, surface charges, active and passive targeting capabilities, and shapes. Surprisingly, the median delivery efficiency demonstrated no significant improvement over 2005 to 2015, the 10-year period of the surveyed literature.[29] These findings highlights a pressing need to design and develop alternate drug delivery platforms that are adequately equipped to address these biological transport barriers. The current thesis deals with the development of multifunctional, protein-based and biopolymer-based nanoparticles as efficient drug delivery vehicles addressing the immune system barrier, the blood-brain barrier, and the oral mucosal barrier.

1.2 Biological Barriers Preventing Effective Nanoparticle-based Therapies

Biological barriers are critical arms of the body's defense system to hinder the penetration of foreign materials.[26] Engineering efficient nanoparticle-based delivery systems to address these barriers requires understanding the interactions between nanoparticles and the human body. The human body, being a complex system, imposes several extracellular and intracellular barriers for the successful delivery of nanoparticles, preventing the achievement of proper therapeutic outcomes.[30] Some commonly known pathways that inhibit effective transport, thereby indirectly posing barriers for intravascularly administered nanoparticles, manifest in the form of following cascade: (i) clearance by the immune system, (ii) penetration across the endothelium into target tissue, (iii) transport through the tissue interstitium, (iv) endocytosis in target cells, (v) endosomal

escape and target intracellular organelle if required.[14,26,31,32] Precisely, the first three barriers represent the extracellular barriers, while the rest are categorized as intracellular ones. In this thesis, the focus is on achieving effective nanoparticle-based drug delivery platforms that surpass the extracellular barriers (**Figure 1-1**). The following sections explain the relevant barriers in the human body in detail.

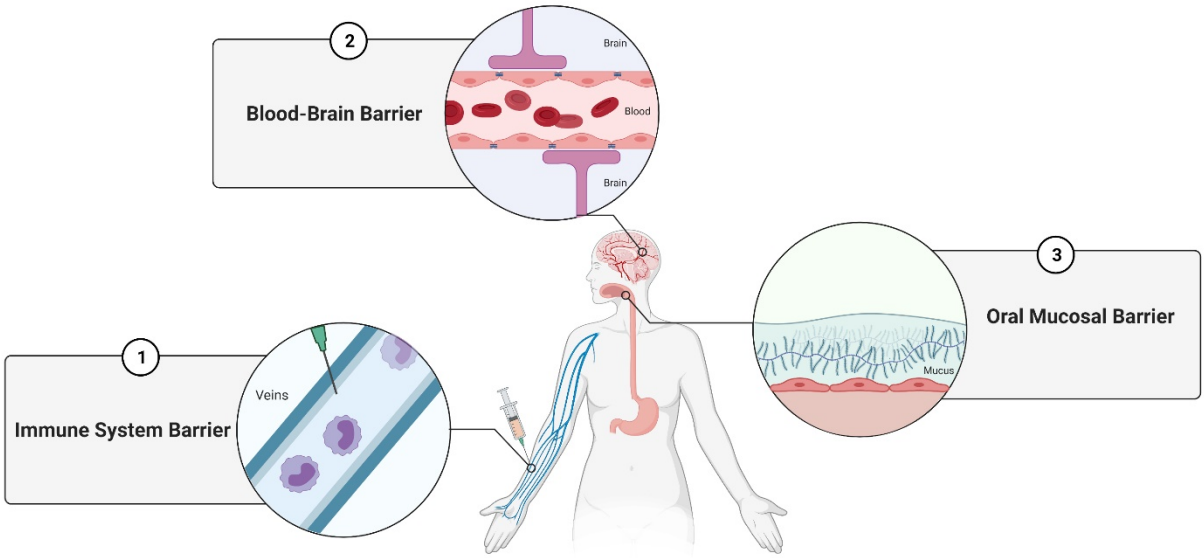

Figure 1-1. Major biological barriers hindering the transport of nanoparticles to reach target cells.

1.2.1 Immune System Barrier

The first barriers faced by nanoparticles upon administration are the opsonization and sequestration by the mononuclear phagocyte system as the body's first line of defense system restricting the penetration of foreign materials.[14,32] Intravenously administered nanoparticles may be rapidly removed from the circulation by the reticuloendothelial system, comprising liver and spleen.[3] The clearance of nanoparticles by the immune system results in their poor circulation time, non-specific distribution, high accumulation in healthy organs, such as the spleen and the

liver, and inadequate delivery to the target organ. An ideal nanoparticle-based carrier should deliver necessary doses at the therapeutic site while maintaining a low amount at undesired sites. **Chapter 4** discusses the strategy employed to make nanoparticles entirely from antigen and take advantage of the preferential uptake of nanoparticles by immune cells to facilitate tumor antigen delivery and elicit immune responses for killing tumor cells.

1.2.2 Blood-brain Barrier

Once the nanoparticles are in blood vessels, their margination to vessel walls and subsequent penetration across the endothelial cell barriers present the next transport barriers. Endothelial cells line the vascular lumen and maintain the integrity of the blood vessels to ensure seamless trafficking of molecules while presenting an obstacle for the extravasation of nanoparticles from the blood into the target tissue.[31] The cellular integrity of the endothelial barrier is highly dependent on specific tissues and pathological conditions.[33] The blood-brain barrier, the endothelial barrier between the blood and the brain, is the tightest endothelium in the body and extremely restrictive due to the high density of endothelial cells and tight junctions between them.[26] Overcoming the blood-brain barrier is proven to be essential for effective drug delivery to the brain in the context of brain diseases such as brain tumors, Alzheimer's disease and Parkinson's disease. **Chapter 5 and Chapter 6** detail the use of a combination of engineered protein nanoparticles with the body's own circulatory cells to augment brain-targeted delivery.

1.2.3 Oral Mucosal Barrier

Besides the immune system and the endothelial barrier, additional tissue-specific barriers to nanoparticles' transport can exist, depending on the target organ and route of administration.[26] For example, all major organs, such as the gastrointestinal tract, lung, urinary bladder, and

reproductive tracts, are protected by mucosal surfaces.[34] As the mucosal tissues' primary defense mechanism, mucus protects the underlying cells by efficiently trapping and removing foreign particulates and pathogens.[34–36] The presence of multiple intermolecular interactions, including hydrogen bonding, hydrophobic forces, and electrostatic interactions, along with physical entanglements between mucus constituents, creates a dense, highly viscoelastic, and adhesive protective barrier.[37,38] Therefore, the mucus layer possesses challenging barrier properties that limit the nanoparticles' residence time and penetration, which subsequently precludes prolonged drug delivery to the respiratory, gastrointestinal, and cervicovaginal tracts.[34,36,39] **Chapter 7** discusses the use of bicompartmental biopolymer-based nanoparticles possessing dual adhesion characteristics in the context of a novel delivery platform across the oral mucosal barrier.

After overcoming the extracellular barriers, upon reaching target cells, nanoparticles encounter with intracellular barriers, starting with passage through the cellular membrane, a negatively charged lipid bilayer, and subsequent endosomal and lysosomal escape.[14,30,32,40,41] Within the scope of this, nanoparticle properties such as size, shape, composition, elasticity, surface chemistry, and targeting ligand density impact the fate of nanoparticles inside the body after administration and ultimately determine the therapeutic outcome.[14] Hence, an enhanced understanding of biological and pathological processes governing the biological barriers coupled with advancement in materials science and engineering will continue to improve the design space of nanoparticles capable of sequential negotiation of biological barriers for achieving more effective site-specific delivery.

1.3 Emerging Trends in Surpassing Biological Barriers[1]

In response to the challenge to navigate, alter, or interact with complex biological, physiological, or pathological processes, nanoparticle designs and architectures have evolved, in an attempt to address these challenges. However, while one class of particle or material may address a single barrier, it is unlikely to address them all. For example, in the case of drug delivery for cancer therapy, the bulk and surface properties best suited for this multi-step process – including systemic transport, tumor localization, cellular uptake and effective drug release – are conflicting.[42] Approaches to address this conundrum include: (i) the design space of nanoparticles in terms of the development of multifunctional particles, and the use of biologically derived materials, termed as carrier design (**Section 1.3.1**) and (ii) the transport of nanoparticles exploiting circulatory cells, termed as cell-mediated delivery of nanoparticles (**Section 1.3.2**).

1.3.1 Carrier Design

1.3.1.1 Multifunctional Synthetic Nanoparticles

Achieving optimal therapeutic efficacy by nanoparticles relies on their response to the series of biological barriers to effective transport to the target cells. The properties that are required to overcome extracellular and intracellular barriers are conflicting. Traditional monofunctional nanoparticles face challenges in negotiating these barriers as they provide a single function. To address limitations faced by traditional nanoparticles in overcoming biological barriers, multifunctional nanoparticles hold great potential to surmount these challenges by imparting dissimilar properties and different functionalities into a single nanoparticle. Multifunctional

[1] Part of the materials in this chapter has been adapted with modifications from the following article:
Nahal Habibi, Daniel F. Quevedo, Jason V. Gregory, Joerg Lahann. Emerging Methods in Therapeutics Using Multifunctional Nanoparticles. *WIREs Nanomedicine & Nanobiotechnology* **2020**, *12*, e1625.

particles can be defined as any particle system with two or more engineered properties. Here, we focus on two distinct types of multifunctional particles – (i) those with surface anisotropy and, (ii) those with bulk anisotropy. In the case of surface anisotropic particles, the bulk composition is often uniform and controlled, post-fabrication surface modifications are used to create non-uniform surface features that diverge from their bulk properties. Conversely, bulk anisotropic particles contain multiple, distinct volumes within a single particle, often comprised of different materials, and as a result have dissimilar bulk properties. Discussed here are a variety of fabrication methods within each class that have been developed.

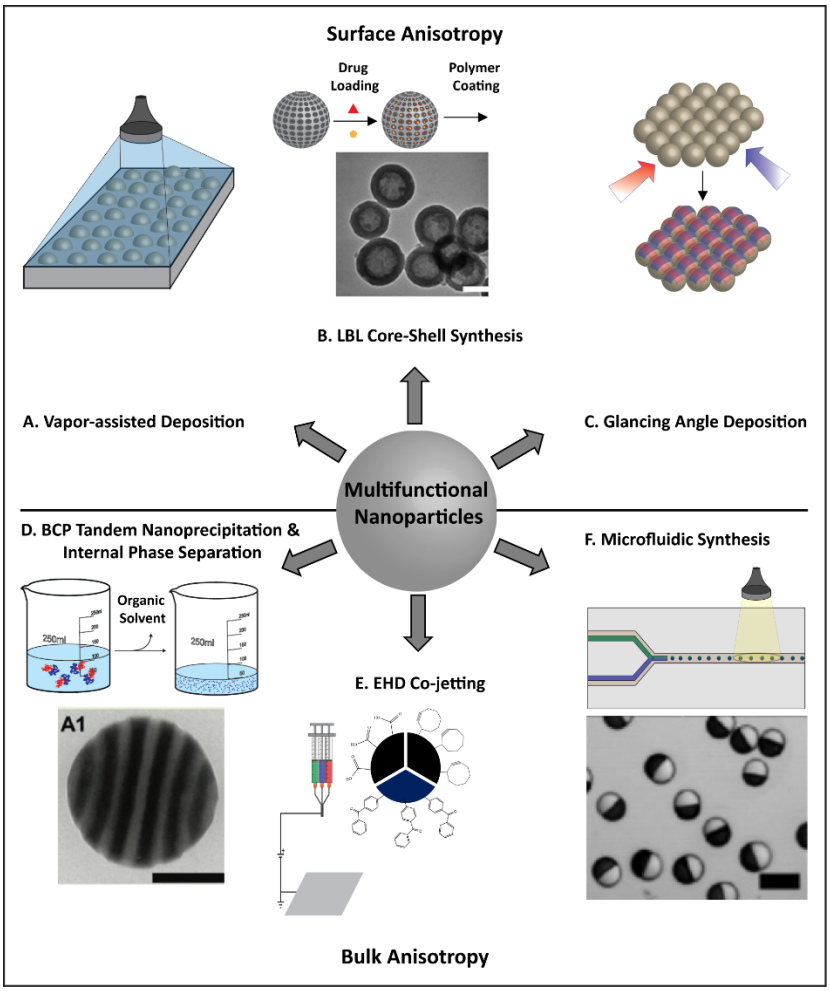

Figure 1-2. Techniques for the synthesis of multifunctional nanoparticles. (A) Vapor-assisted deposition of macromolecules to select areas of nanoparticles through matrix assisted pulsed laser evaporation (MAPLE). Scale bar, 200 nm. Adapted from [43]. (B) Layer-by-layer fabrication of polymer-coated, hollow silica nanoparticles for temporally controlled release of encapsulated drugs. Scale bar, 100 nm. Adapted from [44] (C) Anisotropic, multifunctional patchy nanoparticles formed through the use of glancing angle deposition (GLAD). Scale bar, 2 μm. Adapted from [45] (D) Tandem nanoprecipitation and internal phase separation employed to create surface-reactive, patchy nanoparticles prepared through the use of block copolymers (BCPs) and tuning of preparation conditions. Scale bar, 100 nm. Adapted from [46] (E) Surface-reactive, multicompartmental particles fabricated using electrohydrodynamic (EHD) co-jetting through the spatially controlled addition of chemically orthogonal surface functional groups. Adapted from [47] (F) Continuous and high-throughput synthesis of multicompartmental nanoparticles through the formation of compound droplets in flow and subsequent UV initiated crosslinking. Scale bar, 100 nm. Adapted from [48].

Nanoparticles Exhibiting Surface Anisotropy

Isotropic particles synthesized through a variety of methods can have anisotropic surface properties that are controlled by post-modification techniques. This can be achieved through the utilization of masks or templates, to controllably restrict the regions of particles to be modified.[49,50] Interfaces (liquid-liquid,[51] liquid-solid,[52] air-liquid,[53] and air-solid[54]), where particles are either mechanically placed or spontaneously accumulate, act to mask a portion of each particle while surface modifications are performed within a single phase of a two-phase system (**Figure 1-2A**). In other instances, the close packing of particles during the process, as in glancing angle deposition, self-imposes restraints on the surface areas of particles available for modification due to shadowing effects caused by neighboring particles (**Figure 1-2C**).[45,55] Here, it is through the control of the deposition angle that dictates the surface area and pattern achieved. Processes such as physical deposition including etching,[56] chemical vapor deposition,[43,57] or lithography,[58] are used to selectively modify the exposed surfaces producing "patchy" particles. Finally, there are instances where uniform modification of the surface is performed to impart dissimilar particle characteristics from the bulk material (**Figure 1-2B**). In all cases, the result is a particle with regions of their surface with varied chemical, electrical, or amphiphilic properties distinct from their bulk properties. Together, these varied properties can be used to selectively modify particle surfaces.[59] Examples with biomedical relevance include the covalent attachment of ligands for systemic targeting[60] or PEGylation to alter particle pharmacokinetics.[61] One of the more popular approaches for biological applications is the attachment of biomolecules to inorganic particles such as gold, or mesoporous silica that would otherwise have no targeting properties and lack biocompatibility.[62]

Nanoparticles Exhibiting Bulk Anisotropy

In contrast to the post-modification routes that are used to create multifunctional nanoparticles with surface anisotropy, one or more bulk materials with distinct properties are used to create compositionally anisotropic particles. For example, the synthesis of complex nanoparticles through controlled self-assembly processes can be achieved using block copolymers and variations in the solvent mixture (**Figure 1-2D**).[46,63] On a larger scale, the selective surface functionalization of smaller building block particles can result in the formation of more complex supracolloidal assemblies.[64,65] The production of liposomes[66,67] or disk shaped particles[68,69] made of amphiphilic molecules such as lipids can be formed through similar self-assembly processes. In contrast, flow processes, including microfluidics (**Figure 1-2F**)[48,70] and electrohydrodynamic (EHD) co-jetting (**Figure 1-2E**)[71–74], utilize the controlled flow of polymer solutions in specific orientations to one another in combination with a method of solidifying the individual particles to form stable colloids. Particularly, EHD co-jetting will be discussed in **Section 1.3.1.3** as a primary particle formulation technology used in this thesis. In a brief description, relying on the orientation of the individual flows, the distinct regions within the resulting particles can be radially anisotropic as is the case with core-shell particles,[75,76] or adjacent to one another giving rise to a Janus structure.[48,77] In the latter case, the bulk anisotropy directly translates to a surface anisotropy, which in some cases can be further modified for application specific properties. Alternatively, by taking a layer-by-layer (LBL) approach, nanoparticles can be assembled in a stepwise fashion, again resulting in layered particles with homogeneous surfaces.[44,78–80] In each of the aforementioned processes, particles with chemically distinct regions and properties can be synthesized. Nanoparticle research has long been applied for the delivery of therapeutics and biomedical imaging.[81–84] The synthesis of nanoparticles with bulk anisotropy lends itself to the

development of multifunctional particles with a unique control over their interactions with other particles or biological systems.[85–87] For example, the use of dissimilar pH responsive polymers to form distinct regions within a single nanoparticle can be used to individually load and tune the release of encapsulated cargo.[85,86] In another example, Varadharajan and co-workers, working with block copolymers, recently employed tandem nanoprecipitation and internal phase separation techniques to produce nanoparticles with complex structural and chemical anisotropy.[46] Such multifunctional and patterned particles clearly show potential for use in nanomedicine as both functionalization and morphological tuning creates opportunities to circumvent specific problems for targeted delivery.

1.3.1.2 Protein Nanoparticles[2]

A recent development in the field of nanoparticle-based drug delivery replaces synthetic polymers with proteins as the primary building blocks of nanoparticles. As a material, proteins show great promise due to their variety, function, design flexibility through genetic engineering, and potential lack of immunogenicity. Protein-based nanomedicine is founded on the premise to explore the endogenous properties of proteins to design carrier systems with improved drug delivery profiles. Protein nanoparticles (PNPs) are biocompatible, biodegradable, and metabolizable.[88–91] As one of the essential macromolecules of life,[92] proteins possess attractive properties that position them as a compelling alternative to synthetic polymeric materials commonly utilized in traditional nanomedicine formulations.[91] These properties include: (i) biocompatibility, (ii) biodegradability, (iii) versatility, (iv) chemical conjugation capabilities, and (v) unique

[2] Part of the materials in this chapter has been adapted with modifications from the following submitted articles:
Nahal Habibi, Daniel F. Quevedo, Jason V. Gregory, Joerg Lahann. Emerging Methods in Therapeutics Using Multifunctional Nanoparticles. *WIREs Nanomedicine & Nanobiotechnology* **2020**, *12*, e1625.
Nahal Habibi, Ava Mauser, Yeongun Ko, Joerg Lahann. Harnessing The Power of Protein Nanoparticles for Medicine. *In Preparation.*

endogenous mechanisms that can be leveraged to address the challenges faced by traditional drug delivery systems. Their primary structure with various chemically reactive side groups allows for effective surface modifications.[91,93] Moreover, the amphiphilic nature of proteins enables encapsulation of both, hydrophilic and hydrophobic drug molecules.[94,95] Recombinant protein technologies can provide access to a variety of protein building blocks with precisely engineered functions.[90,92,96] The increased interest in PNPs can be deduced from a review of recent nanoparticle formulations that are evaluated in clinical trials. Based on clinicaltraisl.gov for a time period from 2001 to 2021, it is evident that there have been more protein-based particles in the development pipeline than any other materials class (**Figure 1-3).** Categorizing the clinical trials based on the nanoparticles composition (lipids, protein, polymer, inorganic, and unclassified) demonstrate protein-based nanoparticle drug delivery systems gained a lot of attention comprising 62% of the total 234 clinical trials.

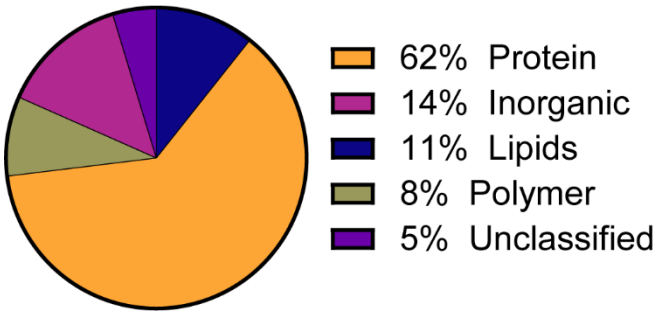

Figure 1-3. Clinical trials from 2001 to 2021 with the search term, "nanoparticles" on clinicaltrails.gov.

Further clinical translation of PNPs critically hinges upon the availability of suitable manufacturing processes. In the following, we highlight the most abandon processes used to formulate PNPs: Nanoparticle albumin bound (nab) technology, self-assembly and coacervation.

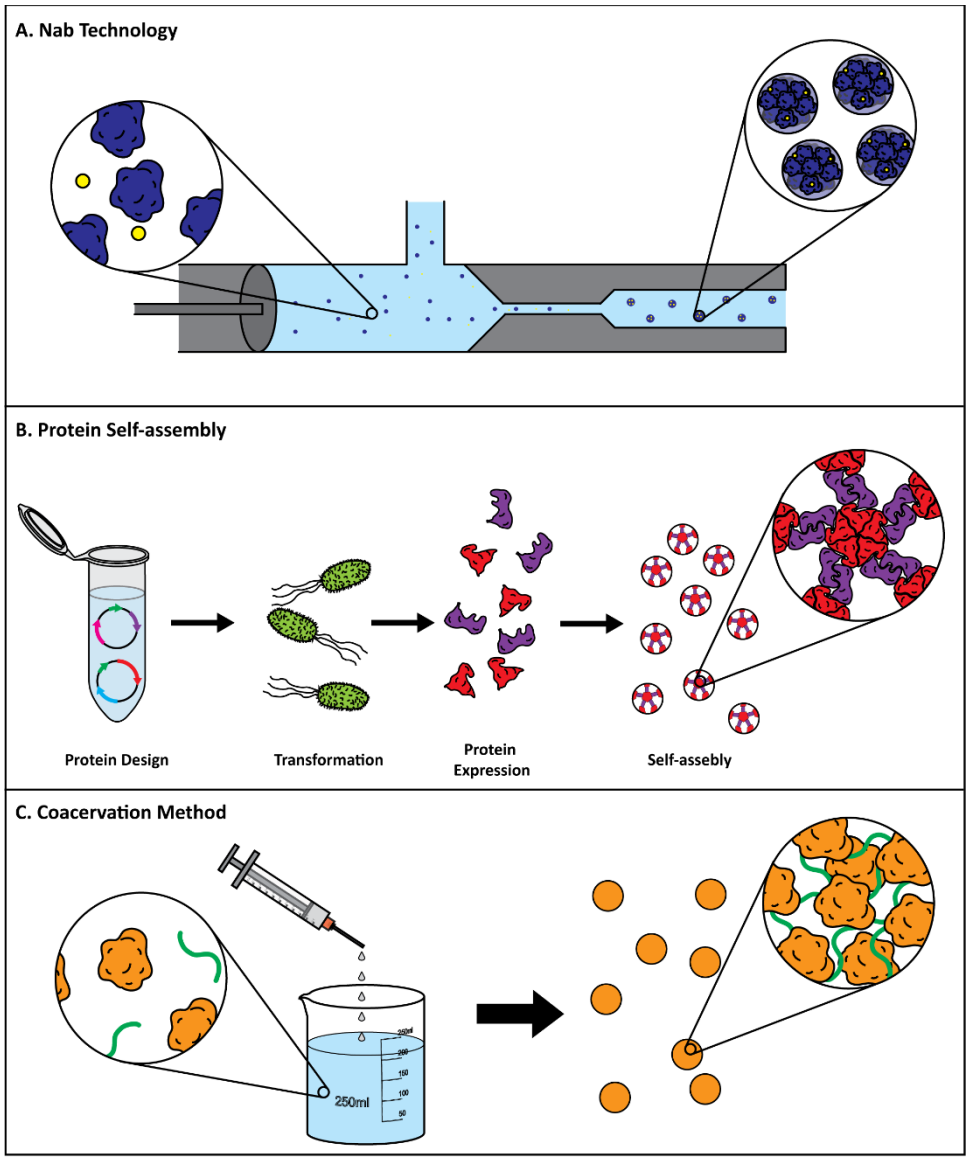

Figure 1-4. Protein nanoparticles hold great promise in medicine due to their variety and inherent functionalities. Three main methods exist to synthesize these particles. (A) Nab technology works by using a sheer mediated process to force hydrophobic drugs within proteins and subsequently cause the proteins to aggregate into nanoscale particles. (B) Self-assembly techniques use the expression of specially designed proteins by microorganisms that subsequently self-assemble into structures that can be used for broad variety of therapeutic applications. (C) Coacervation functions by the addition of an organic solvent or reagent to a protein solution, which causes the formation of particles that are subsequently crosslinked using bifunctional crosslinkers.

Nanoparticle Albumin-bound Technology

Nanoparticle albumin-bound technology (nab) technology is one of the oldest and most developed methods for making PNPs. Developed by Abraxis Bioscience (now a part of Celgene) to create a way of delivering paclitaxel, *nab*-technology forces highly hydrophobic drugs into the internal hydrophobic pockets of human serum albumin (HSA) using a high-pressure manufacturing process (**Figure 1-4A**). Paclitaxel is normally administered using harsh organic solvents.[97] By packaging the drug in albumin, a common protein in human blood that is not only water soluble but also has a naturally long circulation time, the drug can be delivered with reduced side effects.[98] The first FDA approved nab product was Abraxane, which has been approved for use as a first line therapy for non-small cell lung cancer, metastatic adenocarcinoma, and as treatment for metastatic breast cancer. Additionally, Abraxane is in Japanese clinical trials by Celgene for use in metastatic pancreatic cancer and gastric metastatic cancer.

In addition to the success of Abraxane, multiple other nab technologies are under investigation at both the industrial and academic level. ABI-008 through ABI-011 are a family of nab based drugs that are undergoing clinical trials. In addition to multiple clinical trials, next generation nab technologies are actively being investigated. For example, actively targeted variants of nab particles have been made.[99,100]While showing great potential, nab technologies have potential downsides. Early work has shown that Abraxane is associated with more rapid plasma clearance compared to the traditional liposomal formulation of paclitaxel (Taxol).[101] Abraxane nanoparticles are stable in ex vivo saline solutions, but the particles quickly break down into albumin-paclitaxel complexes following administration.[98] This poor colloidal stability has been suggested as the reason behind the rapid clearance of the nanoparticles.[102] In addition to poor clearance profiles, nab technology has the inherent downside of harsh synthetic conditions.[103]

This potentially limits the use of nab technology to deliver active proteins, such as enzymes, in ways that other synthetic routes that are able to.[104] Excellent reviews of nab technologies have been written by Hawkins et al. and Tan et al. among others, which we recommend for further reading.[105,106] Nab technology has nonetheless shown the clinical potential of proteins as nanocarriers in medicine.

Protein Nanoparticles by Self-assembly

Self-assembled nanoparticles are nanoscale structures made of protein complexes that can self-assemble to form PNPs (**Figure 1-4B**). These structures are designed by creating recombinant proteins that contain oligomerization-domains that create structure, and then a variety of other domains that can result in specific activity.[107] The synthetic methods and design strategies for nanoscale protein structures have been excellently summarized in recent reviews.[107,108] An interesting application of self-assembled PNPs in the medical space is the use of caged protein nanoparticles.[109] These particles are made up of protein units that self-assemble under specific conditions into hollow cage-like structures. Inside these structures it is then possible to load a variety of therapeutic molecules such as enzymes[110] and small molecules.[111] In a recent study, Kawakami et al. designed a 60-mer protein cage with a defined structure. Notably, they were able to design the particle so that specific residues faced either the exterior or interior of the cage, and subsequently were able to covalently modify these particles.[112] These covalent modifications were done using disulfide bonds, and thus this system could be designed to carry a drug in the inside of the cage, and then be released in a reducing environment. These self-assembled nanoparticle technologies are elegant, sophisticated, and complicated, but these very characteristics call to question their potential for translation into the clinic in the near future. Most of the proteins used in these nanoparticles are not only novel recombinant proteins, but are also

expressed in non-mammalian organisms such as *Escherichia coli*.[112] Expression in non-human organisms of recombinant proteins presents many regulatory problems and costs, as has been shown though the past 30 years with the rise of recombinant antibody and antibody fragment (Fab) technology.[113] Yet, with careful development, the rise of the multi-billion dollar biological therapeutics field shows the potential for progressively more sophisticated therapies to enter the market.

Coacervation-synthesized Protein Nanoparticles

During coacervation, a "coacervation agent", usually an organic solvent such as acetone or ethanol, is added to a concentrated aqueous solution of a protein of interest. The coacervating agent dehydrates the proteins and causes the precipitation of nanoparticles from the solution. The particles can then be crosslinked, rendering them water insoluble (**Figure 1-4C**). By controlling a variety of conditions, including the protein type, the rate of addition of the coacervating agent, the temperature of the procedure, the salt content of the solution, and the crosslinking agent and time, the resulting nanoparticle size, mechanical properties, and functionalities can be tailored to fit the needs of the application.[114,115] In addition, the process is highly reproducible, and the particles can be surface functionalized and loaded with a variety of therapeutics.[116–118] Initial work using coacervation focused on albumin proteins, but the field is now expanding to a variety of different proteins and applications. A wide variety of different proteins have been formulated into nanoparticles, as detailed in a recent review.[119] These proteins have been used in applications such as the packaging of small molecules and micro-nutrients for the food industry[120]. Through coacervation techniques, PNPs have been prepared from a wide variety of polypeptides and proteins for therapeutic purposes.[104,121,122] A recent publication that used the PNP technologies developed by the Champion lab demonstrated a proof of concept of a universal influenza virus.[123]

While the use of the highly conserved M2e epitopes has been attempted before in vaccines, these vaccines were constructed from virus-like particles (VLP) loaded with epitopes and resulted in off target immune responses due to the carrier proteins in the VLP.[124,125] PNPs made almost entirely of proteins of interest, as was demonstrated in the work by Deng et al. can avoid off target effect problems.[123] Additionally, coacervation-manufactured PNPs, as opposed to the self-assembled or VLP counterparts, have greater stability over a large range of physiological environments, and studies have shown that they can potentially create cold chain-independent therapies.[126] A clear downside of coacervation particles is inherent in the simplicity of their synthetic method, in that it creates homogeneous distributions of proteins throughout each particle. Only radial complexity through surface modifications methods is able to provide any kind of anisotropy to the particles, as opposed to technologies such as those discussed in previous sections.

In summary, different fabrication methods have been discussed with respect to both multifunctional synthetic and protein nanoparticles. However, more robust synthesis techniques will be needed to allow mass production of PNPs encompassing attributes such as multi-functionality and greater control over their anisotropy. In this thesis, a versatile technology to prepare any desired type of nanoparticle with tailored functionality and properties has been used: EHD co-jetting. The following **section 1.3.1.3** explains in detail this technology as a key methodology employed to fabricate nanocarriers to pass relevant barriers in the human body.

1.3.1.3 Electrohydrodynamic Co-jetting

EHD co-jetting as a variation of the electrospraying process, is a versatile technology that was pioneered in the Lahann Lab at the University of Michigan. This technique has been used to fabricate anisotropic multicompartmental micro- and nanoparticles with various applications in drug delivery.[86,127–139] EHD co-jetting process uses relatively simple manipulation of liquid geometries followed by rapid solidification to design multicompartmental particles that would be otherwise impossible, or at least extremely difficult, to achieve.[140] Overcoming series of biological barriers for successful drug delivery requires presence of orthogonal properties on the delivery platform. EHD co-jetting provides access to independently control the composition of individual compartments on the same particle and to incorporate different materials with dissimilar properties[128] with the goal of addressing multiple biological barriers. EHD co-jetting allows for control of the shape, size, and bulk and surface composition of particles or their individual compartments.[141] Incorporation of different materials in a single particle leads to multifunctionality and co-presentation of orthogonal properties.[141]

In electrohydrodynamic co-jetting, two or more needles are used as capillaries in a side-by-side configuration.[141] Two different miscible polymeric solutions are pumped through capillaries at a rate forming laminar co-flow to ensure a stable interface between the two jetting solutions without any convective mixing.[141] When a droplet forms at the outlet of the needles, an electric field is applied to the system that distorts the droplet into a Taylor cone and subsequent formation of an electrified polymer jet (**Figure 1-5**).[142–144] Rapid acceleration of electrified jet causes the jet diameter to decrease by several order of magnitude and the surface area to increase.[143–145] This process induces rapid solvent evaporation and therefore solidification of the nonvolatile components into micro- to nanoscale particles.[141] Due to rapid solvent evaporation, the surface

energy-driven reorientation to a more thermodynamically favorable configuration, usually a core/shell, is restricted; therefore, the initial flow-determined arrangement of the input polymer solutions will be mirrored in the solidified nanoparticles.[140,141]

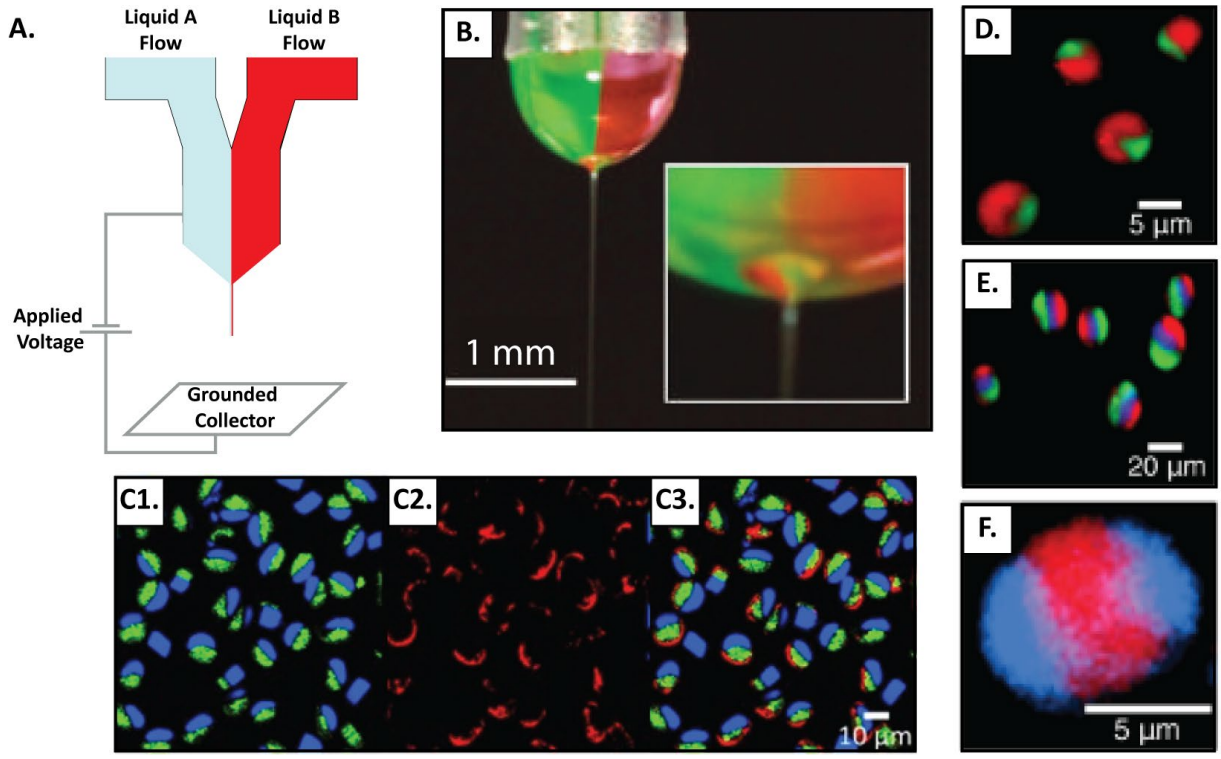

Figure 1-5. Multifunctional and multicompartment nanoparticles fabricated by electrohydrodynamic (EHD) co-jetting technique. Adapted from [127] (A) Schematic description of the EHD co-jetting setup. (B) A photograph of a Taylor cone after application of an electric field to the system. Adapted from [127]. (C1-C3) Selective surface modification of microparticles through incorporating a functionalized polymer only in one hemisphere. Adapted from [128] (D-F) Examples of multicompartmental particles engineered by the EHD co-jetting. Particles were prepared from poly(lactide-co-glycolide) polymers. To visualize the anisotropic nature of the particles by confocal laser scanning microscopy, each compartment was loaded with a different fluorescent dye. Adapted from [140].

EHD co-jetting allows for fabrication of multicompartmental carriers incorporating cancer drug,[146] siRNA,[131,138] and imaging agents[147] in different compartments. Furthermore, stimuli responsive particles are feasible when fabricated with responsive materials.[131] Nanoparticles have been utilized for the delivery of therapeutic and biomedical imaging agents.[140] The use of multi-compartment particles may allow for these to be incorporated into a single particle system and coupled with controlled release of drugs.[133] Combining the delivery and release of therapeutics while also providing a method of monitoring biodistribution and intracellular fate, termed theranostics, can prove to be a valuable tool within the clinic.[133,140] Misra et al. demonstrated the ability to create biphasic nanoparticles comprising of a PLGA compartment loaded with an imaging agent alongside a second pH-sensing, siRNA-loaded compartment.[148] The synthesized particles demonstrated not only the ability to serve the dual function of particle tracking and therapeutic release but also made use of significant swelling of a single hemisphere to facilitate endosomal escape.[148]

Creating bulk anisotropic Janus particles allows for selective and controlled modifications to be performed on the surface. Rahmani et al. demonstrated this through the synthesis and subsequent surface modification of tri-compartmental particles.[47] To fabricate the anisotropic particles, a similar poly(lactide-co-glycolide) (PLGA) base was used in combination with dopants of functional polylactide polymers.[47] It was shown that by incorporating small amounts of a functional polymer within the bulk of an otherwise isotropic particle system, controlled surface functionalization through orthogonal click chemistry reactions could be used to selectively decorate the particle surface.[47] This approach allows for the covalent attachment of specific targeting or stealth moieties with control over density, placement, and relative orientation of individual ligands relative to one another. Furthermore, the adaptability of the process suggests

that the number of compartments and attached ligands is limited only by the number of orthogonal chemistries that can be performed on the resulting particle.[47]

Engineering a multitude of particles with defined sizes, shapes and surface chemistries is achievable through tuning the parameters forming a multidimensional design space. The input parameters that affect the resulting particles can be categorized into (i) jetting solutions, (ii) process and (iii) environmental-related parameters.[149] Firstly, jetting parameters are directly associated with the composition of the jetting material, precisely their chemical nature, their molar mass, concentration in solution, surface tension, dielectric constant, density, viscosity or vapor pressure of the jetting solution itself.[149] Secondly, the process-related parameters entail the fluid flow rate, applied electrical voltage, the diameter of the flow cell, i.e., the needle diameter, and the distance between the tip of the needle and grounded plate.[149] Lastly, EHD jetting process can also be influenced by a number of environmental variables, such as temperature, pressure, and humidity.[149]

Transitioning between different size ranges requires simultaneous control of the aforementioned factors.[150] For example, large particles can be targeted with higher polymer concentration and an increased fluid flow rate, while simultaneously influencing the final morphology of the particles by altering the viscosity of the resultant solution. Playing with the same parameter, one can increase the solution viscosity to reach a state where as a result of decreased break-up tendency of the flowing jet and decreased evaporation of the solvent at this state, unique morphology like fibers can be obtained.[150,151] Consequently, EHD can be considered as a robust multifaceted technology that aptly fits as a design technology to fabricate nanomaterials, and in particular nanoparticles with varying chemistries , morphologies, and targets.[141,149] Capitalizing on this technology, focus is laid on the design and preparation of protein nanoparticles made from human

serum albumin, bovine serum albumin, human transferrin, ovalbumin, insulin, hemoglobin, lysozyme, and mucin. The compartmentalization capability of EHD co-jetting was utilized to fabricate bicompartmental PLGA-chitosan nanoparticles. Furthermore, these particles were ready for either (i) direct transportation through a selected biological barrier, or (ii) designed for attachment onto a carrier cell such as monocytes and red blood cells. In the former category, ovalbumin, human serum albumin and transferrin, and PLGA-chitosan nanoparticles were precisely engineered to transport across the immune system, BBB, and oral mucosal barriers, respectively. Likewise, in the latter, human serum albumin and transferrin nanoparticles were hitchhiked onto monocytes, while HSA nanoparticles were additionally hitchhiked onto RBCs to transport them across the BBB. A detailed evaluation of both aspects has been discussed in the forthcoming chapters. The next section addresses the use of circulatory cells in our body (red blood cells, leukocytes, and stem cells) as a natural delivery vehicle to transport the nanoparticles to the target tissues.

1.3.2 Cell-mediated Delivery of Nanoparticles[3]

Circulatory cells, as the body's own delivery vehicles, possess inherent abilities specifically long circulation times, natural tissue targeting, and the ability to cross impermeable barriers. These significant properties make them great candidates to address some challenges concerning nanoparticle drug delivery systems.[27,152] One such delivery systems, termed "cellular hitchhiking" is an enhancement of the traditional ones, wherein targeted delivery via body's natural vehicle, i.e., circulatory cells and optimal release of the cargo from engineered nanoparticles are realized in one delivery platform. Cellular hitchhiking has been performed using

[3] Part of the materials in this chapter has been adapted with minor modifications from the following article: Nahal Habibi, Daniel F. Quevedo, Jason V. Gregory, Joerg Lahann. Emerging Methods in Therapeutics Using Multifunctional Nanoparticles. *WIREs Nanomedicine & Nanobiotechnology* **2020**, *12*, e1625.

a variety of cell types (**Table 1-1**). This section focuses on red blood cells, leukocytes, and stem cells, all of which have been exploited for the cell-mediated transport of nanoparticles. We furthermore elaborate on various strategies that have been used to incorporate nanoparticles into or conjugate them onto the surface of these circulatory cells.

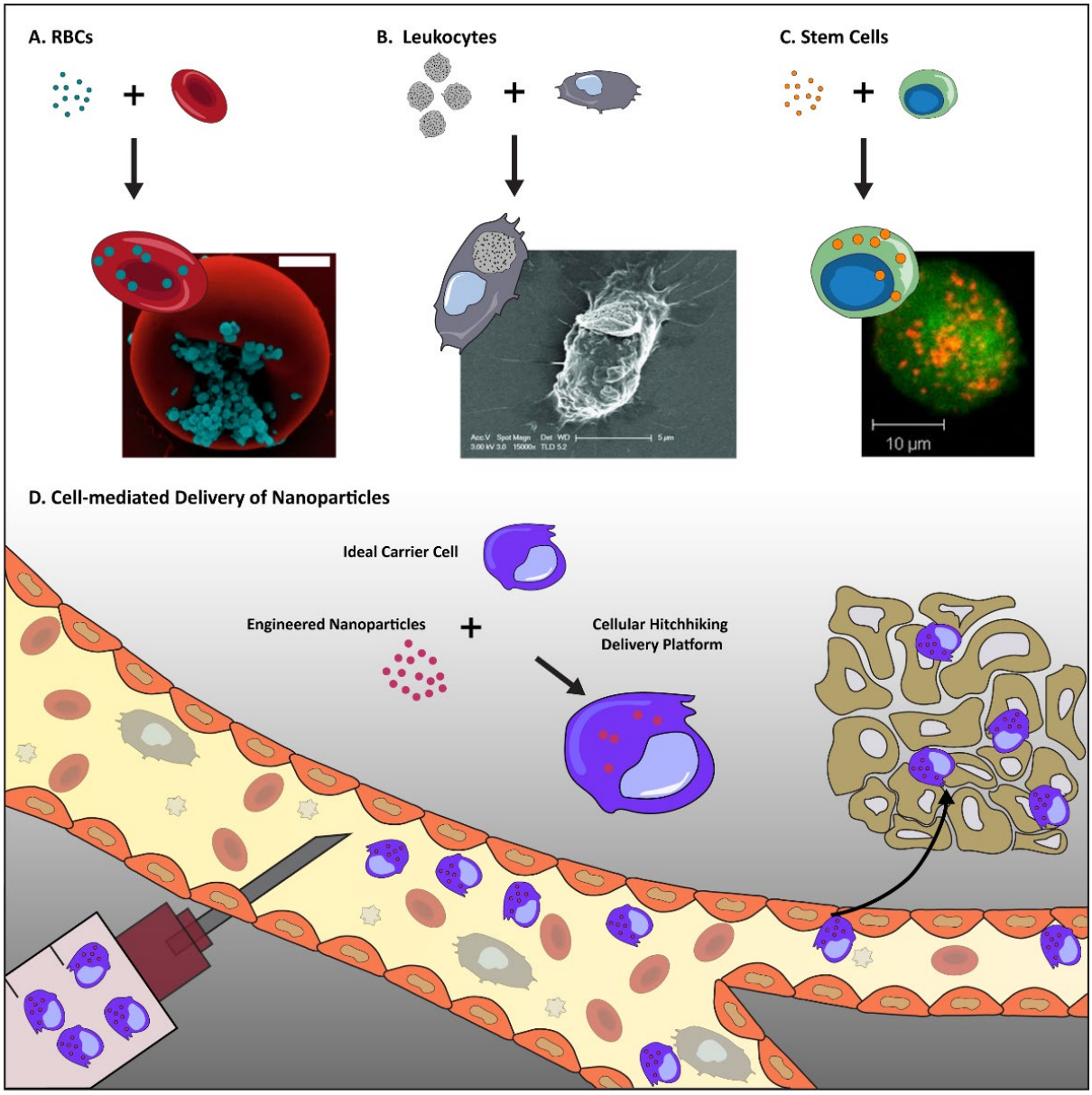

Figure 1-6. Different circulatory cells used in cellular hitchhiking formulations. (A) Scanning electron micrographs of nanogels adsorbed onto the surface of murine RBCs in vitro. Scale bar = 1 µm. Adapted from [153] (B) Scanning electron micrographs of hyaluronic acid coated backpack attached to the surface of J774 mouse macrophages after 3 hours incubation in cell culture conditions. Scale bar = 5 µm. Adapted from [154] (C) Confocal image of fluorescently labeled nanoparticles conjugated to biotinylated neural stem cell stained with calcein-AM. Scale bar = 10 µm. Adapted from [155] (D) Schematic drawing of circulatory cell-mediated targeting and delivery of nanoparticles.

1.3.2.1 Red Blood Cells (RBCs)

Constituting > 99% of total blood cells, RBCs are long-circulating cells with a lifespan of 100-120 days in humans and natural carriers of many substances, especially oxygen, in the blood stream.[156] The innate properties of RBCs, such as a long circulation time, reversible deformation, and ability to squeeze through capillaries smaller than their diameter[27,157] make them suitable candidates as platforms for drug delivery systems.[156,158] In general, there exists two main methods to obtain RBC-mediated nanoparticle drug delivery systems: (i) to internally load the nanoparticles into RBCs, or (ii) to attach them onto the surface of the cells. Wu et al. fabricated RBC-based micromotors, wherein iron oxide nanoparticles were encapsulated into the RBCs and the motors were powered and activated by ultrasound and an applied magnetic field, respectively.[159] Encapsulation of cargoes into RBCs using hypotonic dilution methods requires the formation of transient pores in the RBC membrane for diffusion of nanoparticles into cells[159] making it more invasive in comparison to anchoring the cargoes on their surface.[160,161] Surface loading can be achieved via non-specific binding (electrostatic, van der Waals, hydrogen bonding and hydrophobic forces),[162]or specific binding (ligand-receptor interactions or chemical conjugation).[160,163]

Adsorption of nanoparticles onto RBCs surfaces has been explored as a means of avoiding rapid clearance by the reticuloendothelial system (RES).[162,164] As an example, RBC-hitchhiking of model polystyrene nanoparticles led to a 100-fold increase of nanoparticles in vivo circulation time.[162] Because surface adsorbed nanoparticles will eventually detach from carrier RBCs due to cell-cell interaction and shear forces, engineering the detachment of nanoparticles and their transfer to microvasculature endothelium will enable targeted organ delivery using RBC hitchhiking.[165–167] In a recent study, nanoparticles adsorbed onto RBCs were delivered to the first

microcapillary bed that the RBC-NP conjugates encountered downstream to their injection site (**Figure 1-6A**).[166]

1.3.2.2 Leukocytes

Serving as major components of the adaptive and innate immune system, leukocytes are responsible for fighting inflammation, infection, and tumor growth.[168,169] Leukocytes inherently migrate to areas hard-to-reach by traditional nanoparticles such as inflamed tissue,[170] migrate across endothelial barriers,[171] and reach the hypoxic area of tumors,[172,173] and thus are an attractive cell choice for hitchhiking.[158]

Macrophages and monocytes as phagocytic cells can naturally internalize nanoparticles and carry them to target sites that are otherwise largely inaccessible.[174–178] For example, macrophages have been used for delivering various nanocarriers across the blood-brain barrier such as self-assembled polyethyleneimine-poly(ethylene glycol) catalase in a Parkinson's Disease model,[179] and gold-silica nanoshells for photothermal therapy for glioma in vitro[180] and in vivo.[181] As an alternative approach, nanoparticles can be engineered to be immobilized on cell surfaces while avoiding phagocytosis (**Figure 1-6B**).[154,182,183] Klyachko et al. showed that "backpacks" loaded with a potent antioxidant, catalase, were attached to the surface of macrophages and transmigrated across inflamed BBB in a mouse model of LPS-induced encephalitis.[184]. Alongside macrophages, a typical feature of monocytes as circulatory cells to migrate towards inflammation sites along a chemoattractant gradient[185] made them suitable to carry particles to inflamed tissues. Anselmo et al. took advantage of IgG-Fc receptor interactions to attach cellular "backpacks" on the surface of monocytes while avoiding phagocytosis due to the polymeric backpacks size, disc like shape, and flexibility. Cellular functions such as transmigration through endothelium, or differentiation into macrophages were unimpaired after attachment of the backpacks onto monocytes. Monocyte-

hitchhiked backpacks showed a 9-fold higher accumulation in the inflamed skin compared to non-cell attached backpacks and a 2-fold higher targeting of inflamed lungs than to normal lungs.[186] T cells as key components of adaptive immune system have been used as platforms for cellular hitchhiking.[187,188] These cells are capable of sensing danger signals from invading pathogens and cancer. Upon antigen presentation, tumor specific T cells become activated to eliminate tumor cells.[189] In the context of adoptive T cell-based strategies, utilizing patient's natural T cells or engineered T cells with chimeric antigen receptors (CAR) to mediate tumor cell eradication has suggested promising new directions.[189] However, one of the major barriers for cell-based therapies is loss of transplanted cell viability and function. Showing the enhancement of cell therapy outcome, Stephan et al. reported the immobilization of adjuvant drug-loaded nanoparticles to the surface of therapeutic cells via maleimide-thiol conjugation to provide sustained pseudoautocrine stimulation of the transferred cells in vivo.[190]

1.3.2.3 Stem Cells

Stem cell therapy often considered to be vital for tissue engineering and regenerative medicine.[191] A more recent development is the use of specific stem cell lineages such as mesenchymal stem cells (MSCs) and neural stem cells (NSCs) for drug delivery applications.[192] Their tumoritropic migratory nature make them desirable for targeted delivery of therapeutics[193,194] and multimodality imaging agents[195] in cancer therapy. To design stem cell mediated delivery platforms, two approaches can be used: (i) nanoparticles can be loaded onto the cells surface as a first approach[155,196] (**Figure 1-6C)**, and (ii) nanoparticles can be encapsulated into the stem cells.[197,198] However, in this thesis, stem-cells as delivery platform has not been discussed as a viable option.

Table 1-1. Advantages, limitations, and examples of in vivo applications of cellular hitchhiking formulations.

Hitchhiked Cell Type	Cell Type Advantages	Cell Type Limitations	Particle Cargo	Benefits of Cellular Hitchhiking	Ref.
Red blood cells	-Abundant -Long circulation time -Easy isolation	-Limited tissue targeting	-200nm spheres and Rod shape polystyrene particles	-Increased lung targeting	[167,199]
Macrophages /Monocytes	-Ability to phagocytose nanoparticles -Cross biological barriers -Naturally migrate to sites of inflammation -Reach hypoxic areas of tumors	-Low drug loading efficiency -Endosomal degradation of phagocytosed cargo	-Self-assembled polyethyleneimine-poly(ethylene glycol) catalase	-Enhanced delivery of catalase to PD-affected brain regions (crossing blood-brain barrier)	[179,200]
T cells	-Ability to target specific cells -Dual carrier and therapy capability	-Difficult harvesting and handling, -Short in vivo lifespan	-300-nm multilamellar lipid nanoparticles loaded with IL-15 and IL-21	-Enhanced tumor elimination in established B16 melanomas	[190,201]
Stem cells	-Ability to internalize nanoparticles -Tumoritropic migratory ability	-Difficult isolation and expansion -Reports of MSCs association with promoting primary and metastatic tumor growth	-Poly(ethylene glycol)-poly(diisopropyl amino) ethyl methacrylate nanoparticles loaded with docetaxel	-Enhanced tumor delivery due to improved migration to hypoxic tumor cores in a triple negative breast cancer (TNBC) mouse model	[155,194]

When designing efficient cell-mediated nanoparticle delivery systems for targeting specific organs, a rational selection of appropriate cells is as important as precisely tuning the properties of nanoparticles. Nonetheless, challenges to this approach include sufficient drug loading capacity, premature drug release, triggered controlled release, preservation of the drug cargo from intracellular degradation, and protection of cell carriers from drug cytotoxic effects. Moreover, cost barriers and sufficient harvesting, or expanding of cells without contamination for reinjection into the body, and efficient migration of cell carriers to the target site are other important concerns. Although there are challenges that needs to be addressed, cell-mediated delivery platforms offer promising opportunities in improving diagnosis and therapeutics for various chronic diseases such as cancer. Developing smart biomaterials, engineering particle design parameters, and utilizing

deliberate methods to conjugate nanoparticles to suitable cells can address some of the above-mentioned challenges.

1.4 Objectives

The overarching theme of this dissertation is to engineer efficient nanoparticle-based drug delivery systems to overcome the three major biological barriers: the immune system barrier, the blood-brain barrier, and the oral mucosal barrier. The particle design encompasses the incorporation of tailored anisotropic properties into a single particle system. Such a system requires understanding the interactions between nanoparticles and the body's intracellular and extracellular barriers for successful delivery to a target tissue.[30] Given the complex nature of these inherent barriers, a particle with multiple functions and properties has a higher potential to successfully overcome all the barriers to reach a specific target.

My work extends the application of electrohydrodynamic (EHD) co-jetting, originally developed in the Lahann Lab, from synthetic polymers to protein-based and biopolymer-based nanoparticle systems with the goal of addressing multiple biological transport barriers. The research provides a perspective on the synergies between protein-based and multicompartmental nanoparticle designs and their delivery by cell-mediated approaches to enhance the outcomes of nanoparticle-based drug delivery. Specifically, the following aims outline the work presented in this dissertation.

Aim 1: Particle Design Platform – Developing Synthetic Protein Nanoparticles. Given the protein nanoparticle's favorable property profiles such as biocompatibility, biodegradability, versatility, chemical conjugation and surface modification capabilities, and their natural ability to interact with biopharmaceutical drugs have placed them at the forefront of nanomedicine in recent years. In **Chapter 2** and **Chapter 3**, the design space for developing synthetic protein nanoparticles is expanded by the EHD co-jetting technique in terms of the protein composition, its stabilization strategies, and compartmentalization.

Aim 2: Immune System Barrier – Nanoparticles Composed Entirely of Antigen for Cancer Immunotherapy. Eliciting potent and antigen-specific cellular and humoral immune responses remains a major challenge in cancer immunotherapy. **Chapter 4** details the design and fabrication of antigen-based nanoparticles with tunable physicochemical properties. The key particle parameters that influence the immunological response are identified. We demonstrate that delivering the antigen by precisely engineered antigen-based nanoparticles outperforms solute antigen in the overall anti-tumor response.

Aim 3: Blood-brain Barrier – Engineered Protein Nanoparticle-based Platforms for Cell-mediated Targeted Brain Delivery. To deliver the therapeutics to the brain, a series of biological barriers need to be addressed, including clearance by the reticuloendothelial system and the blood-brain barrier. Cellular hitchhiking formulations enable the integration of multiple functionalities into a single carrier by merging the benefits of the body's delivery vehicles, circulatory cells, with engineered nanoparticles in one single delivery platform to address multiple transport barriers. In **Chapter 5**, the long circulation and vascular mobility of red blood cells are combined with human serum albumin nanoparticles to cross the blood-brain barrier. In addition to red blood cells, in **Chapter 6**, the ability of monocytes to readily recruit to the inflamed brain and cross the blood-brain barrier was utilized to deliver a wide range of nanoparticles with different physicochemical properties.

Aim 4: Oral Mucosal Barrier – Janus Nanoparticles for Field-coverage Chemoprevention of Oral Squamous Cell Carcinoma. Given the ability of the EHD co-jetting technique to endow dissimilar and orthogonal properties to the particle system by fabricating multicompartmental nanoparticles, Janus nanoparticles are designed in **Chapter 7** to cross the oral mucosa and mediate tocilizumab delivery for oral cancer chemoprevention.

Chapter 2
Multifunctional Synthetic Protein Nanoparticles via Reactive Electrojetting

The material in this chapter has been adapted with minor modifications from the following article: Daniel F. Quevedo*, Nahal Habibi*, Jason V. Gregory, Yazmin Hernandez, Tyler D. Brown, Rikako Miki, Bradley N. Plummer, Sahar Rahmani, Jeffery E. Raymond, Samir Mitragotri, Joerg Lahann. Multifunctional Synthetic Protein Nanoparticles via Reactive Electrojetting. *Macromolecular Rapid Communications* **2020**, *41*, 2000425. (* Equal Contributions)
Nahal Habibi and Daniel F. Quevedo contributed equally to this work. Part of the material in this chapter with modifications is discussed in the following thesis document:
Daniel F. Quevedo. Design, Applications, and Processing of Synthetic Protein Nanoparticles. (Doctoral Dissertation) **2020**.

2.1 Abstract

Protein nanoparticles are a promising approach for nanotherapeutics, as proteins combine versatile chemical and biological function with controlled biodegradability. In this work, the development of an adaptable synthesis method is presented for synthetic protein nanoparticles (SPNPs) based on reactive electrojetting. In contrast to past work with electrohydrodynamic co-jetting using inert polymers, the jetting solutions are comprised of proteins and chemically activated macromers, designed to react with each other during the processing step, to form insoluble nanogel particles. SPNPs made from a variety of different proteins, such as transferrin, insulin or hemoglobin, are stable and uniform under physiological conditions and maintain uniform sizes of around 200 nm. SPNPs comprised of transferrin and a disulfide containing macromer, are stimuli-responsive and

serve as markers of oxidative stress within HeLa cells. Beyond isotropic SPNPs, bicompartmental nanoparticles containing human serum albumin and transferrin in two distinct hemispheres are prepared via reactive electrojetting. This novel platform provides access to a novel class of versatile protein particles with nanoscale architectures that (i) can be made from a variety of proteins and macromers, (ii) have tunable biological responses, and (iii) can be multicompartmental, a prerequisite for controlled release of multiple drugs.

2.2 Introduction

Nanoparticle-based drug delivery systems provide improved drug stability, reduced drug toxicity and improved biodistribution compared to free drugs.[202–204] There are a number of nanoparticle therapeutic platforms such as PEGylated liposomal doxorubicin (Doxil) and liposomal vincristine (Marqibo) that have been approved for cancer treatment.[10,205] Despite the progress made in the field of nanoparticle-based drug delivery, there are still unmet challenges such as poor circulation times, unwanted immunogenicity and a lack of adequate functional materials.[6,206] Solutions to these challenges often conflict with each other, leading to the development of multifunctional, multicompartmental nanoparticles.[141] Multifunctional nanoparticles have traditionally been made of synthetic polymers, such as polyethylene glycol (PEG),[59] Poly(lactide-co-glycolide) (PLGA),[47] or block copolymer systems.[46] Using proteins as the primary building block of nanocarriers could be an appealing alternative due to their chemical diversity, inherent biological functions, and a potentially reduced risk for immunogenicity.[94] Protein nanoparticles (PNPs)[6,94] have been pursued for drug delivery applications including the clinically approved drug Abraxane[101] and other preclinically studied candidates.[207–209] Common PNP fabrication methods include, among others, nab technologies,[99,210] coacervation,[104,211] and self-assembly.[112,212] Despite undoubtable progress in recent years, PNP technologies are still hampered by a range of

drawbacks. While PNPs prepared via nab technologies have been implicated with decreased morbidity,[213] the processing conditions during particle preparation have been showed to cause protein denaturation.[214] Coacervation can create large quantities of PNPs,[116] but generally lacks sufficient control to prepare multifunctional nanoparticles. Self-assembly can provide more structural diversity,[108] but requires *ab initio* design of new protein building blocks that has to be done separately for each application. Except for the more involved self-assembly route, none of these techniques has so far resulted in architecturally controlled protein nanocarriers, such as bi- or multicompartmental nanoparticles.

Electrohydrodynamic (EHD) co-jetting has previously been shown to be effective at creating multicompartmental particles with nanoscale anisotropy.[141] EHD co-jetting relies on laminar co-flow of two or more polymer solutions prior to the jet ejection to pre-template compartmentalized nanoparticles and nanofibers, with fine control over size, shape, composition, and spatial distribution of matter at the surface and bulk level.[147,215] EHD co-jetting has been used to fabricate multicompartmental polymer particles that incorporate various functionalities, such as stealth modalities,[137] targeting/tracing,[216] and encapsulation of different cargos such as siRNA,[131] imaging agents,[136] and small molecule cancer drugs.[146]

As traditional protein nanoparticle synthesis methods lack control over anisotropy, we have developed reactive electrojetting as a method for making anisotropic Synthetic Protein Nanoparticles (SPNPs). Reactive electrojetting takes advantage of the anisotropic control afforded by EHD co-jetting to create protein nanoparticles, and then introduces a second chemical step that converts the particles into nanogels through a sol-gel transition using a variety of macromers.

2.3 Materials and Methods

2.3.1 Materials

Recombinant human serum albumin (Cellastim S) was purchased from InVitria. Human transferrin, human hemoglobin, lysozyme, human recombinant insulin, 2KDa O,O′-Bis[2-(N-Succinimidyl-succinylamino)ethyl]polyethylene glycol (PEG-NHS) or 4,7,10,13,16,19,22,25,32,35,38,41,44,47,50,53-Hexadecaoxa-28,29-dithiahexapentacontanedioic acid di-N-succinimidyl ester (PEG-NHS-S) were acquired from Sigma Aldrich. All buffers, purchased in solution form, and all other reagents used were of lab grade and acquired from Sigma Aldrich or Thermo Fisher.

2.3.2 Fabrication of SPNPs Using Electrohydrodynamic Co-jetting

All protein nanoparticles were synthesized using EHD jetting, with differences in the protein solution used and subsequent processing resulting in different copolymer SPNPs. In general, the EHD jetting method was done as previously described[86,128,139,217], where a protein solution is pressure driven through a 25G blunt tip needle at a flow rate of 0.1 mL h^{-1}, and a sufficient voltage applied between the needle and a collecting surface to produce a stable Taylor cone. The voltage causes the droplet to be pulled towards the collecting substrate, and the stream subsequently breaks up into nanometer sized spheres. In mid-flight, the solvents rapidly evaporate to form solid nanoparticles. For fluorescent tagging, BSA-Alexa Fluor dyes were incorporated into the protein solution at a concentration of 0.8% (w/w) of the total mass of protein unless otherwise noted.

SPNP Synthesis Using PEG-NHS and PEG-NHS-S

For SPNPs made with ester-based macromers, a protein solution was made by fully dissolving a protein of interest at 10% (w/v) in a 90:10 (Ultra-Pure H_2O:EtOH) solution. Depending on the

method, PEG-NHS or PEG-NHS-S was added at 10% (w/w) of protein mass to the solution. After EHD jetting, the nanoparticles were placed in a dry 37 °C oven for 7 days, and subsequently collected by scraping them off the collection surface using a solution of DPBS supplemented with 0.01% Tween 20.

SPNP Synthesis Using GA

To synthesize SPNPs polymerized with Vapor-Phase Glutaraldehyde (GA), a protein solution was made by fully dissolving a protein of interest at 10% (w/v) in a 90:10 (Ultra-Pure H_2O:EtOH) solution. After EHD co-jetting the resulting particles were incubated at room temperature in a closed container, which contained 2.5 mL of 20% Glutaraldehyde in a plastic reservoir, for 30 minutes. The unreacted glutaraldehyde was quenched by collecting the particles by scraping them off the collecting surface using Ultra-Pure H_2O supplemented with glycine (100 mM) and 0.01% Tween 20.

SPNP Synthesis Using S-S

SPNPs synthesized through macromer-free disulfide bonds (S-S) were made by dissolving the protein of interest at 2.5% (w/v) in a 90:10 (2,2,2-Trifluoroethanol: Ultra-pure H_2O) solution, and the protein allowed to denature for 2 hours in order to fully break all disulfide bonds. 2-Mercaptoethanol was then added at a 10x molar excess to the number of disulfide bonds in the protein and allowed to incubate for 30 minutes at room temperature. The solution was then jetted and the resulting particles collected as previously described.

2.3.3 SPNPs Collection Procedure

After collection, the collected solution was sonicated on ice, run through a 40um cell filter, and then centrifuged at 3200 rcf for 5 minutes to remove large particles. The resulting supernatant was

then centrifuged at 21130 rcf for 40 minutes to collect the desired particles. The final particles were washed at least 5 times through centrifugation using DPBS supplemented with 0.01% Tween 20.

2.3.4 SPNPs Characterization

Particles, prior to collection, were imaged using Scanning Electron Microscopy (Thermo Fisher Nova 200 Nanolab Dualbeam FIB). Particle diameters were measured using the protocol outlined below. To determine their hydrodynamic size distribution after isolation, the particles were suspended in 0.22 μm filtered DPBS supplemented with 0.01% Tween 20, sonicated on ice, and measured using dynamic light scattering (Malvern ZSP ZEN-5600). Standard settings were used and an average of 3 measurements are reported. Particle zeta potential was measured on the same instrument using a disposable folded capillary cell (DTS1070, Malvern) and using standard settings. Particle concentration was measured using a BCA assay, using a BSA standard for a standard curve. Particle number concentrations were measured using Nanoparticle Tracking Analysis on a Malvern Nanosight.

2.3.5 Circular Dichroism Spectroscopy Analysis of SPNPs

Circular dichroism (CD) spectroscopy was used to study the effects of EHD jetting on the proteins that compose SPNPs prior to polymerization. Fully synthesized SPNPs were not studied using CD spectroscopy due to the method's inability to obtain measurements that can be analyzed with deconvolution based secondary structure analysis from aggregated protein complexes.[218] The different methods used to polymerize the SPNPs were carried out, without the corresponding macromers, for the NHS-PEG, NHS-PEG-S and GA Macromers. As S-S crosslinking occurs immediately during the jetting process, it was not possible to quantitatively study the effect of

jetting on the proteins, but since the process for S-S includes purposeful denaturation of the proteins with a strong organic solvent and a reducing agent, it stands to reason that little to no of the original secondary structure would be maintained after the jetting process.

Particles were jetted, but no macromers were included in the jetting formulations or post-jetting. The particles were then treated identically as they would have been if macromers were added, with incubation at 37°C for 7 days for PEG-NHS based macromers, and storage at 4°C overnight for GA treated SPNPs. After treatment, the particles were collected and treated following protocols for secondary structure analysis based on deconvolution of CD signals.[218] Briefly, the particles were collected using a 10 mM Potassium Phosphate, 100 mM potassium fluoride (pH: 7.4) buffer. The collected solution was filtered using a 0.22 um syringe filter, and the protein concentration measured using a Nanodrop 2000c Spectrophotometer (Thermo Fisher Scientific), with the absorption at 280nm measured and converted to mass concentration using an extinction coefficient of 85.1 $M^{-1}cm^{-1}$.[219]

The samples were then diluted to a concentration of 0.15 mg/mL and measured in a 0.1 cm pathlength Hellma quartz cuvette in a Jasco J-815 CD Spectrometer. Temperatures were controlled using a Peltier stage. Spectra were acquired at a stage temperature of 20°C from 185-260 nm, using a data pitch of 0.2 nm, D.I.T. of 1 sec, bandwidth of 1 nm, and a scan speed of 50 nm/min. Each sample was measured for a total of 10 accumulations and was smoothed using Savitzky-Golay algorithm (Convolution Width of 21) and normalized to the buffer. Native and denatured proteins were measured by dissolving undisturbed protein in the same buffer at the nanoparticle samples. A thin layer of mineral oil was placed atop the sample to reduce evaporation, and the sample was measured at 20°C for the native protein control measurement. The sample was then heated to 90°C

and subsequently allowed to equilibrate for 5 min prior to measurement for the denatured sample. The smoothed signals were analyzed for secondary structure using DichroWeb.[220–224]

2.3.6 SEM Particle Analysis

The SEM image presented and analyzed post-jetting and prior to resuspension. The images were assessed sequentially for different regions of the samples until the total number of particles assessed were greater than 200 for each formulation (uncrosslinked and crosslinked). The images were then assessed *via* ImageJ (FIJI distribution ImageJ 1.53c) (**Figure 2-1**). Briefly, the methodology employed is as follows.

1. Intensity histograms of the raw 16-bit images were assessed.
2. Image balancing was performed such that rescaling of the intensity distribution per pixel was set to span the entire intensity range.
3. Images were converted to 8-bit and a single gaussian average was taken (0.5 pixel sigma).
4. Thresholding was performed such that the kept binary image represented all pixels that were more intense than the trailing inflection point on the histogram associated with the background (dark) pixels.
5. Watershed separation of overlapping particles was then performed, with manual separation of unseparated particles based on observations in the raw image.
6. Particle analysis was performed for all systems utilizing an area threshold of >500 nm^2 and a circularity of >0.50, with collection of the Feret diameter, area, and circularity being paramount.
7. Resulting data sets were compiled and untilized for bulk number average statistics (average diameter and sample distribution presented as the standard deviation of diameter).

8. A calculated PDI (polydispersity index), denoted by PDI*, was generated via the following method in order to relate dry state (SEM) data to hydrodynamic state (DLS) data:
    a. The data sets for diameter were binned in 10 nm bins centered on increments of 10 nm.
    b. These bins were then converted to arbitrary mass units, using half of the diameter as the radius while converting to volume.
    c. Number average, weight average, and z-average molecular weights were determined for each data set.
    d. PDI* was then calculated using the number average standard deviation divided by the z-average molecular weight derived diameter (in a accordance with the PDI reported by light scattering methods; PDI = S/dz) allowing direct comparison to the DLS data.

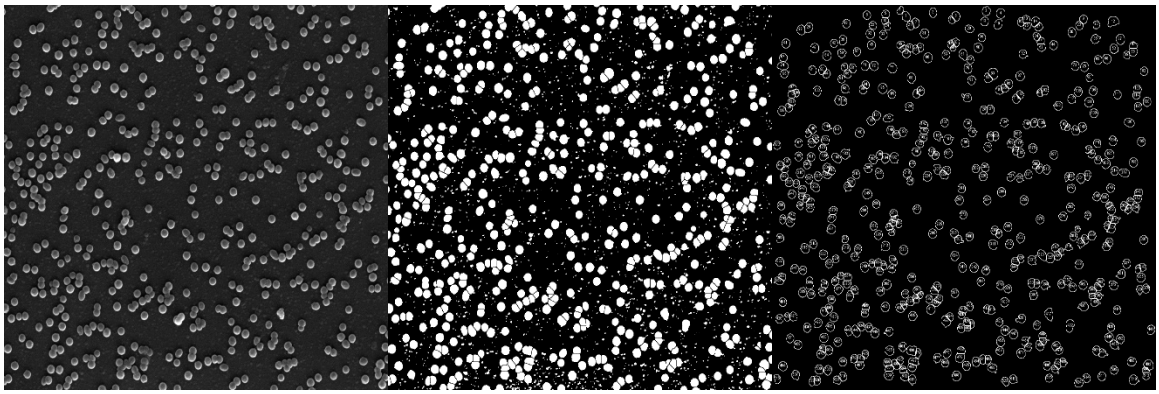

Figure 2-1. Example of inputs and outputs for particle characterization. Left: well contrasted and calibrated SEM image. Center: Binary representation of thresholded image. Right annotated skeletonized plot of particles for which data was extracted.

Assessment of the resulting SEM-based data sets was performed using GraphPad Prism software (v. 8.4.3), to include all summary statistics and the fitting of diameter histograms for the purpose of comparisons to DLS results. Fitting of the histograms was performed by using the lognormal distribution function and the least-square method. All fits were reasonably well correlated to the distributions, having R^2 values ranging from 0.89 to 0.98 and a 95% confidence interval of the geometric mean being less than ±4 nm in all cases. Graphical presentation of the comparison of the SEM particle diameter distribution fitted lognormal equations to the DLS intensity-based results exist for ease of communication; direct comparison between an intensity-based and count-based system via statistical methods would be inappropriate. Instead, result summary statistics (diameter-SEM v. diameter-DLS, PDI* v. PDI) should be compared.

Assessment of the SEM diameter was performed using one-way ANOVA, with Tukey's post-test, between raw data sets. Presentation of the ANOVA results are presented as embedded tables in the figures where this was performed. *P*-values for failing to accept statistical equivalency between distributions are presented with conventional denotation: ns ($P > 0.05$), * ($P < 0.05$), ** ($P < 0.01$), **** ($P < 0.001$), and **** ($P < 0.0001$). Assessment of the profiles for DLS results, which are intensity derived and not based on counts, was instead performed with conversion of the intensity data into whole counts. These counts were normalized to n = 200 in order to have statistical significance similar to the SEM data (which was performed until n > 200 was reached).

2.3.7 Cell Culture

HeLa cells (ATCC) were grown at 37C in a humidified environment at 5% CO_2. Cells were cultured in DMEM media supplemented with 10% fetal bovine serum (FBS), 1% Non-essential Amino Acids (NEAA), D-glucose (25 mM), and Sodium Pyruvate (1 mM). Cells were passaged at 70-80% confluence and media changed as needed.

The immortalized human cerebral microvascular endothelial cell line hCMEC/D3 (Millipore Sigma) was grown at 37C in a humidified environment at 5% CO_2. Cells were maintained using the EndoGRO-MV Complete Culture Media Kit supplemented with 1 ng/mL human animal-free basic fibroblast growth factor (bFGF-AF) and 1% Penicillin–Streptomycin. Cells were cultured on collagen-coated tissue culture flasks, which was prepared using a 1:20 dilution of Collagen Type I, Rat Tail, and allowed to coat in the incubator for 1 hour prior to use. Cells were passaged at 70-80% confluence, between passage 27 and 36, and media was changed as needed.

2.3.8 SPNPs Uptake by HeLa Cells

Confocal Microscopy

HeLa cells were seeded in 8 well chamber slides at a concentration of 50000 cells per well and allowed to adhere overnight. SPNPs were sonicated in ice, and immediately added at a concentration of 10 μg mL^{-1} to cell media supplemented with penicillin (100 Units mL^{-1}), streptomycin (100 μg mL^{-1}), and Amphotericin B (250 ng mL^{-1}). 200 μL of SPNP solution was incubated with the particles for 1h. Particle media was removed following incubation, and the cells thoroughly washed with DPBS. Cells were fixed with 4% paraformaldehyde, washed with DPBS, and then stained with Alexa Fluor 488 Phalloidin following manufacturer recommendations. The samples were then air dried, mounted using ProLong Diamond Antifade Mountant with DAPI, and allowed to cure for 24h prior to imaging. Confocal micrographs were obtained using a Nikon A1si inverted confocal microscope. A 60X water objective with excitation at 401, 488, and 641nm for the cell nuclei, actin fibers, and SPNPs, respectively was used for image acquisition. NIS-Elements and ImageJ software was used for image acquisition and processing.

Flow Cytometry

HeLa cells were seeded in a 96-well plate at a density of 30000 cells per well. After overnight incubation at 37°C and 5% CO2, the media was then removed from the wells, and fresh media containing each SPNPs group at 10 μg mL^{-1} was added to the wells. The cells were incubated with SPNPs for 24h. The cells were washed with DPBS three times and then trypsinized. The cells were washed two more times and stained with DAPI before analyzing them with Cytoflex (Beckman Coulter) cell analyzer located at the Flow Cytometry Core of the University of Michigan. FlowJo software was used for data analysis. Statistical analysis was conducted using a one-way ANOVA, followed by Tukey's post-test, using GraphPad software. A *P*-value of <0.05 was considered statistically significant (*$P < 0.05$, **$P < 0.01$, ***$P < 0.001$, and ****$P < 0.0001$).

2.3.9 Blood Brain Barrier Transwell Assay

Transwell inserts (6.5 mm, 3.0 μm Pore Polyester Membrane) were coated with 50 μL of diluted human fibronectin to achieve 10 μg/cm^2 and allowed to coat for at least 1hour at 37°C. Upon removing excess coating solution, inserts were washed with Dulbecco's phosphate-buffered saline (DPBS) before immediate use. hCMEC/D3 cells were seeded into the apical compartment at a density of 330,000 cells/mL in 100 μL of complete media. The basolateral compartment was filled with 600 μL of complete media. Inserts were incubated at 37°C, 95% humidity and 5% CO_2. Media was changed every other day. Transendothelial electrical resistance (TEER) was monitored throughout the growth. Models were used for particle transport studies after 7 days of culture.

For particle transport studies, 5×10^{10} nanoparticles/mL hTF- or HSA-SPNPs were prepared in complete cell culture media and added to the apical compartment of the blood brain barrier transwell insert after the 7 days of culture. The companion plate in the basolateral compartment contained only complete culture media. At each hour timepoint for 6 hours, a 100 μL aliquot was

sampled from the basolateral compartment and pipetted into a 96-well plate. 100 µL of fresh complete cell culture media was immediately added to the basolateral compartment upon removal. Fluorescence intensities of samples obtained from the basolateral medium after 1hour, 2 hours, 3 hours, 4 hours, 5 hours, and 6 hours were measured in triplicate using the BioTek Synergy H1 Hybrid Multi-Mode Microplate Reader. Solute concentration was determined based on calibration curves of standard fluorescence intensities created in triplicate. Percent transport (%) of SPNPs were then calculated.

2.3.10 Bicompartmental SPNPs Synthesis

Bicompartmental SPNPs were synthesized using GA but using a parallel capillary EHD co-jetting setup previously described.[86,128,139,217]

2.3.11 SIM Microscopy of Bicompartmental SPNPs

Anisotropic SPNPs with two compartments were synthesized as described above using HSA and hTf. To facilitate imaging of the resulting particles, BSA Alexa 488 and hTf Alexa 647 were incorporated, at 0.08% of the total protein mass, into the albumin and transferrin protein jetting solutions, respectively. GA was used to crosslink the resulting ASPNPs. Albumin-transferrin ASPNPs were collected and purified as previously described and finally suspended directly in Prolong Diamond before being deposited onto glass slides. Samples were allowed to cure for at least 24h prior to imaging. Structured illumination microscopy (SIM) imaging was conducted using a Nikon N-SIM +A1R confocal microscope equipped with a 100x objective oil objective. Excitation using the 488 and 647 lasers were used for image acquisition. Three-dimensional z-stacks of multiple regions were collected and deconvoluted using the Nikon Elements software. The resulting z-stacks were analyzed to confirm bicompartmental particle architecture.

2.3.12 Statistical Analysis

Statistical analyses were performed using Graphpad, Prism 8.3.0, (GraphPad Software, LaJolla, CA). One-way analysis of variance (one-way ANOVA), followed by Tukey's post-test was used in the Hela cell SPNP uptake experiment and non-paired, two-tailed *t*-test was used in the blood brain barrier SPNP transport assay to determine significance among groups. A *P*-value of < 0.05 was considered statistically significant ($*P < 0.05$, $**P < 0.01$, $***P < 0.001$, and $****P < 0.0001$); *P*-values of >0.05 were considered not significant (ns).

2.4 Results and Discussion

2.4.1 Fabrication of SPNPs via EHD jetting

To prepare SPNPs using reactive electrojetting, particles are first made using EHD jetting. Protein is dissolved in an aqueous solvent system with 10% ethanol. The addition of an organic solvent increases the volatility and decreases the surface tension of the solution.[225] Solid nanoparticles are then prepared by accelerating the jetting solution in an electrical field created between the tip of the jetting needle and a collection plate (**Figure 2-2A**). Once the electrical potential is applied, a Taylor cone is spontaneously formed[226] and the jet is ejected from the Taylor cone towards the collection plate. In EHD jetting, conditions (i.e., surface tension, flow rate, solute concentration, applied electric field) can be controlled to result in either particle or fibral formation. The protein concentrations in all jetting solutions were maintained 10% (w/v) or lower to ensure that only particles were formed. After EHD jetting, particles were examined for uniformity and sphericity using scanning electron microscopy (SEM) (**Figure 2-2B**).

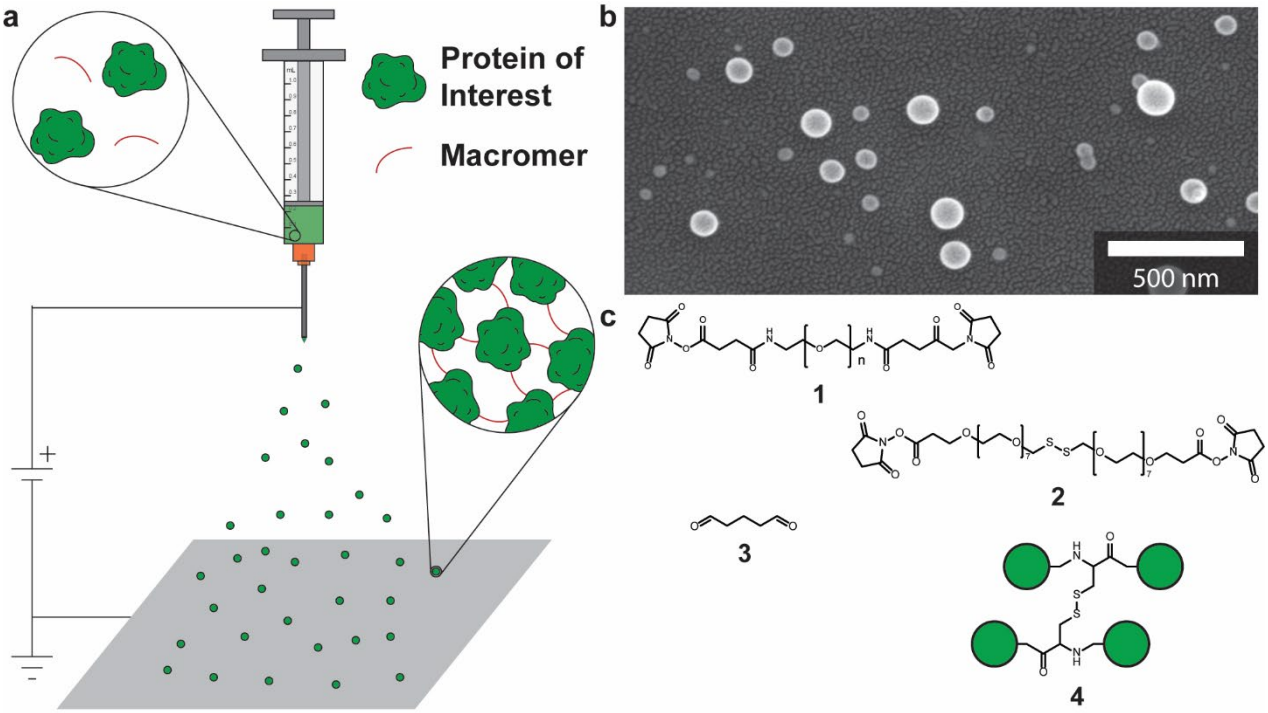

Figure 2-2. Preparation of synthetic protein nanoparticles using reactive electrojetting. (A) Schematic of reactive electrojetting setup. (B) SEM images of particles made using EHD jetting. Particles are jetted, and subsequently (C) polymerized using a variety of different macromers: 1. (PEG-NHS), 2. (PEG-NHS-S), 3. (GA), and 4. (S-S)

Circular dichroism (CD) spectroscopy demonstrated that component proteins had unchanged secondary structures compared to their native confirmations (**Figure 2-3** and **Table 2-1)**.

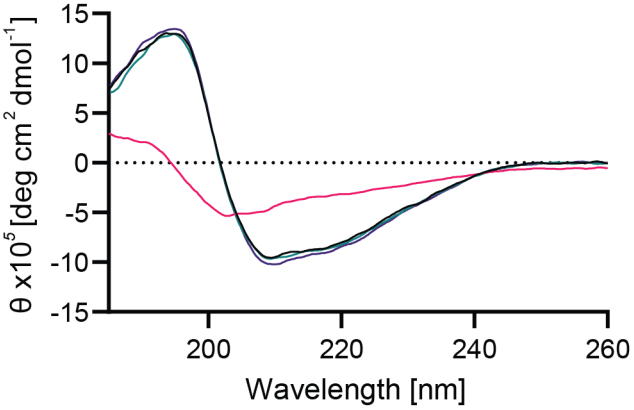

Figure 2-3. The effect of EHD jetting on proteins was analyzed using CD spectroscopy. Transferrin was jetted and treated as described in the text but did not include macromer for NHS-

PEG and NHS-PEG-S (purple) or GA (green). Native (black) and heat denatured transferrin (pink) were measured as controls.

Table 2-1. The measured CD spectra for free transferrin controls and analogues for methods 1-3 were deconvoluted using the different algorithms and neural networks available in Dichroweb. For all but the denatured transferrin, most of the algorithms were able to fit the measured signals within high degrees of certainty, and the ratios of secondary structures were similar to those found using X-Ray crystallography (from PDB). Additionally, the ratios found for all algorithms matched almost identically for the different polymerization methods studied.

Sample	Sample Treatment	Structure	X-Ray	Selcon3	Contin-LL	CDSSTR	K2d
Free Transferrin	Native	α-Helix	0.34	0.29	0.25	0.24	0.29
		β-Sheet	0.19	0.24	0.27	0.30	0.27
		Turn	0.22	0.23	0.23	0.22	ND
		Unordered	0.25	0.28	0.26	0.26	0.43
	Denatured	α-Helix	NA	0.07	0.15	0.06	0.09
		β-Sheet		0.32	0.32	0.33	0.39
		Turn		0.19	0.23	0.27	ND
		Unordered		0.30	0.30	0.33	0.52
Jetted Transferrin	Methods 1 and 2	α-Helix	NA	0.25	0.25	0.24	0.29
		β-Sheet		0.24	0.27	0.28	0.30
		Turn		0.23	0.22	0.22	ND
		Unordered		0.28	0.26	0.26	0.41
	Method 3	α-Helix	NA	0.25	0.25	0.24	0.29
		β-Sheet		0.24	0.27	0.28	0.30
		Turn		0.23	0.22	0.22	ND
		Unordered		0.28	0.26	0.26	0.41

2.4.2 Library of SPNPs – Different Reactive Macromers

The second step of reactive electrojetting is the reaction of the proteins in the nanoparticles with a variety of reactive macromers, such as short NHS-ester functionalized polyethylene glycol (PEG)

chains (**Figure 2-2C**). The reaction occurs during or immediately after the EHD jetting process, rendering the SPNPs stable in aqueous environments and locking in their geometry. A small library of commercially available macromers was selected to investigate different sol/gel transitions. The first two macromers, 2KDa O,O′-Bis[2-(N-Succinimidyl-succinylamino)ethyl]polyethylene glycol (PEG-NHS) and 4,7,10,13,16,19,22,25,32,35,38,41,44,47,50,53-Hexadecaoxa-28,29-dithiahexapentacontanedioic acid di-N-succinimidyl ester (PEG-NHS-S), react the macromers' ester functional groups with the proteins' amine groups. This reaction completes after SPNPs are deposited by EHD jetting onto the collecting surface and then placed at 37 °C for 7 days. The third macromer, glutaraldehyde (GA), binds proteins together by reacting aldehyde groups with a variety of protein residues.[227] GA crosslinking is conducted immediately after EHD jetting, when dried protein particles are placed in a sealed container containing 20% glutaraldehyde, which vaporizes and reacts at room temperature. The last crosslinking method does not rely on a macromer but instead takes advantage of native disulfide bonds within proteins (S-S). Prior to EHD jetting, proteins are treated with trifluoroethanol (TFE) and β-mercaptoethanol (BME) to disrupt native protein structure and break intermolecular disulfide bonds.[228,229] The solution is then jetted as described previously. While droplets are traveling to the collecting surface, TFE and BME evaporate allowing the disulfide bonds to reform between proteins, resulting in insoluble SPNPs on the collecting surface.

PEG-NHS was selected as a biocompatible and biodegradable macromer that can be imparted with functional groups. PEG-NHS-S showcases the flexibility of macromers based on PEG-NHS. By incorporating stimuli responsive groups into the PEG chain, such as the disulfide in the PEG-NHS-S, particles can be made to react in response to different environments. GA vapor treatment was developed as a faster alternative to PEG-NHS macromers, as the vapor-phase reaction occurs in

as little as 30 minutes to form fully water insoluble SPNPs. Thus, GA allows for the incorporation of time sensitive agents into SPNPs, such as radiotherapeutics. S-S was developed to have a method which does not use any available functional groups on the protein residues, unlike the three other macromers. Additionally, S-S takes place in an organic solvent system, as opposed to the aqueous system used for the other macromers. This different solvent system introduces the ability for SPNPs to be loaded with hydrophobic drugs, opening up a large number of potential therapeutics for drug delivery with SPNPs.

To further narrow particle size distribution, particles were first collected, then sonicated to cause disaggregation, and were size purified using a previously established serial centrifugation technique.[136] After hydration, particles made with human transferrin (hTf) and each of the different macromers were measured using dynamic and electrophoretic light scattering (DLS and ELS), and were found to have similar size distributions and zeta potentials (**Figure 2-4**).

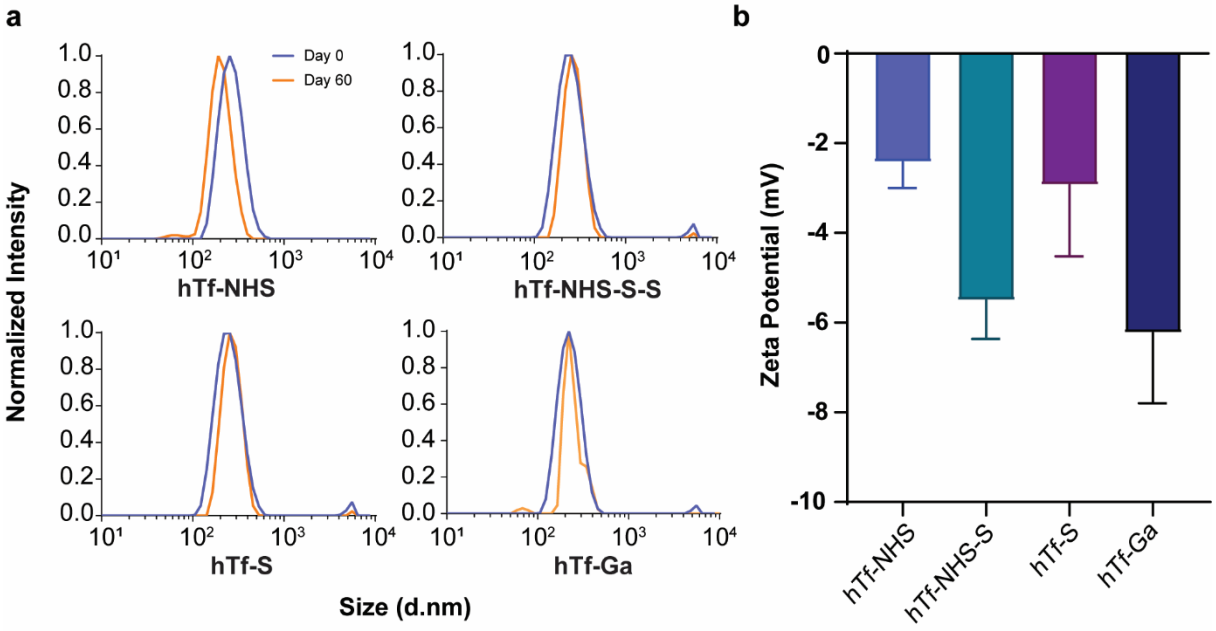

Figure 2-4. Different macromers do not significantly change size or zeta potential and are stable over a 1 month period. hTf SPNPs were made with all 4 different macromers, and (A) their sizes after synthesis and 60 days later were measured using DLS. Macromers were found to not affect

particle size, and the particles maintained stability over the time period. (B) The same SPNPs were measured using ELS and found to not have significantly different zeta potentials.

To show how macromer conditions can be used to tailor SPNPs hydrodynamic size, human serum albumin (HSA) particles were made with PEG-NHS. The hydrodynamic size was tuned by changing the macromer to protein ratio. Increasing the ratio of macromer to protein does not overtly appear to alter the diameter of the particles in the dry state relative to increasing ratio.

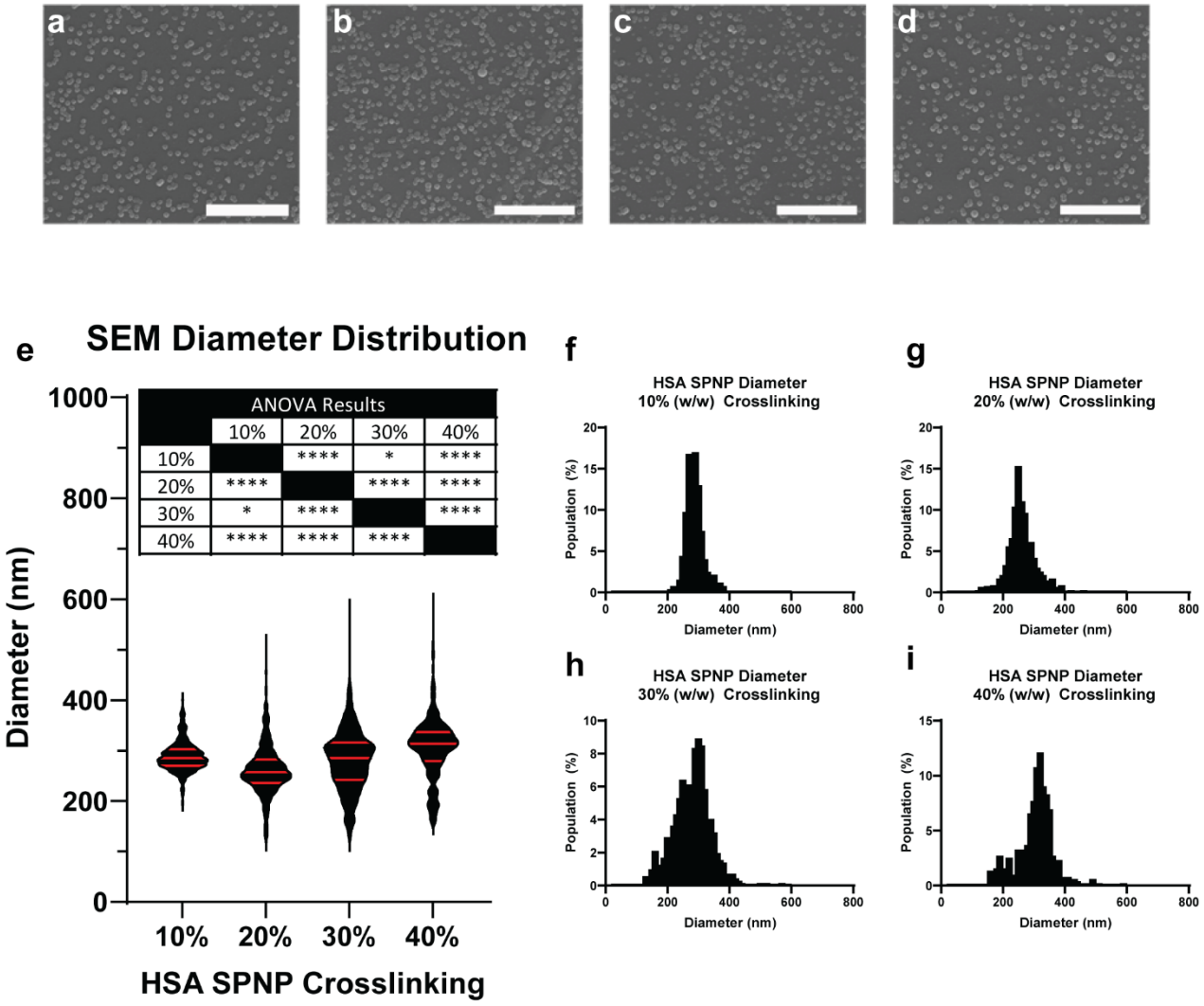

Figure 2-5. SEM diameters for varied content of crosslinking macromer in HSA SPNPs. Images (A-D): SEM images of SPNPs synthesized with (A) 10%, (B) 20%, (C) 30%, and (D) 40% (w/w) of crosslinking macromer relative to HSA; scale bars are 4 μm. (E) Diameter distributions for the SEM micrographs of SPNPs presenting as a count distribution violin graph (with mean and quartile

markers in red) and the associated ANOVA results. (F-I) Diameter histograms of SPNP made with (F) 10%, (G) 20%, (H) 30%, and (I) 40% crosslinking macromer relative to HSA content. Note that no clear pattern arises from assessing crosslinking extent in the dry state.

However, as the amount of macromer is increased, the SPNPs expand less under hydrodynamic conditions. This can be seen observed as a 33% decrease in the mean hydrodynamic diameter as one goes through the series from 10% to 40% macromer (**Figure 2-5**, **Figure 2-6**, and **Table 2-2**). It should be noted that these measurements were of centrifuged particles in their hydrated state, in order to allow for an accurate comparison to particles in their dry state.

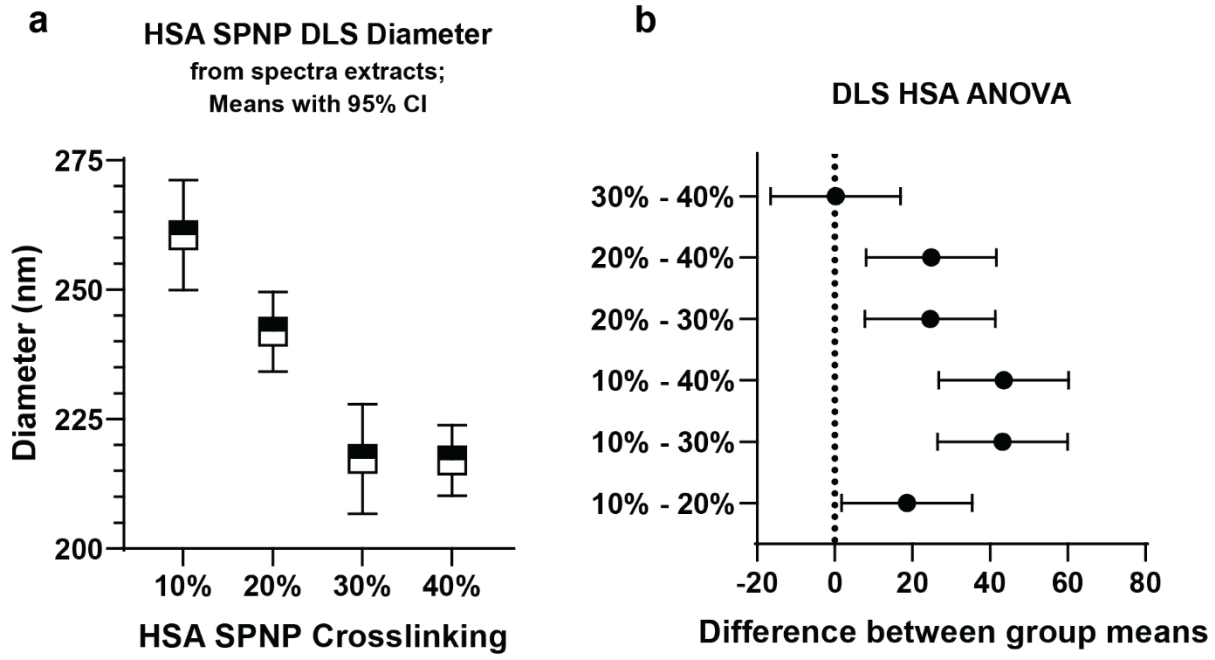

Figure 2-6. HSA SPNP diameter by degree of crosslinking. (A) statistical means with 95% confidence interval of the error in the mean. (B) Graphical presentation of the ANOVA results indicating that 10% < 20% < 30% ≈ 40% in terms of hydrodynamic diameter. This indicates that particle swelling is constrained with increased crosslinking. This data was obtained from the samples presented in **Figure 2-5** with explanation of methodology above in the experimental section.

Table 2-2. Summary dimensional data for all SPNPs presented in this work.

	SEM Diameters (dry)		DLS Diameters (hydrodynamic)	
	Diameter (nm)	PDI*	Diameter (nm)	PDI
hTf-PEG-NHS	99 ± 33	0.20	223 ± 12	0.23
Ins-PEG-NHS	68 ± 27	0.15	224 ± 25	0.47
Hem-PEG-NHS	79 ± 49	0.16	269 ± 21	0.26
Lys-PEG-NHS	75 ± 30	0.23	264 ± 10	0.42
HSA (10%)	288 ± 29	0.10	273 ± 75	0.29
HSA (20%)	261 ± 48	0.14	237 ± 76	0.38
HSA (30%)	280 ± 60	0.16	212 ± 55	0.36
HSA (40%)	305 ± 60	0.15	182 ± 58	0.28
hTf-PEG-NHS (day 7)	-	-	204 ± 10	0.28
Ins-PEG-NHS (day 7)	-	-	243 ± 11	0.41
Hem-PEG-NHS (day 7)	-	-	253 ± 18	0.28
Lys-PEG-NHS (day7)	-	-	278 ± 19	0.37
hTf-NHS (Day 0)	-	-	263 ± 32	0.497
hTf-NHS-S (Day 0)	-	-	220 ± 28	0.478
hTf-S (Day 0)	-	-	262 ± 16	0.31
hTf-Ga (day 0)	-	-	256 ± 9	0.577
hTf-NHS (Day 60)	-	-	207 ± 16	0.43
hTf-NHS-S (Day 60)	-	-	209 ± 35	0.52
hTf-S (Day 60)	-	-	272 ± 6	0.35
hTf-Ga (day 60)	-	-	215 ± 39	0.57

Variances expressed are sample standard deviations of the distributions and do not represent uncertainty of measurments, confidence intervals, fitted parameters, or standard errors. Where present in this study, distributions of raw data should be compared.

2.4.3 Library of SPNPs – Different Proteins

We also explored how reactive electrojetting can make SPNPs from a variety of proteins. A small library of proteins was selected to synthesize SPNPs, each with potential biomedical applications: human transferrin,[230] insulin (Ins),[231] hemoglobin (Hem),[232] and lysozyme (Lys).[233] For these experiments, each protein was used to fabricate stable SPNPs with PEG-NHS. Proteins were dissolved as previously described, with the exception of Ins which was dissolved by adding 10% acetic acid to the solvent mixture, due to poor solubility in neutral aqueous conditions.

SEM images of SPNPs as sampled from the collecting surface demonstrated that different proteins did not affect the morphology of the resulting particles (**Figure 2-7A-D**). After the reactive electrojetting process, the resulting particles have typical diameters at or below 100 nm and are monodisperse (PDIs range from 0.15 to 0.23), as seen by SEM (**Figure 2-8**, **Figure 2-9**, **Figure 2-10**, and **Table 2-2**).

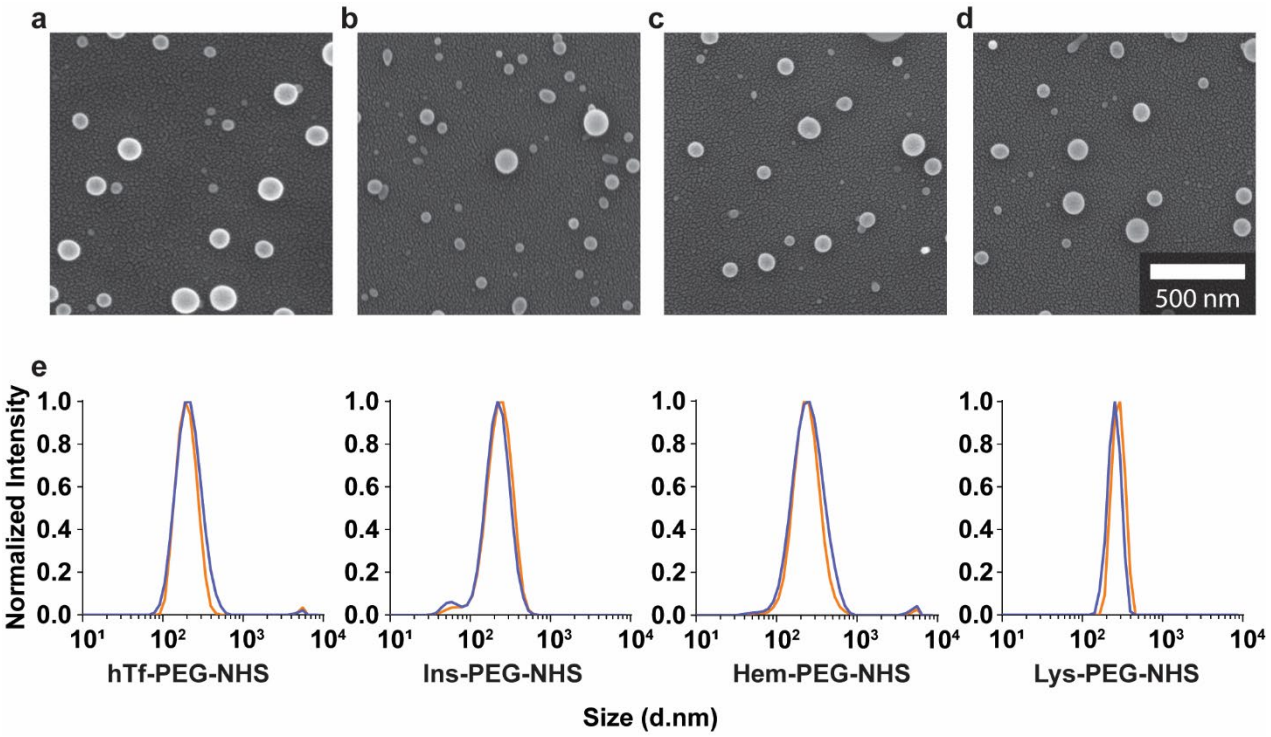

Figure 2-7. Stable synthetic PNPs can be made using a variety of proteins. SEM images of SPNPs made from (A) hTf-PEG-NHS, (B) Ins-PEG-NHS, (C) Hem-PEG-NHS, and (D) Lys-PEG-NHS. (E) The stability of particles in PBS over a one-week period was characterized by measuring the particles using DLS 1 day (blue trace) and 7 days (red trace) after synthesis and size purification.

To evaluate the stability of the particles, SPNPs were collected, size purified, and stored at 4 °C for 7 days. Their size distributions after a week showed no significant difference, confirming particle stability after storage (**Figure 2-7E** and **Table 2-2**).

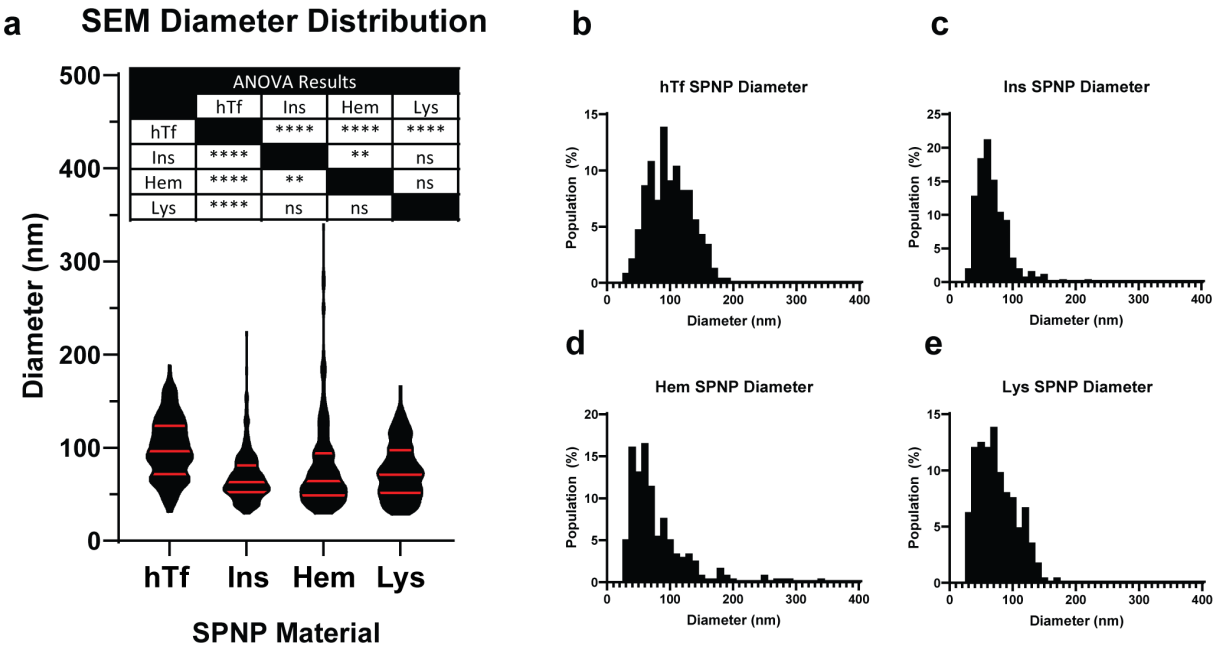

Figure 2-8. Diameters measured by SEM. (A) Diameter distributions for the SEM micrographs of SPNPs presenting as a count distribution violin graph (with mean and quartile markers in red) and the associated ANOVA results. (B-E): diameter histograms of SPNP made with (B) hTf, (C) Ins, (D) Hem, and (E) Lys. This data was obtained from the samples presented in **Figure 2-7**.

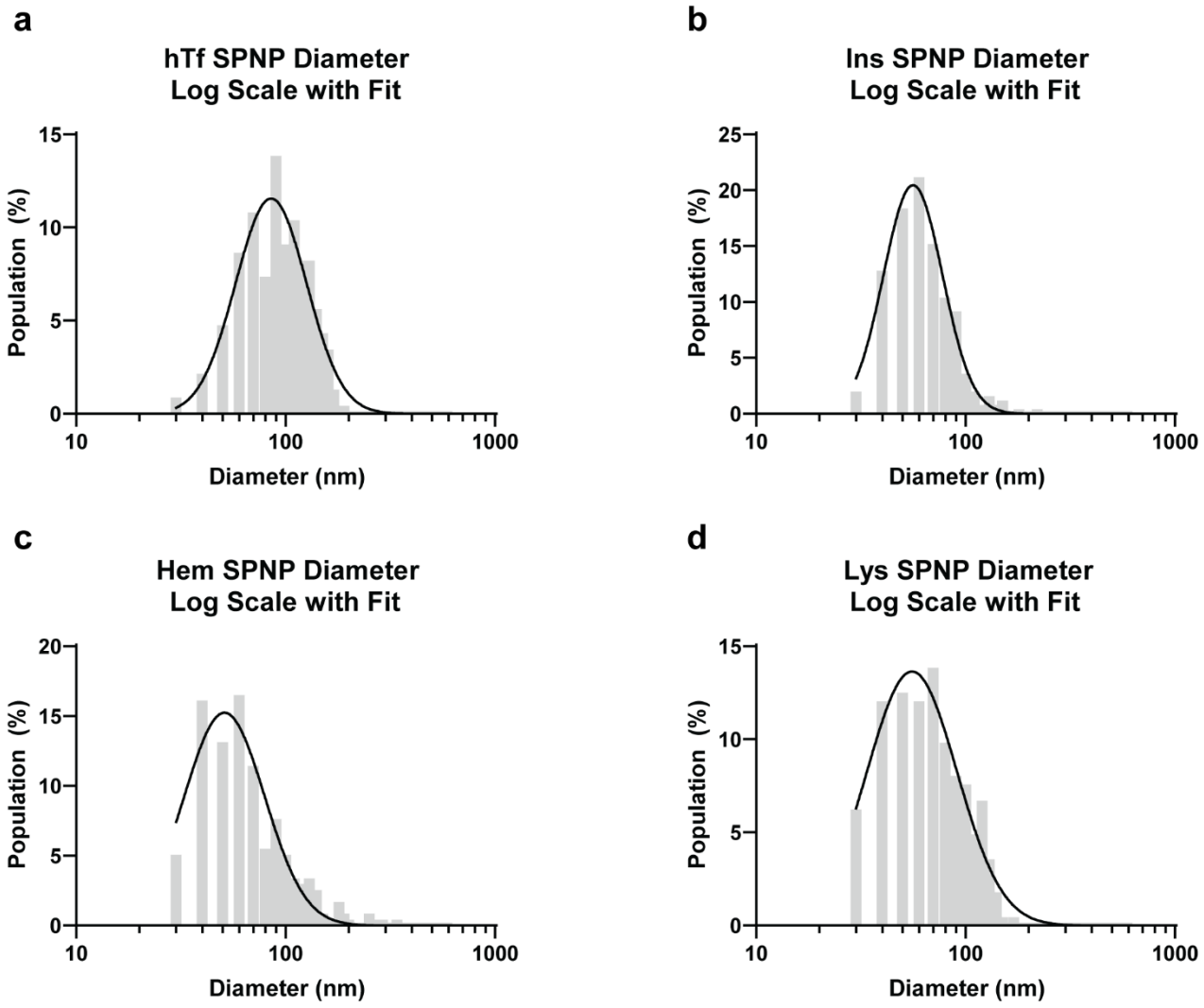

Figure 2-9. Lognormal fitting of diameter histograms measured by SEM. Fitted diameter histograms of SPNP made with (A) hTf, (B) Ins, (C) Hem, and (D) Lys. This data was obtained from the samples presented in **Figure 2-7** with explanation of methodology above in the experimental section.

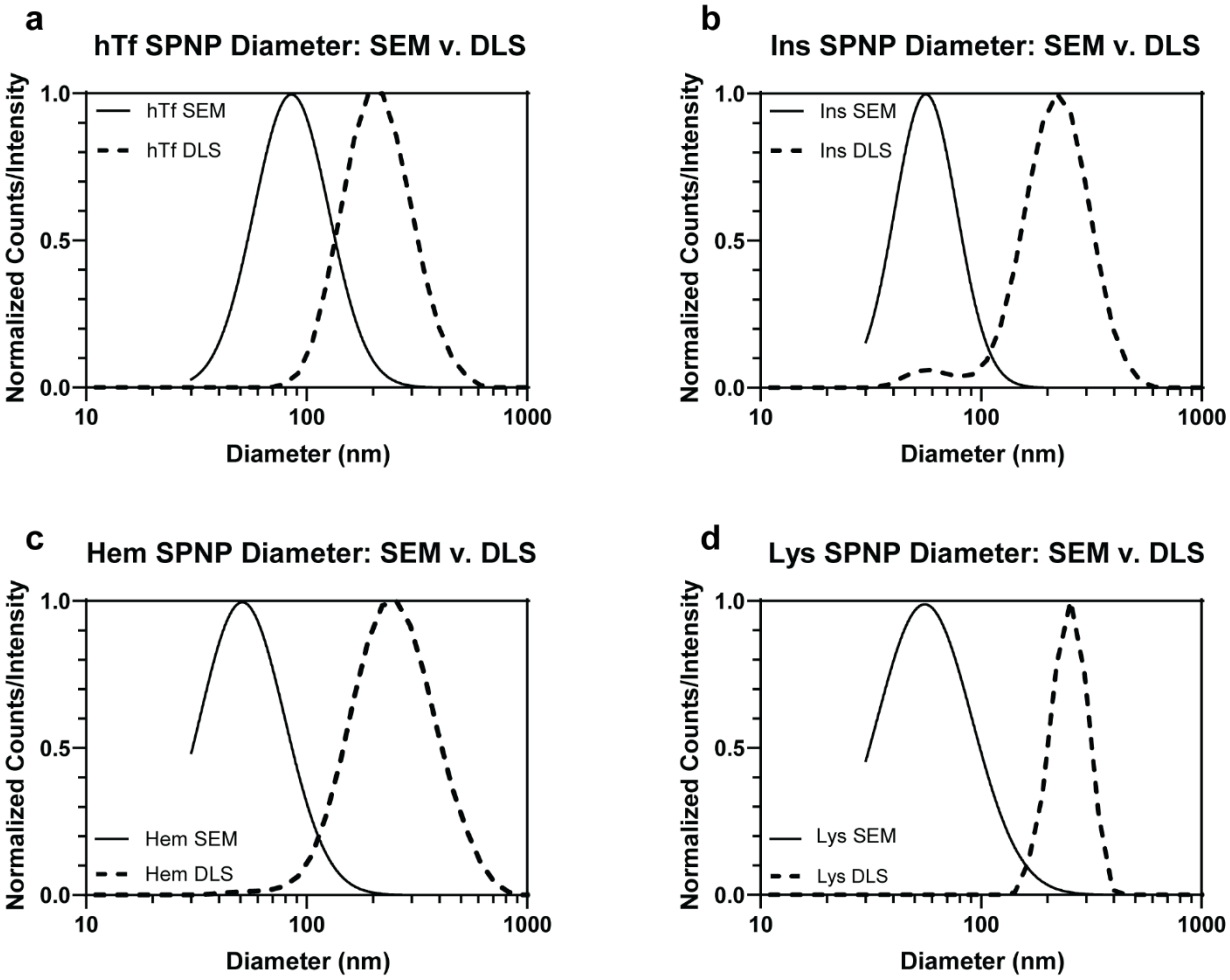

Figure 2-10. Comparison of fitted SEM diameter data from **Figure 2-9** and the DLS results for SPNP made with (A) hTf, (B) Ins, (C) Hem, and (D) Lys. This data was obtained from the samples presented in **Figure 2-7**.

Various experiments were conducted to explore how protein and macromer choice affects SPNP behavior in biological systems. To investigate the effects of different macromers on the in vitro behavior of SPNPs, hTf SPNPs were synthesized with each of the different macromers and loaded with fluorescently labeled bovine serum albumin. SPNPs were then incubated with HeLa cells. SPNPs behaved differently depending on their macromer. hTf-PEG-NHS and hTf-GA SPNPs remained punctate when observed using confocal microscopy (**Figure 2-11A** and **Figure 2-11B**). In contrast, hTf-PEG-NHS-S and hTf-S-S SPNPs, which rely on disulfide-bonds for structure,

were more diffuse (**Figure 2-11C** and **Figure 2-11D**). It is likely that these particles degraded due to disulfide bonds breaking in the cellular redox/reducing environment.[234] These effects have been observed in other particles made with similar chemical principles.[104]

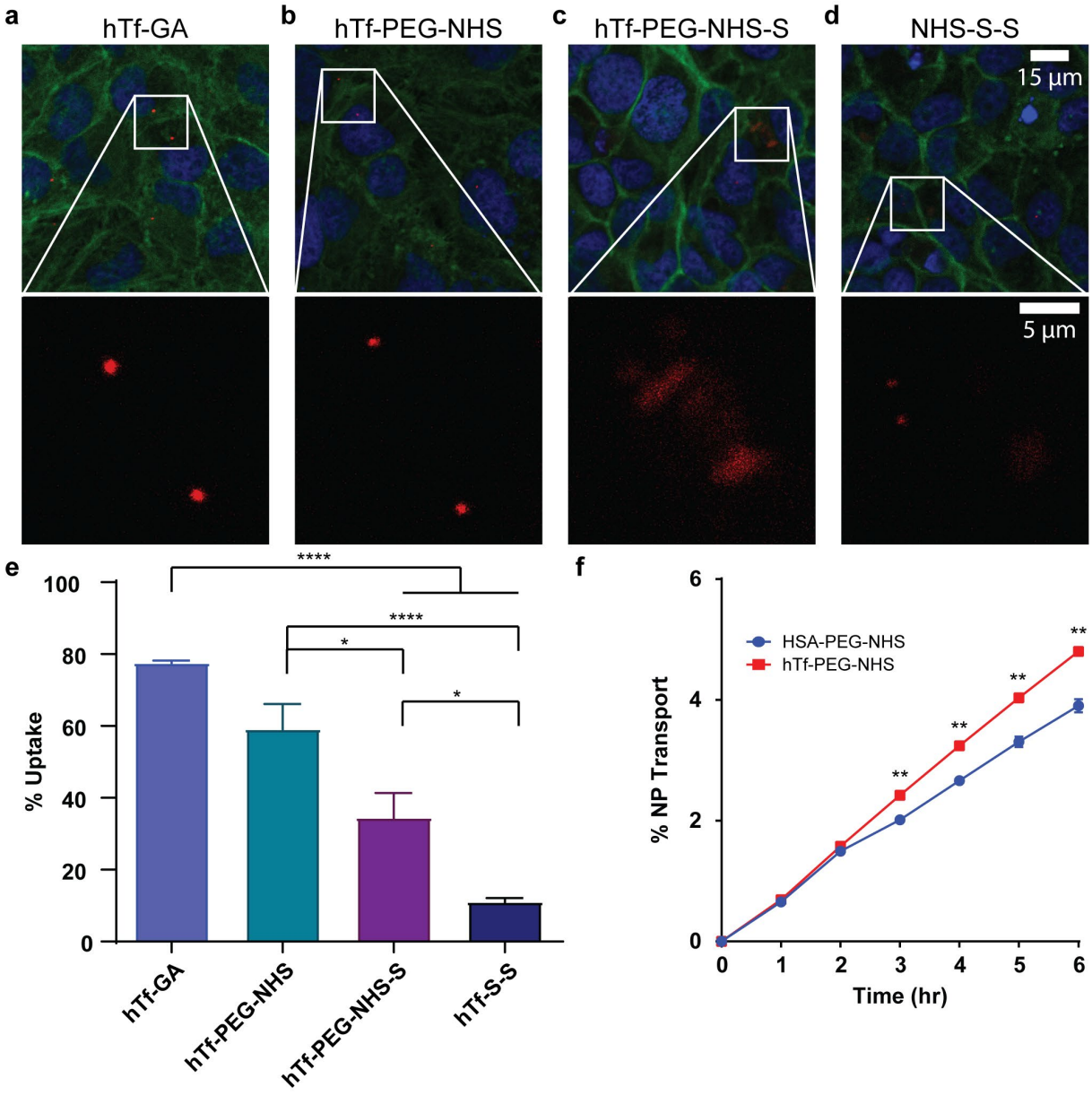

Figure 2-11. SPNPs can be made using different methods that have a distinct effect on the in vitro uptake and behavior of the particles. (A-D) Fluorescent SPNPs made with different macromers were added to HeLa cells for 1 hour, and their behavior studied using confocal microscopy. (E) Uptake was quantified using confocal microscopy using HeLa cells cultured at equivalent conditions and with SPNPs incubated for 24 hours. (One-way ANOVA, followed by Tukey's post-test). (F) SPNP BBB transport. Percentage transport of HSA and hTF SPNS across hCMEC/D3

monolayers in Transwell inserts (non-paired, two-tailed t-test). (*$P < 0.05$, **$P < 0.01$, ***$P < 0.001$, and ****$P < 0.0001$). Values are reported as mean ± SEM (standard error of the mean).

The uptake of SPNPs was evaluated quantitatively by flow cytometry (**Figure 2-11E**). There was an observed difference in the uptake level for SPNPs based on macromer. Cells incubated with hTf-GA showed a 7-fold greater uptake percentage than those exposed to hTf-S-S ($P < 0.0001$), and a 2-fold increase compared with hTf-S-S ($P < 0.0001$). Uptake values for cells incubated with hTf-GA and hTf-PEG-NHS were not statistically different. As the particles made using different macromers had no significant differences in size distributions or zeta potentials, the reasons for these observed differences are yet unknown. We hypothesize that these effects may be caused by differences in the secondary structures of the proteins after they undergo polymerization following jetting, or in the mechanical properties of the SPNPs, and this will be explored in future studies.

To demonstrate the potential of SPNPs' variable protein composition biologically, we compared the blood brain barrier (BBB) permeability of hTf-PEG-NHS SPNPs to human serum albumin SPNPs (HSA-PEG-NHS), which have been previously developed.[235]. A static in vitro BBB model was constructed using a Transwell® migration assay which analyzes cellular transport across an analogue of the BBB, where hCMEC and D3 cells are placed in the apical compartment.[236] SPNPs were fluorescently tagged, and particles that were able to go from the apical to the basolateral compartments of the assay were measured using fluorometry. hTF-PEG-NHS SPNPs exhibited higher percentage transport across the BBB model ($P < 0.01$), compared to HSA-PEG-NHS SPNPs (**Figure 2-11F**) as expected, due to the overexpression of transferrin receptors on brain endothelium. This proof-of-concept study shows potential for these SPNPs to be explored for BBB targeting in future studies.

2.4.4 Fabrication of Anisotropic SPNPs via EHD Co-jetting

Finally, we sought to demonstrate how reactive electrojetting can synthesize anisotropic SPNPs (ASPNPs). Co-jetting is a well-established method where a parallel capillary system is used to create laminar co-flow in EHD jetting.[71] To demonstrate that this technology can be applied to SPNPs, particles were made that had one compartment containing fluorescent BSA, and the other fluorescent hTf. These particles were processed as previously described and then imaged using structured illumination microscopy (SIM). As can be seen in **Figure 2-12**, the resulting particles are clearly composed of two separate compartments that are easily resolved.

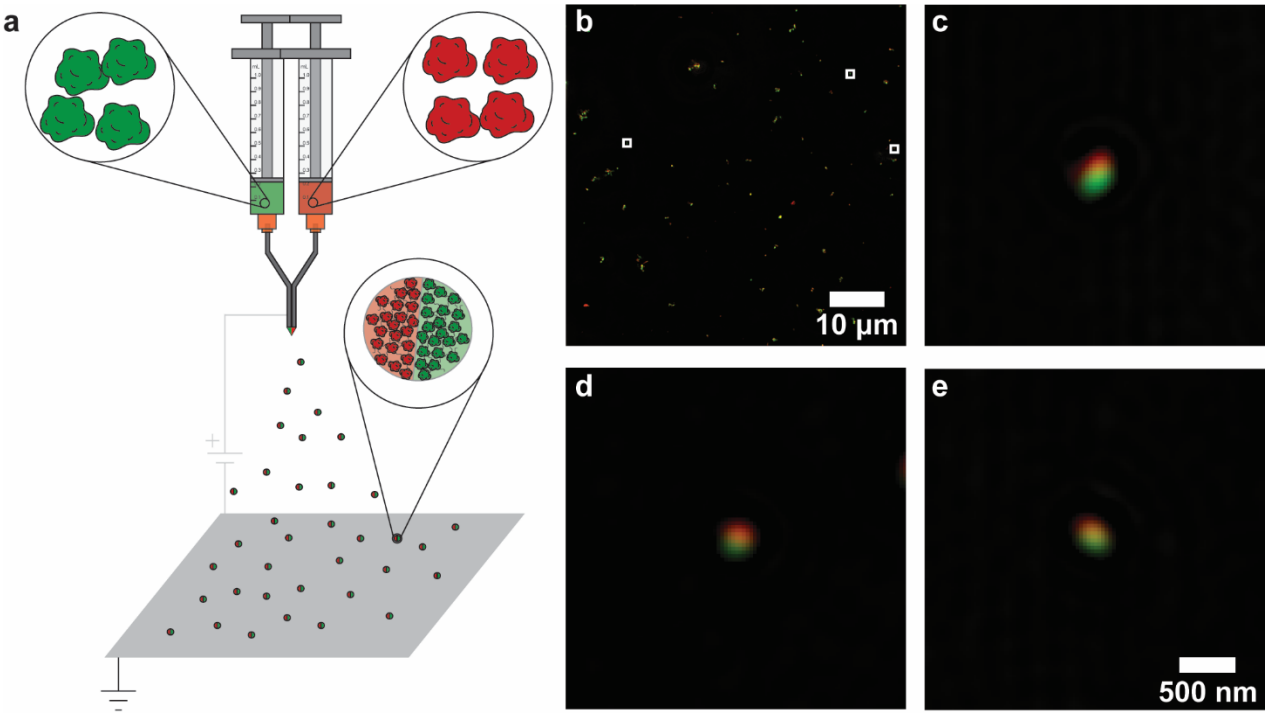

Figure 2-12. EHD co-jetting can be used to make bicompartmental SPNPs. (a) SPNPs containing HSA in one compartment and hTf in the other were synthesized, with each compartment doped with BSA-Alexa-488 or hTf-Alexa-647, respectively. The particles were imaged using SIM. (b) The images were then deconvoluted. (c-e) Zoomed in images of individual particles are shown to showcase the bicompartmental nature of the particles.

2.5 Conclusions

In this work, we have developed a method for the synthesis of synthetic protein nanoparticles fabricated using reactive electrojetting with tunable material compositions. Anisotropic SPNPs were also developed. As each compartment can be individually designed, this technique allows for the development of complex nanoparticles such that release kinetics of drug cargo from each compartment could be independently controlled, as shown in previous studies.[135,146] Novel nanoparticle-based cancer vaccines, where each compartment is made of a different cancer antigen, could provide significant therapeutic advantages. Additionally, the use of functional proteins could also lead to the delivery of protein antigen,[237] active gene therapy enzymes and nucleic acids. Recent work has shown how a treatment based on SPNPs cured mice in an intracranial murine glioblastoma model and prevented subsequent tumor recurrence from a secondary implant, suggesting immunity to cancer recurrence.[235] SPNPs have thus already started to demonstrate their potential in both the therapeutic and preventive clinical spaces. In the future, we aim to further develop these ASPNPs into a variety of clinical applications.

Chapter 3
Systematic Studies into Monodisperse Synthetic Protein Nanoparticles

The material in this chapter has been adapted with minor modifications from the following article: Nahal Habibi, Ava Mauser, Jeffery E. Raymond, Joerg Lahann. Systematic Studies into Monodisperse Synthetic Protein Nanoparticles. *In Preparation.*

3.1 Abstract

Nanoparticles are frequently discussed as drug delivery carriers, but their utility in nanomedicine is often hampered by limited control of their physical properties, such as shape, size or monodispersity. Electrohydrodynamic (EHD) jetting is a probate method to formulate synthetic protein nanoparticles (SPNPs). Here, we systematically evaluate formulation trends in SPNPs by EHD jetting a series of SPNPs comprised of 1:1 blends of carrier proteins (hemoglobin, transferrin, mucin, or insulin) and human serum albumin. All SPNPs present monodisperse populations with minimum diameters between 43 and 65 nm. Size distributions of as-jetted SPNPs approach monodispersity as indicated by polydispersity indices (PDI_{SEM}) ranging from 0.11-0.19. Geometric factor analysis reveals high circularities (0.82 – 0.90), low anisotropy (< 1.45) and excellent roundness (0.76 – 0.89) for all SPNPs prepared via EHD jetting. Tentatively, blended SPNPs display even higher circularity and lower anisotropy, as compared to single protein SPNPs. Secondary statistical analysis indicates that blended SPNPs generally present combined features of their substituents, with some properties driven by a dominant constituent protein. Given the ease manufacturing, the versatility of composition, and control of nanoparticle size, shape, and

monodispersity, our study suggests that SPNPs from protein blends could be promising candidates as drug delivery carriers.

3.2 Introduction

As nanoparticle platforms for drug delivery transition from novelties to foundational technologies in biomedical applications,[114,238,239] it is critical that additional strategies be sought to develop nanocarriers with suitable biological and physical properties to overcome the host of barriers that exist in clinical translation.[240] Nanoparticles made of proteins hold significant promise in this respect and different methods have been adopted to fabricate protein-based nanoparticles including nab technology,[238] desolvation methods,[114] and self-assembly.[239]

The human protein albumin, a natural carrier of endogenous hydrophobic molecules,[241] has been shown to be an attractive vehicle for hydrophobic drugs in several clinical and preclinical applications.[242] Using albumin as a carrier unit, the nab technology has led to protein-based drug delivery platforms (abraxane^{TM}) that received clinical approval for the treatment of breast cancer for the delivery of Paclitaxel.[105] Paclitaxel, a hydrophobic cancer therapeutic, has historically been administered using harsh organic solvents with adverse side effects[243] and it's delivery by way of protein-based carriers helps to address mitigate harmful side effects. To leverage the endogenous properties of albumin, *nab*-technology uses a high-pressure manufacturing process to force hydrophobic drugs into the internal hydrophobic pockets of human serum albumin (HSA).[244] This leads to the formation of albumin-bound, paclitaxel loaded HSA particles with diameters of approximately 130 nm.[105,244] Since then, Abraxane^{TM} has been used for non-small cell lung cancer, late-stage pancreatic cancer, and as a treatment for metastatic breast cancer.[245,246] Nevertheless, nab-based nanoparticles suffer from significant drawbacks, such as poorly defined physical properties and/or stability in the bloodstream.[247]

Desolvation, another protein nanoparticle preparation method, has been widely used to prepare various therapeutic protein nanoparticles.[104,248,249] The desolvation process uses the addition of desolvating agents, such as ethanol or acetone to induce changes in protein structure (sometimes fully denaturing the system) and to cause subsequent precipitation of protein aggregates.[90] Self-assembly strategies also provide access to a variety of structurally diverse[96] protein nanoparticles. With the advent of *in silico* design and subsequent production of a *de novo* protein nanoparticle systems, the number of specific protein building blocks that can be designed for self-assembly strategies has increased in recent years. If a protein system can successfully be designed, these synthetic proteins allow for tunable functionality and/or stability profiles.[96] Despite the complexity of processing and using these systems, the research community is exerting significant effort to make a variety of possible platforms more robust, while also increasing the total number of applications on a routine basis.[94,250]

Electrohydrodynamic (EHD) co-jetting is a versatile technology that has been utilized to fabricate compartmentalized microparticles and nanoparticles. A key property for these systems is that they can possess tunable payload delivery kinetics, can possess multiple compartments, and appropriate for a variety of drug delivery applications.[6,133] More recently, this technique has been extended to the manufacture of synthetic protein nanoparticles (SPNPs) using reactive EHD jetting, where suspended nanogels are formed during and immediately after jetting dilute solutions of proteins and reactive macromers.[251] In contrast to the protein nanoparticle methods mentioned above, EHD jetting allows for fabrication of multicompartmental protein particles.[251] Functional proteins nanocarriers are an attractive approach to drug delivery owing to their stealth, biocompatibility, and ability to exhibit the inherent functionality of the native protein. Proteins with intrinsic

function include transferrin, insulin, albumin, mucin, and hemoglobin, and represent a handful of appropriate candidates for functional SPNPs.

Multiple SPNP systems have been shown to display a broad spectrum of sizes, swelling factors, elasticities, and mesh sizes.[237] SPNPs have been used for delivery of *RNAi*-based therapeutics and have resulted in tumor regression and long-term survival in mice with glioblastoma multiforme.[235] Here, we improve on these recent efforts by elucidating the role of blended matrix proteins. Specifically, this work systematically explores the relationship between SPNP formulation parameters and nanoparticle morphology, while also providing detailed analysis of size distributions.

3.3 Materials and Methods

3.3.1 Materials

Recombinant human serum albumin was purchased from InVitria. Mucin from porcine stomach, human transferrin, human hemoglobin, recombinant human insulin, O, O′-bis[2-(N-succinimidyl-succinylamino)ethyl] polyethylene glycol (NHS-PEG-NHS) with a molecular weight of 2000 Da was purchased from Sigma Aldrich, USA. O,O′-bis[2-(N-succinimidyl-succinylamino)ethyl]polyethylene glycol (NHS-PEG-NHS) with a molecular weight of 400 Da was purchased from Nanocs Inc., USA.

3.3.2 SPNP Formulations

EHD jetting followed the protocol published by Rahmani et al.[141] Briefly, a protein solution was pumped at 0.1 mL/hr through a 25 Ga. needle. Once an electric voltage was applied the meniscus was distorted and forms a Taylor cone.[251] An electrically charged protein solution then ejected from the apex of the Taylor cone, directed to a grounded substrate positioned below the cone. The

ejected material dissociated into nanodroplets. After rapid solvent evaporation and solidification of non-volatile components, solid nanoparticles were deposited on the substrate. The reaction between lysine groups and NHS ester groups of the macromer resulted in chemical gelation that was initiated during the jetting and allowed to continue for another 7 days at 37°C in order to complete the reaction and ensure that there were no remaining NHS ester groups.

For SPNPs, the protein of interest was dissolved at 10% (w/v) in a solvent mixture of water and ethanol with a 9:1(v/v) ratio. The exception, in this work, was insulin and mucin based SPNPs. Because insulin has poor solubility at neutral pH, acetic acid 10% (v/v) was added to the solvent mixture to ensure miscibility. Due to its high molecular weight, mucin was used at 2% (w/v). NHS-PEG-NHS macromer with a molecular weight of 400 Da was added to the solution at 10% ($w/w_{protein}$) relative to the protein solution. For all blended SPNPs, a 1:1 (w/w) protein mixture was maintained, where the second protein was always HSA. The exception was the mucin/HSA system, where 4% (w/v) was used.

3.3.3 Collection and Processing of SPNPs

The SPNPs collection process followed standardized protocols previously described.[251] Briefly, a solution of 0.01% of Tween20 in Dulbecco's phosphate buffered saline (DPBS) was added to the crosslinked SPNPs collection plates and physically agitated to release the SPNPs from the surface of the collection plates. This suspension was sonicated to disrupt SPNPs aggregates then filtered through a 40µm cell filter to remove any large debris. To further remove larger SPNPs, undisrupted aggregates and other debris, the following centrifugation steps were followed. First, the SPNPs were subjected to centrifugation at 3220 rcf for 5 minutes whereby the pellet was discarded and the supernatant was further centrifuged at 21500 rcf for 1 hour at 10˚C. The final SPNPs were washed with DPBS to remove remaining Tween20 used in the collection process.

3.3.4 SPNPs Characterization

Scanning Electron Microscopy (SEM)

SEM images of as-jetted particles in their dry state were obtained using a FEI Nova 200 Nanolab SEM/FIB at the Michigan Center for Materials Engineering using an acceleration voltage of 5kV. Particles were sputter coated with gold for 40 seconds using SPI-Module Carbon/Sputter Coater, which is optimized for monolayer deposition. Typical fields of view (FOV) were 5 microns and pixel sizes were in the range of 2 nanometers. Collected images were semi-randomized; A random FOV was selected approximately near the center of mass for the substrate, with subsequent images taken at a set distance in each cardinal direction (+X, -X, +Y, -Y) in order to avoid bias.

Dynamic Light Scattering (DLS)

DLS measurements were performed on particles in their hydrated state using a Zetasizer Nano ZS (Malvern Panalytical). The solution in which the particles were suspended was DPBS. DLS was employed to measure the particle size distribution after particle collection and serial centrifugation (performed to eliminate any large or anomalous structures that are known to compromise DLS results). The average of at least three measurements was reported.

The protein material was chosen with refractive index of 1.45 and absorbance of 0.001. DPBS was used as the dispersant with refractive index of 1.332 and viscosity of 0.9074. Measurements were done at 25 °C, at 3.00 mm position in a disposable microcuvette. (ZEN0040).

3.3.5 Statistical Analysis

Statistical analyses were performed using Graphpad, Prism 9.0.0, (GraphPad Software, LaJolla, CA). Analysis of variance, followed by Tukey's post-test was used. Non-paired, two-tailed *t*-tests were used. A *P*-value of < 0.05 was considered statistically significant ($*P < 0.05$, $**P < 0.01$,

***$P < 0.001$, and ****$P < 0.0001$); P-values of >0.05 were considered not significant (ns). Graphpad Prism 9.0 was used for presentation of distributions, scatter plots, and violin plots. Origin 9 was used for peak extraction. FIJI (a distribution of ImageJ v1.53c) was used for all image analysis.

3.3.6 Analysis and Nomenclature

The analysis of SEM is presented as nSEM distributions (individuals data from n > 1000 particles). In parallel to SEM size analysis, key geometric factors were also extracted. These included minimum diameter, anisotropy, circularity, and roundness. For two-factor analysis, similarity score for comparing the blend SPNPs to single protein SPNPs are reported. Score values are assessed as follows: a score of 0 indicates the system is not discernably impacted by a constituent relative to the other constituent; a score of >0 and ≤1 indicates that a minor impact is observed; a score of >1 and ≤5 indicates a moderate impact is observed; and a score of >5 indicates a major impact. The calculation of this score is derived from comparison of linear regression fits as outlined in the supporting information. While the majority of the discussion is framed in terms of number average results, all (nSEM, nDLS, iSEM, iDLS) distribution data can be found as summary results (**Table 3-2**).

3.4 Results and Discussion

3.4.1 Single Protein SPNPs

EHD jetting was used to prepare both single protein and blended SPNPs (**Figure 3-1A**) from a variety of proteins (**Table 3-1**). A range of SPNP formulations was prepared from hemoglobin (HEM), transferrin (TF), mucin (MUC), insulin (INS) and human serum albumin (HSA).

Table 3-1. Protein physiochemical properties.

Protein	Molecular weight	Ratio of hydrophilic residues / total number of residues[252]	Isoelectric point
HSA	66.5 kda [253]	41%	4.7 [254]
Transferrin	79 kDa [255]	38%	5.6 [256]
Mucin	4000-5,500 kDa [257,258]	19%	2.75 [259]
Hemoglobin	64.5 kDa [260]	30% - alpha subunit 29% - beta subunit	7.0 [261]
Insulin	5.808 kDa [262]	29%	5.5 [263]

Dilute solutions of protein(s) dissolved at 10% (w/v) in a 9:1 (v/v) mixture of water and ethanol were used for all jetting experiments. This inclusion of ethanol decreased the dielectric constant and surface tension of the solution. The exception was insulin- and mucin-based SPNPs, which were manufactured as described in the materials section. Furthermore, a homobifunctional amine-reactive macromer, NHS-PEG-NHS, was added to the jetting solution at 10% ($w/w_{protein}$). Application of bias (voltage) between the needle and collection tray resulted in a field that distorts the solution meniscus into a Taylor cone. The charged solution accelerated downward to form droplets. Rapid solvent evaporation occurred during jetting, with solid SPNPs deposited on the collection plate. Completion of the crosslinking was achieved through SPNP storage at 37 °C for 7 days.

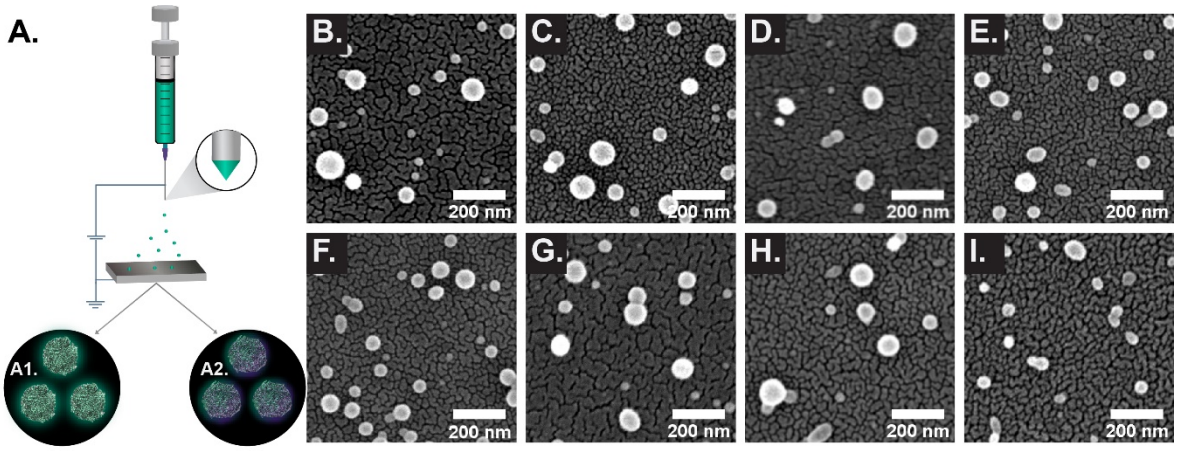

Figure 3-1. EHD jetting process and SEM images of characteristic SPNPs. (A) Synthesis of various SPNPs comprised of (A1) single proteins or (A2) binary protein blends, and PEG macromers. (B-I) SEM images of single protein and blended SPNPs. (B) HEM/HSA, (C) TF/HSA, (D) MUC/HSA, (E) INS/HSA, (F) HEM, (G) TF, (H) MUC, (I) INS. Scale bar: 200 nm.

SPNP images (SEM) and property results (size, geometric factors) are presented in **Figure 3-1B** and **Table 3-2**. A dry state size trend of TF > HSA > MUC ≈ HEM > INS can be observed, when considering mean, median, and interquartile range (IQR) values. Direct inspection of minimum diameter also reveals a similar trend of TF (65 nm) > HSA > HEM ≈ MUC ≈ INS (43 nm). Comparable PDI_{SEM} values can be observed for TF, MUC, HSA and INS (0.16-0.19); HEM is the most monodisperse (0.11) when dry. TF, HEM and HSA have comparable anisotropy and roundness values, with MUC and INS possessing increased anisotropy and lower roundness values. All single protein SPNPs have high circularity (0.82-0.85). While variation in the properties of each single protein SPNP system exist, SPNPs prepared from single proteins via EHD jetting are generally small (<100 nm), circular (>0.8), and monodisperse (SEM PDI_{SEM} < 0.2).

Table 3-2. SPNPs size and secondary geometric factors data. Average diameters are presented based on nSEM, nDLS, iSEM and iDLS results. Minimum diameter, anisotropy, circularity and roundness results are provided as secondary geometric factors.

Formulation Name	Diameter, nSEM	Diameter, nDLS	Diameter, iSEM	Diameter, iDLS	$PDI_{SEM,}$ SEM	PDI, iDLS	Min. Dia., SEM	Anisotropy, SEM	Circularity, SEM	Roundness, SEM
(units)	(nm)	(nm)	(nm)	(nm)	(a.u.)	(a.u.)	(nm)	(a.u.)	(a.u.)	(a.u.)
HEM	65 ± 25	254 ± 157	64 ± 12	382 ± 106	0.11	0.38	53 ± 19	1.20 ± 0.23	0.85 ± 0.08	0.86 ± 0.12
HEM/HSA	51 ± 20	127 ± 108	50 ± 15	475 ± 138	0.15	0.47	43 ± 17	1.14 ± 0.15	0.90 ± 0.09	0.89 ± 0.09
TF	81 ± 36	170 ± 84	109 ± 36	284 ± 124	0.19	0.22	65 ± 29	1.21 ± 0.24	0.85 ± 0.08	0.85 ± 0.12
TF/HSA	59 ± 23	86 ± 48	92 ± 36	328 ± 87	0.16	0.41	49 ± 17	1.17 ± 0.23	0.89 ± 0.11	0.87 ± 0.11
MUC	73 ± 45	39 ± 17	168 ± 79	262 ± 108	0.16	0.35	50 ± 25	1.45 ± 0.59	0.82 ± 0.15	0.76 ± 0.19
MUC/HSA	72 ± 42	55 ± 34	138 ± 61	270 ± 169	0.16	0.38	55 ± 30	1.28 ± 0.33	0.85 ± 0.09	0.81 ± 0.14
INS	60 ± 22	37 ± 15	49 ± 9	220 ± 82	0.17	0.47	43 ± 14	1.36 ± 0.35	0.85 ± 0.13	0.77 ± 0.16
INS/HSA	61 ± 23	70 ± 41	83 ± 38	269 ± 130	0.13	0.5	49 ± 17	1.20 ± 0.25	0.87 ± 0.07	0.86 ± 0.12
HSA	77 ± 37	97 ± 86	116 ± 44	283 ± 115	0.18	0.44	60 ± 27	1.25 ± 0.27	0.83 ± 0.09	0.82 ± 0.13

3.4.2 HEM/HSA Blended SPNPs

Both, the number average (nDLS) and nSEM distributions for the series are presented in **Figure 3-2A**. The HEM/HSA spectra presents as two populations, with a smaller diameter group as the dominant subpopulation (nDLS) and a broader/larger secondary subpopulation. When referring to DLS size results, a denotation of d_1 refers to the average for the smallest diameter distribution. Similarly, d_2 refers to the average of any larger diameter distribution. When multiple subpopulations are assessed within the nDLS distribution, deconvolution is utilized to extract relative subpopulation fractions (α_1, α_2) (**Table 3-3**).

Table 3-3. nDLS results after multipeak deconvolution for SPNPs Series. A multipeak (LogNormal) deconvolution was utilized to extract the average sizes (d1, d2), distribution breadth (σ1, σ2), and population fraction (α1, α2) for both the individual particles (population 1) and the transient clusters (population2).

SPNPs	Population 1			Population 2		
	Dia. (nm)	σ (nm)	α (%)	Dia. (nm)	σ (nm)	α (%)
HEM	91	15	17	347	119	83
HEMHSA	97	19	65	455	159	35
TF	125	29	29	233	98	71
TFHSA	80	16	83	326	136	17
MUC	39	8	95	180	93	5
MUCHSA	30	4	7	68	21	93
INS	35	6	92	144	70	8
INSHSA	64	15	79	138	65	21
HSA	46	10	16	222	121	84

The HEM/HSA population with d_1 = 97 nm is comprised of swollen, individual SPNPs, while the second population with d_2 = 455 nm may be attributed to transient or semi-transient clusters. When compared to the HEM and HSA SPNPs, HEM/HSA SPNPs appear more similar to the sizes of HEM (d_1 = 91 nm, d_2 = 347 nm) than HSA nanoparticles (d_1 = 46 nm, d_2 = 222 nm). The results

from subpopulation extraction are presented in **Table 3-3**. These findings are corroborated by the SEM results that found for HEM/HSA SPNPs a right-skewed population in the 30-100 nm diameter range (d = 51 nm), which is much more aligned with the monomodal HEM distribution (d = 65 nm) than the broader HSA distribution (d = 77 nm).

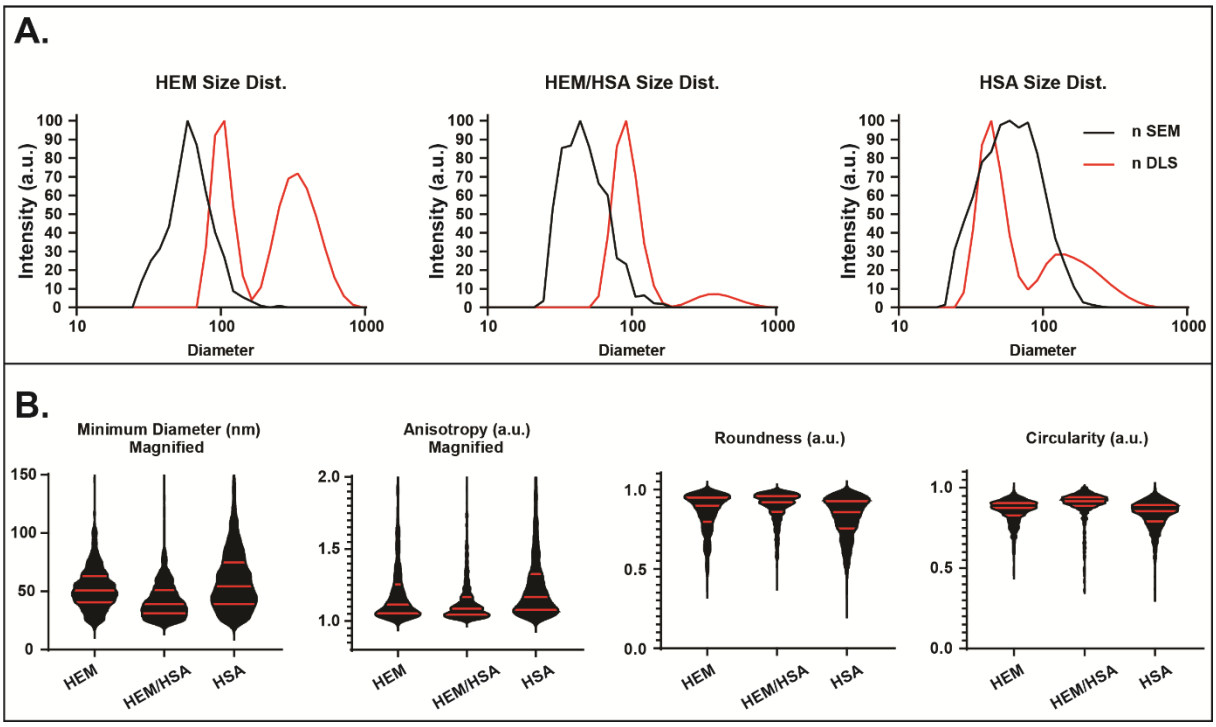

Figure 3-2. Size distribution and secondary geometric factors of HEM SPNPs based on SEM and DLS analysis. (A) Number distributions of SPNP sizes as obtained by SEM and DLS. (B) Violin graphs of minimum diameter, anisotropy, circularity, and roundness (median and interquartile ranges are presented by red lines).

Geometric factors (minimum diameter, circularity, anisotropy and roundness) were assessed by SEM analysis (**Figure 3-2B),** in order to further understand how the shapes of the SPNPs are affected by the choice of protein. Statistical comparisons between the distributions are provided in **Table 3-4**. When considering these factors: the circularity can be thought of as an approximation of circle-like shape, the anisotropy is the aspect ratio of the object as the ratio between major and

minor diameter, and the roundness is an aspect ratio independent factor that describes edge smoothness.[264–266]

Table 3-4. HEM series statistical analysis results of secondary geometric factors and scoring data for two-factor analysis. Minimum diameter, anisotropy, circularity, and roundness results are provided as secondary geometric factors.

SPNPs series	T-Test					Min. Dia			Anisotropy			Circularity			Roundness		
	Diameter	Min. Dia	Anisotropy	Circularity	Roundness	Slope	R^2	Score	Slope	R^2	Score	Slope	R^2	Score	Slope	R^2	Score
HEM	-	-	-	-	-	0.7008	0.8265	-	0.0027	0.0866	-	-0.0012	0.1620	-	-0.0014	0.0803	-
vs.	$P < 0.0001$ ****	$P < 0.0001$ ****	$P < 0.0001$ ****	$P < 0.0001$ ****	$P < 0.0001$ ****	-	-	2.2408	-	-	0	-	-	0.3872	-	-	0
HEM/HSA	-	-	-	-	-	0.7939	0.8191	-	0.0020	0.0675	-	-0.0018	0.1645	-	-0.0010	0.0452	-
vs.	$P < 0.0001$ ****	$P < 0.0001$ ****	$P < 0.0001$ ****	$P < 0.0001$ ****	$P < 0.0001$ ****	-	-	0	-	-	0.7160	-	-	0	-	-	1.6233
HSA	-	-	-	-	-	0.6736	0.8973	-	0.0026	0.1308	-	-0.0012	0.1308	-	-0.0012	0.1308	-
Three-Way	$P < 0.0001$ ****	$P < 0.0001$ ****	$P < 0.0001$ ****	$P < 0.0001$ ****	$P < 0.0001$ ****	-	-	-	-	-	-	-	-	-	-	-	-

Mimicking the diameter results, the HEM/HSA minimum diameter distribution more closely resembles HEM SPNPs, while being smaller than both the HEM and HSA systems. Similar to the minimum diameters, the anisotropy is both less variable and smaller (avg. = 1.14, Q1/Med./Q3 = 1.04/1.09/1.17) for blended SPNPs than HEM (avg. = 1.20, Q1/Med./Q3 = 1.05/1.11/1.25) and HSA (avg. = 1.25, Q1/Med./Q3 = 1.00/1.17/1.33) particles (**Figure 3-2B)**. This indicates that intentional formulation of blended SPNPs with appropriate protein ratios may generate features outside of the range obtained by single protein SPNPs. Circularity follows the trends observed for other geometric factors: HEM/HSA SPNPs mimic HEM more than HSA particles, while possessing a higher circularity and lower variance than either of those. Inspection of roundness, similar to other parameters, appears to indicate that blending of proteins resulted in roundness values closer to 1 with smaller IQRs (avg. = 0.89, Q1/Med./Q3 = 0.86/0.92/0.96) when compared to HEM (avg. = 0.86, Q1/Med./Q3 = 0.80/0.90/0.95) and HSA (avg. = 0.82, Q1/Med./Q3 = 0.75/0.86/0.93). Given that all shape factors indicate that HEM/HSA SPNPs are more controlled, smaller, and more symmetrical, blending may be an effective strategy for modulating SPNP diameter/ minimum diameter.

To assess how the SPNP populations might express secondary geometric factors, HEM/HSA SPNPs were also assessed via two-factor analysis. For each two-factor plot presented in **Figure 3-3**, the diameter of each particle is paired with a geometric factor for that particle. The similarities between these two-factor plots are given a score based on the degree to which HEM/HSA mimics either of the two single protein SPNP plots (**Table 3-4)**.

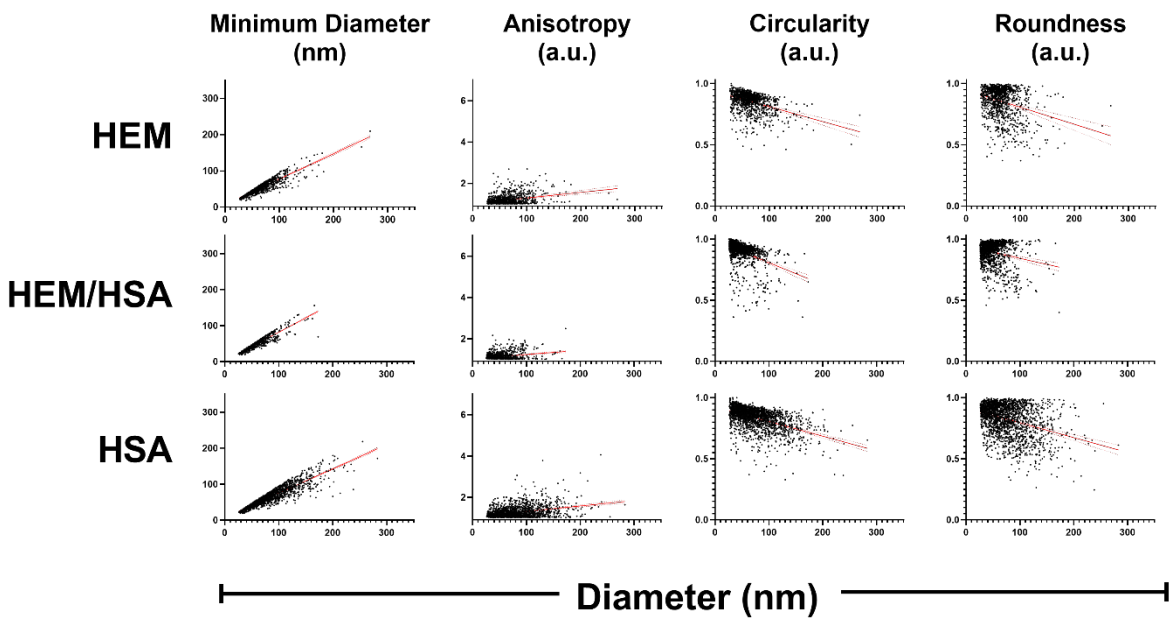

Figure 3-3. Two-factor individual analysis for HEM series. Scatter plots of Minimum diameter, anisotropy, circularity, and roundness vs. diameter.

The HEM/HSA diameter-minimum diameter relationship is moderately (2.2) governed by hemoglobin. The diameter-anisotropy relationship has a minor (0.7) similarity to HSA SPNPs. These types of relationships are not assessable when only single parameters are considered. HEM/HSA diameter-circularity saw a minor (0.4) similarity to HEM, while the diameter-roundness relationship was moderately (1.6) similar to the HSA SPNPs. However, none of the two-factor comparisons were predictive.

3.4.3 TF/HSA Blended SPNPs

The nDLS and nSEM data are presented in **Figure 3-4A**. The nDLS spectra for TF/HSA indicate the existence of two subpopulations that were attributed to individual particles (d_1 = 80 nm) and larger SPNP clusters (d_2 = 326 nm). Compared to the single component SPNPs, a d_1 (80 nm) falls between HSA SPNPs (d_1 = 46 nm) and TF SPNPs (d_1 = 125 nm) (**Table 3-3**).

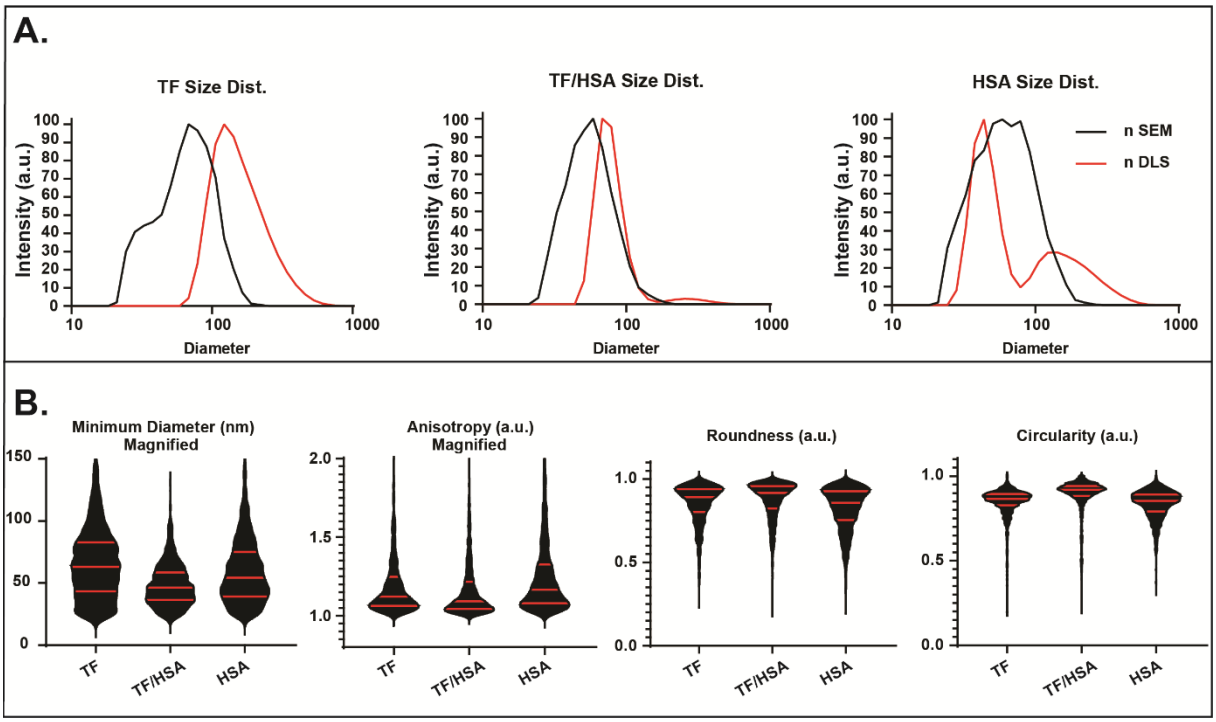

Figure 3-4. Size distribution and secondary geometric factors of TF SPNPs based on SEM and DLS analysis. (A) Number distributions of SPNP sizes as obtained by SEM and DLS. (B) Violin graphs of minimum diameter, anisotropy, circularity, and roundness (median and interquartile ranges are presented by red lines).

In the dry state, TF/HSA SPNPs display an average nSEM diameter (d = 59 nm) that is smaller than both HSA (d = 77 nm) and TF (d = 81 nm) with a narrower size distribution, as confirmed by a lower SEM PDI_{SEM} (0.16). The iSEM data indicates the same trend, where TF/HSA is smaller (d = 92 nm) than TF (d = 109 nm) and HSA SPNPs (d = 116 nm). (**Table 3-2**). Taken together, these results indicate that dry TF/HSA SPNPs are smaller than TF and HSA in the dry state, but swell to an average diameter between the single protein SPNPs.

For the TF/HSA series, the geometric factors are presented in **Figure 3-4B**, **Figure 3-5**, and **Table 3-5**.

Table 3-5. TF series statistical analysis results of secondary geometric factors and scoring data for two-factor analysis. Minimum diameter, anisotropy, circularity, and roundness results are provided as secondary geometric factors.

SPNPs series	T-Test					Min. Dia			Anisotropy			Circularity			Roundness		
	Diameter	Min. Dia	Anisotropy	Circularity	Roundness	Slope	R^2	Score	Slope	R^2	Score	Slope	R^2	Score	Slope	R^2	Score
TF	-	-	-	-	-	0.7296	0.8393	-	0.0019	0.0778	-	-0.0008	0.1298	-	-0.0008	0.0593	-
vs.	$P < 0.0001$ ****	$P < 0.0001$ ****	$P < 0.001$ ***	$P < 0.0001$ ****	$P < 0.0001$ ****	-	-	0	-	-	0	-	-	0	-	-	0
TF/HSA	-	-	-	-	-	0.6694	0.7950	-	0.0043	0.1888	-	-0.0028	0.3610	-	-0.0020	0.1613	-
vs.	$P < 0.0001$ ****	$P < 0.0001$ ****	$P < 0.0001$ ****	$P < 0.0001$ ****	$P < 0.0001$ ****	-	-	8.2418	-	-	2.0913	-	-	0.7741	-	-	2.7017
HSA	-	-	-	-	-	0.6736	0.8973	-	0.0026	0.1308	-	-0.0012	0.1308	-	-0.0012	0.1308	-
Three-Way	$P < 0.0001$ ****	$P < 0.0001$ ****	$P < 0.0001$ ****	$P < 0.0001$ ****	$P < 0.0001$ ****	-	-	-	-	-	-	-	-	-	-	-	-

Similar to the HEM/HSA SPNPs, the TF/HSA minimum diameter distribution was smaller and had lower variance than the TF and HSA SPNPs. For TF/HSA SPNPs, the sizes, anisotropy, and circularity of the system (as well as their variances) indicate a system that is more controlled, smaller, and more symmetrical than the single protein SPNPs. These results further reinforce that protein blending can be a path to improved control of factors such as monodispersity and aspect ratio. The anisotropy of TF/HSA SPNPs (avg. = 1.17, Q1/Med./Q3 = 1.04/1.09/1.22) is more similar to TF (avg. = 1.21, Q1/Med./Q3 = 1.06/1.12/1.25) than HSA (avg. = 1.25, Q1/Med./Q3 = 1.08/1.17/1.33). TF/HSA SPNPs are more circular (avg. = 0.89, Q1/Med./Q3 = 0.88/0.92/0.94) than TF (avg. = 0.85, Q1/Med./Q3 = 0.83/0.87/0.89) and HSA (avg. = 0.83, Q1/Med./Q3 = 0.79/0.85/0.89) SPNPs **(Figure 3-4B)**. TF/HSA roundness (less impacted by anisotropy than circularity) is similar to TF, though with less variance.

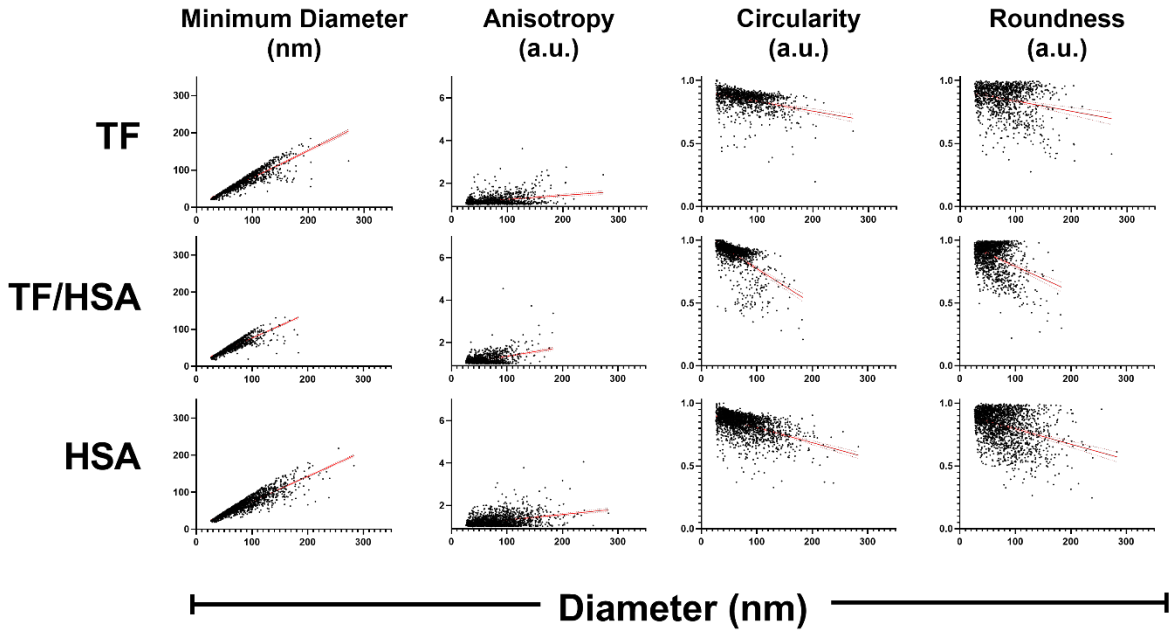

Figure 3-5. Two-factor individual analysis for HEM series. Scatter plots of Minimum diameter, anisotropy, circularity, and roundness vs. diameter.

Accordingly, the TF/HSA diameter-minimum diameter relationship indicates a strong bias towards HSA-like behavior (score = 8.2). The diameter-anisotropy relationship appears to be moderately governed by the HSA (2.1). While the TF/HSA diameter-circularity similarity to HSA appears minor (0.8), there is a moderate similarity between the diameter-roundness relationships (2.7) **(Figure 3-5** and **Table 3-5).** This indicates that the transferrin contribution to the properties of blended SPNPs appears to be eclipsed by the more hydrophobic HSA component.

3.4.4 MUC/HSA Blended SPNPs

DLS and SEM results for MUC/HSA SPNPs are presented in **Figure 3-6A**. From deconvolution, the nDLS spectrum of MUC/HSA SPNPs displays a minor fraction (d_1 = 30 nm, α_1 = 0.07) and a dominant fraction at d_2 = 68 nm. When compared to MUC and HSA SPNPs, MUC (d_1 = 39 nm, d_2 = 180 nm), not HSA (d_1 = 46 nm, d_2 = 222 nm) particles more closely resembles the blended MUC/HSA SPNPs (**Table 3-3**). The nSEM analysis of MUC/HSA SPNPs reveals size distributions similar to both, MUC (d = 73 nm) and HSA (d = 77 nm) SPNPs. The iSEM data suggest that MUC/HSA (d = 138 nm) falls between MUC (d = 168 nm) and HSA (d = 116 nm) SPNPs (**Table 3-2)**. For both MUC and MUCHSA, a significant overlap of the populations for the nSEM and nDLS distributions can be observed (**Figure 3-6A**). Taken together, these results indicate that the MUC/HSA particle sizes are governed by mucin. We note that mucin is the only protein with a lower isoelectric point (IP = 2.75) than HSA (IP = 4.7).

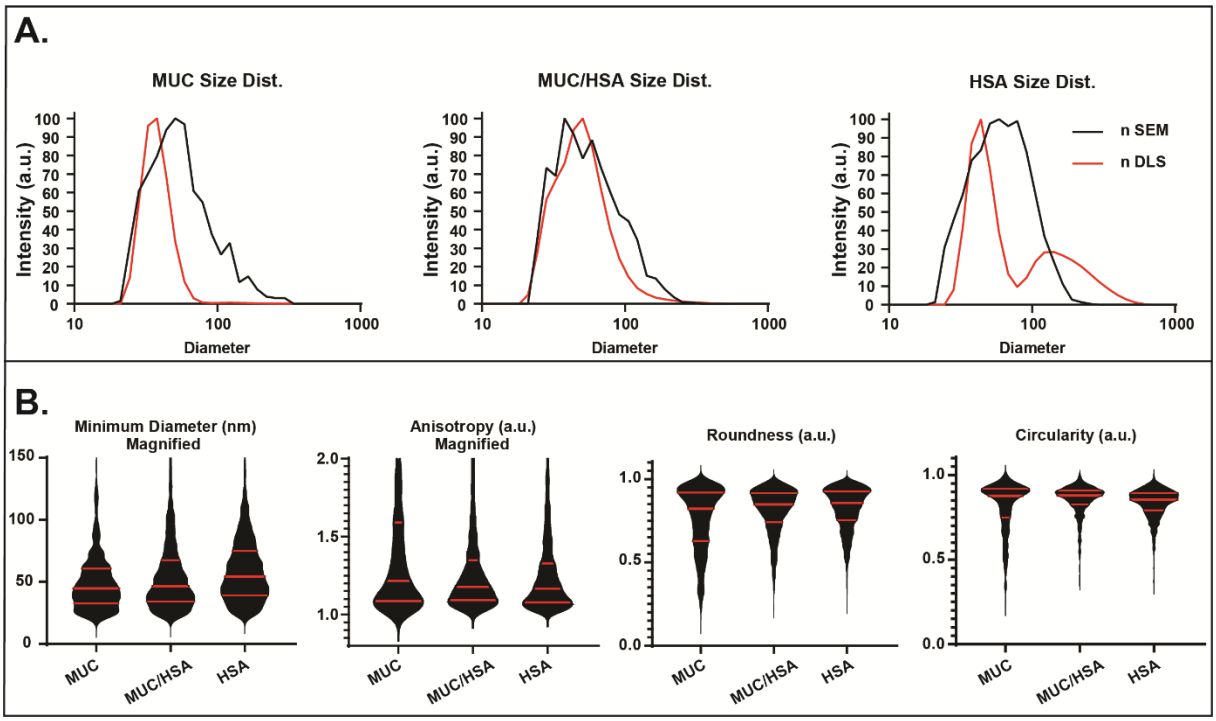

Figure 3-6. Size distribution and secondary geometric factors of MUC SPNPs based on SEM and DLS analysis. **(**A) Number distributions of SPNP sizes as obtained by SEM and DLS. (B) Violin graphs of minimum diameter, anisotropy, circularity, and roundness (median and interquartile ranges are presented by red lines).

A detailed assessment of geometric features is provided **Figure 3-6B, Figure 3-7**, and **Table 3-6.** Assessment of minimum diameter, similar to diameter, indicates that MUC/HSA appears to more closely resemble MUC than HSA. However, the anisotropy of MUC/HSA SPNPs appears to be equally influenced by both the HSA and the MUC components. Although the average circularity of all three SPNP formulations is similar (0.82-0.85), MUC/HSA SPNPs possesses smaller IQRs and has lower variance. MUC/HSA SPNPs' roundness (avg. = 0.81, Q1/Med./Q3 = 0.74/0.85/0.92) rests between those of MUC SPNPs (avg. = 0.76, Q1/Med./Q3 = 0.63/0.82/0.92) and HSA (avg. = 0.82, Q1/Med./Q3 = 0.75/0.85/0.93) **(Figure 3-6B)**.

Table 3-6. MUC series statistical analysis results of secondary geometric factors and scoring data for two-factor analysis. Minimum diameter, anisotropy, circularity, and roundness results are provided as secondary geometric factors.

SPNPs series	T-Test					Min. Dia			Anisotropy			Circularity			Roundness		
	Diameter	Min. Dia	Anisotropy	Circularity	Roundness	Slope	R^2	Score	Slope	R^2	Score	Slope	R^2	Score	Slope	R^2	Score
MUC	-	-	-	-	-	0.4340	0.6186	-	0.0069	0.2886	-	-0.0014	0.2886	-	-0.0020	0.2308	-
vs.	ns	$P < 0.0001$ ****	$P < 0.0001$ ****	$P < 0.0001$ ****	$P < 0.0001$ ****	-	-	0.5579	-	-	0.5105	-	-	0	-	-	0
MUC/HSA	-	-	-	-	-	0.6559	0.8191	-	0.0030	0.1501	-	-0.0010	0.1501	-	-0.0011	0.1073	-
vs.	$P < 0.01$ **	$P < 0.0001$ ****	$P < 0.01$ **	$P < 0.0001$ ****	$P < 0.05$ *	-	-	8.9193	-	-	7.8589	-	-	4.6447	-	-	7.1845
HSA	-	-	-	-	-	0.6736	0.8973	-	0.0026	0.1308	-	-0.0012	0.1308	-	-0.0012	0.1308	-
Three-Way	$P < 0.01$ **	$P < 0.0001$ ****	$P < 0.0001$ ****	$P < 0.0001$ ****	$P < 0.0001$ ****	-	-	-	-	-	-	-	-	-	-	-	-

MUC/HSA SPNP's diameter-minimum diameter relationship appears to strongly mimic the HSA SPNP relationship (8.9), as does the diameter-anisotropy relationship (7.9). The diameter-circularity (4.6) and diameter-roundness (7.2) relationships for MUC/HSA are also aligned with the HSA response (**Figure 3-7**, and **Table 3-6**).

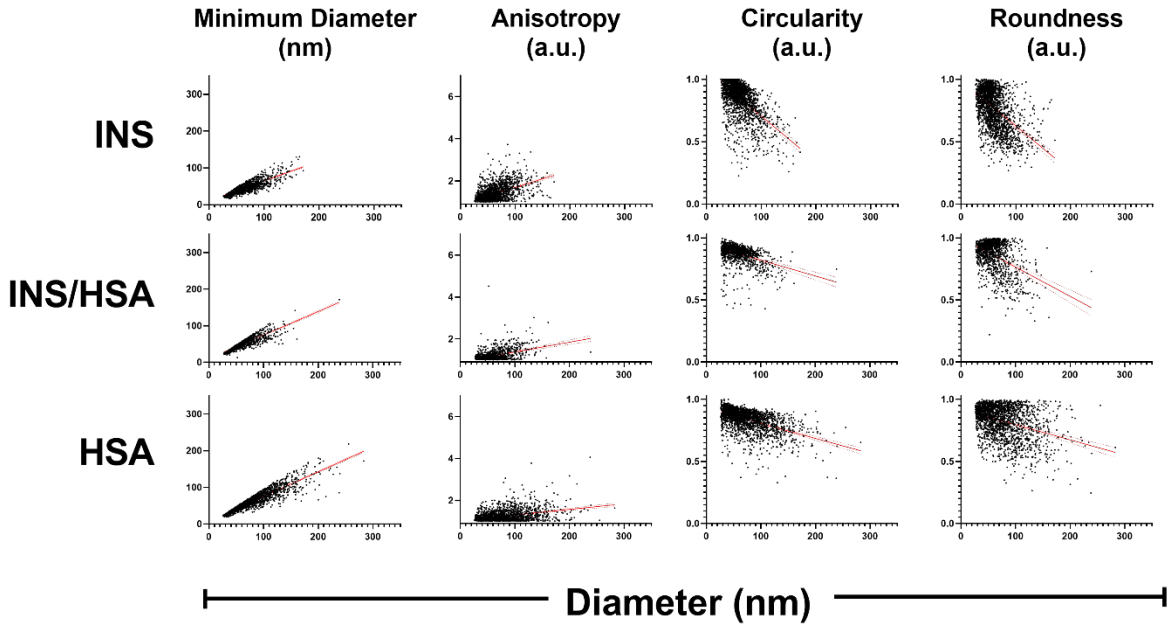

Figure 3-7. Two-factor individual analysis for INS series. Scatter plots of Minimum diameter, anisotropy, circularity, and roundness vs. diameter.

These relationships of secondary geometric attributes to particle diameter indicates that two-factor response of MUC/HSA is dominated by the HSA substituent, a fact that was not evident from assessment of individual SPNPs alone.

3.4.5 INS/HSA Blended SPNPs

The DLS and SEM analysis of INS/HSA SPNPs are presented in **Figure 3-8A**. INS/HSA SPNPs display two populations with nDLS diameter of d_1 = 64 nm and d_2 = 138 nm. When compared to

INS (d_1 = 35 nm, d_2 = 144 nm) and HSA (d_1 = 46 nm, d_2 = 222 nm) the average size of individual INS/HSA SPNPs are significantly larger than both, an effect not observed for the other blended SPNPs (**Table 3-3**). The nSEM distribution of INS/HSA SPNPs (d = 61 nm) more closely aligns with those of INS SPNPs (d = 60 nm) and is clearly different from the larger and broader distribution of HSA SPNPs (d = 77nm). Similar to the other blended SPNPs, the SEM diameter distribution is less influenced by HSA. The iSEM data of INS/HSA SPNPs (d = 83 nm) displays deviation from the INS population (d = 49 nm), with a broader distribution more similar to HSA SPNPs (d = 116 nm) (**Table 3-2)**. The results from SEM and DLS indicate that, while dry INS/HSA SPNPs are more similar in size to INS, they increase in size and variance in the swollen state that approaches a HSA SPNP-like distribution.

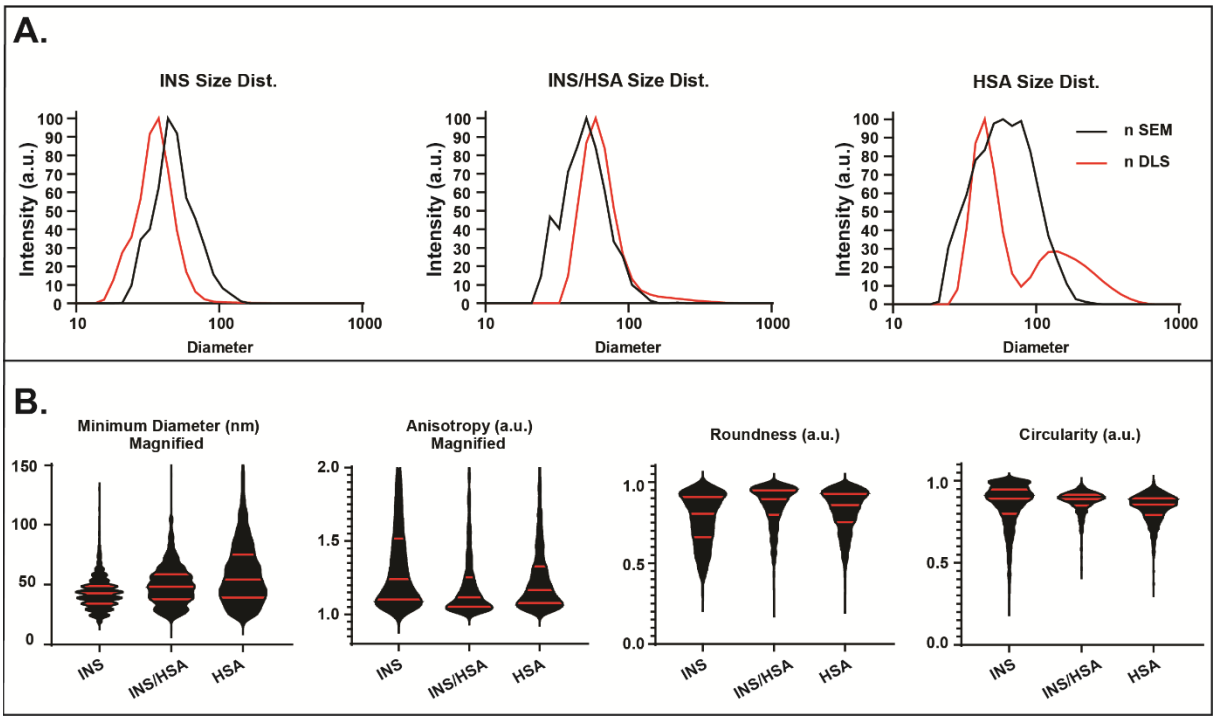

Figure 3-8. Size distribution and secondary geometric factors of INS SPNPs based on SEM and DLS analysis. (A) Number distributions of SPNP sizes as obtained by SEM and DLS. (B) Violin graphs of minimum diameter, anisotropy, circularity, and roundness (median and interquartile ranges are presented by red lines).

The analysis of geometric factors is presented in **Figure 3-8B** and **Figure 3-9** and results are presented in **Table 3-7**. The minimum diameter results of INS/HSA SPNPs lie between the distributions observed for the individual SPNPs, whereas INS/HSA SPNPs' anisotropy is biased towards an HSA-like distribution. However, both the average and IQRs for the anisotropy of the blended SPNP is lower than either INS or HSA (an effect observed in other blended SPNPs as well). The average circularity of INS/HSA SPNPs resembles that of the INS SPNPs. Lastly, the INS/HSA system presents as rounder than either of the other systems by all key metrics (average, IQRs, variance). (**Figure 3-8B**).

Table 3-7. INS series statistical analysis results of secondary geometric factors and scoring data for two-factor analysis. Minimum diameter, anisotropy, circularity, and roundness results are provided as secondary geometric factors.

SPNPs series	T-Test					Min. Dia			Anisotropy			Circularity			Roundness		
	Diameter	Min. Dia	Anisotropy	Circularity	Roundness	Slope	R^2	Score	Slope	R^2	Score	Slope	R^2	Score	Slope	R^2	Score
INS	-	-	-	-	-	0.5347	0.7088	-	0.0081	0.2589	-	-0.0037	0.3622	-	-0.0036	0.2598	-
vs.	ns	$P < 0.0001$ ****	$P < 0.0001$ ****	$P < 0.0001$ ****	$P < 0.0001$ ****	-	-	1.8443	-	-	2.5463	-	-	0.1329	-	-	3.5240
INS/HSA	-	-	-	-	-	0.6449	0.7941	-	0.0046	0.1809	-	-0.0013	0.1603	-	-0.0024	0.1923	-
vs.	$P < 0.0001$ ****	$P < 0.0001$ ****	$P < 0.0001$ ****	$P < 0.0001$ ****	$P < 0.0001$ ****	-	-	7.0213	-	-	4.5864	-	-	7.9147	-	-	3.5636
HSA	-	-	-	-	-	0.6736	0.8973	-	0.0026	0.1308	-	-0.0012	0.1308	-	-0.0012	0.1308	-
Three-Way	$P < 0.0001$ ****	$P < 0.0001$ ****	$P < 0.0001$ ****	$P < 0.0001$ ****	$P < 0.0001$ ****	-	-	-	-	-	-	-	-	-	-	-	-

The properties of INS/HSA SPNPs appear to be a mix of responses guided by both proteins. For comparison, the two-factor results for INS/HSA SPNPs can be found in **Figure 3-9** and **Table 3-7**.

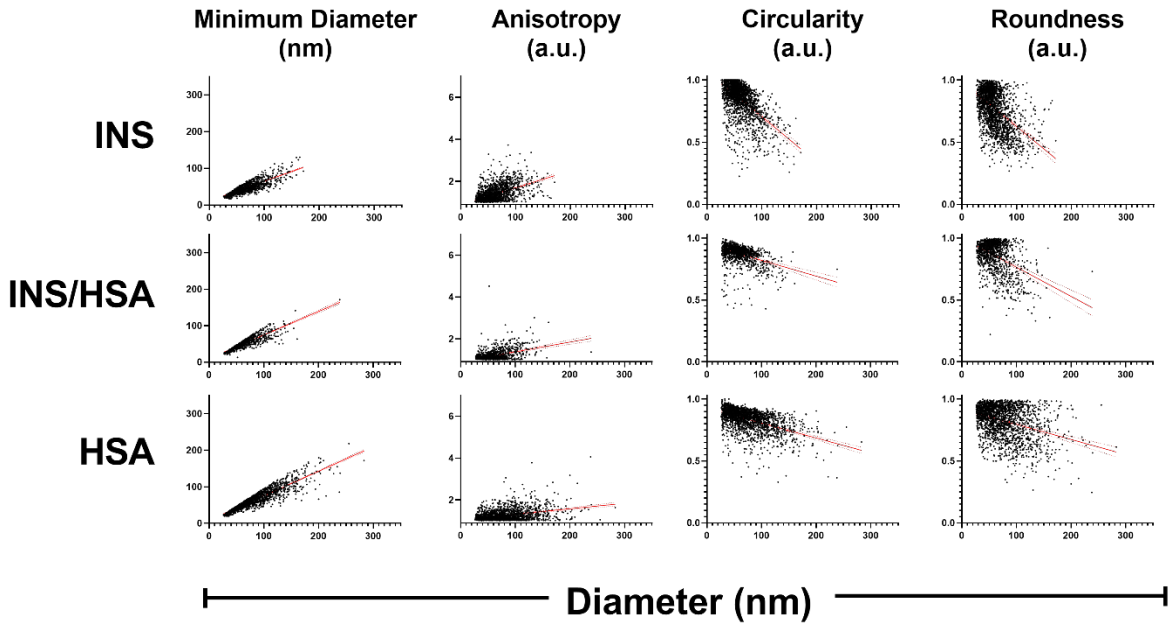

Figure 3-9. Two-factor individual analysis for INS series. Scatter plots of Minimum diameter, anisotropy, circularity, and roundness vs. diameter

The diameter-minimum diameter relationship appears to mirror both HSA (score = 7.0) and INS (score = 1.8) SPNPs. INS/HSA SPNPs' diameter-anisotropy relationship has a moderate agreement with both HSA (4.5) and INS (2.5) particles. HSA SPNPs strongly align with the INS/HSA response for diameter-circularity (7.9) but appear to have very little in common with INS (0.1). The diameter-roundness response of INS/HSA SPNPs is a combination of the factors observed in HSA (3.6) and INS (3.5).

3.5 Conclusions

In this work, we expand the library of SPNPs available as nanocarriers in a systemic way, while exploring the relationships between blended protein and single protein systems in both dry and hydrated states. We have shown that tailoring formulations of SPNPs, through blending and/or protein selection, can result in a robust platform for exploring a variety of sizes, monodisperse size distributions, and shape parameters. One-factor and two-factor SEM, combined with DLS, analysis revealed that most of the blended SPNPs have geometric parameters that align with one constituent protein. Those, blended SPNPs may have predictable physical properties that can be tuned by changing their respective protein-to-protein ratios. Future efforts will include the application of these methods to a range of nanomedicine applications and further studies aimed at correlating these properties with SPNP performance in vitro and in vivo.

Chapter 4
Engineered Ovalbumin Nanoparticles for Cancer Immunotherapy

The material in this chapter has been adapted with minor modifications from the following article: Nahal Habibi*, Stephanie Christau*, Lukasz J. Ochyl, Zixing Fan, Alireza Hassani Najafabadi, Matthias Kuehnhammer, Mengwen Zhang, Matthew Helgeson, Regine von Klitzing, James J. Moon, Joerg Lahann. Engineered Ovalbumin Nanoparticles for Cancer Immunotherapy. *Advanced Therapeutics* **2020**, *3*, 2000100. (* Equal Contributions)

4.1 Abstract

Ovalbumin (OVA) is a protein antigen that is widely used for eliciting cellular and humoral immune responses in cancer immunotherapy. As an alternative to solute OVA, engineering approach is developed herein towards protein nanoparticles (pNPs) based on reactive electrospraying. The resulting pNPs are comprised of polymerized OVA, where individual OVA molecules are chemically linked via poly(ethylene glycol) (PEG) units. Controlling the PEG/OVA ratio allows for fine-tuning of critical physical properties, such as particle size, elasticity, and, at the molecular level, mesh size. As the PEG/OVA ratio decreased, OVA pNPs are more effectively processed by dendritic cells, resulting in higher OT-I CD8+ cells proliferation in vitro. Moreover, pNPs with lower PEG/OVA ratios elicit enhanced lymphatic drainage in vivo and increased uptake by lymph node macrophages, dendritic cells, and B cells, while 500 nm OVA pNPs show poor draining lymph nodes delivery. In addition, pNPs with lower PEG/OVA ratios result in higher anti-OVA antibody titers in vivo, suggesting improved humoral immune responses. Importantly,

OVA pNPs result in significantly increased median survival relative to solute OVA antigen in a mouse model of B16F10-OVA melanoma. This work demonstrates that precisely engineered OVA pNPs can improve the overall anti-tumor response compared to solute antigen.

4.2 Introduction

In cancer immunotherapy, eliciting potent and specific immune responses against advanced tumors remains a major challenge.[267–269] Peptide-based cancer vaccines (subunit vaccines) have been extensively studied in the past, because they have significant advantages (such as safety and ease of manufacturing) over attenuated, inactivated, or biosynthetic vaccines.[270] However, their efficacy in clinical trials has been disappointing, mostly due to inefficient delivery of antigen and adjuvants to draining lymph nodes, resulting in immune tolerance and cytotoxic T lymphocyte fratricide.[271] On the other hand, high levels of vaccine have been linked to T cell sequestration at the vaccination site, resulting in systemic T cell exhaustion and deletion.[272] Nanoparticles have been utilized to enhance the therapeutic outcome of cancer immunotherapies in the context of subunit antigens, dendritic cell-based vaccines, immune checkpoint inhibitors/blockade, adoptive T-cell therapy[273] and immunoenhancing agents for in situ vaccination.[274] Cancer vaccine strategies that aim to improve early steps of antigen delivery and processing can be also beneficial to patients who lack the sufficient pre-existing anti-tumor T cells.[273] Nanoparticle-based delivery platforms hold the potential to improve vaccine immunogenicity[275–288] due to increased antigen stability, sustained release, site-specific delivery, and improved circulation and biodistribution of the antigens.[267,289–296] Parameters such as nanoparticle size,[297–299] shape,[300,301] charge,[302] and administration route[303] are known to affect the immune response, but the mechanism behind cross-presentation and cross-priming of CD8+ T cells remains an active area of research.[304,305]

Typically, antigens have been either encapsulated in the bulk of nanoparticles for subsequent release or were presented on the surface of nanoparticles. Polymer nanoparticles made of natural or synthetic polymers, such as chitosan or poly(lactide-co-glycolide) (PLGA), have been extensively studied for vaccine encapsulation.[287,306,307] Other examples of antigen-encapsulating nanomaterials include lipid nanocapsules[284,286] polyelectrolyte capsules comprised of peptide antigens and adjuvants made by the layer-by-layer technique,[279] or nanoparticles comprised of antigen or adjuvant molecules linked to lipophilic albumin-binding tails.[277] In contrast, antigen conjugation to the surface of nanoparticles[308,309] has been suggested to be superior compared to antigen encapsulation for two main reasons: Firstly, the nanoparticles themselves were found to trigger inflammatory immune responses when encountered by antigen-presenting cells (APCs).[310–312] Secondly, antigens presented on the nanoparticle surface can more effectively interact with surface receptors of APCs, which appears to enhance crosstalk between the innate and adaptive immune system.[313] As an alternative, virus-like particles (VLPs) or protein nanoparticles (pNPs) have been pursued in some instances.[239,276,314–318]. VLPs are biomimetic engineered particles, which mirror viruses in their structural properties. The main concern of VLPs is the risk of inducing anti-carrier antibody production. This could potentially limit their clinical translation, because repeated dosing could lead to neutralization or reactive toxicities in patients.[319] In addition, off-target immune response can be caused by the competition between the carrier antigen and the target antigen.[320] Using pNPs comprised of the actual antigen as the main structural unit eliminates the need for a separate nanoparticle carrier.[321–327] If the entire particle, or its majority, is comprised of antigen, pNPs have the potential for enhancing dendritic cell surface receptor engagement, prolonging tissue persistence, sustaining antigen activity and minimizing off-target material delivery.[320] In the past, proteins have been assembled into particles through structurally ordered assembly, unstructured hydrophobic assembly and electrostatic

assembly.[320] However, these protein assemblies driven by fusion and sequence modification are more likely affected by antigenic variability and the loss of their capacity to self-assemble and preserve antigen recognition.[320] Compared to fusion and sequence modification, chemical conjugation to proteins, lipids or polymers, promises versatility and broader applicability to a wider spectrum of antigens, but requires multiple processing steps.[320] For example, crosslinked peptide nanoclusters were fabricated for delivery of oncofetal antigen by desolvation and were stabilized through disulfide bonds.[326] However, changes to the primary structure of the protein, such as addition of cysteine to the C-terminus of the peptide, was necessary to ensure successful crosslinking.

Another method of nanoparticle fabrication is electrospraying, which involves liquid atomization through electrical forces.[328] Electrospraying has been employed in biomedical research for fabrication of different types of nanoparticles based on natural materials, such as elastin-like polypeptide nanoparticles[329] or insulin particles.[330] Electrospraying is a one-step process, which can be applied to a range of proteins and protein mixtures without significantly increasing the engineering effort.[328] Another potential advantage of electrospraying is its proven scalability, which makes it a valuable method of particle fabrication in industrial applications.[331] In electrospraying, the liquid is transported through a metal capillary, which is connected to a conductive substrate. The characteristic Taylor cone is formed at the tip of the capillary after applying high voltage; nanoparticles are formed after evaporation of the solvent and collected on a conductive substrate.[328]

Here, we report a novel synthetic route towards pNPs comprised of polymerized ovalbumin (OVA) linked by poly(ethylene glycol) (PEG) units based on reactive electrospraying. This scalable particle fabrication technique limits denaturation of proteins as confirmed by circular dichroism spectroscopy.[332] Reactive electrospraying can be extended to fabricate bicomparmental protein

nanoparticles[6]; therefore, fabrication of multicompartmental nanoparticles where each compartment is made of a different antigen can be feasible with this method which is hard-to-achieve otherwise. Conceptually, this approach has the potential to reduce competing anti-carrier responses, because the target antigen becomes the actual structural building block in pNPs. This novel type of pNPs ensures presentation of dense arrays of antigen that should be readily recognizable by APCs. In pNPs comprised of polymerized OVA, antigen presentation is critically influenced by the crosslinker:protein ratio. Specifically, we have evaluated four types of polymerized OVA pNPs with various PEG/OVA ratios in terms of their uptake by dendritic cells, T cell activation, lymphatic drainage, antibody production, and anti-tumor efficacy.

4.3 Materials and Methods

4.3.1 Materials

Ovalbumin (OVA), O, O′-bis[2-(N-succinimidyl-succinylamino)ethyl] polyethylene glycol (NHS-PEG-NHS) with a molecular weight of 2000 Da, ethylene glycol, 4,6-diamidino-2-phenylindole dihydrochloride (DAPI), carboxyfluorescein diacetate N-succinimidyl ester (CFSE), Triton-X 100, and tween 20 were used as purchased from Sigma Aldrich, USA. O,O′-bis[2-(N-succinimidyl-succinylamino)ethyl]polyethylene glycol (NHS-PEG-NHS) with a molecular weight of 20,000 Da was purchased from Nanocs Inc., USA. BCA assay, endotoxin removal spin columns, methanol-free formaldehyde, Alexa Flour™ 488 phalloidin, Alexa Fluor™ 647 conjugated albumin from bovine serum (BSA), ProLong™ Gold Antifade Mountant, and 96-well flat bottom immunoplates were purchased from ThermoFisher Scientific, USA. Endotoxin free water was obtained from G- Biosciences, USA. Endotoxin-Free Dulbecco's PBS was purchased from EMD Millipore, USA. RPMI 1640 media, fetal bovine serum (FBS), penicillin–streptomycin, b-mercaptoethanol, and ACK lysis buffer were obtained from Life Technologies.

Granulocyte macrophage-colony-stimulating factor (GM-CSF) was the product of PeproTech, USA. PE/Cy7 anti-mouse CD11c antibody was purchased from Biolegend, USA. Anti-mouse CD8 antibody (CD8α-APC) was purchased from BD Biosciences, USA. EasySep™ Mouse CD8+ T Cell Isolation Kit was purchased from STEMCELL Technologies, Canada. Biotinylated Rabbit/goat anti-mouse IgG was purchased from Southern Biotech, USA. Streptavidin-HRP was purchased from R&D Systems, USA. 3,3',5,5'-Tetramethylbenzidine (TMB) substrate was purchased from Surmodics, USA.

4.3.2 Fabrication and Characterization of Ovalbumin Nanoparticles

Ovalbumin nanoparticles (OVA pNPs) were prepared using electrospraying. Prior to pNP fabrication, endotoxin-free OVA was prepared using spin columns according to manufacturer's instructions. Protein solutions were prepared by dissolving endotoxin-free ovalbumin at 7.5% (w/v) and the desired amount of NHS-PEG-NHS crosslinker (5, 10, 30 or 50% ($w/w_{protein}$)) in mixtures of endotoxin-free water and ethylene glycol. Water-to-ethylene glycol ratios of 80:20 vol% or 40:60 vol% were used depending on the formulation. OVA/PEG solutions were pumped at a flow rate of 0.1 mL/h. After a droplet had been formed at the outlet of the needle, an electric field was applied which resulted in formation of the characteristic Taylor cone. After application of ≈10-12kV of voltage, OVA pNPs were electrosprayed onto a collector sheet (the distance between the needle tip and the collector sheet was adjusted to 20 cm). Afterwards, the pNPs were kept at 37 °C for 7 days to complete the crosslinking reaction before being collected in phosphate-buffered saline (PBS) buffer containing 0.01% Tween20. Serial centrifugation was employed to separate the desired nanoparticles from larger particles. Lastly, OVA pNPs were re-dispersed in PBS buffer and stored at 4 °C until further use. The concentration of pNPs was assessed using bicinchoninic acid (BCA) assay according to manufacturer's instructions.

Scanning Electron Microscopy (SEM)

SEM images were recorded using a FEI Nova 200 Nanolab SEM/FIB at the Michigan Center for Materials Engineering at acceleration voltages of 5kV. Images were processed using ImageJ (Wayne Rasband, NIH) to obtain the respective nanoparticle size distribution. For particle size determination, >500 particles/sample were measured using ImageJ.

Dynamic/Electrophoretic Light Scattering (DLS/ELS)

DLS/ELS measurements were carried out using a Zetasizer Nano ZS (Malvern Panalytical). DLS was employed to measure the particle size distribution in PBS buffer after particle collection. ELS was employed to determine the zeta potential of OVA NPs. 3 individual measurements were carried out per sample and averaged to determine the particle size and zeta potential.

Atomic Force Microscopy (AFM)

AFM force-distance profiles were obtained by jetting the OVA nanoparticles onto an amine-reactive polymer coating, namely poly(4-Pentafluorophenyl-p-xylene)-coatings. This was done to ensure that the nanoparticles remain on the surface during the AFM measurements in PBS buffer. The amine-reactive coating was prepared on silicon substrates using chemical vapor deposition (CVD) polymerization, as previously reported elsewhere.[333] Afterwards, the coatings were rinsed with acetone and dried under a stream of nitrogen. OVA NPs were directly jetted onto the coated substrates. They were left at room temperature for about two weeks before conducting the AFM measurements.

AFM measurements were carried out using an MFP-3D (Oxford Instruments, UK) using CSC-38noAl-A cantilevers (Micromash, USA) with a spring constant of 0.09 N/m. Samples were prepared by electrospraying OVA pNPs directly onto silicon substrates coated with poly(4-Penta fluorocphenyl-p-xylylene) via CVD polymerization; the substrates were allowed to crosslink at 37

°C for several days prior to use. OVA NPs were localized by scanning the surface in tapping mode over a (5 x 5) μm^2 area and then decreasing the scan area for visualization of a single nanoparticle. The force curves were obtained by indenting the tip into the center of an individual nanoparticle and recording the deflection of the cantilever.

Small Angle Neutron Scattering (SANS)

SANS experiments were carried out at the NIST Center for Neutron Research using the NGB30 instrument. Using neutron wavelength of $\lambda = 6$ Å and $\Delta\lambda/\lambda=0.11$ at detector distances 1.3 m, 4.0 m, and 13.2 m, we provided a *q*-range of 0.003 $Å^{-1}$ to 0.5 $Å^{-1}$. OVA pNPs with PEG/OVA ratio of 10% and 50% dispersed in D_2O (2 mg/mL) were loaded into 1 mm titanium scattering cells between mounted quartz windows, and a Julabo temperature-controlled bath was used to maintain the sample temperature at 37 ˚C. SANS data were then collected and reduced using the NCNR IGOR software.[334] Data analysis was performed subsequently using the Sasview software.

4.3.3 Preparation of Bone Marrow-derived Dendritic Cells

Bone marrow-derived dendritic cells (BMDCs) were prepared according to literature protocols.[335] C57BL/6 mice were kept in a pathogen-free environment and allowed to acclimate for at least one week before experiments. All animal experiments described in this protocol were compliant with the Committee on Use and Care of Animals (UCUCA) at the University of Michigan and performed according to the established policies and guidelines. Briefly, femur and tibia were harvested from C57BL/6 mice. Bone marrow was flushed with a syringe and collected. The cell suspension was passed through a 40 μm cell strainer. After centrifugation, cells were plated into non-tissue culture treated Petri-dishes at a concentration of 2 million cells per dish in dendritic cells media (RPMI 1640 supplemented with 10% FBS, 1% penicillin-streptomycin, 50 μM β-

mercaptoethanol and 20 ng/mL GM-CSF) at 37 °C with 5% CO_2. The media was refreshed on days 3, 6, and 8. BMDCs were used for experiments on days 10-12.

4.3.4 Ovalbumin Nanoparticles Uptake by Bone Marrow-derived Dendritic Cells

Internalization of fluorescent OVA pNPs by BMDCs was visualized using confocal microscopy and quantified using flow cytometry. Fluorescent OVA pNPs were obtained by addition of AlexaFluor 647-conjugated albumin from bovine serum (BSA) at 1 mg/mL to the solvent mixture for electrospraying of the nanoparticles. For confocal imaging, BMDCs were seeded on chamber slides (10^5 cells/well) and maintained in a humidified incubator at 37°C and 5% CO_2. Cells were incubated with 10 μg/mL of OVA NPs for 24 hours. The cells were then washed three times with PBS, fixed with 4% paraformaldehyde, washed, and permeabilized with 0.1% Triton-X solution which was followed by treatment with blocking solution of 1% BSA. The actin filaments were stained with AlexaFluor 488-Phalloidin and the nucleus was stained with DAPI. The samples were imaged using a 63x oil-immersion lens on a Nikon A-1 spectral confocal microscope located at the microscopy and image analysis laboratory (MIL) at the University of Michigan.

Flow cytometry was used for quantitative uptake studies. BMDCs were plated in a 12-well plate at a density of 1 million cells per well in dendritic cells media. After 24 hours, media was removed from the wells to remove non-adherent cells, and fresh media containing different nanoparticle groups at 10 μg/mL was added to the wells. After 24-hour incubation of cells with OVA nanoparticles, the cells were washed with PBS three times and then trypsinized. The cells were washed two more times and stained with CD11c-PE/Cy7 and DAPI before analyzing them via flow cytometry using a Cytoflex (Beckman Coulter) cell analyzer located at the Flow Cytometry Core of the University of Michigan. Data were analyzed using FlowJo software.

4.3.5 CFSE Dilution Assay

CFSE dilution assay was performed to evaluate the proliferation of OT-I CD8+ cells after co-culture with OVA pNP-treated BMDCs. BMDCs were seeded in 96-well plates at a density of 50,000 cells/well and then incubated with the respective OVA NPs groups, soluble OVA, SIINFEKL (positive control), and PBS (negative control) overnight. Naive $CD8^+$ T cells were isolated from the spleen of OT-I transgenic mice using a magnetic $CD8^+$ T-cell-negative selection kit. OT-I CD8+ cells were fluorescently labeled by incubation with CFSE (1 μM) for 10 min at 37°C. CFSE-labeled OT-I CD8+ T cells were then co-cultured with OVA pNP-treated BMDCs in 96 well plates at a density of 50,000 cells/well for 72 hours. BMDCs were washed with PBS three times before co-culture. Cells were then stained with CD8α-APC and DAPI, and flow cytometry (Cytoflex, Beckman Coulter) was used to determine the percentage of live, proliferated OT-I CD8+ cells. The data was processed using FlowJo software and reported as % CFSE dilution, which is proportional to OT-I CD8+ cell proliferation.

4.3.6 Immunization Study

Six-week-old, female C57BL/6 mice were purchased from Jackson Laboratory. Mice (n=5 per group) were immunized subcutaneously at the tail base at a dose of 10 μg OVA with 15 μg CpG in 100 μl sterile PBS buffer (primary immunization). Boost immunization was performed on day 21 after primary immunization. On days 20 and 42, blood was collected by submandibular bleed for serum antibody titers analysis. To separate serum, the collected blood was centrifuged at 10,000 x g for 5 mins. Serum was then stored at -80°C until analysis.

4.3.7 Enzyme-Linked Immunosorbent Assay

For enzyme-linked immunosorbent assay (ELISA) analysis, 96 well flat bottom Immunoplates (Thermo Scientific) were coated with 1 µg/well OVA solution in 0.05 M carbonate-bicarbonate buffer (pH 9.6) and incubated overnight at 4°C. Plates were then washed with 50 mM Tris, 0.14 M NaCl, 10.05% Tween 20 (pH 8) followed by blocking with 50 mM Tris, 0.14 M NaCl, 1% BSA (pH 8) for 1 hour at room temperature. Samples were diluted in 50 mM Tris, 0.14 M NaCl, 0.05% Tween 20, 1% BSA and added to each well for an hour incubation at room temperature. After washing, the plates were incubated with diluted horseradish peroxidase enzyme (HRP) conjugated Rabbit anti-mouse IgG for an hour. The plates were then washed and incubated with TMB substrate solution for 10 minutes. The reaction was stopped by addition of 2 M H_2SO_4 solution. The plates were read at the wavelength of 450 nm using a plate reader.

4.3.8 Statistical Analysis

All quantitative experiments were performed in triplicate and are presented as arithmetic mean ± SEM. Statistical analyses were performed using SPSS Statistics 24 software. One-way ANOVA with Tukey's post-test was used to determine significance among groups. A P-value of < 0.05 was considered statistically significant ($*P < 0.05$, $**P < 0.01$, $***P < 0.001$, and $****P < 0.0001$); P-values of > 0.05 were considered not significant (ns).

4.4 Results and Discussion

4.4.1 Preparation of Ovalbumin Nanoparticles

OVA pNPs were prepared using reactive electrospraying, as shown in **Figure 4-1A**. To synthesize OVA pNPs, OVA was dissolved at 7.5% (w/v) in water/ethylene glycol mixture. The OVA solution was mixed with the amine-reactive crosslinker NHS-PEG-NHS at variable ratios. During

reactive electrospraying, we employed a solvent mixture comprised of water and ethylene glycol (80:20 vol%) and used NHS-PEG-NHS with molecular weight of 2kDa. Under these conditions, the PEG units form amide-bonds with amino groups in the antigen, such as OVA's lysine residues, resulting in stable, polymerized OVA pNPs. To ensure completion of the reaction, OVA pNPs were stored at 37 °C for 7 days prior to collection. To adjust the network structure of OVA pNPs, we varied the PEG/OVA ratio as follows: 10% to 30% and 50% ($w/w_{protein}$). Electrospraying resulted in pNPs of 200-300 nm in their fully hydrated state (**Figure 4-1F**). We found parameters, such as protein concentration, solvent viscosity, and solvent dielectric constant, can be adjusted to control the size and network structure in pNPs. To increase the size of hydrated OVA pNPs to 500 nm, the ratio of water-to-ethylene glycol was decreased to 40:60 (vol%), which effectively decreases the overall dielectric constant of the solvent system and increases nanoparticle size.[151] However, additional optimization was required to obtain 500 nm OVA pNPs. First, the PEG/OVA ratio was decreased to 5% (w/w). Second, the molecular weight of the PEG crosslinker was increased from 2 kDa to 20 kDa. Through these modifications, we were able to reliably prepare hydrated OVA pNPs with size of 500 nm, as confirmed by dynamic light scattering.

Figure 4-1B-E show SEM images of the different OVA pNPs as collected on the counter electrode. To assess the size distribution of OVA pNPs at their dry state, more than 500 particles per group was analyzed using ImageJ. The pNPs were dispersed in PBS buffer, and their zeta potential and size were measured using ELS and DLS. The zeta potentials among four types of OVA pNPs were not statistically significant different (**Table 4-1**).

Table 4-1. Zeta potential of OVA pNPs (mV).

Particle Group	Zeta Potential (mV) Average	SD
5% 20k	-6.3	0.3
10% 2k	-6.8	0.5
30% 2k	-6.6	0.7
50% 2k	-5.9	0.4

The stability of OVA pNPs was confirmed using DLS measurements over a time period of 36 days. The size of hydrated nanoparticles characteristically increased with lower PEG/OVA ratio (**Figure 4-1F**).

The swelling of the particles with respect to their SEM dry size was estimated using **Equation 4-1**[336]:

$$\text{Swelling ratio} = \frac{V_{swollen}}{V_{dry}} \qquad \textbf{Equation 4-1}$$

where d_{DLS} and d_{SEM} are the nanoparticle diameters obtained from DLS and SEM (**Table 4-2**) that were used to calculate $V_{Swollen}$ *and* V_{dry} *, respectively,* assuming a spherical geometry for nanoparticles.

Table 4-2. Size data that were used for calculation of pNPs swelling. The SEM size (dry size) was measured using ImageJ. The reported DLS size (swollen size) was obtained from Gaussian fits of raw DLS data.

Particle Group	5% 20k	10% 2k	30% 2k	50% 2k
SEM size (nm)	176.6	86.6	85.2	78.4
DLS size (nm)	514.1	266.1	202.0	165.2

OVA pNPs with PEG/OVA ratios of 5, 10, 30 and 50% showed swelling ratios of 24.7, 29, 13.3 and 9.4, respectively. These differences in the swelling behavior suggest substantial differences in the mesh sizes of the protein gels that the pNPs are comprised of. The dependency of pNP swelling on crosslinker amount indicates that our reactive electrospraying procedure, in fact, does yield particles with different mesh size. However, we aimed at quantifying the mesh size more

accurately using small-angle neutron scattering to evaluate the network density of polymerized pNPs.

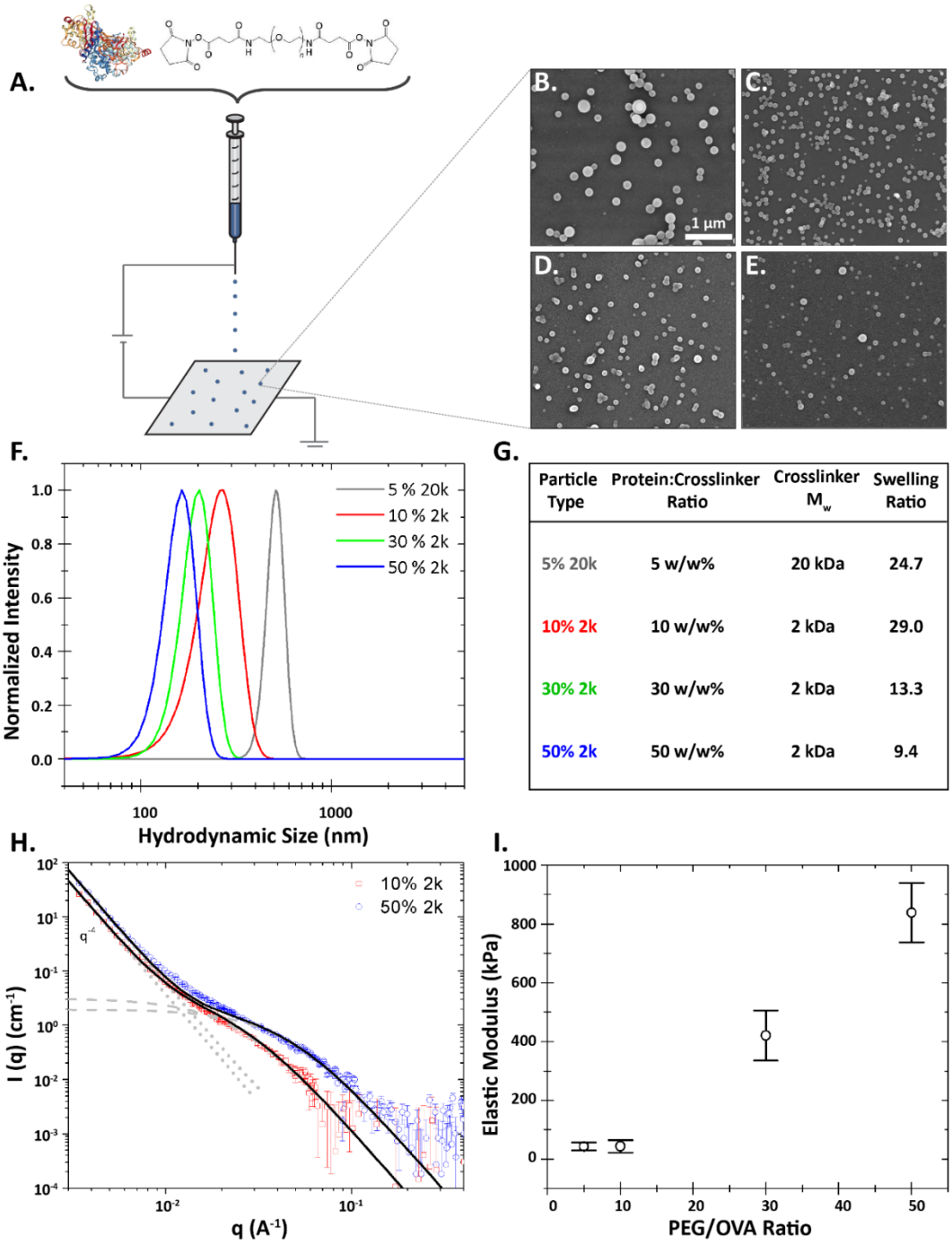

Figure 4-1. Preparation and characterization of four types of engineered OVA pNPs via reactive electrospraying. (A) Setup for electrospraying used for preparation of engineered OVA pNPs. SEM images of OVA pNPs with (B) 5% ($w/w_{protein}$) 20kDa crosslinker, (C) 10% ($w/w_{protein}$) 2kDa crosslinker, (D) 30% ($w/w_{protein}$) 2kDa crosslinker, and (E) 50% ($w/w_{protein}$) 2kDa crosslinker. (F)

The size of hydrated pNPs was measured using DLS after pNPs collection and dispersion in PBS buffer. (G) shows a table with parameters/conditions for electrospraying of the OVA pNPs. (H) SANS data and fits for OVA pNPs with 10% and 50% PEG/OVA ratio. OVA pNPs were dispersed in D_2O at 2 mg/mL. Data were fitted using the Debye-Anderson-Brumberger (DAB) model (see main text for more information). (I) Young's modulus as a function of the pNP PEG/OVA ratio. Data were obtained by fitting the force-distance profiles obtained from AFM measurements using the Hertz model for a conical indenter.

4.4.2 Mesh size of Ovalbumin Nanoparticles

We conducted SANS measurements of two representative OVA pNPs, 10% and 50% PEG/OVA NPs dispersed in D_2O (2 mg/mL). We expected that the scattering from the hydrated protein network resembles the scattering from heterogeneous synthetic polymer hydrogels,[337] which can be modeled as a disordered two-phase system with a protein-rich network phase and a protein-poor polymer phase. Accordingly, the scattering curves were fitted to a combined Porod model[338] and the Debye-Anderson-Brumberger (DAB) model[339] (solid black lines in **Figure 4-1H**) according to

$$I(q) = \frac{8\pi\Phi(1-\Phi)(\Delta\rho)^2\xi^3}{(1+(q\xi)^2)^2} + \frac{A}{q^4} \qquad \textbf{Equation 4-2}$$

where A is a coefficient that determines the relative magnitude of Porod scattering. The DAB model (first term in **Equation 4-2**)describes scattering from the concentration correlations between the protein-rich phase with volume fraction Φ and scattering length density contrast $\Delta\rho$ with the surrounding fluid that is randomly distributed into domains of average spacing ξ. The Porod model (second term in **Equation 4-2**) represents scattering from smooth interfaces between the protein-rich and protein-poor domains.

Equation 4-2 provides fits of the observed SANS spectra from the two samples. At low q-values, we observe a q^{-4} dependence of the scattering data, consistent with scattering from a smooth interface. At moderate q-values, the length scale ξ is apparent as a shoulder in the scattering curve.

It should be noted that the overall fit for 50% PEG/OVA pNPs is poor in the region where the Porod and the DAB model contributions are of similar magnitude (q~0.01-0.02 Å^{-1}). The explanation for this lies in the interference between the Porod scattering from the interfaces of the protein-rich domains and the DAB scattering from polymer chains inside the domains. This is not accounted for in the model and would likely show up in the mid q-range, where the model gives a poor fit.

We found that the DAB scale factor ($8\pi\Phi(1-\Phi)(\Delta\rho)^2$) increases four-fold as the PEG/OVA ratio increased from 10% to 50%, confirming the densification of the protein network as the degree of crosslinking increases. Furthermore, ξ decreased nearly two-fold as the PEG/OVA ratio increased from 10% to 50% (**Table 4-3**), thus revealing a more finely divided structure with increasing PEG/OVA ratio. Together, these results suggest that the protein network becomes denser and more finely heterogeneous with increasing PEG/OVA ratio, consistent with a more porous but smaller mesh structure at higher crosslink density.

Table 4-3. Fit parameters from DAB model.

Particle Group	10 % PEG/OVA	50% PEG/OVA
Porod scale factor, A	$3.70 \times 10^{-9} \pm 2.99 \times 10^{-13}$	$5.92 \times 10^{-9} \pm 1.02 \times 10^{-13}$
DAB scale factor, $8\pi\Phi(1-\Phi)(\Delta\rho)^2$	$4.92 \times 10^{-6} \pm 1.32 \times 10^{-7}$	$1.95 \times 10^{-5} \pm 1.60 \times 10^{-7}$
Correlation length, ξ (nm)	3.98 ± 0.12	2.15 ± 0.01

4.4.3 Elasticity of Ovalbumin Nanoparticles

Since the ability for the uptake of pNPs by cells might be affected by the mechanical properties of the pNPs, we measured the elastic moduli of the OVA pNPs. We conducted AFM indentation measurements to obtain the elastic moduli for polymerized OVA pNPs (**Figure 4-2** and **Figure 4-1I**).

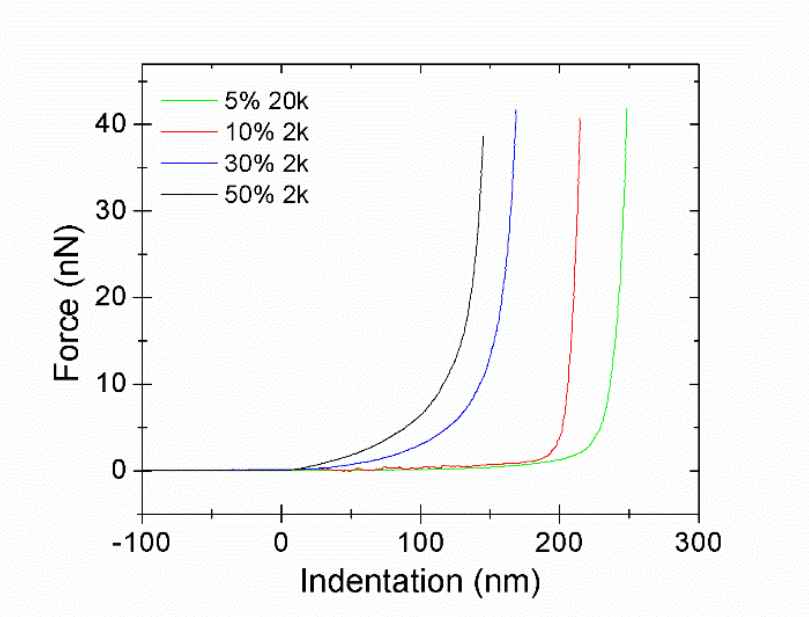

Figure 4-2. Force-indentation profiles from which Young's moduli were calculated using the Hertz model for a conical indenter.

All AFM force measurements were conducted at 37 °C to mimic cellular uptake experimental conditions. Elastic (E) moduli were extracted from the experimental force-indentation profiles by fitting the profiles using the Hertz model for a conical indenter according to

$$F = \frac{2E\ tan\theta}{\pi\ (1-\nu^2)}\ \delta^2 \qquad \textbf{Equation 4-3}$$

where F is the indentation force, δ is the indentation, θ is the half-opening angle of the indenter, E is the E modulus of the nanoparticles, and ν is the Poisson ratio of the nanoparticles.[340] A value of ν = 0.5 was used to fit the profiles using **Equation 4-3**.[341] The Hertz model assumes that the nanoparticles exhibit a uniform E modulus. It can be applied even for heterogeneous nanoparticles such as our OVA pNPs, as the length scale over which the probe deforms the pNPs is large relative to the size of the density heterogeneities. Our results show that the E modulus increases with increasing PEG/OVA ratio. This dependency of crosslinker density and E modulus has been previously observed[342] and was associated with increasing stiffness of the OVA pNPs with

increasing PEG/OVA ratio. In our study, the increase in E modulus was directly correlated to the increase in PEG/OVA ratio, as expected for rubber-like materials such as polymer hydrogels.[343] The increase in stiffness coincides well with the decrease in correlation length from SANS (**Table 4-3**) and the decrease in swelling ability (**Figure 4-1G**).

4.4.4 Cellular Uptake of Ovalbumin Nanoparticles

The uptake of engineered OVA pNPs by BMDCs was evaluated quantitively by flow cytometry (**Figure 4-3A**) and further visualized by confocal microscopy (**Figure 4-3B-E**) using AlexaFluor 647-labeled OVA pNPs. The fluorescence intensity of OVA pNPs (10 μg/mL) was quantified using a plate reader; we found no significant differences in fluorescence intensity between the different nanoparticle groups. To investigate the interaction between OVA pNPs and BMDCs, confocal microscopy was used. BMDCs were incubated with AlexaFluor 647-labeled OVA pNPS with different PEG/OVA ratio for 24 hours at 37℃. The actin filaments were stained with AlexaFluor 488-Phalloidin and the nucleus was stained with DAPI. As shown in **Figure 4-3B-E**, OVA pNPs of different PEG/OVA ratio were successfully internalized by BMDCs allowing for intracellular antigen delivery to BMDCs. As seen in the confocal images, pNPs with higher PEG/OVA ratio showed reduced uptake. To quantify the uptake of OVA pNPs by BMDCs, flow cytometry was used. OVA pNPs were incubated with BMDCs for 24 hours at a concentration of 10 μg/mL. Cellular uptake was quantified using flow cytometry by comparing the mean fluorescence intensity (MFI) values. Our data show that there is a difference in the MFI values for OVA pNPs with different crosslinking density. MFI values were increased for pNPs with lower PEG/OVA ratio (10%), which correlated with higher cellular uptake, compared to the other groups. Cells incubated with pNPs with a 10% PEG/OVA ratio showed 6.9-fold greater MFI than those exposed to pNPs comprised of 50% PEG/OVA ($P < 0.0001$). However, MFI values for cells

incubated with pNPs with 5% and 10% PEG/OVA ratios were not statistically different ($P > 0.05$). It has been shown previously that the elasticity of nanoparticles affected cellular uptake: Nanoparticles with Young's moduli between 30 and 140 kPa showed the highest uptake by RAW 264.7 macrophages, while softer (<30 kPa) or harder (>140 kPa) NPs showed reduced uptake.[344] In our case, pNPs with PEG/OVA ratios of 5% and 10%, which had intermediate elasticity as indicated by E moduli of E = 43 kPa, were associated with the highest levels of cellular uptake.

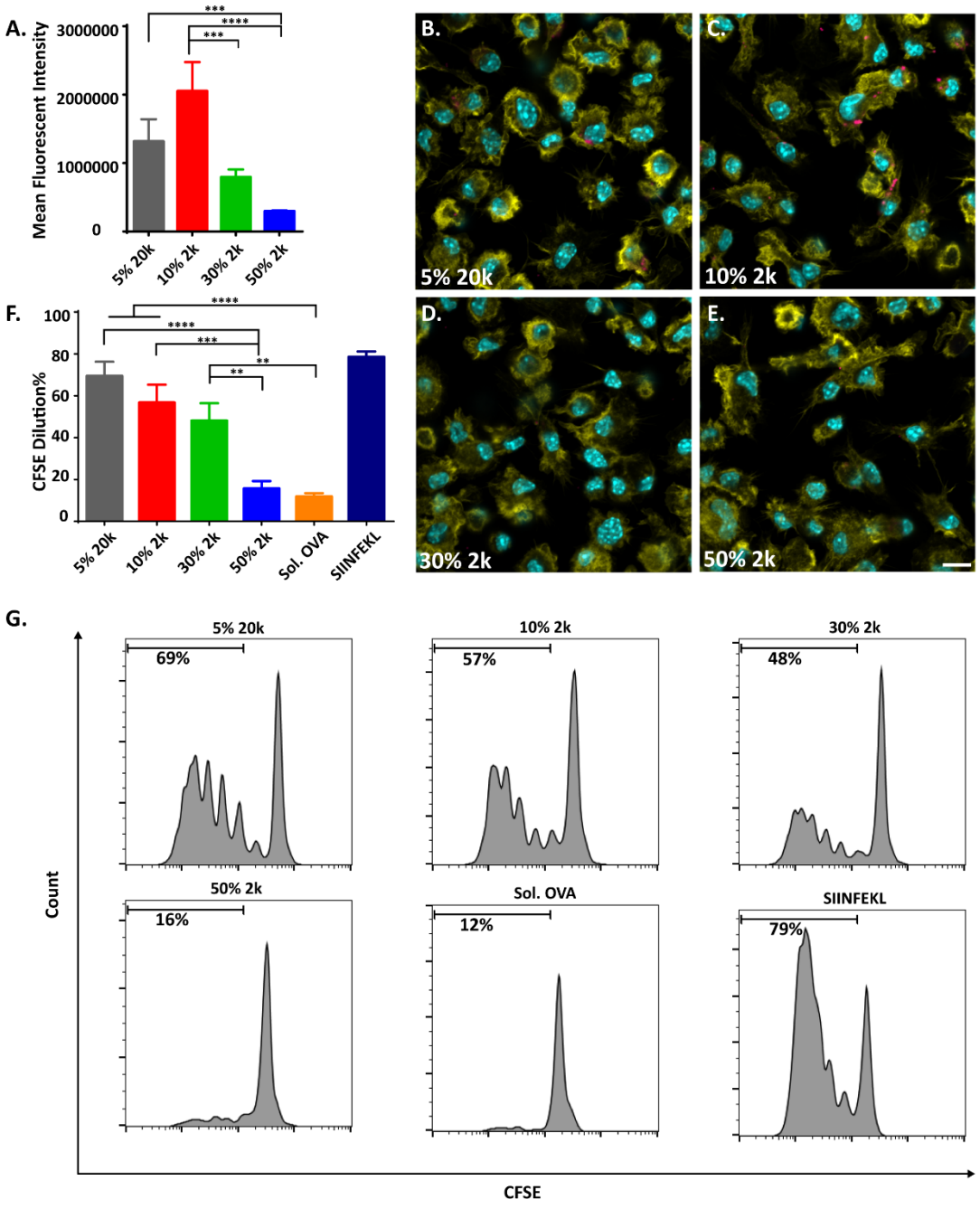

Figure 4-3. In vitro cell uptake of fluorescently labeled OVA pNPs by BMDCs. (A) Quantitative uptake data (MFI values) were obtained by flow cytometry. The data represent the mean ± SEM using triplicates. (B-E) Uptake was further visualized by confocal microscopy. BMDCs were incubated with OVA pNPs (magenta) at 10 µg/mL for 24h. The actin filaments were stained with AlexaFluor 488-Phalloidin (yellow) and the nucleus was stained with DAPI (blue). For flow cytometry, BMDCs were stained for dendritic cell marker CD11c+ using anti-CD11c+ PE-Cy7; they were also stained with DAPI. For confocal microscopy, actin was stained with phalloidin488 and nuclei were stained with DAPI. OVA pNP-treated BMDCs induce proliferation of OT-I CD8+

cells. (F) Percentage of proliferated OT-I CD8+ cells after co-culture with BMDCs incubated with 10 μg/mL OVA pNPs (5% 20k XL, 10% 2k XL, 30% 2k XL, 50% 2k XL). The data represent the mean ± SEM from triplicates of three experiments. (G) Representative flow cytometry histograms of (F). All shown data were analyzed by one-way ANOVA, followed by Tukey's post-test. A *P*-value of <0.05 was considered statistically significant (*$P < 0.05$, **$P < 0.01$, ***$P < 0.001$, and **** $P < 0.0001$); *P*-values of >0.05 were considered not significant (ns).

4.4.5 Antigen Cross-presentation by Ovalbumin Nanoparticles

Eliciting an effective immune response requires delivery of OVA to APCs, such as dendritic cells. Dendritic cells digest OVA through a process called cross-presentation, which results in the activation and proliferation of CD8+ T cells. Thus, the ability of OVA pNP-treated BMDCs to promote antigen cross-presentation and induce antigen-specific proliferation of OT-I CD8+ cells were evaluated using a CFSE dilution assay (**Figure 4-3F** and **Figure 4-3G**). CFSE dilution is proportional to the proliferation of OT-I CD8+ cells. Therefore, BMDCs were first incubated with OVA pNPs or soluble OVA (control) at 10 μg/mL for 24h. BMDCs were then co-cultured with CFSE-labeled naïve OT-I CD8+ T cells, which recognize the OVA-derived epitope SIINFEKL presented in the context of MHC-I $H2K^b$. After 72h of co-culture, the population of proliferated CD8+ T cells was assessed using flow cytometry. We found that proliferation was affected by the PEG/OVA ratios of the pNPs. The OVA pNPs with PEG/OVA ratio of 5% showed 4.4-fold ($P < 0.0001$) higher proliferation rates than pNPs with a 50% PEG/OVA ratio. Similarly, pNPs with PEG/OVA ratio of of 10% and 30% showed 3.6-fold ($P < 0.001$) and 3.1-fold ($P < 0.01$) higher proliferation rates than pNPs comprised of 50% PEG/OVA, respectively. Cross-priming and proliferation of the OT-I CD8+ cells were significantly enhanced for OVA pNPs with 5% ($P < 0.0001$), 10% ($P < 0.0001$) and 30% ($P < 0.01$) PEG/OVA ratios as compared to solute OVA (**Figure 4-3F**). While all pNP groups outperformed solute OVA, 5% and 10% PEG/OVA pNPs

were most efficient in promoting antigen cross-presentation and proliferation of OT-I CD8+ cells. This result suggests (1) greater uptake of 5% and 10% PEG/OVA pNPs by BMDCs and (2) facilitated the processing of OVA pNPs by BMDCs due to lower crosslinking density and larger size of 5 and 10% PEG/OVA pNPs. There is some evidence that larger particles can direct antigen to the class I antigen presentation pathway more efficiently,[345] which might explain the higher proliferation values for 5% PEG/OVA pNPs (500 nm vs. 200 nm). Once internalized by BMDCs, smaller particles are shuttled more rapidly to an acidic environment than larger ones,[304] which can lead to fast and unregulated degradation and inefficient cross-presentation.[304] Larger particles remain longer in a neutral environment, thus preserving the antigens for more efficient cross-presentation.[304] Our results indicate that the PEG/OVA ratio is an important parameter for enhancing proliferation of CD8+ T cells, lower PEG/OVA ratios resulting in higher proliferation rates.

4.4.6 Humoral Immune Responses After Subcutaneous Delivery of Ovalbumin Nanoparticles

Our next aim was to investigate the in vivo performance of the pNPs by evaluating their ability to induce humoral immune responses in mice. Following the prime-boost vaccine regimen shown in **Figure 4-4A**, we injected C57BL/6 mice subcutaneously at the tail base with OVA pNPs of varying PEG/OVA ratio (10, 30, 50 %) and size (200 nm, 500 nm) or solute OVA (10 μg OVA/100 μL dose), co-administered with CpG (15 μg/dose). Boost immunization was performed on day 21 after primary immunization. Anti-OVA serum IgG responses were measured on days 20 and 42 using an ELISA assay. Compared to soluble OVA, pNPs with a 10% PEG/OVA ratio elicited 49.4-fold increase in anti-OVA serum IgG titers in prime ($P < 0.0001$) and 9.1-fold increase in boost immunization ($P < 0.05$), respectively. In addition, anti-OVA serum IgG titers

induced after prime immunization with pNPs of 30% and 50% PEG/OVA ratios exhibited 39.9-fold ($P < 0.0001$) and 26.5-fold ($P < 0.01$) increase compared to soluble OVA, respectively. Among the pNPs groups, 10% PEG/OVA ratio pNPs outperformed pNPs comprised of 50% PEG/OVA, as indicated by a 1.9-fold increase in anti-OVA serum IgG titers after prime immunization ($P < 0.01$). Our results show that 2 doses of OVA pNPs administered in a prime-boost regimen elicited stronger humoral immune responses than the equivalent doses and regimen of soluble OVA (**Figure 4-4B** and **Figure 4-4C**). While the larger, 5% PEG/OVA pNPs showed stronger CD8+ T cell responses in vitro, the same particles elicited a weaker humoral immune response in vivo (comparable to soluble OVA). Because the elasticity of 5% and 10% PEG/OVA pNPs was similar, the weaker humoral immune response of 5% PEG/OVA pNPs can be attributed to their larger size (500 nm). Larger pNPs may have limited lymphatic drainage due to extended tissue persistence at the injection site.

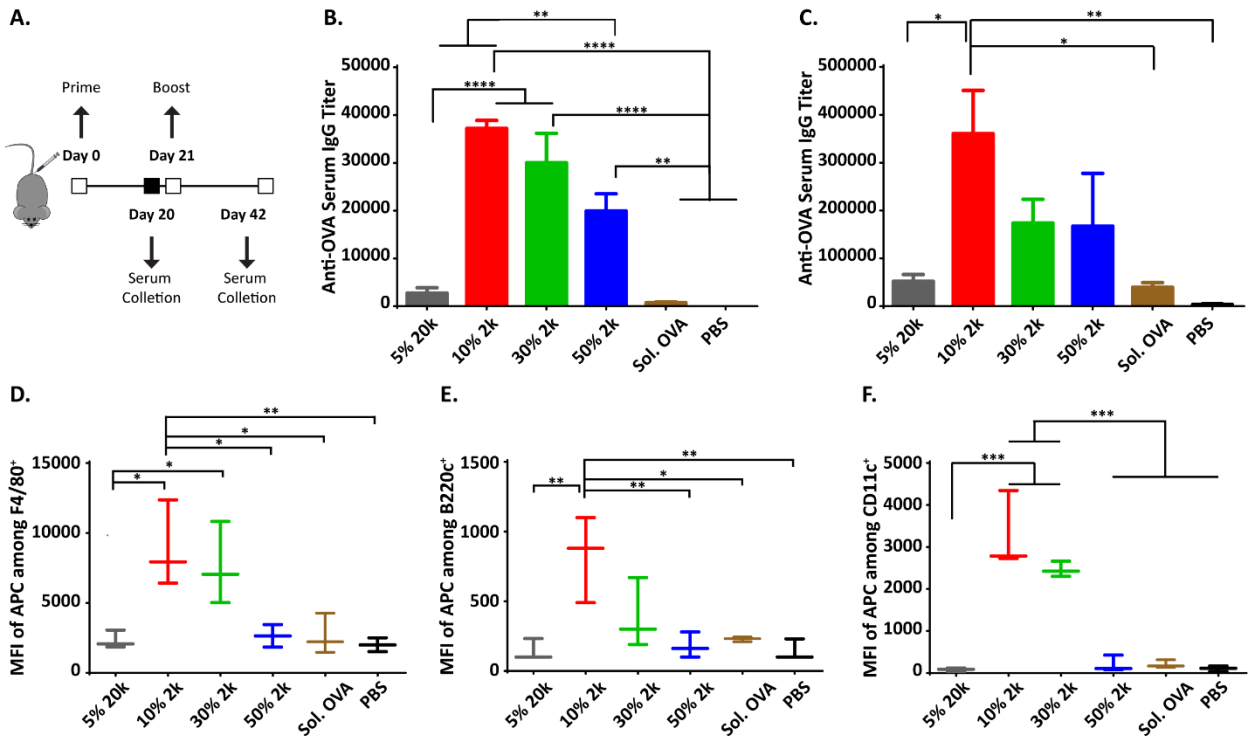

Figure 4-4. Humoral responses elicited by engineered OVA pNPs in immune competent mice. (A) Vaccine doses and regimen. Naïve C57BL/6 mice were injected with OVA pNPs and soluble CpG subcutaneously at the tail base on Day 0 (prime immunization) and 21 (boost immunization). Serum anti-OVA IgG titers were measured on (B) Day 20 (prime response) and (C) Day 28 (boost response). The data were fitted by logarithmic regression. The titer was calculated by solving for the inverse dilution factor resulting in an absorbance value of 0.5. Data represent mean ± SEM (n=5). Groups were compared using one-way ANOVA with Tukey's post-test. $P < 0.05$ was considered statistically different (*$P < 0.05$, **$P < 0.01$, ***$P < 0.001$, and ****$P < 0.0001$). $P > 0.05$ was considered not significant. Delivery of pNPs to draining lymph nodes: MFI of AlexaFluor 647 associated with OVA NPs among (D) F4/80+ macrophages, (E) B220+ B cells and (F) CD11c+ dendritic cells obtained from a single cell suspension from draining lymph nodes. Groups were compared using one-way ANOVA with Tukey's post-test. $P < 0.05$ was considered statistically different (*$P < 0.05$, **$P < 0.01$, ***$P < 0.005$). $P > 0.05$ was considered not significant.

4.4.7 Ovalbumin Nanoparticles Delivery to Lymph Nodes

We evaluated the pNPs targeting of the draining lymph nodes using AlexaFluor 647-labeled pNPs. OVA pNPs of varying PEG/OVA ratio (10, 30, 50 %) and size (200 nm, 500 nm) were injected subcutaneously at the tail base of C57BL/6 mice (10 μg OVA/100 µL dose). The inguinal draining lymph nodes were harvested 48h after injection. We prepared single-cell suspensions from the

draining lymph nodes and analyzed pNPs uptake among the different populations of antigen-presenting cells (dendritic cells, macrophages and B cells) using flow cytometry by comparing the MFI values of the cells. We found that the MFI values of F4/80+ macrophages, B220+ B cells and CD11c+ dendritic cells (**Figure 4-4D-F**) increased with decreasing PEG/OVA ratio for the smaller (200 nm) pNPs with 10%, 30% and 50% PEG/OVA ratio. 50% PEG/OVA pNPs did not show any significant difference compared to soluble OVA. However, 10% PEG/OVA pNPs were delivered more efficiently to F4/80+ macrophages ($P < 0.05$), B220+ B cells ($P < 0.01$) and CD11c+ dendritic cells ($P < 0.005$) compared to 50% PEG/OVA pNPs. Specifically, the antigen delivery to B220+ B cells by 10% PEG/OVA pNPs, even at short time point, was increased compared to 50% ($P < 0.01$), 5% PEG/OVA pNPs ($P < 0.01$) and soluble OVA ($P < 0.05$), which correlated well with the trend of induction of anti-OVA serum IgG titers measured by ELISA. The MFI values of cells with larger (500 nm) 5% PEG/OVA pNPs was significantly lower than 10% PEG/OVA pNPs, indicating that the pNPs were not delivered to draining lymph nodes efficiently due to their larger size. In the past, many different particle sizes have been studied with respect to their lymphatic drainage.[283,297,298,345–348] It has been shown that particles exceeding 500 nm can be trapped at the injection site. Nanoparticles smaller than 10 nm, or soluble antigen, diffuse into the lymphatic system easily, but their retention time in the lymph nodes is too short to provide sustained antigen delivery.[268] This may explain why OVA pNPs with 500 nm size and soluble OVA were not delivered to the lymph nodes efficiently, while we observed improved NP uptake by lymph node cells for the smaller OVA pNPs. For smaller pNPs sizes, improved uptake was observed for pNP with lower PEG/OVA ratio.

4.4.8 Therapeutic Efficacy of Ovalbumin Nanoparticles in a Model of Melanoma

Encouraged by the fact that OVA pNPs with 10% PEG/OVA ratio resulted in increased OT-I CD8+ cell proliferation in vitro, improved uptake by APCs (both in vitro and in vivo), and enhanced humoral immune response in vivo, we employed a murine model of B16F10-OVA melanoma to evaluate the therapeutic efficacy of pNPs with a PEG/OVA ratio of 10% compared to solute OVA. Tumor-bearing mice were treated with 10 % PEG/OVA pNPs or solute OVA (10 μg OVA/ 100 μL dose), co-administered with CpG (15 μg/dose). Following the regimen shown in **Figure 4-5A**, we inoculated C57BL/6 mice (10 mice/treatment group) with 1×10^5 B16F10-OVA cells in the SC flank on day 0. Treatments with either 10 % PEG/OVA pNPs or solute OVA were initiated on day 7 after tumor inoculation. A second treatment was given on day 14. Mice were euthanized after their tumors reached 15 mm in any dimension. Compared to the no treatment control group, mice treated with solute OVA showed slightly better survival (**Figure 4-5B)**.

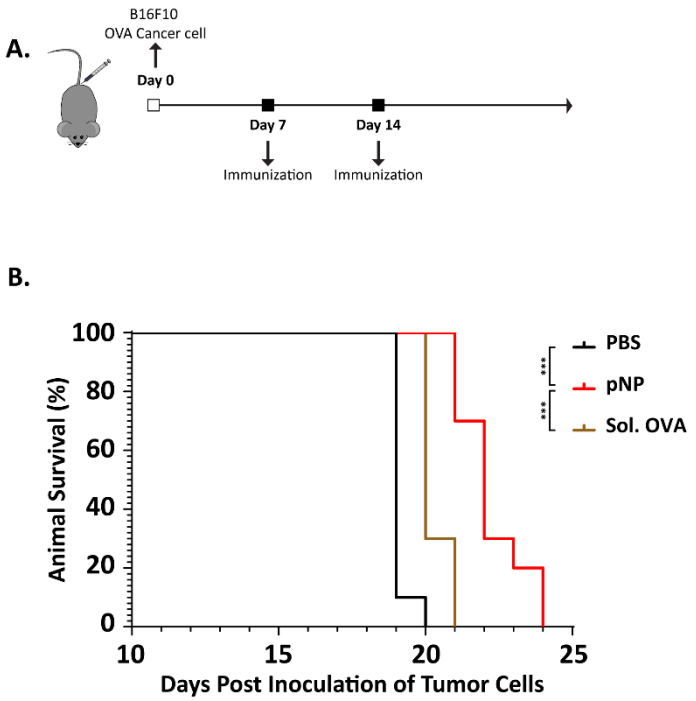

Figure 4-5. Therapeutic effect of engineered OVA pNPs in melanoma-bearing mice. (A) Vaccine doses and regimen and (B) animal survival. C57BL/6 mice were inoculated subcutaneously with 1×10^5 B16F10-OVA cells on day 0. On day 7 and 14, mice were treated with indicated formulations (OVA pNP, soluble OVA, PBS) containing 10 μg/dose OVA and 15 μg/dose CpG (100µL dose). Data represent mean ± SEM (n=10). Groups were compared using Kaplan-Meier estimator analysis. $P < 0.05$ was considered statistically different (*$P < 0.05$, **$P < 0.01$, and ***$P < 0.001$). $P > 0.05$ was considered not significant.

More than 50 % of mice treated with solute OVA were euthanized due to large tumor burden on day 20, and 100 % of the mice were euthanized on day 21. In contrast, 100 % of mice treated with 10 % PEG/OVA pNPs were alive on day 21 and showed improved survival until the endpoint of the study (day 24). Treatment with 10% PEG/OVA pNPs significantly enhanced antigen-specific CD8+ T cell immune response compared to solute antigen and PBS groups (**Figure 4-6**).

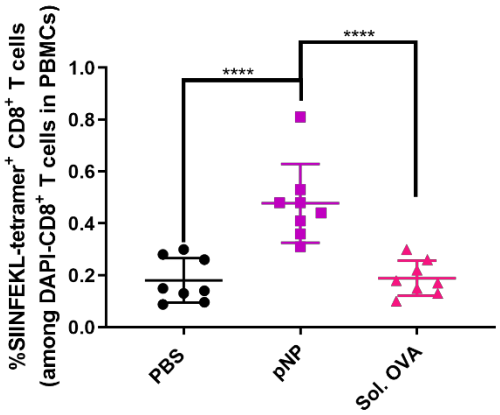

Figure 4-6. The percentage of SIINFEKL-tetramer+ CD8+ T cells among total CD8+ T cells in PBMCs on day 13.

The survival rate of B16F10-OVA tumor-bearing mice were increased after immunization with OVA pNPs compared to solute antigen treatment. The survival data observed with OVA pNPs is comparable to previous studies that conducted delivery of OVA antigen in the same B16F10-OVA model.[349–353]

4.5 Conclusions

We employed reactive electrospraying, a novel, yet scalable and versatile nanoparticle manufacturing process, for development of engineered OVA pNPs with defined physico-chemical properties. We identified key parameters (e.g., size or PEG/OVA ratio) that determined the immunological responses of pNPs. Specifically, lower PEG/OVA ratios resulted in softer pNPs with larger mesh sizes, which, in turn, resulted in improved CD8+ T cell activation in vitro and improved lymph node drainage and humoral immune response in vivo. Identifying the significance of these parameters allowed us to design a pNP formulation with preclinical potential. In a preclinical murine model of melanoma, we found that the smaller (200 nm) pNPs of 10% PEG/OVA ratio resulted in improved survival of mice bearing advanced melanoma tumors. In

future studies, to improve the clinical relevance, a combination strategy using different types of immunotherapies should be employed. In this case, a combination of OVA pNP administration with adjuvant therapy and immune checkpoint inhibitor therapy could result in further improvement of the preclinical outcomes.

Conflict of Interest. The University of University of Michigan has filed a patent application (US 62/931,512) on materials related to the work described in this manuscript.

Chapter 5
Engineered Protein Nanoparticles for Red Blood Cell-mediated Brain Delivery

The material in this chapter has been adapted with minor modifications from the following article: Nahal Habibi, Daniel C. Pan, Oscar A. Marcos-Contreras, Jacob W. Myerson, Jia Nong, Samir Mitragotri, Jacob S. Brenner, Vladimir R. Muzykantov, Joerg Lahann. Engineered Protein Nanoparticles for Red Blood Cell-mediated Brain Delivery. *In Preparation*.

5.1 Abstract

One major hurdle to the efficient delivery of therapeutics to the brain is the presence of the blood-brain barrier (BBB). Protein nanoparticles (PNPs) are biocompatible, biodegradable, and easily amenable to surface modifications. Since albumin, as a natural protein, can bind to endothelial cell surface receptors such as albumin-binding glycoprotein (gp60) and mediate endothelium transcytosis, human serum albumin (HSA) PNPs are developed herein to create a brain drug delivery platform using the electrohydrodynamic jetting technique. This study reports a novel type of nanoparticle-based system that combines HSA PNPs unique physiological properties with the circulation and vascular mobility of red blood cells (RBCs) to enhance the brain uptake of nanoparticles. These HSA PNPs present a monodisperse population with an average diameter of 99 nm. Geometric factor analysis demonstrates that HSA PNPs possess high circularity (0.82), low anisotropy (1.26), and high roundness (0.83). HSA PNPs effectively associate with RBCs with an average of 126 particles per RBC with no adverse effect on RBCs as demonstrated by agglutination assay, phosphatidylserine exposure, and ektacytometry. In a mouse model of acute

brain inflammation, HSA PNPs associated with RBCs prior to intraarterial injections show 19 times higher brain uptake compared to free HSA PNPs. These findings are corroborated by a 113-fold increase in the brain-to-(liver and spleen) ratio and an 8-fold increase in the brain-to-blood ratio. High levels of brain targeting, combined with reduced accumulation in the liver and spleen, are hallmarks of an effective nanomedicine platform, a technological advancement that is desperately needed for a wide range of debilitating diseases of the central nervous system ranging from encephalitis to Alzheimer's and Parkinson's diseases.

5.2 Introduction

Central nervous system (CNS) drugs have higher failure rates than non-CNS drugs, both in preclinical and clinical trials.[354] Analysis of the probability of launch from phases I, II, and III for drugs within different therapeutic areas from 2010 to 2017 demonstrated that nervous system disorders were among the areas with the lowest probability of success.[355] A significant challenge in drug development for CNS diseases is the lack of efficient strategies to deliver systemically administered drugs into the CNS compartment. The brain is protected by the blood-brain barrier (BBB), which maintains hemostasis and strictly regulates the transport of compounds into the brain parenchyma.[356] The BBB, as a dynamic barrier protecting the brain against unwanted substances, imposes a significant challenge to drug transport into the brain via blood circulation.[357] The BBB is mainly composed of tightly connected brain microvascular endothelial cells lining the brain's surrounding blood vessels. Characteristic features of the brain endothelium include the expression of tight junctions and adherens junctions as well as the lack of fenestrations.[358] The unique features of the BBB, including its low and selective permeability,[359] lead to the restriction of entry of almost 100% of large-molecule and 98% of small-molecule neurotherapeutics to the brain.[360,361]

Several approaches have been pursued to overcome the BBB and enhance drug transport to the brain.[362] Conventional methods to enhance the drug delivery across the BBB include the application of focused ultrasound to induce localized and transient disruption of the BBB,[363] intracarotid injection of hyperosmotic solutions such as mannitol to shrink the endothelial cells and widen tight junctions,[364] and convection-enhanced delivery (CED) via implantable infusion catheters to enhance the bulk convective flow of the drug in the interstitial space by using positive pressure gradients.[365,366] However, the broad clinical translation of these approaches is still limited due to a series of bottlenecks. The transient disruption of the BBB and opening of tight junctions using microbubbles, ultrasound, and osmotic pressure may damage the integrity of the BBB and cause an uncontrolled and nonspecific influx of drugs and unwanted compounds into the CNS.[367] Due to the possible leakage of membrane proteins, entry of toxins, release of cytokines, and imbalance of ions, these methods may lead to neuronal dysfunction or inflammation.[367] Additionally, CED by direct injection is an invasive approach that comes with several challenges limiting its efficacy. These limitations can be specific to CED, such as backflow, or they can be related to pathological conditions, such as increased interstitial pressure and heterogeneous blood vessel distributions.[368] Although this strategy has been used in several phase I-III clinical trials for the treatment of glioblastoma, the improvement in patient survival remains modest.[362]

Bridging nanotechnology and medicine has yielded opportunities to develop novel nanoparticle-based systems for non-invasive brain drug delivery. Nanoparticle technologies hold great promise for addressing at least some of the limitations of systemic drug delivery to the brain[367] due to their biocompatibility, biodegradability, and ability to encapsulate a wide range of drugs with different physicochemical properties while protecting them against degradation.[13–16,369] However, the amount of nanoparticles that reach the brain is currently still dissatisfactory. Poor brain uptake of

intravenously administered nanoparticles results from the series of biological barriers they face in reaching the brain, including clearance by the reticuloendothelial system (RES) and penetration across the BBB.[6] Despite significant progress in this field,[6] after more than two decades since the first FDA-approved nano-based drug, there is still no FDA-approved nanoparticle formulation for drug delivery to the brain.[370,371] Developing nanoparticles with suitable biological and physical properties that can overcome this conundrum is critical. Various strategies have been implemented, including the use of targeting antibodies to improve brain uptake.[230,372] However, in the case of transferrin receptor targeting, which is one of the more promising approaches, only about 1% of the injected dose per gram (%ID/g) of brain tissue was delivered to the brain.[373] Therefore, novel nanoparticle-based delivery platforms capable of sequentially addressing multiple biological barriers are needed to enhance their clinical translation.[206]

An ideal nanoparticle-based delivery system would combine the biocompatibility, biodegradability, drug encapsulation capability, and size customizability of nanoparticles with strategies to increase their blood circulation time, accumulation at brain endothelium, and penetration across the BBB. While it is challenging for synthetic nanoparticles to address this array of biological barriers, circulatory cells have innate properties as the body's natural delivery vehicles to negotiate these barriers and optimally perform delivery functions.[374] The inherent properties of circulatory cells, including their long circulation lifespan, natural stealth properties, and natural tissue targeting, parallel ideal nanoparticle-based systems features. One approach to improve the overall biological outcome of nanoparticle-based drug delivery systems is to impart these inherent properties of circulatory cells to the delivery platforms through a concept known as "cellular hitchhiking."[374] In this strategy, the advantages of circulatory cells and synthetic

nanoparticles are combined and simultaneously utilized to address multiple biological barriers, which would be hard-to-achieve by traditional nanomedicine.[375]

A rational selection of appropriate cells and well-designed nanoparticle properties are recognized as essential prerequisites for designing successful cellular hitchhiking platforms. Specifically, monocytes and macrophages have been used as brain delivery vehicles for nanoparticles due to their ability to internalize nanoparticles and cross the BBB.[176,376] For example, to improve photothermal therapy efficiency, gold-silica nanoshells-loaded macrophages have been used to deliver nanoshells into gliomas in vitro [180] and in vivo.[377] In another study, bone-marrow derived macrophages were used to internalize self-assembled polyethyleneimine-poly(ethylene glycol) (PEI-PEG)/ catalase both to protect antioxidant activity of catalase and deliver it to the brain in a Parkinson's disease (PD) model.[179] Although the internalization route leaves the cell membrane intact, following phagocytosis the nanoparticles are subject to endosomal degradation within the carrier cells causing premature drug release, loss of therapeutic effect, or impairing essential cell functions such as migration.[378,379]

As an alternative approach, red blood cells (RBC) can be used as non-phagocytic cell carriers for drug delivery to the brain. RBCs, the most abundant cellular component of the blood (>99%), have many attributes of an ideal carrier, such as their longevity in circulation, bioavailability, biocompatibility, large surface area, and reversible deformation facilitating navigation through microvasculatures smaller than their diameter.[156,158,375,380] By attaching nanoparticles to RBCs, some of these unique properties can be transferred to nanoparticles in vivo, such as prolonging the circulation time[162,164] and targeted organ delivery by detachment and transfer of nanoparticles to the first microcapillary bed, downstream of the injection site.[165,166] However, successful translation of RBCs properties into nanoparticle systems requires understanding nanoparticle

adsorption effects on the carrier RBCs. The adsorption of nanoparticles to RBCs must not adversely affect the carrier cells at loadings required for optimal therapeutic efficiency.[381] It was shown that adsorption of model polystyrene nanoparticles onto RBCs induced agglutination and sensitized RBCs to damage by various stresses (e.g., osmotic, mechanical, oxidative).[381,382] Moreover, the stiffness of RBCs and surface exposure of phosphatidylserine were increased as a result of binding polystyrene nanoparticles to RBCs.[381] All of these adverse changes in RBCs' physiological characteristics are known to accelerate their clearance in vivo.[382] The adsorption of model polystyrene nanoparticles at even 50:1 nanoparticle to RBC ratio caused RBCs agglutination.[381,382] Interestingly, coating the polystyrene nanoparticles with IgG or albumin protein was able to inhibit the induced agglutination even at higher nanoparticle to RBC ratios.[166,382]

An emerging trend in nanoparticle-based drug delivery focuses on substituting synthetic polymers with proteins as the primary component of nanoparticles. Increased attention has been given to proteins due to their inherent properties such as (i) biocompatibility, (ii) biodegradability, (iii) versatility, (iv) unique functionalities and endogenous mechanisms, (v) metabolizability, (vi) surface modification capabilities, and (vii) potential lack of immunogenicity.[6,94] Specifically, human serum albumin (HSA), a long-circulating and the most abundant plasma protein has key characteristics including its clinical relevance such as abraxane™[105] and its preferential accumulation in tumor and inflamed tissue[383–386] which makes it a compelling candidate as drug delivery system. Albumin and albumin-based nanomedicine have been shown to engage in transcytosis across the vascular endothelium mediated by receptors such as gp60 and SPARC[386–388] which are overexpressed on glioma cells,[389] tumor vessel endothelium,[390] and inflamed cerebral endothelia.[383] All of these properties make HSA an attractive candidate for designing

protein nanoparticle (PNP)-based systems for brain drug delivery. Here, we engineered HSA PNPs, surface-decorated with IgG antibody, which allowed for binding onto RBCs with no apparent adverse effects on the carrier cells. Intracarotid injection of RBC-bound HSA PNPs greatly improved brain delivery compared to their free HSA PNPs counterparts in naive and brain-injured mice.

5.3 Materials and Methods

5.3.1 Materials

Recombinant human serum Albumin (Cellastim S) was purchased from InVitria. *O*,*O*′-bis[2-(*N*-succinimidyl-succinylamino)ethyl]polyethylene glycol (NHS-PEG-NHS) with a molecular weight of 2000 Da, polyvinylpyrrolidone were obtained from Sigma-Aldrich (St. Louis, MO). Alexa Fluor 488 conjugated albumin from bovine serum and Alexa Fluor 647 conjugated albumin from bovine serum were purchased from Thermo Fisher Scientific Waltham, MA. Iodobeads were pbrained from Perkin-Elmer. CJ7BL/6 mice were purchased from the Charles River Laboratory (Wilmington, MA). Sulfo-(N-hydroxysulfosuccinimide)(NHS) and 1-ethyl-3-(3-dimethylaminopropyl)carbodiimide hydrochloride (EDC) were obtained from Thermo Fisher Scientific. 4′,6- Diamidino-2-phenylindole (DAPI) was purchased from Southern Biotech. protein G Sepharose was obtained from GE Healthcare BioSciences.

5.3.2 Electrohydrodynamic Jetting of Human Serum Albumin Nanoparticles

HSA PNPs were fabricated using EHD jetting. Briefly, HSA was dissolved at 7.5% (w/v) in a solvent mixture of ultrapure water and ethylene glycol at 4:1 ratio. NHS-PEG-NHS at 10% ($w/w_{protein}$) was used as a crosslinker. The mixture of dissolved HSA and the crosslinker was pumped at a flow rate of 0.1 mL/h in a syringe capped with a needle serving as a capillary. After

forming a droplet at the tip of the needle, the electric field was applied to the needle, distorting the droplet to a Tayler cone. The particles from the apex of the Taylor cone were jetted onto the grounded plate followed by incubation at 37°C for 7 days to allow completion of crosslinking reaction.

The HSA PNPs were radiolabeled using Iodobeads as previously described.[332] First, at least 100 µL of HSA PNPs solution was added to a borosilicate tube that contained two Iodobeads. Then 100 µCi of $Na^{125}I$ per 100 µL of solution was added. For a total of 30 minutes with gentle shaking every 10 minutes, particles were incubated with radioiodine and Iodobeads at room temperature. To remove free iodine, centrifugation cycles were performed to wash the particles and assure >95% of radioactivity was associated with HSA PNPs.

For surface modification of HSA PNPs with IgG, EDC/Sulfo-NHS chemistry was performed. To activate the carboxyl groups of HSA PNPs, they were incubated with 5 mg EDC in PBS buffer with 0.01% Tween20 for 20 minutes, followed with 20 minutes incubation with 5 mg Sulfo-NHS. IgG was added to the activated HSA PNPs at 1000 IgG per HSA PNP and incubated for 2 hours on a rotator at room temperature. The HSA PNPs were then washed multiple times with centrifugation cycles to remove unreacted materials.

5.3.3 Characterization of Human Serum Albumin Nanoparticles

Scanning Electron Microscopy (SEM)

SEM images of HSA PNPs were obtained using a FEI Nova 200 Nanolab SEM/FIB at the Michigan Center for Materials Engineering at acceleration voltages of 5kV. Images were analyzed using ImageJ (Wayne Rasband, NIH) to obtain nanoparticles size distribution and secondary geometric factors. For image analysis, more than 1000 particles per sample were measured by ImageJ.

Dynamic Light Scattering (DLS)

To measure the particles size distribution in PBS buffer, DLS measurements were performed using a Zetasizer Nano ZS (Malvern Panalytical). Every measurement was done in triplicate and the results were averaged to report the particle size.

5.3.4 Blood Collection and Isolation of Red Blood Cells

Ethics Statement

All animal studies were carried out in strict accordance with Guide for the Care and Use of Laboratory Animals as adopted by National Institute of Health, approved by Harvard University and the University of Pennsylvania IACUC. Mice were housed in cages with free access to water and food, located in a well-ventilated temperature-controlled room between 18-23 ºC with relative humidity ranging from 40-60% under a 12-hour light/dark period).

Blood from CJ7BL/6J mice was harvested as previously described.[382] Whole blood, collected in EDTA coated tubes, was centrifuged at 1000 g for 10 minutes at 4ºC to remove plasma as well as platelets and white blood cells. Isolated erythrocytes (RBCs) were extensively washed with 1x Dulbecco's-Phosphate-Buffered-Saline (DPBS), pH 7.4, centrifuged at 500 ×g, 15 min, 4°C the and supernatant was discarded. This wash step was repeated three times.

5.3.5 Adsorption of Nanoparticles to Red Blood Cells

Adsorption of PNPs onto RBCs was performed as previously described.[166] Murine RBCs were incubated with either unmodified HSA PNPs or IgG-modified HSA PNPs (IgG-HSA PNPs) at a RBC:PNP ratio of 1:1000 for 1 hour under constant rotation at 4°C. RBC-PNP solutions were washed with PBS three times at 100 ×g for 8 minutes to remove non-adsorbed BSA PNPs prior to experiments.

5.3.6 Assessment of Nanoparticles Adsorption onto Red Blood Cells by Flow Cytometry

Washed naive RBC and washed RBC-PNP suspensions (5 µL) at 10% Hematocrit were added to 995 µL of PBS, gently vortexed, and ran on a BD LSRFortessa cell analyzer (BD Biosciences, San Jose, CA USA), gated at 10,000 events.

5.3.7 Phosphatidylserine Exposure on RBCs

The amount of RBC suspended at 10% Hematocrit, exposing phosphatidylserine was measured. Briefly, washed RBC and RBC-PNP suspensions at 10% Hemocrit were incubated at room temperature with annexin V-FITC in buffer containing 2mM CaCl2 for 15 min. After incubation, an aliquot was aspirated into a BD LSRFortessa cell analyzer (BD Biosciences, San Jose, CA USA) for analysis, gated at 10,000 events. Results were expressed a percentage of Annexin V positive RBCs.

5.3.8 Red Blood Cells Agglutination

Agglutination assay was performed as previous described.[381] Briefly, naive RBC and RBC:PNP suspensions (1% Hematocrit) were dispensed onto a 96 U-shaped plate and visually accessed after 24h at room temperature after RBC suspension had fully sedimented. Carboxylated polystyrene beads was used as a positive control.

5.3.9 Red Blood Cells Deformability

RBC deformability measurements were performed as previously described by ektacytometry (Rheo Meditech, South Korea).[381] Briefly, 10% hematocrit suspension of naive RBC and RBC-PNP was mixed, at room temperature, with 675 µL of 5.5% (w/v) 360 kDa polyvinylpyrrolidone. Solutions were placed into the flow channel and then subjected to various amount of shear stress ranging from 0 Pa to 18 Pa. Ellipsoidal diffraction patterns were produced. Maximum elongation

index (EI_{max}) and half maximum shear stress ($SS_{1/2}$) were measured. Each experiment was repeated at least three times.

5.3.10 Acute Neurovascular Inflammation Model and Intraarterial Injections

A unilateral striatal injection of tumor necrosis factor alpha (TNFα, 0.5 μg in 2.5 μL) was performed in the following stereotaxic coordinates ventral to the bregma: 0.5 mm anterior, 2.0 mm lateral, − 3 mm as previously described.[391] Control animals did not have any surgical procedure before injection. Anesthetized animals, 20 hours after intrastriatal injection, received the free IgG-HSA PNPs or RBC hitchhiked IgG-HSA PNPs. The injections were performed intraarterially through a mouse arterial catheter placed into the common carotid artery. In order to direct the blood flow to the internal carotid artery (artery that irrigates the brain), the external carotid artery was ligated. Then, 100 μL were infused within 30 seconds, followed by the infusion of 200 μL of saline through the same catheter to perfuse the vessel. Ischemia was prevented due to the collateral circulation. 30 minutes after the injection, animals were sacrificed, tissues were isolated, rinsed in PBS and their residual radioactivity was measured in a gamma counter (Wizard2, Perkin Elmer).

5.3.11 Immunohistology

Alexa Fluor-647 labeled IgG-HSA PNPs were adsorbed onto RBC as previous described and injected through internal carotid artery 24 hours after TNFα intra-striatal injection. Thirty minutes later, the brain was perfused with cold PBS, harvested, fixed and sectioned at 10μm. For tissue staining, tissue sections were blocked using blocking buffer (5% goat serum in PBS with 0.4% Triton) for 1 hour at room temperature, then incubated with primary antibodies overnight at 4°C. The antibodies used were: rat anti-mouse CD45 to identify leukocytes, rat anti-mouse Ly76 (clone Ter-119) to identify red blood cells, and rat anti-mouse VCAM (clone Mk2.7) to identify

endothelial cells. Anti-Ly76 and anti-VCAM were produced by culturing hybridoma cells, purified using protein G sepharose and dialyzed in PBS. After washing, the sections were incubated with secondary antibodies conjugated with Alexa fluorophores at room temperature for 2 hours. All sections were counterstained with DAPI. Leica confocal microscopy was used to visualize the localization of the particles and their interactions with cells of interest.

5.3.12 Statistical Analysis

Statistical analyses were performed using SPSS Statistics 24 software. One-way ANOVA with Tukey's post-test was used to determine significance among groups. For biodistribution studies non-paired, two-tailed *t*-test was used to determine significance among groups. A *P*-value of < 0.05 was considered statistically significant ($*P < 0.05$, $**P < 0.01$, $***P < 0.001$, and $****P < 0.0001$); *P*-values of > 0.05 were considered not significant (ns).

5.4 Results and Discussion

5.4.1 Design, Formulation, and Characterization of Human Serum Albumin Nanoparticles

To engineer a novel brain drug delivery platform the advantages of RBCs with attributes of HSA were integrated (**Figure 5-1A**). HSA PNPs were prepared using EHD jetting, as shown in **Figure 5-1B**. EHD co-jetting is a versatile particle fabrication technique that has been utilized previously to fabricate polymeric and protein nanoparticles for various drug delivery applications.[86,128,130–133,135,137,216,237,251,392–396] In this process, the protein solution is pumped through a needle, acting as a capillary, with a constant flow rate to form laminar flow regime. Once a droplet is formed at the needle, electric voltage is applied to the system leading to distortion of the droplet into a Taylor cone. Then, the solution splits into a spray of droplets leading to a size reduction by several orders of magnitudes, rapid solvent evaporation, and solidification of the non-volatile components into

nanoparticles on the counter electrode. Here, to fabricate HSA nanoparticles, HSA was dissolved at 7.5% (w/v) in a solvent mixture of water and ethylene glycol with a 4:1 ratio. Homobifunctional amine-reactive PEG-based macromer, NHS-PEG-NHS, with 2kDa molecular weight was added to the mixture at 10% ($w/w_{protein}$) concentration. The PEG-based macromer would then form amide bonds with amine groups of HSA, such as lysine residues, resulting in stabilized HSA PNPs. To ensure the completion of the reaction, the solidified HSA PNPs were incubated at 37°C for seven days. The fabricated HSA PNPs were visualized using SEM to study their morphology and size distribution (**Figure 5-1C**). SEM images of HSA PNPs were analyzed using ImageJ to assess their size distribution and key geometric factors (i.e., anisotropy, circularity, and roundness). These conditions resulted in monodisperse nanoparticles (PDI_{SEM}=0.15) with an average diameter of 99 nm (Q1/Med./Q3 = 63/96/126) in their dry state. The secondary geometric factors analysis demonstrated high circularity (Avg.=0.82, Q1/Med./Q3 = 0.78/0.88/0.91), high roundness (Avg.=0.83, Q1/Med./Q3 = 0.72/0.89/0.95), and low anisotropy (Avg.=1.26, Q1/Med./Q3 = 1.06/1.13/1.38) for HSA PNPs (**Figure 5-1D**). Once fully hydrated, dynamic light scattering (DLS) measurements were used for determining particles size distributions after dispersion in phosphate buffered saline (PBS) and all further surface modifications.

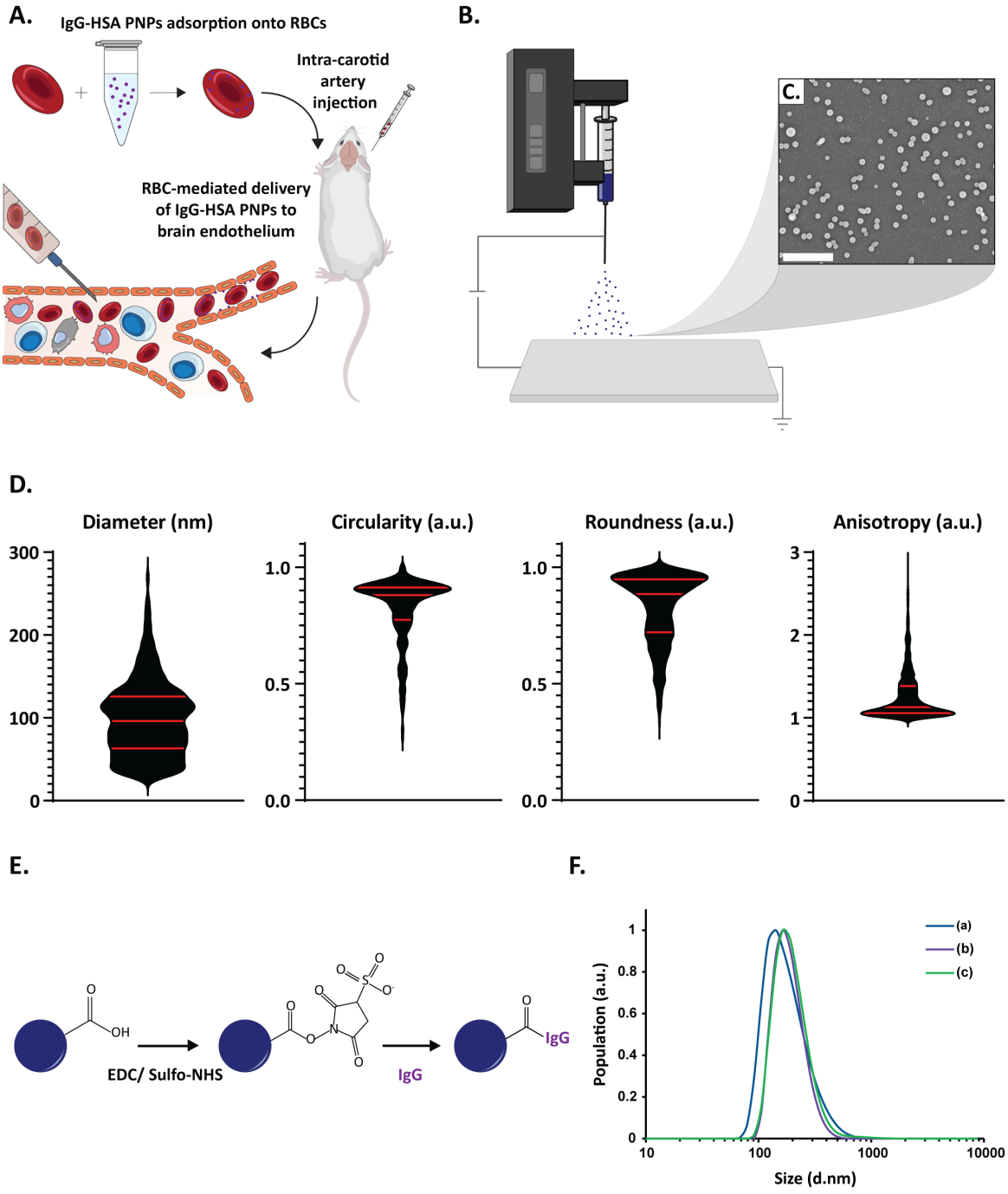

Figure 5-1. Design and characterization of HSA PNPs for RBC hitchhiking. (A) Illustration of workflow resulting in RBC-bound PNPs. HSA PNPs are surface decorated with IgG antibody and adsorbed onto RBCs ex vivo. RBC-hitchhiked IgG-HSA PNPs are then injected into carotid artery, after which the IgG-HSA PNPs transfer from the RBCs to the brain endothelium. (B) Schematic of electrohydrodynamic jetting setup for HSA PNPs fabrication. (C) SEM images of HSA PNPs using EHD jetting. Scale bar is 1 µm. (D) Size distribution and geometric factors of HSA PNPs based on ImageJ analysis of SEM images, (E) Reaction scheme for conjugation of IgG antibody to HSA PNPs. (F) Size distribution of HSA PNPs at different stages of the antibody conjugation:

(a) Initial size before reaction, (b) after addition and conjugation of IgG antibody, and (c) after storing the IgG decorated HSA particles at 4°C after 7 days.

In order to enhance the absorption efficiency of nanoparticles onto RBCs, IgG was covalently coupled to carboxylate groups on HSA PNPs using EDC sulfo-NHS reaction (**Figure 5-1D**). To confirm no aggregation occurred during the IgG conjugation to surface of HSA PNPs, the size distribution of nanoparticles was measured at each stage. As shown in **Figure 5-1F,** HSA PNPs demonstrated a monomodal size distributions with mode diameters of ~140 nm, and a 20 nm increase in size after IgG addition. The IgG modified HSA PNPs (IgG-HSA PNPs) were stable for at least 7 days at 4°C with no change in their size distribution, proving that the reaction condition did not cause any aggregations between particles. To determine the conjugation efficacy of IgG onto HSA PNPs, radiolabeled IgG was included. Using radiolabeling revealed that IgG molecules were conjugated to the surface of HSA PNPs at an average efficacy of 9.4%, corresponding to an average of 94 IgG per PNP.

5.4.2 Association of Human Serum Albumin Nanoparticles onto Red Blood Cells

The binding of both HSA and IgG-HSA PNPs was confirmed by flow cytometry. As shown in **Figure 5-2A**, the presence of IgG on HSA PNPs dramatically increased their adsorption onto RBC. Nearly 16% of RBCs have unmodified HSA PNPs adsorbed on their surface, whereas 33% of RBCs have IgG-HSA PNPs. Surface-coating of other nanoparticles, such as liposomes and nanogels, with IgG was also found to increase their adsorption onto RBCs.[166,381] However, it is yet unclear why IgG alters the binding onto RBC. Binding of both HSA PNPs and IgG-HSA PNPs onto RBC was further investigated in the presence of serum. Increasing concentrations of serum severely inhibited the biding of both particles onto RBCs. Similar to IgG modified liposomes, the increasing concentrations of serum decreased the biding of IgG-HSA PNPs onto RBCs. By using

radiolabeled IgG-HSA PNPs, their coupling efficiency onto RBCs was determined. The IgG-HSA PNPs were able to bind to RBCs at an efficiency of 12.6%, which corresponds to an average of 126 IgG-HSA PNPs per RBCs.

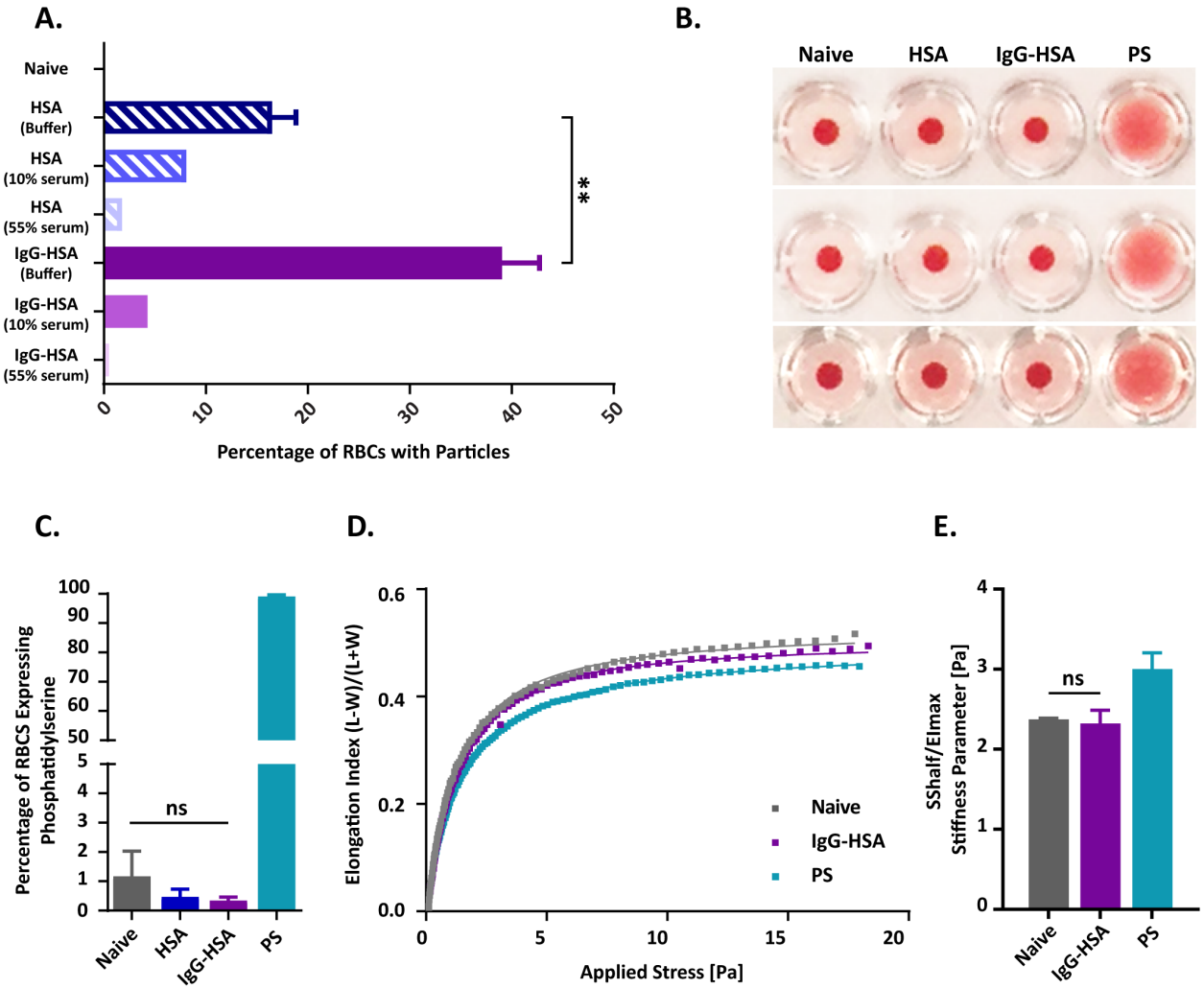

Figure 5-2. HSA PNPs adsorb onto RBCs with no adverse effects on carrier cells. (A) Assessing adsorption of HSA and IgG conjugated HSA PNPs on RBCs at various mouse serum concentration using flow cytometry. (B) RBC agglutination to HSA and IgG-HSA PNPs. Carboxylated polystyrene beads (PS) were used as positive control. (C) Measurement of phosphatidylserine exposure on RBCs based on the binding of Annexin V-Alexa Fluor 488 to phosphatidylserine. (D) Elongation Index of RBCs with nanoparticles adsorbed onto their surface compared to naive RBCs and PS treated RBCs. (E) Deformability of RBCs with nanoparticles adsorbed onto their surface compared to naive RBCs.

To investigate the biocompatibility of the binding of both types of HSA PNPs onto RBCs, agglutination, phosphatidylserine, and ektacytometry assays were performed. Similar to IgG-liposome, unmodified nanogels, and IgG-nanogels,[166,381] no clumps or aggregates were seen when HSA or IgG-HSA PNPs were adsorbed onto RBC at a RBC:PNP ratio as high as 1:1000 (**Figure 5-2B**), suggesting both types of HSA PNPs did not promote agglutination. Since both phosphatidylserine exposure and membrane rigidity are key determinants for RBCs phagocytosis by the RES, changes in these two properties were studied upon binding HSA and IgG-HSA PNPs onto RBCs. The adsorption of both types of HSA PNPs, similar to nanogels and IgG-nanogels,[381] did not induce an increase in RBCs expressing phosphatidylserine (**Figure 5-2C**) compared to their naive counterparts (≤ 1%). Unlike IgG-nanogels,[381] adsorbed IgG-HSA PNPs did not affect the deformability of the RBCs. The EI_{max} at RBC:PNP loading ratios as high as 1:1000 did not result in a significant shift in the elongation index curve (**Figure 5-2D**) compared to its naive counterpart. $SS_{1/2}$ / EI_{max} values also were statistically similar to naive RBC (**Figure 5-2E**). Taken together, these data imply that HSA and IgG-HSA PNPs can be used in RBC hitchhiking formulations since their adsorption was not detrimental for RBCs.

5.4.3 Systemic Delivery and Brain-targeting of Human Serum Albumin Nanoparticles

After confirming that IgG-HSA PNPs can bind to RBCs at a higher efficiency with no adverse effects on carrier cells, this group of PNPs was used in naive and brain-injured mice models to evaluate their brain-targeting capacities. Our groups have previously demonstrated the benefits of using RBC hitchhiking for targeted delivery of nanoparticles to different tissues, but most of the effects have been demonstrated in the lung vasculature, as it represents the largest vasculature in the body.[165,166] In contrast to our previous studies, to study the brain-targeting efficacy of RBC hitchhiked HSA PNPs, a murine model of neurovascular inflammation was used. A systematic

quantitative analysis of the biodistribution parameters of radiolabeled IgG-HSA PNPs and radiolabeled RBC hitchhiked IgG-HSA PNPs was performed, both in naive mice and a mouse model of acute brain inflammation induced by local tumor necrosis factor alpha (TNFα).

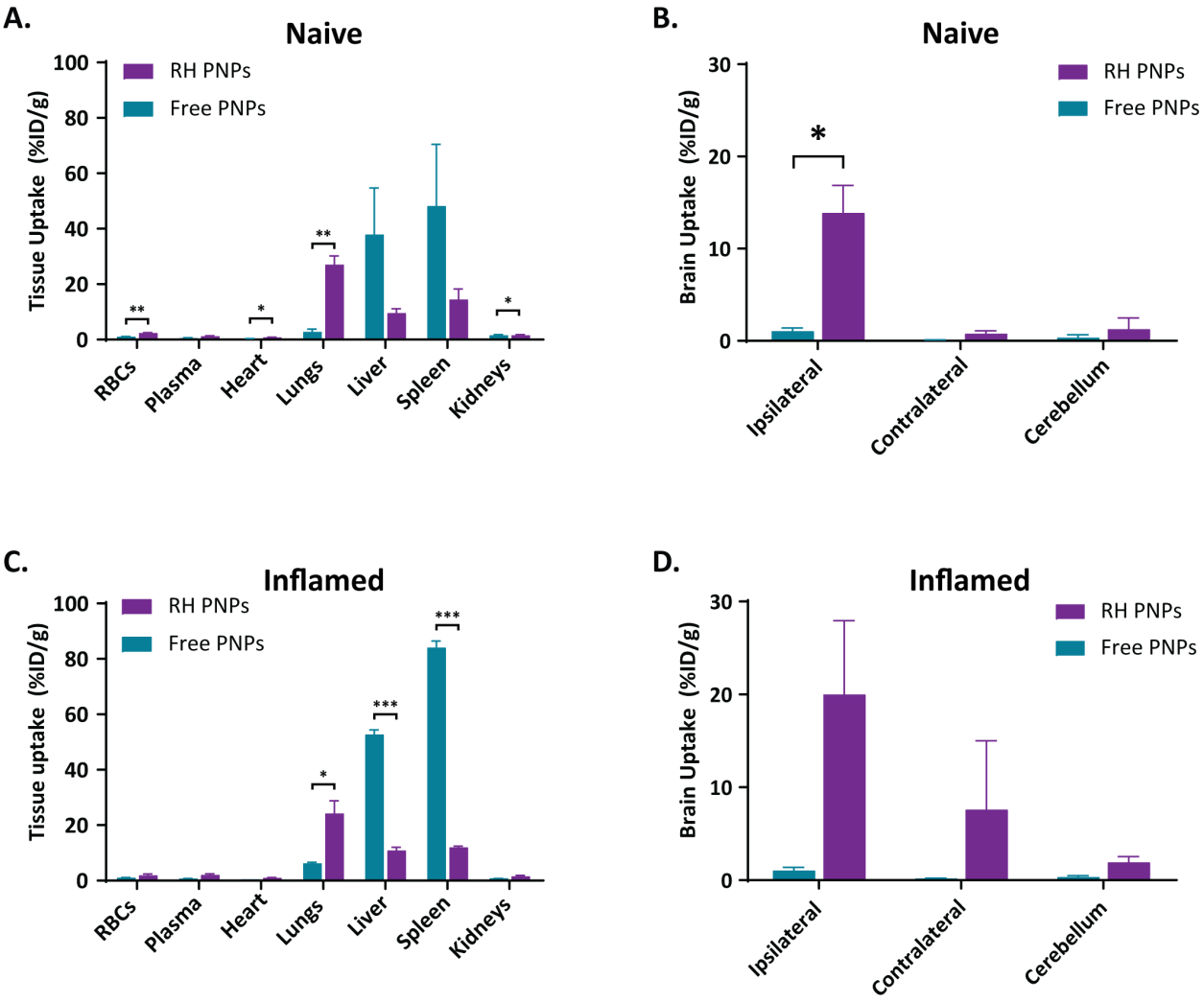

Figure 5-3. RBC hitchhiking alters the biodistribution of HSA nanoparticles. Biodistribution of radiolabeled nanoparticles (free and hitchhikers) in both inflamed and healthy mice models. The percent injected I-125 dose (%ID/g) for each organ in (A) naive mice and (C) inflamed mice. The % injected dose (%ID/g) in the (B) healthy brain and (D) inflamed brain sections are displayed; ipsilateral, contralateral, cerebellum.

Radiolabeled IgG-HSA PNPs, free or RBC-hitchhiked, were injected intravascularly through the internal carotid artery, one of the arteries that irrigates mostly one hemisphere of the brain, in naive

and TNFα-injured mice. The residual radioactivity was analyzed in the different tissues 30 min after injection. **Figure 5-3A** and **Figure 5-3C** show the biodistribution of IgG-HSA PNPs in the main tissues and **Figure 5-3B** and **Figure 5-3D** demonstrate their biodistribution in the brain for naive animals and for TNFα-injured ones, respectively. The biodistribution in the main organs showed that nanoparticles were cleared from the circulation 30 min after the injection. Similarly to our previous studies,[397] RBC-hitchhiked IgG-HSA PNPs showed a significant increase for the uptake of nanoparticles in the lungs compared to free IgG-HSA PNPs (2.8 ± 1.6 ID/g vs 27.1 ± 5.35, $P < 0.01$, and 6.2±0.7 ID/g vs 24.1 ± 7.9, $P < 0.05$, for naive and TNFα-injured mice respectively, **Figure 5-3A** and **Figure 5-3C**). The main nanoparticles clearance organs (liver and spleen) showed a decrease, only significant for the liver and spleen of TNFα-injured mice (52.7 ± 2.9 %ID/g for free vs 10.85 ± 2.035 %ID/g and 84.0 ± 4.1 %ID/g vs 11.9 ± 0.8 %ID/g, respectively, $P < 0.001$). As shown in **Figure 5-4A**, it is important to remark how the ratio between the downstream organ (ipsilateral part of the brain) and the RES organs (liver+spleen) showed a 10-fold increase for naive (0.04 ± 0.06 %ID/g vs 0.61 ± 0.25%ID/g, $P < 0.05$) and over 100 times for TNFα-injured mice (0.007 ± 0.004%ID/g vs 0.84 ± 0.50, $P < 0.05$). These results suggest a reduction of the clearance from the RES due to the first pass through the brain and lungs before reaching the liver and spleen.

In order to analyze the brain uptake, the brains were separated into their two hemispheres and the cerebellum **(Figure 5-3B** naive and **Figure 5-3D** TNFα-injured mice). Poor uptake was observed for the free IgG-HSA PNPs in the brains of naive (0.09 ± 0.05 %ID/g, 1.05 ± 0.56 %ID/g, and 0.34 ± 0.53 %ID/g for the contralateral hemisphere, ipsilateral hemisphere, and cerebellum, respectively) and TNFα-injured mice (1.03 ± 0.63 ID/g, 0.18 ± 0,06, and 0.33 ± 0.28 %ID/g, contralateral hemisphere, ipsilateral hemisphere, and cerebellum, respectively). In contrast, RBC

hitchhiking greatly increased the IgG-HSA PNPs uptake, predominantly in the ipsilateral hemisphere (13.87 ± 5.16 and 19.98 ± 13.76 %ID/g, for naive and TNFα-injured respectively, $P < 0.05$ vs free IgG-HSA PNPs in the naive mice) vs the contralateral (0.76 ± 0.56 %ID/g naive and 7.6 ± 12.83 %ID/g TNFα, $P < 0.05$ vs ipsilateral) and vs the cerebellum (1.27 ± 2.09 %ID/g naive and 1.9 ± 1.1 ID/g TNFα, $P < 0.05$ vs ipsilateral only for the naive animals). Despite the apparent trend of increased uptake of the RBC hitchhiked IgG-HSA PNPs, however, due to the large variability, a significant change in the total %ID/g for the ipsilateral hemisphere in the TNFα-injured mice was not observed. However, blood normalized uptake (%ID/g in the target tissue/%ID/g in the blood for each individual animal) showed a significant increase of the RBC hitchhiked IgG-HSA PNPs in the ipsilateral part of the brain compared to the free IgG-HSA PNPs (1.18 ± 0.63 vs 10.00 ± 3.21, $P < 0.05$, **Figure 5-4B**). Importantly, the brain uptake of IgG-HSA PNPs after RBC hitchhiking was not different for the brain under acute inflammation vs the naive. Altogether, data suggests that the RBC hitchhiking efficiently released the IgG-HSA PNPs in the downstream ipsilateral part of the brain mainly after the first pass.

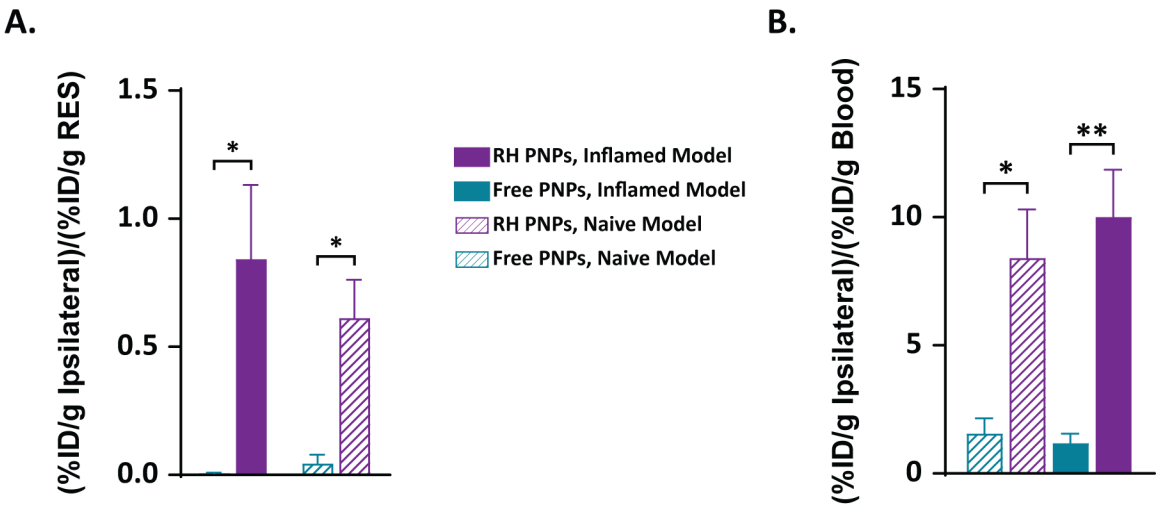

Figure 5-4. RBC hitchhiking improves brain delivery of HSA nanoparticles measured by effective targeting modalities. (A) Ipsilateral brain uptake of IgG-HSA PNPs normalized by liver and spleen uptake, (B) Blood normalized uptake of IgG-HSA PNPs into the ipsilateral brain of TNFα-injured mice in both inflamed and naive model, with and without RBC hitchhiking.

Catheter-driven nanoparticle delivery is an attractive approach, since thrombectomies are considered the gold standard for the treatment of ischemic stroke when possible.[398,399] Importantly, to apply this procedure, the catheterization of the brain vessel is required. The infusion through the same catheter and increase of the nanoparticle concentration in the injured area of the brain can then be easily achieved. RBC hitchhiking drastically increased the uptake in the brain compared to the targeting of transferrin receptor (about 1%ID/g[373]), which was previously considered one of the more promising brain-targeting affinity moieties. In addition, transferrin receptor is constitutively expressed in the endothelial brain cells having no selective uptake in the injured side of the brain. In summary, RBC hitchhiking of IgG-HSA PNPs highly increased the nanoparticle uptake in the injured brain after catheter-driven delivery, likely due to the first pass uptake. In future studies, the combination of RBC-mediated delivery of IgG-HSA PNPs with the incorporation of brain compartment-specific targeting antibodies on nanoparticles

such as antibody to vascular cell adhesion molecule 1 (anti-VCAM) should be explored to enhance the brain uptake of particles even further, which is elaborated in detail in **Chapter 8**.

5.4.4 RBC-hitchhiked Human Serum Albumin Nanoparticles Localization in the Brain

To identify the localization and types of the cells taking up the RBC-hitchhiked IgG-HSA PNPs, brains from both naive and TNFα-injured mice were sectioned and stained. In both hemispheres of the brain and cerebellum, IgG-HSA PNPs were found within the blood vessels and in the brain parenchyma (**Figure 5-5A** and **Figure 5-5D**). A few RBCs were observed in the blood vessel lumen after perfusion, and IgG-HSA PNPs were observed to be colocalized with the RBCs (**Figure 5-5B**). This confirms the delivery mechanism in which the nanoparticles were carried by RBC to the microcapillary bed of the brain.

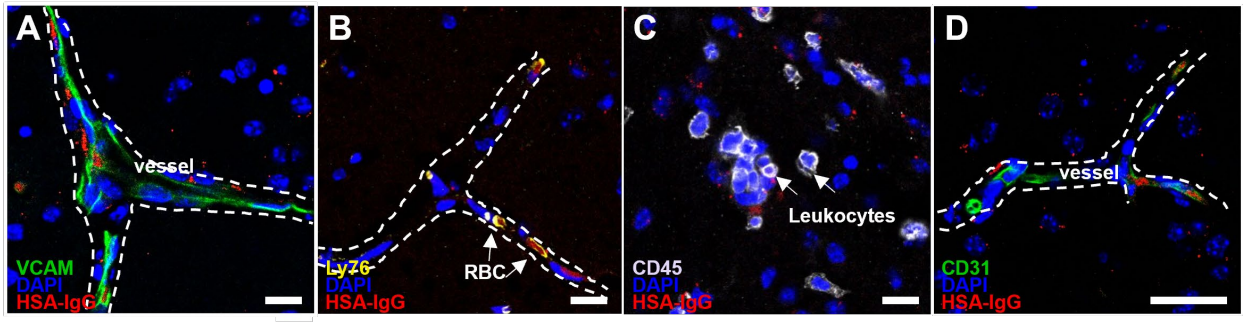

Figure 5-5. RBC hitchhiked IgG-HSA PNPs localize in the brain compartment after injection**.** 10-micromiter frozen sections from TNFα-injured brain injected with RBC-hitchhiked Alexa fluor-627 labeled IgG-HSA PNPs were stained with different antibodies: (A) endothelial cells (VCAM), (B) RBC (Ly76), and (C) leukocytes (CD45). Scale bar = 10μm. (D) 10-micromiter frozen sections from naive brain injected with RBC-hitchhiked Alexa fluor-647 labeled IgG-HSA PNPs were stained for endothelial cells (CD31). Scale bar = 25μm.

In TNFα-injured brain, a number of infiltrated leukocytes were found in the parenchyma (**Figure 5-5C**), where some were associated with IgG-HSA PNPs. The presence of leukocytes in the TNFα-injured brains indicated elevated inflammation as expected, while no leukocytes were observed in naive brains (data not shown). All together, these observations suggest that the IgG-

HSA PNPs s were carried by RBCs to the cerebral vasculatures, crossed the BBB and entered the brain.

5.5 Conclusions

Targeted drug delivery to the brain still remains to be challenging, but with the advent of nanotechnology, nanoparticle-based drug delivery systems have been pursued to mitigate some of the shortcomings of systemic drug delivery to the brain. However, due to the sequential biological barriers encountered by intravenously administered nanoparticles, their uptake in the brain remains low. Improving the efficacy of nanoparticles delivery to the brain endothelium can help facilitate the clinical translation of nanomedicine in this field. In this study, to increase the local concentration of nanoparticles at the brain endothelium, RBC hitchhiking and intra-carotid artery injection of nanoparticles were utilized. Since albumin-based nanoparticles have shown to be able to cross the BBB by engaging specific albumin-binding cell-surface receptors, HSA PNPs were engineered by electrohydrodynamic jetting technique to bind to RBCs to further enhance the brain delivery of our cellular hitchhiking platform. Results from this study demonstrated that engineered HSA PNPs decorated with IgG antibody can be utilized for binding onto RBCs with no detrimental effects on RBCs. Intracarotid injection of RBC hitchhiked IgG-HSA PNPs greatly improved brain delivery compared to their free IgG-HSA PNPs counterparts in naive and brain-injured mice. Multi-fold increases in brain-to-blood and brain-to-RES ratios achieved by RBC hitchhiked IgG-HSA PNPs highlight the potential of this platform for brain drug delivery with favored bio-distribution.

Chapter 6

Nanoparticle Properties Affect Monocyte Transcytosis across Blood-brain Barrier

The material in this chapter has been adapted with minor modifications from the following article: Nahal Habibi, Tyler D. Brown, Kwasi Adu-Berchie, David J. Mooney, Samir Mitragotri, Joerg Lahann. Nanoparticle Properties Affect Monocyte Transcytosis across Blood-brain Barrier. *In Preparation.*

6.1 Abstract

Nanoparticle-based delivery of therapeutics to the brain has achieved limited clinical impact due to the challenges in crossing the blood-brain barrier (BBB). The ability of monocytes to naturally travel towards a chemotactic gradient and migrate across the BBB make them attractive candidates as nanoparticle carriers for targeted delivery of drugs to the brain. However, few studies have been conducted on the effect of the nanoparticle parameters on the transendothelial migration behavior of the monocytes. In this work, we use electrohydrodynamic jetting to prepare nanoparticles of varying size, composition, and elasticity in order to elucidate their role in THP-1 monocytes uptake and migration behavior and ultimately design a successful platform for cellular hitchhiking. To evaluate the migration behavior of the THP-1 monocytes loaded with the different nanoparticle types, an in vitro human BBB model is developed using human cerebral microvascular endothelial cells (hCMEC/D3). The library of nanoparticles is comprised of synthetic protein nanoparticles (SPNPs) and polymeric nanoparticles. Our findings reveal that the SPNPs (human serum albumin or human transferrin) are better suited for monocyte-mediated transport across the BBB in

comparison to polymeric nanoparticles (polystyrene or poly(methyl methacrylate)) with respect to their uptake level and impact on monocytes' transendothelial migration. Specifically, transferrin SPNPs (diameter = 200 nm) are readily taken up by monocytes with an average uptake of 138 particles per cell. Nanoparticle uptake influences the migration behavior of THP-1 monocytes as evaluated in an in vitro human BBB model. The monocytes loaded with 200 nm transferrin and 200 nm human serum albumin SPNPs demonstrate 2.3-fold and 2.1-fold higher migration than the control monocytes without nanoparticles, respectively. Meanwhile the migration of monocytes treated with 500 nm poly(methyl methacrylate) particles is reduced by nearly one-half. RNA-seq analysis on THP-1 monocytes loaded with transferrin SPNPs and poly(methyl methacrylate) suggests that upregulation of several migration genes such as integrin subunit alpha M (ITGAM) and integrin subunit alpha L (ITGAL) may be implicated with the increased migration of transferrin SPNPs loaded monocytes. ITGAM and ITGAL in combination with the integrin beta 2 chain form macrophage antigen 1 (MAC1) and lymphocyte function-associated antigen 1 (LFA1) integrins, respectively, which have been shown to play a pivotal role in critical adhesion steps of the transendothelial migration cascade. Our findings highlight the potential of protein-based nanoparticles as a drug delivery platform in monocyte-mediated BBB transport.

6.2 Introduction

Efficient delivery of therapeutics to the brain is of particular interest and importance as neurological disorders are recognized as the second leading cause of death worldwide and pose a substantial burden on society.[400] In the United States, the annual cost associated with the nine common neurological diseases, including Alzheimer's disease and other dementias, stroke, traumatic brain injuries and Parkinson's disease, was an estimated $800 billion dollars; costs for dementia and stroke alone are projected to exceed $600 billion by 2030.[401] One of the major

roadblocks to effective treating brain disorders remains overcoming the transport barrier upon the entry of drugs into the brain: the blood-brain barrier (BBB), which is composed of endothelial cells connected via highly restrictive tight junctions, poses a significant challenge for transporting drugs from the bloodstream to the brain.[361] Efficient and non-invasive drug delivery across the BBB remains elusive in pharmaceutical research and development. Given the lack of satisfactory treatments for many neurological diseases, there is an immense need for the development of more-efficient drug delivery platforms. Recent efforts have aimed at designing nanoparticles that can deliver therapeutics to the brain;[402,403] however, since many nanocarriers have limited or poor ability to cross the BBB, increased attention is being paid to therapeutic approaches that combine nanomedicine and cell-based drug delivery.[404]

In the case of brain diseases, sites of inflammation present an ideal opportunity to utilize this combined approach. Inflammation is considered one of the hallmarks of various brain diseases, including Alzheimer's disease,[405] Parkinson's disease,[406,407] and cancer,[408] and is characterized by the recruitment of leukocytes, such as monocytes, to the affected tissue via diapedesis and chemotaxis.[171,409] Thus the innate ability of circulating monocytes to migrate to sites of inflammation and cross the BBB[6,200] makes them attractive candidates as nanoparticles' carriers for targeted delivery, a concept known as "cellular hitchhiking."[200] Leveraging monocytes as nanoparticles' delivery vehicles was found to increase the ability of nanoparticles to cross the BBB and reach the brain.[410,411]

In addition, both monocytes and macrophages are phagocytic cells that can internalize foreign particles while leaving their membranes intact. Monocyte and macrophage-based platforms have recently been evaluated in terms of their potential for targeted delivery of nanoparticles to the brain.[184,412–415] Bone marrow-derived macrophages loaded with nanoformulated catalase were

utilized to attenuate neuroinflammatory processes in Parkinson's disease mouse models.[412,413] In another study, the delivery of serotonin to the brain by negatively charged liposomes was shown to be mediated by circulating monocytes due to the selective entry of leukocytes into the central nervous system.[415] Likewise, Hou et al. reported that cRGD [cyclo (Arg-Gly-Asp-D-Tyr-Lys)]-decorated liposomes utilized monocytes and neutrophils as delivery vehicles to reach the cerebral parenchyma and deliver neuroprotective reagents for the treatment of cerebral ischemia.[414] Apart from internalization, ligand-receptor interactions have also been leveraged to attach microparticles known as "cellular backpacks" to the surface of leukocytes. Catalase-loaded backpacks attached to macrophages successfully crossed mouse brain endothelial cell monolayers in an in vitro BBB model; they were also successful in vivo, crossing the inflamed BBB of a lipopolysaccharide-induced encephalitis mouse model.[184] Similarly, using monocytes as delivery vehicles improved the transmigration of these backpacks across an endothelial monolayer in vitro.[416] The disadvantage of this technique is the possibility of a weak binding affinity between ligands and receptors which could result in detachment of the particles, non-specific attachment to unwanted cells, or specific cellular functions that might be triggered upon ligand-receptor interaction.[374] Therefore, in this study, we focused on internalization as the method for loading nanoparticles into monocytes.

Although studies extensively highlight the role of nanoparticle properties such as size,[417] shape,[418] and elasticity[419] on their uptake by leukocytes, very few reports investigate how different types of nanoparticles may inherently modulate the migration behavior of these hitchhiked cells. Designing an efficient cellular hitchhiking nanoparticle platform requires a balance between an optimal uptake level and an ideal migration behavior. Addressing these specific challenges, we capitalize on electrohydrodynamic (EHD) jetting to fabricate nanoparticles

with varying composition and size to subsequently elucidate their influence on cellular uptake and migration of monocytes. Specifically, we used EHD jetting to fabricate nanoparticles composed of poly(methyl methacrylate) (PMMA), human serum albumin (HSA), and human transferrin (TF). Furthermore, the library also included commercially obtained polystyrene (PS) nanoparticles. Aforementioned particles were chosen deliberately, for reasons outlined in the following.

PMMA as a synthetic polyester has been widely explored for various biomedical applications[420,421] due to its biocompatibility; it has been increasingly employed as a drug carrier, e.g., for sustained local delivery of anti-inflammatory and antibiotic drugs.[422,423] In cancer therapy, PMMA nanoparticles were used for loading curcuminoid because of their high permeability for many drugs and lack of toxicity.[424] RGD-modified PMMA nanoparticles were used as a drug delivery platform for paclitaxel.[425] Therefore, in this work, we included PMMA in the nanoparticle library. An emerging trend in the field of nanoparticle-based delivery systems replaces synthetic polymers with proteins as the major building block of nanoparticles.[6] The inherent properties of proteins, such as their biocompatibility, biodegradability, endogenous pathways and variety of surface modification possibilities, makes them a suitable material for particle-based delivery systems.[93,250,251,426] In this work, we specifically focus on HSA and TF. As the most abundant plasma protein and a natural carrier of endogenous hydrophobic molecules, HSA has been shown to preferentially accumulate in tumor and inflamed tissue.[383–386] As transferrin receptors are exclusively expressed on the endothelial cells of the brain capillaries and absent from the endothelial cells in other tissues, TF has previously been used as a potential target for brain drug delivery.[427,428] Consequently, TF nanoparticles were included as another protein-based nanoparticle group.

The size of the nanoparticles, an important design parameter, can be engineered to tailor the nanoparticle biodistribution in vivo.[206] It has been shown that intravenously administered nanoparticles with diameters <~ 5 nm undergo rapid renal clearance.[429] Particles with diameters > 1 μm may cause occlusion of lung capillaries[430] and thrombosis.[415,431] Due to the size range of splenic interendothelial cell slits (200-500 nm), particles with diameters of 200 nm and above will be retained, allowing them to preferentially interact with immune cells.[19,206,432] Passive targeting of circulating monocytes can be achieved by fine-tuning the size of the particles, since particles larger than 100 nm are more likely to be cleared from circulation by monocyte uptake.[415,431,433] A previous study used this approach to deliver serotonin to the brain, tailoring the size of liposomes to be preferentially taken up by monocytes.[415] Therefore, due to their preferential interaction with immune cells, in this study we focus on nanoparticles with sizes of 200 nm and 500 nm.

While it is widely accepted that particle size is one of the most important physical attributes in altering the biological function of particles, the elasticity of nanoparticles has emerged as another critical design parameter, and a growing body of literature details the impact of nanoparticle elasticity on circulation, in vivo targeting, and cellular uptake.[419,434,435] In this current study, the role of nanoparticle stiffness on their internalization by the monocytes and the migration behavior of the monocytes cannot be decoupled completely from nanoparticle composition as an independent parameter, but it was evaluated specifically in tandem. This library of nanoparticles with defined size and composition enables a deeper understanding of the interplay between nanoparticle properties and monocyte behavior, which can be leveraged to design more effective cellular hitchhiking-based drug delivery platforms.

6.3 Materials and Methods

6.3.1 Materials

Carboxylate polystyrene particles were purchased from Polysciences Inc., USA. Polyvinyl alcohol, glycerol, human transferrin, and O,O′-Bis[2-(N-Succinimidyl-succinylamino)ethyl]polyethylene glycol with a molecular weight of 2000 Da were purchased from Sigma-Aldrich, USA. O,O′-Bis[2-(N-Succinimidyl-succinylamino)ethyl]polyethylene glycol with a molecular weight of 20,000 Da was purchased from Nanocs Inc., USA. Human serum albumin was purchased from Invitria, USA. Paraformaldehyde (16% w/v), PrestoBlue™ Cell Viability Reagent, Pierce® RIPA Lysis and Extraction Buffer, 4'6-diamidino-2-phenylindole (DAPI), and Alexa Fluor™ 488 conjugated albumin from bovine serum (BSA) were obtained from Thermo Fisher Scientific, USA. EndoGRO-MV Complete Culture Media Kit, human plasma fibronectin purified protein, and fibroblast growth factor basic protein human animal-free recombinant (bFGF-AF) were obtained from Millipore Sigma, USA. Hank's balanced salt solution (HBSS), Dulbecco's phosphate-buffered saline (DPBS), penicillin-streptomycin solution, 0.25% trypsin solution, and Sephadex G-25 PD-10 columns were purchased from GE Healthcare Life Sciences, USA.

6.3.2 Fabrication of Protein-based and Polymer-based Nanoparticles

HSA and TF SPNPs were fabricated using EHD jetting as described in previous reports.[251,370] Briefly, to prepare 200 nm-sized SPNPs, a dilute solution of protein (HSA or TF) was dissolved at 7.5% (w/v) in a 4:1 mixture of distilled water and ethylene glycol. Then, the amine-reactive crosslinker NHS-PEG-NHS (2kDa) was added at 10% ($w/w_{protein}$). As previous studies have found, nanoparticle size can be controlled by changing the dielectric constant of the solvent and the

molecular weight, or length, of the crosslinker.[136,237] By decreasing the dielectric constant and increasing the length of the crosslinker, the target size of 500 nm was achieved; specifically, the molecular weight of NHS-PEG-NHS was increased from 2kDa to 20kDa at a 5% ($w/w_{protein}$). The protein concentration was maintained at 7.5% (w/v), but the solvent ratio was changed; a 2:3 (v/v) distilled water to ethylene glycol solvent mixture was used to dissolve the protein. For fluorescently labeled protein-based particles, Alexa Fluor 488-conjugated bovine serum albumin (1 mg/ml) was added to the protein and crosslinker solution. Then, the solution was pumped at 0.1 mL/hr. Upon formation of a droplet at the tip of the needle, an electric voltage was applied, which distorted the meniscus to a Taylor cone. Charged protein solution was ejected from the apex of the Taylor cone. Due to rapid solvent evaporation, solid SPNPs were produced on the grounded plate. After a 7-day incubation time at 37 °C to allow for completion of the crosslinking reaction, stable polymerized SPNPs were obtained. Then, the nanoparticles were collected in phosphate buffer saline (PBS), followed by serial centrifugation to achieve the target size of 200 nm or 500 nm. For PMMA nanoparticles preparation, the formulation was optimized to produce 200 nm and 500 nm nanoparticles. The polymer solution was composed of a 1:1 ratio of PMMA with molecular weights of 120kDa and 15kDa dissolved at 10% (w/v). The solvent system was a mixture composed of tetrahydrofuran (THF) and Dimethylformamide (DMF) at a 27:75 ratio. To fluorescently label nanoparticles ADS133YE, poly[(9,9-dioctylfluorenyl-2,7-diyl)-alt-co-(1,4-benzo-{2,1',3}-thiadiazole)], was used. The fabricated nanoparticles were collected in PBS buffer. To separate the particles into the target size of 200 nm and 500 nm, serial centrifugation was conducted.

6.3.3 Characterization of the Nanoparticle Library

The nomenclature of the nanoparticle library is defined by the composition of the particle (polystyrene = PS, human serum albumin = HSA, human transferrin = TF and poly(methyl methacrylate) = PMMA) followed by the target particle diameter (e.g., 200 nm diameter = 200 and 500 nm diameter = 500). For instance, 200 nm HSA particles are denoted as HSA-200. Scanning electron microscopy (SEM) was used to study the shape and size of the as-jetted nanoparticles before collection and suspension in buffer. Polystyrene nanoparticles (200 nm and 500 nm) were assessed using a Zeiss Ultra Plus Field Emission Scanning Electron Microscope (FESEM). To prepare samples for SEM, dilute solutions of the particles were dried on an aluminum stub overnight prior to a 5-nm sputter coating of a platinum/palladium (80/20) alloy using a Turbo-Pumped Sputter and Carbon Coater (EMS150T ES Plus). A beam voltage of 2kV at 60K magnification was used to analyze the polystyrene nanoparticles. The EHD jetted nanoparticles were evaluated using the FEI Nova 200 Nanolab SEM/FIB at the Michigan Center for Materials Engineering at acceleration voltages of 5kV. An SPI-Module Carbon/Sputter Coater was used to sputter-coat the nanoparticles with gold for 60 seconds. For all particle types, dynamic light scattering (DLS) was employed with a Malvern Instruments Zen 3600 Zetasizer to measure the particle size distribution in PBS after collection and serial centrifugation. Electrophoretic light scattering (ELS) was used to determine the zeta potential of fabricated nanoparticles. The nanoparticle concentration was determined by nanoparticle tracking analysis (NTA) using a Nanosight NS300.

6.3.4 Culture of Human Monocytic Cell Line and Human Cerebral Microvascular Endothelial Cell Line

Human Monocytic Cell Line (THP-1)

The human monocytic cell line THP-1 was obtained from ATCC (ATCC #TIB-202) and maintained with complete medium composed of RPMI-1640 medium (ATCC #30-2001) supplemented with 10% of fetal bovine serum (FBS) and 1% of penicillin-streptomycin. Suspension cultures were maintained by the addition of fresh medium or replacement of medium every 2 to 3 days. The cells were incubated at 37°C, 95% humidity and 5% CO_2. The cell cultures were maintained at 2 to 4×10^5 viable cells/mL. When the cell concentration reached 8×10^5 cells/mL, the cells were subcultured. The cell concentration was not allowed to exceed 1×10^6cells/mL. Centrifugation at 130 ×g for 5 minutes was used to subculture the cells. Then, the cells were resuspended using complete culture media. Non-tissue cultured-treated T-75 and T-150 flasks were used to minimize adhesion of the suspension cells to the flask surface.

Human Cerebral Microvascular Endothelial Cell Line (hCMEC/D3)

The immortalized human cerebral microvascular endothelial cell line hCMEC/D3 was obtained from Millipore Sigma and maintained with EndoGRO-MV Complete Culture Media Kit supplemented with 1 ng/mL human animal-free basic fibroblast growth factor (bFGF-AF) and 1% penicillin-streptomycin. Collagen-coated T-150 tissue culture flasks were coated with 1:20 dilution of Corning® Collagen Type I, Rat Tail for at least 1 hour prior to the hCMEC/D3 culture. The media was refreshed every 2-3 days until 80% confluency was reached. To passage the cells every 3-5 days at 70% confluency, 0.25% trypsine-EDTA was used. The cells were incubated at 37°C, 95% humidity and 5% CO_2. The cells used were between passage 27 and 35.

6.3.5 Culture of Static, In Vitro BBB Model for Monocyte Migration Studies

For monocyte migration studies, static in vitro BBB models were constructed using Transwell® migration assays, and FluoroBlok™ inserts with an 8.0μm pore size were used. First, the inserts were coated with 50 μL of human fibronectin solution to coat the surface at 10 μg/cm^2 for at least 1 hour at 37 °C. Then, the excess fibronectin solution was removed, and the inserts were washed with DPBS at least two times. hCMEC/D3 cells were seeded into the apical compartment at a density of 300,000 cells/mL in 200 μL of complete media. The basolateral compartment of the FluoroBlok™ was filled with 700 μL of complete media. The inserts with seeded cells were incubated at 37°C, 95% humidity and 5% CO_2. The media was refreshed every other day. Transendothelial electrical resistance (TEER) measurements were measured every day for at least 7 days. Static in vitro BBB models were utilized in monocyte migration studies after 7 days.

6.3.6 Nanoparticle Cytotoxicity Assay

To assess the nanoparticle toxicity on the THP-1 cells, the PrestoBlue™ cell viability reagent assay was used. To ensure the number of seeded cells for this study resided within the linear range of the PrestoBlue™ cell viability reagent assay, known concentrations of THP-1 cells were seeded (90 μL each) in non-tissue culture-treated 96-well plates and incubated at 37°C, 95% humidity and 5% CO_2 overnight. The following day, 10 μL of PrestoBlue™ cell viability reagent was added to each well and incubated at least 10 minutes at 37°C. The fluorescence intensities (Ex. 560nm / Ems. 590nm) were then measured by the BioTek Synergy H1 Hybrid Multi-Mode Microplate Reader. All cell concentrations were found to reside in the linear regime using a standard linear regression analysis. Thus, 100,000 THP-1 cells per well were used in subsequent studies. To evaluate the nanoparticle toxicity on THP-1 cells, 100,000 cells were seeded in a 96-well non-tissue culture-treated plate and incubated with the nanoparticles at 1×10^9 nanoparticles/mL for

each group. The nanoparticles were incubated with the THP-1 cells overnight in triplicate in a total of 90 μL with complete cell culture media at 37°C, 95% humidity and 5% CO2. The following day, 10 μL of PrestoBlue™ cell viability reagent was added to each well and incubated at 37°C for at least 10 minutes before measuring the fluorescence intensities using the BioTek Synergy H1 Hybrid Multi-Mode Microplate Reader (Ex. 560nm / Ems. 590nm).

6.3.7 Nanoparticle Uptake By THP-1 Cells

To evaluate and compare the THP-1 cells uptake of different nanoparticles, 100,000 THP-1 cells were seeded per well in a non-tissue culture-treated 96-well plate. Fluorescently labeled nanoparticles were incubated with THP-1 cells at a final concentration of 1×10^9 nanoparticles/mL per well in triplicate. The cells were incubated with the nanoparticles overnight at 37°C, 95% humidity and 5% CO_2. The following day, cells of each condition were harvested and washed three times with serum-free RPMI-1640 to remove non-internalized nanoparticles. After the third wash, each group of cells was resuspended in 1 mL of serum-free RPMI-1640 and counted. Then, the cells were pelleted and lysed with 400 μL of PierceR RIPA buffer. Fluorescence intensities of the samples were measured in triplicate using the BioTek Synergy H1 Hybrid Multi-Mode Microplate Reader (Ex. 490 nm / Ems. 525 nm). The nanoparticle concentrations were determined according to the respective calibration curves of standard fluorescence intensities. The average number of nanoparticles taken up by THP-1 cells was calculated by dividing the average number of particles in each condition by the average number of cells. Statistical analyses were performed using SPSS Statistics 24 software. One-way ANOVA with Tukey's post-test was used to determine significance among groups. A P-value of < 0.05 was considered statistically significant ($*P < 0.05$, $**P < 0.01$, $***P < 0.001$, and $****P < 0.0001$); P-values of > 0.05 were considered not significant (ns).

6.3.8 In Vitro Migration Behavior of Monocytes across hCMEC/D3 Monolayers in FluoroBlok™ Assays

The THP-1 cell migration across hCMEC/D3 monolayers was assessed using the confluent static in vitro BBB model of cultured hCMEC/D3 on FluoroBlok™ supports described above. On the sixth day of culture of the hCMEC/D3 monolayers on the FluoroBlok™ permeable supports, the THP-1 cells were seeded at 100,000 cells per well in a 96-well non-tissue culture-treated plate. Non-fluorescent nanoparticles were incubated with THP-1 cells at 1×10^{9} nanoparticles/mL for each particle type overnight at 37°C, 95% humidity and 5% CO2. Afterwards, the cells of each condition were harvested and washed for three times with serum-free RPMI-1640 to remove any non-internalized nanoparticles. The cells were then resuspended in 1 mL of serum-free RPMI-1640 and counted. Calcein AM fluorescent dye was used to stain the cells at a concentration of 1.5 μM and incubated at 37 °C for 30 min. In living cells, the nonfluorescent calcein AM is then converted to green-fluorescent calcein after cetoxymethyl ester hydrolysis by intracellular esterases and is cell-permeant. Stained cells were pelleted and resuspended in serum-free RPMI-1640 medium to achieve a final concentration of 0.5 million cells per mL. To evaluate the migration behavior of each group of THP-1 cells, monolayers of hCMEC/D3 cells grown on FluoroBlok™ were washed twice with DPBS on day 7 of culture. For each particle condition, 100,000 THP-1 cells per insert were added to the apical compartment of the FluoroBlock. The basolateral compartment contained 700 μL of 100 ng/mL of MCP-1 in serum-free RPMI-1640 medium at the start of the experiment. The 24-well plate was immediately placed in a pre-warmed BioTek Synergy™ NEO HTS Mugti-Mode Microplate Reader at 37°C. Fluorescence measurements (Ex. 485 nm/ Ems. 530 nm) were taken every 15 minutes for 3 hours from the bottom of the plate to track the monocyte migration from the apical compartment to the basolateral

compartment. Statistical analyses were performed using SPSS Statistics 24 software. One-way ANOVA with Tukey's post-test was used to determine significance among groups. A *P*-value of < 0.05 was considered statistically significant (*$P < 0.05$, **$P < 0.01$, ***$P < 0.001$, and ****$P < 0.0001$); *P*-values of > 0.05 were considered not significant (ns).

6.3.9 Bulk RNA-seq

To perform bulk RNA-seq, 100,000 THP-1 cells were added to each well of a non-tissue culture-treated 96-well plate. Each particle group (TF-200, TF-500, and PMMA-500) was added to 5 different wells in duplicate at a concentration of $1x10^9$ NPs/mL and allowed to incubate overnight. Control groups (THP-1 without nanoparticles) were also prepared. All cell groups were collected into 1.5 mL Eppendorf tubes and washed three times with serum-free RPMI-1640 medium for 5 minutes at 200 ×g. After the final wash, RNA was isolated using the RNeasy Mini Kit (QIAGEN# 74104), using the manufacturer's protocol. The purified RNA solution was stored at -80°C prior to use. The quantity and purity of isolated RNA were assessed using an Agilent TapeStation 2200. RNA quality was high for all samples, with RNA integrity numbers (RIN) varying between 6.9 and 8.8. RNA-seq libraries were prepared from 200 ng of total RNA using a Kapa mRNA HyperPrep Kit for Illumina platforms. Final library products were quantified using the Qubit Fluorometer, and the fragment size distribution was determined with the Agilent TapeStation 2200. The libraries were then pooled in equimolar amounts, and the final pool was quantified by qPCR. The pool was sequenced in an Illumnia NextSeq 500 platform at the Harvard University Bauer Core using a Mid-output flow cell configuration for paired-end reads with a read length of 75 bp. Transcript alignment and quantification was then performed using Salmon,[436] quasi-mapped onto the hg38 reference cDNA.[437] Transcript level estimates were converted to gene levels abundances and counts using tximport in R.

Unsupervised analysis was performed by first filtering out low expressed genes (with less than 10 counts across all samples) and performing regularized log (Rlog) transformation on the gene counts using the DESeq2[438] package in R. This was followed by principal component analysis (PCA) for the different conditions using all the genes to investigate their relative similarities. Differential expression analysis was then performed between the different NP treated conditions and the control, with FDR adjusted *P*-value significance threshold of <=0.1. Gene enrichment analysis was performed on the differentially expressed genes using Enrichr,[439] focusing on migration and trans-endothelial migration related pathways from Kegg, Elsevier and GO Biological Process. The significance of these migration and trans-endothelial migration related pathways for the nanoparticles treated conditions relative to the control were then compared using bar plots. Focusing on genes implicated in pathway terms related to migration, and specifically trans-endothelial migration (Leukocyte transendothelial migration, Leukocyte Migration toward the Endothelial Cell in Ulcerative Colitis), unsupervised analysis was performed to investigate the relative similarities of the different conditions using PCA. The aggregate distribution of gene expression for migration and trans-endothelial migration related genes were then estimated by performing a z-score normalization of the Rlog transformed gene counts for each gene set and visualizing the expression distribution using violin plots. Statistical analyses were performed with the Wilcox Test, using FDR for *P*-value adjustment. To find genes that could be important to the observed differences in trans-endothelial migration between the TF and PMMA conditions, differential expression analysis was performed between TF-200 and PMMA-500 as well as TF-500 and PMMA-500. The log2FoldChange of trans-endothelial migration related genes enriched in either the TF-200 or TF-500 conditions were then plotted against each other to compare their relative significance between the TF conditions.

6.3.10 Statistical Analysis

Statistical analyses were performed using SPSS Statistics 24 software. One-way ANOVA with Tukey's post-test was used to determine significance among groups. A P-value of < 0.05 was considered statistically significant (*$P < 0.05$, **$P < 0.01$, ***$P < 0.001$, and ****$P < 0.0001$); P-values of > 0.05 were considered not significant (ns).

6.4 Results and Discussion

6.4.1 Synthesis and Characterization of Nanoparticles

Recent efforts have focused on designing nanoparticle-based systems for cellular hitchhiking to overcome the blood-brain barrier.[377,440] However, these systems have not yet been fully characterized in terms of the effect of nanoparticle properties on the cellular uptake and the resulting migration behavior of the carrier cells, which impacts the overall efficacy of the cell-mediated brain delivery platform. To address this gap, we fabricated a small library of nanoparticles with an emphasis on their size, composition, and elasticity; these properties collectively impact their internalization by the monocytes as well as the subsequent migration behavior of the monocytes. This library of nanoparticles includes synthetic polymeric particles (PMMA-200, PMMA-500, PS-200 and PS-500 particles) in addition to synthetic protein nanoparticles (HSA-200, HSA-500, TF-200 and TF-500 particles).

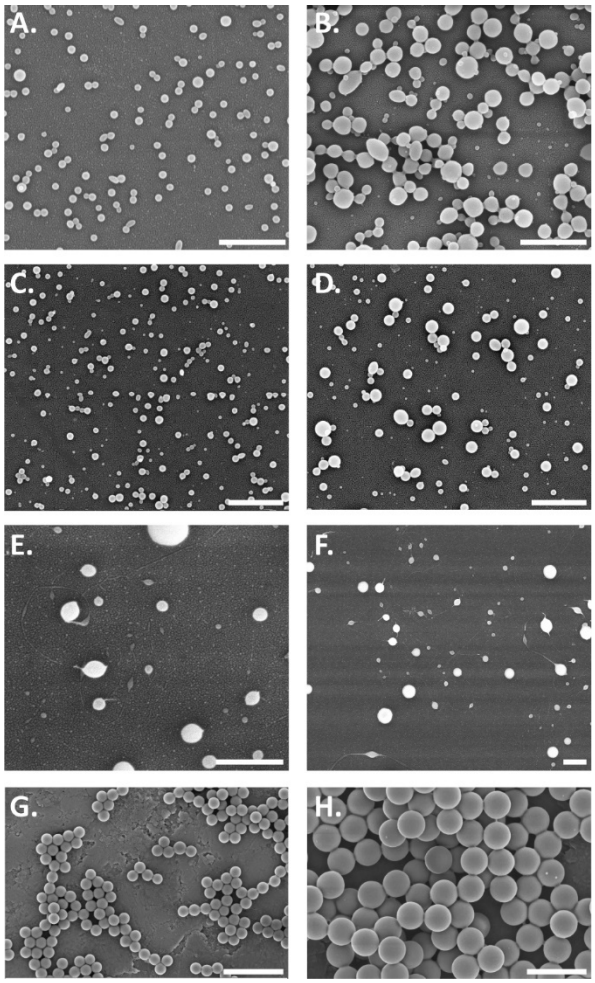

Figure 6-1. SEM images of the library of nanoparticles. (A) HSA-200 nm, (B) HSA-500 nm, (C) TF-200 nm, (D) TF-500 nm, (E-F) PMMA, (G) PS-200 nm, (H) PS 500-nm. Scale bar is 1 μm.

EHD jetting was utilized to fabricate the polymer- and protein-based nanoparticles to systematically study the effect of the nanoparticle properties on the uptake by the monocytes and the migration behavior of the cells. As depicted in **Figure 6-1,** the preparation of PMMA-200, PMMA-500, HSA-200, HSA-500, TF-200 and TF-500 particles was achieved by the EHD jetting process outlined in the Methods section. Their size and geometric factors based on scanning electron microscopy (SEM) analysis are summarized in **Table 6-1.** A direct inspection of diameter and circularity revealed values of 108 nm and 0.88 nm for HSA-200, and 93 nm and 0.83 for TF-

200, respectively. Decreasing the dielectric constant in the formulation of the 500 nm-sized protein particles resulted in an increase in their dry-state diameter to 193 nm for HSA-500, and 134 nm for TF-500. All protein particles showed high values of circularity (0.83 – 0.88) and roundness (0.82 – 0.93). The PMMA particles had an average diameter of 302 nm. This particle group had the lowest circularity (0.66) and roundness (0.69) when compared with the other particle groups. The diameters of PS-200 and PS-500 were in agreement with the information provided by the manufacturer. Secondary geometric factor analysis of the PS particles showed that these manufactured particles had a circulatory value of about 0.85 and roundness value of 0.92, which is comparable to the protein particles fabricated by the EHD jetting process. Once the fabricated particles were collected and dispersed in PBS, nanoparticles with the targeted hydrated sizes of 200 nm or 500 nm were separated by means of serial centrifugation. The size distribution of all particle groups dispersed in PBS was measured by DLS and is summarized in **Table 6-1**. Slightly to moderately negative zeta potential values were observed for all particle groups; the PS particles exhibited the least negative surface charge.

Table 6-1. Summary of size, geometric factors, and zeta potential values of nanoparticles.

Particle Type	Dry-state Diameter (nm)	Anisotropy (a.u.)	Circularity (a.u.)	Roundness (a.u.)	Hydrated-State Diameter (nm)	Zeta Potential (mV)
HSA-200	108 ± 37	1.09 ± 0.14	0.88 ± 0.06	0.93 ± 0.08	253 ± 51	-4.9 ± 2.1
HSA-500	193 ± 104	1.32 ± 0.63	0.83 ± 0.12	0.82 ± 0.16	487 ± 66	-8.2 ± 1.6
TF-200	93 ± 32	1.13 ± 0.18	0.88 ± 0.08	0.90 ± 0.10	240 ± 55	-6.3 ± 2.4
TF-500	134 ± 80	1.19 ± 0.44	0.86 ± 0.10	0.89 ± 0.15	476 ± 78	-5.5 ± 2.4
PMMA	302 ± 195	1.78 ± 1.14	0.66 ± 0.20	0.69 ± 0.23	243 ± 30 505 ± 43	-5.6 ± 1.6 -6.8 ± 1.9
PS-200	199 ± 13	1.09 ± 0.11	0.86 ± 0.04	0.92 ± 0.08	203 ± 11	-31.4 ± 2.2
PS-500	519 ± 17	1.11 ± 0.21	0.84 ± 0.07	0.92 ± 0.10	590 ± 20	-31.4 ± 2.3

6.4.2 Nanoparticle Uptake by THP-1 Cells

Followed by the optimization and fabrication of the TF, HSA, and PMMA nanoparticles, they were evaluated in terms of their uptake by THP-1 cells. First, nanoparticle toxicity to THP-1 cells was analyzed by PrestoBlue™ Cell Viability assay. Monocytes treated with all particle groups showed high viability **(Figure 6-2)**.

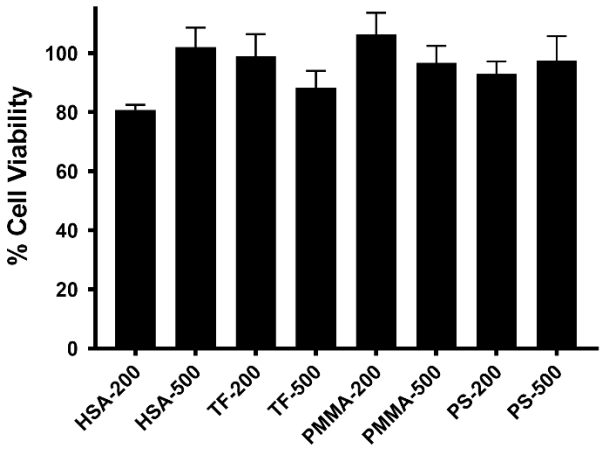

Figure 6-2. THP-1 cell viability after nanoparticles uptake as measured by PrestoBlue.

After having confirmed that the nanoparticles were non-cytotoxic to the cells, their uptake in THP-1 monocytes was evaluated quantitatively by a plate reader-based technique. For this purpose, all particle groups were incubated with the THP-1 monocytes overnight at 1×10^9 nanoparticles/mL. The number of particles internalized by the THP-1 cells was quantified by a plate reader and normalized to the number of THP-1 cells (**Figure 6-3**). Among the 200 nm particle groups, largest uptake for the PMMA-200 nanoparticles was seen; their uptake values being 5.0 times ($P < 0.001$) and 4.4 times ($P < 0.001$) higher than those of the TF-200 and HSA-200 particles, respectively (**Figure 6-3A**).

As shown in **Figure 6-3B**, a higher uptake was observed for the 500 nm particles compared to their 200 nm counterparts; this result is line with the study of He et al. which showed that phagocytic cells favored the uptake of larger particles.[417] Significant uptake levels were observed for all 500 nm particles except for PS-500; the uptake of PMMA-500 by the THP-1 cells was 1.9 times higher than that of HSA-500 ($P < 0.001$) and 1.7 times higher than that of TF-500 ($P < 0.001$).

It has been shown previously that the elasticity of particles plays an important role in regulating their interaction with cells and cellular uptake.[419,434] In a previous study conducted by our group, the Young's modulus of similar protein particles fabricated by EHD jetting was found to be 43 kPa,[237] which is lower than the reported Young's modulus values of pristine PMMA (5537.42 MPa),[441] PMMA fibers (4.38GPa),[442] and PS (~3 GPa).[443] Hui et al. found that particles with higher Young's moduli retained their spherical morphology during cellular uptake.[434] However, due to ligand-receptor interactions and membrane wrapping, softer nanoparticles were deformed, resulting in reduced cellular binding and a lower endocytosis rate.[434] Specifically, in macrophages, the data showed that the uptake of stiff nanoparticles was three times higher than that of soft nanoparticles.[434] A similar trend was observed for the uptake of polyethylene glycol (PEG) – based hydrogels by J774 macrophages, where hard nanoparticles were phagocytosed over 3.5-fold more than their soft counterparts after a 12-hour incubation time.[419] Concurrent with these observations, we hypothesize that the different uptake levels observed for the PMMA and protein nanoparticles may be related to their mechanical properties. Moreover, no statistical difference in the zeta potential values was observed across these particles.

In contrast to PMMA-500 particles, the uptake of PS-200 nm particles was 1.8 and 2 times lower than the uptake of HSA-200 and TF-200, respectively. Comparing the 500 nm particle groups, the

uptake of TF-500 was slightly higher than that of HSA-500; however, both groups had about 15 times higher uptake levels than PS-500. Since the surface charge of the nanoparticles affects cellular uptake,[444] the more negatively charged surfaces of PS-200 and PS-500 may be the reason for the lower uptake of these particles by the THP-1 cells despite their higher elastic moduli. This is in line with a previous study of carboxylated PS particles, which had the lowest uptake level among the studied particles groups with less negative or more positive zeta potential values; the negative surface charge of PS particles hindered the uptake of particles in THP-1 cells.[444]

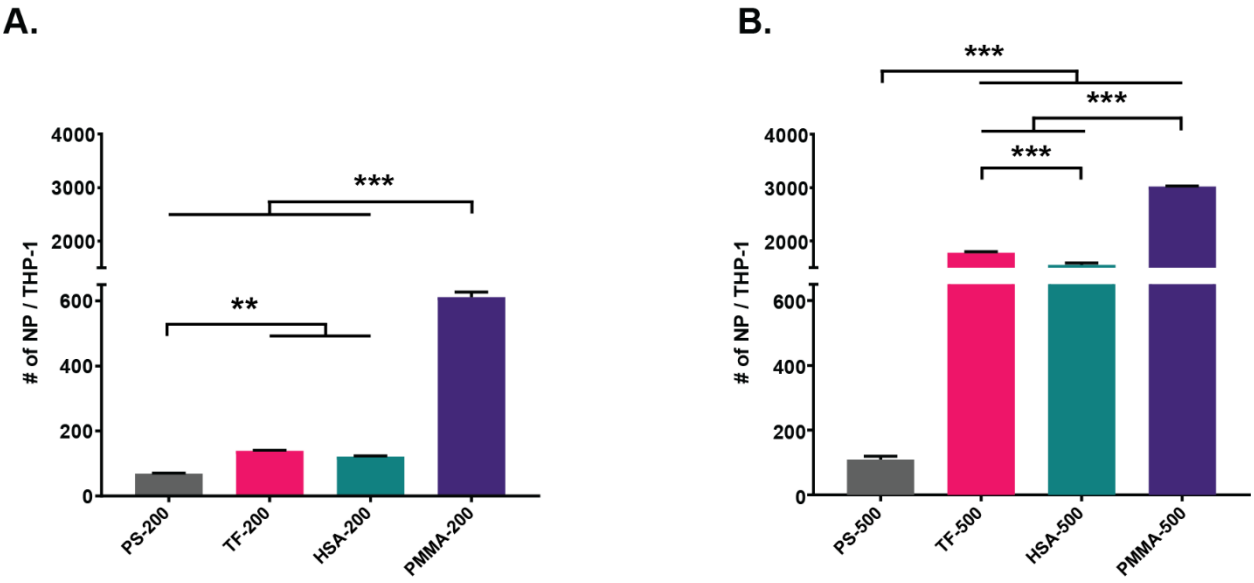

Figure 6-3. Nanoparticles uptake by THP-1 cells. (A) 200 nm nanoparticles and (B) 500 nm nanoparticle uptake by THP-1 cells normalized to the number of THP-1 cells measured by plate reader.

6.4.3 Migration Behavior of THP-1 Monocytes upon Nanoparticles Uptake

The migration behavior of particle-loaded THP-1 cells across confluent static in vitro BBB model was assessed using hCMEC/D3 monolayers cultured on FluoroBlock™ ™ permeable supports. Transendothelial electrical resistance (TEER) measurements were recorded every day for at least

7 days (**Figure 6-4**). A plateau of 40 Ω×cm^2 was reached after a period of 7 days of culture, then the confluent BBB models were used in the migration studies.

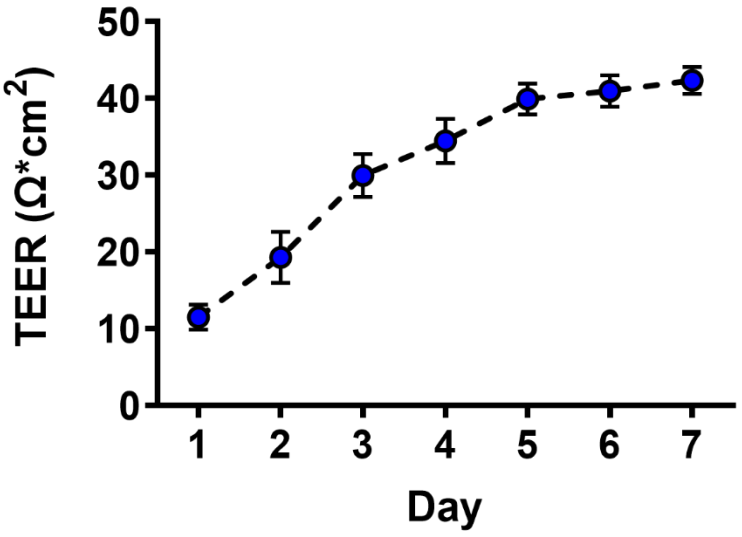

Figure 6-4. TEER measurements for hCMEC/D3 monolayers on 8.0 µm pore size FluoroBlock™.

The THP-1 cells were allowed to migrate towards MCP-1 for three hours, and the results indicate that the type of nanoparticles loaded onto the monocytes directly impacted their migration behavior. The migration of the nanoparticle-loaded monocytes was normalized to the migration of unloaded monocytes, and the results were reported as fold changes (**Figure 6-5**). Surprisingly, the migration of monocytes loaded with HSA-200 and TF-200 nanoparticles nearly doubled, whereas the migration of monocytes loaded with PMMA-500 nanoparticles was reduced by one-half. Among all particle groups, PMMA-500 particles were internalized the most, which may induce a physical burden onto the monocytes, thereby reducing their ability to migrate within the three-hour time period. The high stiffness of the PMMA nanoparticles, as compared to the softer protein nanoparticles, could potentially affect the THP-1 cells after internalization. The cells stiffness and ability to deform are two important characteristics that can regulate cellular migration.[445]

The uptake of PS-200 and PMMA-200 did not alter the migration behavior of the monocytes compared to the control group represented by a fold change of one, although the uptake level of PMMA-200 particles was 8.9 times higher than that of PS-200. HSA-200 and TF-200 nanoparticles elicited 1.8-fold ($P < 0.05$) and 2-fold ($P < 0.01$) higher monocyte migration than PMMA-200. HSA-200 and TF-200 elicited 2.1-fold ($P < 0.01$) and 2.3-fold ($P < 0.01$) higher monocyte migration than PS-200 (**Figure 6-5A**). Comparing the 500 nm particle groups (**Figure 6-5B**), monocytes loaded with the PMMA particles showed a 2-fold and 1.8-fold lower migration than the monocytes loaded with TF and HSA nanoparticles, respectively ($P < 0.05$).

For optimal delivery performance of any cellular hitchhiking platform, a balance between uptake level and migration behavior needs to be achieved. Given the impact of the particle properties on THP-1 monocyte uptake and migration, protein nanoparticles provided reasonable uptake levels but outperformed the other particle groups in terms of the migration behavior of the nanoparticle-loaded monocytes. This may suggest that protein nanoparticles are suitable candidates for consideration when designing a monocyte-mediated drug delivery platform to cross the BBB.

To gain more insight into the underlying mechanism for the difference in the migration behavior of monocytes loaded with PMMA-500 and protein nanoparticles, RNAseq was performed on monocytes loaded with PMMA-500, TF-200 and TF-500. Unfortunately, we were not able to perform RNAseq with all particle groups; PMMA-500, TF-200 and TF-500 were chosen as these groups reflect the different scenarios: (1) higher particle uptake but lower monocyte migration (PMMA-500) and (2) lower particle uptake but higher monocyte migration (TF-200). TF-500 was included to disentangle the effect of size (when compared to TF-200) and composition (when compared to PMMA-500).

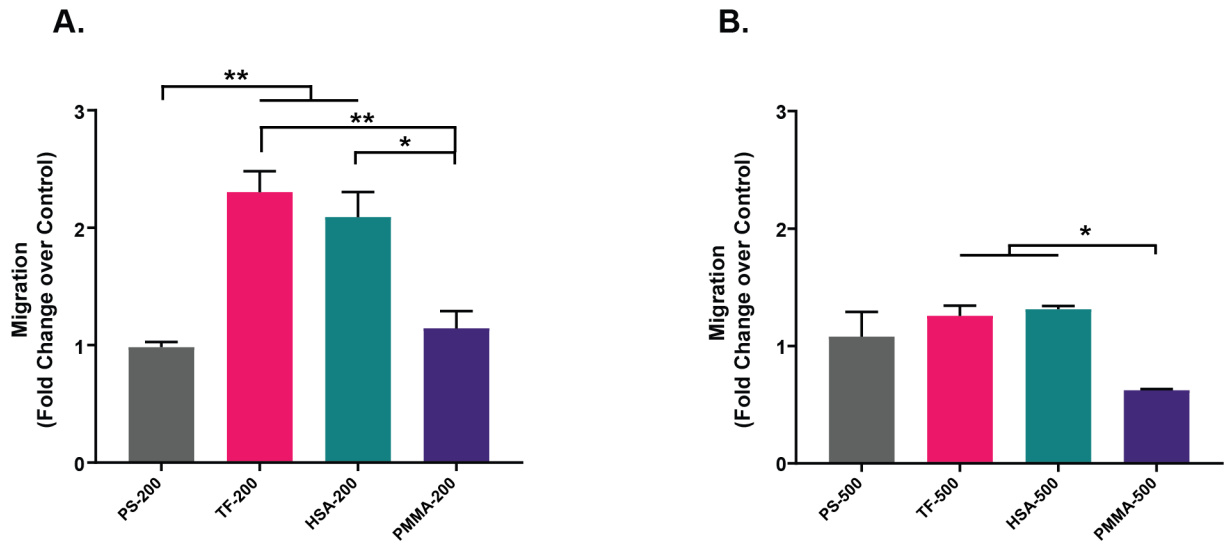

Figure 6-5. Fold change migration of THP-1 cells loaded with different (A) 200 nm and (B) 500 nanoparticle groups compared to untreated THP-1 cells.

6.4.4 Relating Migratory Differences of Nanoparticle-treated THP-1 Cells to Their Transcriptomic Profiles Using RNA Sequencing

To elucidate the differences in the observed migration behavior of monocytes after particle uptake, RNA-seq was performed on the nanoparticle-treated THP-1 cells and a non-treated THP-1 control to explore the differences in their transcriptomic profiles. Unsupervised analysis of nanoparticle-treated THP1 and non-treated THP-1 cells for all genes using Principal Component Analysis (PCA) showed a separation between nanoparticle-treated THP-1 and non-treated THP-1 cells along the first principal component (PC1), but very little clustering within the treated samples (**Figure 6-6A**), suggesting a broad indiscriminate effect of nanoparticle uptake on THP-1 cells. To investigate migration specific effects of nanoparticle uptake, gene enrichment analysis was performed on genes that were differentially expressed between each of the nanoparticle-treated THP-1 conditions and the non-treated THP-1 control, focusing on pathways directly related to leukocyte migration, mononuclear and neutrophil migration, as well as trans-endothelial

migration. **Figure 6-6B** compares the significance of these pathways for the TF-200, TF-500 and PMMA-500 treated THP-1 conditions and shows that the TF conditions have a higher enrichment of genes associated with migration.

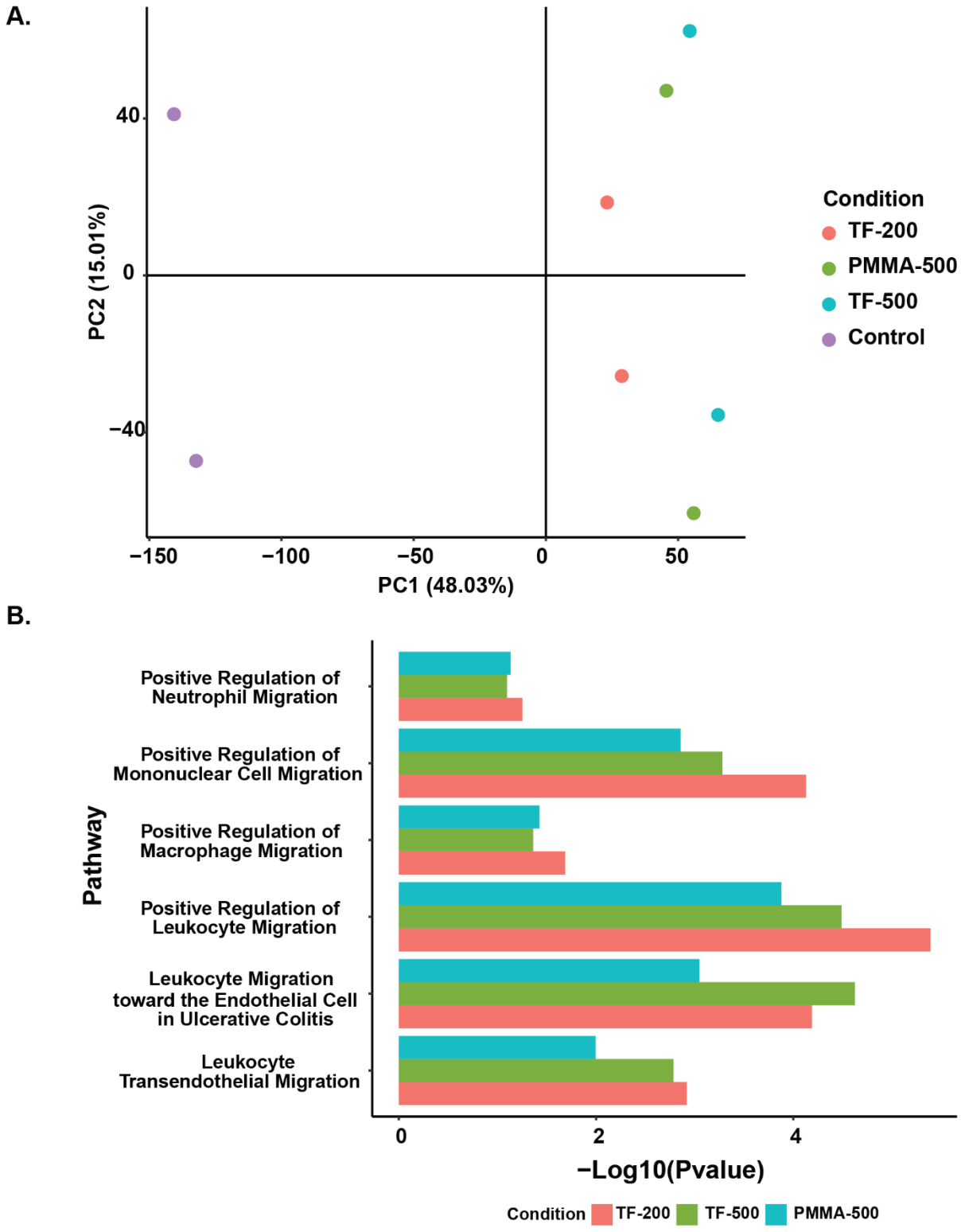

Figure 6-6. The effect of nanoparticles uptake on THP-1 cells gene expression. (A) Plot showing PCA of nanoparticle-treated and non-treated THP-1 cells for all genes. Axes are labeled with the percentage variance explained for the two principal components. (B) Migration specific pathway

analysis comparing significance of the indicated pathways after differential expression analysis between each of the nanoparticle-treated THP-1 conditions and the non-treated THP-1 control.

PCA focusing on genes implicated in pathway terms related to leukocyte migration, and specifically to the trans-endothelial migration pathway, showed distinct clustering of the different nanoparticle treatment groups, with TF-treated THP-1 cells grouping distinctly from PMMA-treated THP-1 cells (**Figure 6-7A** and **Figure 6-7B**). To further explore the effects of nanoparticle treatment on leukocyte migration and specifically on trans-endothelial migration, gene expression signatures were generated by finding the aggregate expression distribution of all the genes implicated in each pathway. The violin plots shown in **Figure 6-7C** and **Figure 6-7D** show significantly higher levels of both migration and trans-endothelial migration gene signatures in the TF-treated conditions relative to the PMMA-treated condition.

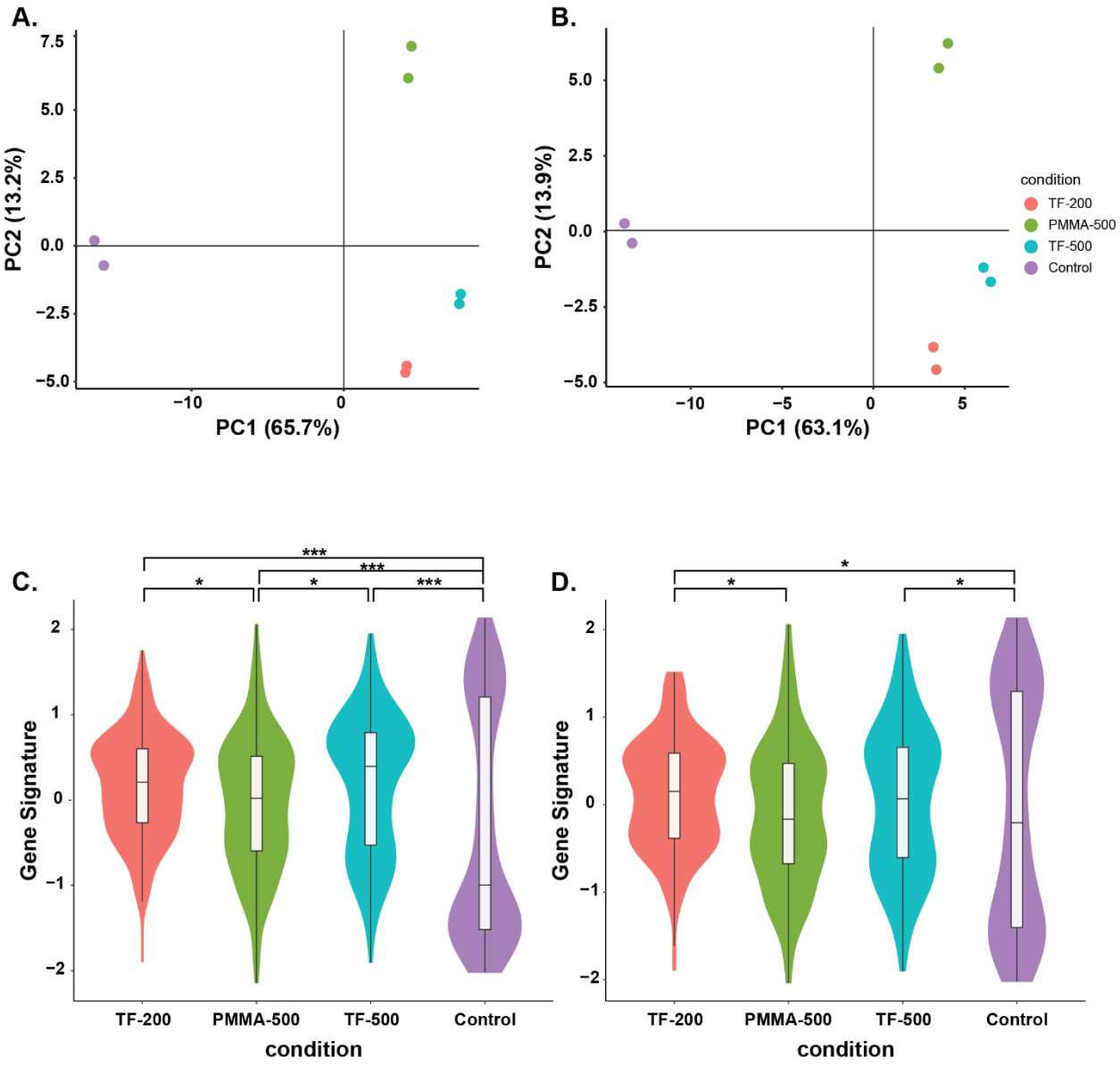

Figure 6-7. Migration-specific effects of nanoparticles uptake on THP-1 cells gene expression. (A) Plot showing PCA of nanoparticle-treated and non-treated THP-1 cells for migration related terms. (B) PCA plot focusing on genes implicated in trans-endothelial migration. Violin plots comparing aggregate expression distribution of genes related to (C) migration and (D) trans-endothelial migration related genes.

Furthermore, differential expression analysis was performed between TF-200 and PMMA-500 as well as TF-500 and PMMA-500. The levels of expression of trans-endothelial migration related genes enriched for TF-200 and TF-500 conditions were then compared to identify common

upregulated genes that could be driving the observed increase in trans-endothelial migration for the TF conditions (**Figure 6-8)**. Several genes were identified as highly upregulated in both TF-200 and TF-500 versus PMMA-500, including CXCL10, VCAM1 and ITGAM, while ITGAL was upregulated in the TF-200 condition. In particular, ITGAM encodes the integrin alpha M chain, which combines with the beta 2 chain (ITGB2) to form a leukocyte-specific integrin referred to as the macrophage antigen 1 (MAC1). This complex, together with LFA1: a complex between ITGAL and ITGB2, plays an important role in the cascade of leukocyte adhesion and transmigration through blood-vessel walls.[446] This cascade includes leukocyte capture, rolling, slow rolling, arrest, adhesion strengthening and spreading, intravascular crawling, and paracellular and transcellular transmigration.[446] Integrins contribute to rolling and mediate firm adhesion of leukocytes. Specifically, β_2-integrins and particularly αLβ2 (LFA1) support firm adhesion but can also cooperate in supporting rolling adhesion.[446,447] Recent studies suggest that integrin LFA1 serves as a rolling and signaling molecule.[447,448] LFA1 can also increase its ligand-binding affinity under shear stress by changing its conformation.[449] Engagement of β_2-integrins, specifically LFA1 and MAC1, was shown to contribute to slowing down rolling leukocytes in tumor necrosis factor-α treated mice.[450,451] Moreover, the leukocyte arrest during rolling and slowing down is mediated by the interaction of leukocyte integrins, mostly β1-integrin and β2-integrin subfamilies, to their endothelial-cell ligands (such as VCAM1 and ICAM1).[446] Among the integrins involved to leukocyte arrest, β1-integrin VLA4 and β2-integrin LFA1 have been studied most excessively[446,452]. Studies showing the detachment of neutrophils in the lack of outside-in signaling mediated by the B2-integin[453] provide evidence for a leukocyte adhesion-stabilization step after arrest. Crawling, transendothelial migration of leukocytes through venular walls is the final step in this cascade.[446] Efficient crawling of monocytes to the nearby endothelial junction

has been shown to be mediated by the interaction of LFA1 and MAC1 integrins mostly with ICAM1 and ICAM2.[454] Extension of leukocyte membrane protrusions into the endothelial-cell body and endothelial-cell junctions is mediated by the interaction of MAC1 and ICAM1.[446] Researchers stated the importance of maintaining the ITGAM/ITGB2 (CD11b/CD18) axis for migration across the BBB.[455,456] Thus, based on the critical role of MAC1 and LFA1 integrins in the cascade of leukocytes migration across endothelial cells, it is likely that the uptake of TF-200 and TF-500 by THP-1 cells results in the upregulation of several migration specific genes, including ITGAM (in both TF-200 and TF-500) and ITGAL (only in TF-200 loaded monocytes). These in combination with ITGB2 increases migration of monocytes in a MAC1- and LFA1-dependent manner and can help explain the observed increase in trans-endothelial migration of TF-treated THP-1 cells from the transcriptomic level.

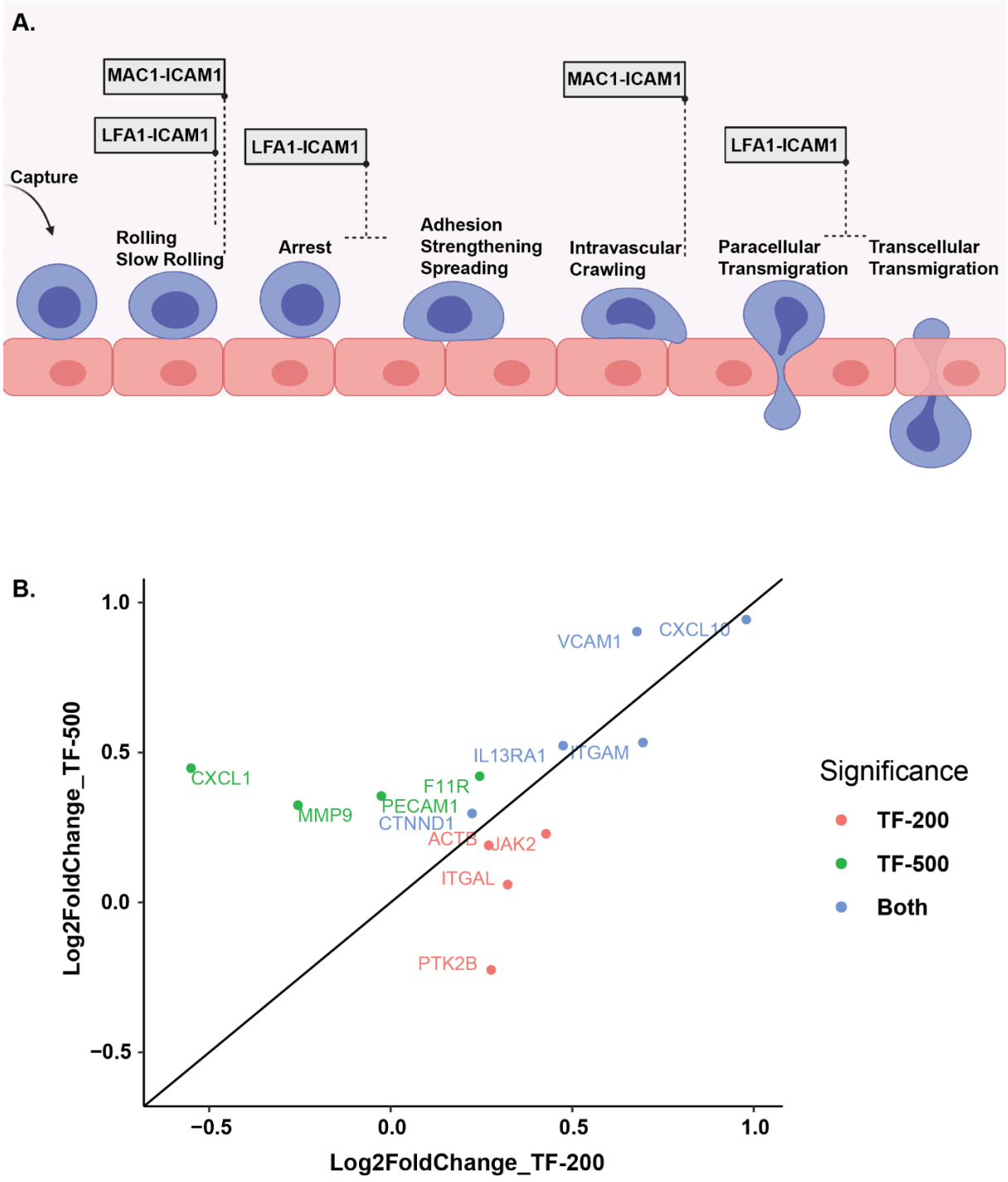

Figure 6-8. Specific trans-endothelial migration related genes enriched for TF-200 and TF-500 treated monocytes. (A) Schematic of the leukocyte adhesion and transmigration cascade, (B) plot showing levels of expression of trans-endothelial migration related genes enriched for TF-200 and TF-500 conditions after differential expression analysis between the two TF conditions and the PMMA-500 condition.

6.5 Conclusions

Monocyte-mediated delivery of nanoparticles to the brain has gained increasing attention due to the natural ability of monocytes to cross the BBB. In this study, the effect of nanoparticle size, composition, and elasticity on the uptake by THP-1 monocytes and their transport across a static human BBB model were investigated. High cell viability was observed for all particle groups. Overall, larger particles demonstrated higher uptake levels, but among similarly sized and surface-charged particles, harder particles were found to be internalized in greater quantities; more negatively surface-charged particles showed lower uptake levels.

An evaluation of the effect of the particle parameters on the migratory behavior of the particle-loaded monocytes revealed that 200 nm-sized protein-based particles increased the migration by 2-fold, whereas PMMA-500 reduced the migration by half. The findings of this study demonstrate that nanoparticle parameters, such as size, composition, and elasticity modulate the migration behavior of monocytes. The high migration observed for TF-200 nanoparticle-loaded monocytes may be mediated in an ITGAM/ITGB2 and ITGAL/ITGB2-dependent manner. These findings should be further explored in vivo to shed light on the exact mechanisms involved in the increased migration behavior of protein particle-loaded monocytes. Upon further investigation of their in vivo performance, these particles offer new opportunities for monocyte-mediated brain drug delivery platforms.

Chapter 7

Engineered Mucoadhesive Janus Nanoparticles Deliver Bioactive Tocilizumab: Prospects for Field-Coverage Oral Cancer Chemoprevention

The material in this chapter has been adapted with minor modifications from the following article: Nahal Habibi*, Caroline Bissonnette*, Daren Wang, Ping Pei, Susan R. Mallery, Joerg Lahann. Engineered Mucoadhesive Janus Nanoparticles Deliver Bioactive Tocilizumab: Prospects for Field-Coverage Oral Cancer Chemoprevention. *In Preparation.* (* Equal Contributions)

7.1 Abstract

Treatment of oral squamous cell carcinoma (OSCC) normally entails radical surgery that results in significant morbidity and is often not curative. Although interventions such as local delivery of chemopreventive agents to prevent the premalignant disease from progressing to OSCC is a better therapeutic option, the oral mucosa presents a significant transport barrier for therapeutics to reach the underlying epithelium by rapidly removing them. Here, poly(lactide-co-glycolide) (PLGA)-chitosan Janus nanoparticles (JNP) are engineered using electrohydrodynamic co-jetting to specifically promote dual adhesion properties, such as hydrophobic and electrostatic interactions to augment mucoadhesion and avoid rapid mucus clearance mechanisms. Tocilizumab (TCZ) as the interleukin-6 (IL-6) receptor antagonist is used as the JNP drug delivery cargo (JNP-TCZ) owing to IL-6's contributory role in OSCC development. Studies show a controlled-release of the drug from the JNP-TCZ particle matrix while preserving its immunoreactivity and bioactivity. For

TCZ released from JNP-TCZ, we could prove 71% and 50% reduced detection of soluble and membrane-bound IL-6Rα, respectively, compared to 55% and 42% by conventional pharmaceutically dispensed TCZ. The JNP are also shown to be readily internalized by the oral keratinocytes. Further, it is shown that 76% of the JNP penetrate past the stratum corneum and a consequent 41% reach the targeted proliferative basal cell epithelial layer in a mucus-covered full-thickness oral mucosal explant. Finally, in vivo OSCC tumor reduction studies demonstrate JNP-TCZ's chemopreventive efficacy. JNP-delivered TCZ significantly inhibits tumor cell proliferation, rate of tumor growth, and final tumor size relative to TCZ bolus injections or control (drug-free) JNP. Thus, such engineered JNP serve as potential drug delivery platforms amenable to intraoral field-coverage chemoprevention.

7.2 Introduction

Oral cancer represents a highly debilitating disease that dramatically impacts the lives of patients (an estimated 54,010 new oral and oropharyngeal cancer cases and 10,850 deaths to occur in U.S. during 2021).[457] Notably, oral squamous cell carcinoma (OSCC) is one of the most challenging-to-treat human cancers. Clinical issues are elevated by the insidious nature of its early disease and the reliance upon radical surgery as the primary treatment modality.[458,459] Even if patients achieve a surgical cure, they are still destined to suffer significant morbidity due to loss of vital facial structures essential for eating, speaking, and esthetics. Similar to many carcinomas, OSCC does not occur de novo, but arises from a precursor surface epithelial lesion termed oral intraepithelial neoplasia (OIN). While not all OIN lesions progress to OSCC, up to one-third recur following complete, microscopically-confirmed excision, and up to 87% of high risk lesions (WHO-based binary grading system) progress to OSCC.[460] In addition, persons suffering from DNA repair deficits, e.g., Fanconia anemia (FA), are also susceptible to field cancerization and OSCC.[461]

Finally, there is a patient cohort, often with social histories negative for established OSCC risk factors, e.g., tobacco use, oncogenic HPV, that develop multifocal premalignant lesions (proliferative verrucous leukoplakia) throughout the oral cavity.[462]

Due to its pro-inflammatory, pro-angiogenic and pro-proliferative effects, interleukin-6 (IL-6) is a key cytokine in the development of many cancers including OSCC.[463] In addition, levels of IL-6 are often elevated in the sera and saliva of patients with OIN lesions, which support the importance of IL-6 even prior to overt OSCC development.[464,465] Our labs have shown that OSCC cells release soluble IL-6 receptor (IL-6R), which enables IL-6 growth enhancement even in IL-6R negative cells.[466] Consequently, local injections of the IL-6R antagonist, tocilizumab (TCZ), significantly suppressed growth of OSCC xenografts.[466]

Previous OSCC cancer prevention trials have primarily relied on systemic administration, which conceptually would deliver drug throughout the mouth.[467] Systemic administration, however, has proven ineffective for OSCC chemoprevention.[467,468] In contrast to systemic delivery, local delivery formulations provide a pharmacologic advantage by delivering therapeutically-relevant agent levels at the target tissue without deleterious drug-related systemic effects.[203,469] It is thus plausible that a therapeutically effective, localized strategy to provide nontoxic, effective, chemopreventive coverage throughout the entire mouth is needed to address these clinical problems.

The oral mucosa, however, presents major challenges for local mucosal drug delivery systems. Mucus as a viscoelastic and adhesive hydrogel, protects the underlying epithelium by rapidly trapping and removing foreign particles and pathogens. The characteristics of mucus stem from its dense network of highly crosslinked and entangled mucin fibers that contain glycosylated segments with high affinity for positively charged molecules.[470] In addition, the hydrophobic

domains of the mucin fibers network interacts with hydrophobic particles.[470] An effective formulation needs to penetrate the mucus to reach the underlying epithelium, and evade clearance by intraepithelial langerhans cells.[471]

Nanoparticles possess unique properties, such as their size, surface chemistry, capacity to encapsulate, bind, and transport therapeutic agents making them desirable candidates for mucosal drug delivery. The small size range of nanoparticles is amenable to cell internalization via passive diffusion or endocytosis.[472,473] Treatment selectivity can also be enhanced by strategies such as decoration with molecules that bind to overexpressed target cell antigens or use of agents to augment target cell binding.[472] In addition to the protection of the drug and minimizing off-target side effects, mucoadhesive and mucopenetrating nanoparticles can prolong the contact time of the formulation with oral mucosa and facilitate delivery to the underlying cells.[474] A variety of materials, including polymers, lipids, inorganic carriers, polymeric hydrogels and biomolecular scaffolds and device configurations e.g., cylindrical implants, thin films, microspheres, have been successfully employed to increase therapeutic efficacy by controlled drug delivery formulations.[475,476]

Considering the variety of biological barriers facing traditional nanoparticles, novel Janus multifunctional particles allow bulk and surface feature modulation which enables the design of more effective therapies.[6] Multifunctional particles can be categorized as anisotropic particles that incorporate two or more engineered properties in a single particulate entity.[6] Electrohydrodynamic (EHD) co-jetting utilizes laminar flow of two streams in parallel capillary needles without convective mixing to create Janus nanoparticles (JNP).[147] Application of a voltage at the capillary needles, causes distortion of the droplet into a Taylor cone. The electrified polymer jet then splits into droplets that undergo rapid solvent evaporation resulting in solidified

micro- to nanoparticles. Due to rapid solvent evaporation, the initial flow-determined arrangement of the input polymers will be mirrored in the fabricated nanoparticles.[133,141] EHD co-jetting has been used to fabricate multicompartmental carriers incorporating cancer drugs,[146] siRNA,[131,216] and imaging agents[147] in different compartments.

Based on the importance of IL-6 in OSCC development, the purpose of this study is to formulate, characterize, and evaluate TCZ-loaded JNP in vitro and in vivo for OSCC chemoprevention.

7.3 Materials and Methods

7.3.1 Materials

PLGA (85:15 lactide:glycolide, 50-75 kg/mol), poly(ethylene glycol) diglycidyl ether, and glycol chitosan were purchased from Sigma-Aldrich (St. Louis, MO). Alexa Fluor 488 conjugated albumin from bovine serum, Advanced DMEM (Gibco), RIPA Lysis and Extraction Buffer 1x, StemPro Accutase, Micro BCA™ Protein Assay Kit, and NucBlue Fixed cells ReadyProbes reagent were obtained from Thermo Fisher Scientific (Waltham, MA). Fanconi Anemia patient (FASCC) cells were a generous gift from Dr. Susanna Wells. HPV E6/E7 transduced human normal oral epithelial cells (Epi) were obtained from ScienCell Research Labs (Carlsbad, CA). OSCC cell line (CRL-2095™) and U-937 cell line (CRL-1593.2™) were purchased from ATCC (Manassas, VA). µ-Slide VI0.4 was purchased from Ibidi (Fitchburg, WI). The Anti-LAMP1 primary antibody (ab24170) and Goat Anti-Rabbit IgG H&L Alexa Fluor 555 (ab150078) was purchased from Abcam (Cambridge, MA). VECTASHEILD mounting medium was purchased from Vector Laboratories (Burlingame, CA). Pre-wetted (2 mL), sterile non-stick pads were purchased from Walgreens (Deerfield, IL). Uncoated 6-well cell culture plate and Matrigel were purchased from Corning Life Sciences (Corning, NY). Transparent dressing (Nexcare™ Tegaderm™) was obtained from 3M (St. Paul, MN). Plastic molds (Tissue-Tek® Cryomold®

Molds) and Healthcare™ Tissue-Plus™ O.C.T. Compound were purchased from Fisher Scientific (Waltham, MA). Isopentane was purchased from Fisher chemical (Waltham, MA). hL-6Rα alpha DuoSet ELISA was purchased from R&D System (Minneapolis, MN). Tocilizumab was purchased from ACTEMRA, Genentech (San Francisco, CA).

7.3.2 Electrohydrodynamic Co-jetting of Janus Poly(lactide-co-glycolide)-chitosan Nanoparticles

Poly(lactide-co-glycolide) (PLGA)-chitosan JNP were made using the electrohydrodynamic (EHD) co-jetting technique. In EHD co-jetting, two needles were used as capillaries in a side-by-side configuration. The two different polymeric solutions were pumped at a rate forming laminar flow to ensure a stable interface between the two jetting solutions without any convective mixing. When a droplet was formed at the outlet of the needles, the electric field was applied to the system. Due to rapid evaporation, the initial flow-determined configuration was maintained. The two solutions were made with the following formulations: 1) 1.3% (w/v), 5:2 (w/w) glycol chitosan: poly(ethylene glycol) diglycidyl ether in 1:1 v/v% ultrapure water : Ethylene glycol and 2) 1% (w/v) PLGA in dimethylformamide. EHD co-jetting was performed at a flow rate of 0.1 ml/h. After application of voltage and formation of Tayler cone, the PLGA-chitosan JNP were electrosprayed onto a collector sheet with a distance of 20 cm to the needle tip. Afterwards, completion of crosslinking reaction and removal of residue solvents were ensured by maintaining the fabricated particles under vacuum for at least a week. To enable visualization of JNP by fluorescence or confocal microscopy, fluorescently labeled PLGA-chitosan JNP were prepared by addition of Alexa Fluor 488 conjugated albumin from bovine serum at 1 mg/ml to the jetting solution. The polydisperse particles were collected and separated via serial centrifugation to retrieve the desired size for cell internalization and membrane interactions i.e., 360 nm particles. The nanoparticles

were analyzed with Dynamic Light Scattering (DLS) to determine their size distribution and the particles' concentration was measured using Nanosight Nanoparticles Tracking Analysis (NTA) (Malvern Panalytical, UK).

7.3.3 Characterization of Janus Poly(lactide-co-glycolide)-chitosan Nanoparticles

Scanning Electron Microscopy (SEM)

SEM images were obtained using a FEI Nova 200 Nanolab SEM/FIB at the Michigan Center for Materials Engineering at acceleration voltages of 5kV. Images were processed using ImageJ (Wayne Rasband, NIH) to obtain the respective nanoparticle size distribution. For particle size distribution, more than 1000 particles per samples were measured by ImageJ.

Dynamic/Electrophoretic Light Scattering (DLS/ELS)

DLS/ELS measurements were performed using a Zetasizer Nano ZS (Malvern Panalytical). DLS was employed to measure the particle size distribution in phosphate buffered saline (PBS) after particle collection and size separation. ELS was employed to determine the zeta potential of Janus particles. Every measurement was done in triplicate and averaged to determine the particle size and zeta potential.

7.3.4 Tocilizumab Encapsulation and Assessment of Bioactive Tocilizumab Release from Janus Nanoparticles

Tocilizumab loaded PLGA-chitosan JNP were fabricated using the same procedure as described above. Only the chitosan compartment was used for TCZ encapsulation. Here, TCZ, was mixed in the jetting solution of chitosan compartment prior to jetting, substituting the amount of deionized water previously used for empty nanoparticles. The encapsulation was done at a drug-to-particle

ratio (30:100) taking into account both compartments. The drug loading was calculated as the mass of the drug divided by the combined mass of the drug and polymer in both compartments.

For release studies, the TCZ loaded nanoparticles were collected and after serial centrifugation, they were dispersed in 2 ml optimized TCZ buffer (100 mM L-arginine hydrochloride, 10 mM L-histidine, 10 mM L-histidine hydrochloride monohydrate, 30 mM L-methionine, 150 μM Polysorbate 80, pH 6.37). The nanoparticle-containing tubes were then placed into a rotator in the incubator at 37°C. At specific time intervals, the particle suspensions were centrifuged to pellet the particles. The supernatant was removed and analyzed to measure the amount of released TCZ. The particles were re-suspended in a fresh buffer. To determine whether JNP-released TCZ retained immunoreactivity, a TCZ mAb-based ELISA (IBL, Minneapolis, MN) was conducted. At every time point, the amount of immunoreactive released TCZ was measured in accordance with the calibration curve. At subsequent time points, the total amount of TCZ released was calculated by addition of the current and previously released TCZ amounts. Notably, released TCZ levels were within the range of the ELISA standard curve. The release of immunoreactive TCZ was plotted as a function of the total cumulative release versus time.

7.3.5 Nanoparticle Internalization by Human Oral Keratinocytes

An oral squamous cell carcinoma cell line derived from a Fanconi Anemia patient and HPV E6/E7 transduced human normal oral epithelial cells were cultured in Advanced DMEM supplemented with 1X Glutamax and 5% heat-inactivated FBS (GIBCO; Life Technologies; “complete” medium). Cell lines were authenticated via short tandem repeat analyses conducted by Johns Hopkins Genetic Resources Core Facility. Cells were seeded at 2.1×10^4 cells in a μ-Slide VI0.4 then incubated at $37^{O}C$, 5% CO_2 with PLGA-chitosan nanoparticle suspensions (final concentration of 1.67×10^9 NP/mL, 1×10^8 NPs per channel). Experimental controls were: cells

without nanoparticles, cells without nanoparticles and primary antibody, and nanoparticles alone. Monolayer cells were co-incubated with NPs for 1, 3, and 18 hours, then fixed in 4% formaldehyde. All cells, except the primary antibody control, were stained with the Anti-LAMP1 primary antibody followed by a cocktail of secondary antibodies i.e., Goat Anti-Rabbit IgG H&L Alexa Fluor 555, Phalloidin Alexa Fluor 647, and a 1 % BSA PBS solution. A high purity form of the nuclear stain DAPI, was added to each chamber, followed by VECTASHEILD mounting medium. A FV3000 confocal microscope from Olympus (Olympus Life Sciences, Waltham MA) was used for imaging. Four fluorescent channels i.e., nucleus – DAPI (Ex/Em wavelength: 358/461), Blue; PLGA-Chitosan– Alexa Fluor 488 (Ex/Em: 490/525), Green; lysosomes – Alexa Fluor 555 (Ex/Em: 555/565), Red; actin – Phalloidin Alexa Fluor 647 (Ex/Em: 650/668), Yellow. The composite images were captured with the Olympus FV3000 RS fluoview software (Olympus Life Sciences, Waltham MA).

7.3.6 Assessment of Nanoparticle Penetration Through Surface Epithelium in Human Oral Mucosal Explants

In accordance with our IRB approved protocol (OSU Study Number: 2018H0059), human oral mucosal samples were obtained in a coded fashion from consented participants undergoing elective surgical procedures. Patient demographics and social history data were also obtained, coded, and securely stored. The mucosal explants (connective tissue side down) were placed on pre-trimmed, Advanced DMEM ((Gibco, Thermo Fisher Scientific, Waltham, MA) pre-wetted (2 mL), sterile non-stick pads (Walgreens, Deerfield, IL), to line the bottom of a chamber of a flat, uncoated 6-well cell culture plate. After gentle sonication, the fluorescent-tagged PLGA-chitosan JNP suspension (Average size: 344 nm, 1.4 E11 NPs/ml) was placed at a tissue-specific volume to coat the explant epithelial surface (volumes ranged from 1 to 4 µL due to differences in explant

sizes). The tissue was then covered by a sterile, adhesive, waterproof, transparent dressing (Nexcare™ Tegaderm™) prior to a three-hour incubation at 37°C, 5% CO_2 on a gently moving microplate shaker, then embedded on edge in clear, plastic molds (Tissue-Tek® Cryomold® Molds) using Healthcare™ Tissue-Plus™ O.C.T. Compound. The tissue blocks were snap frozen with liquid nitrogen cooled isopentane, covered in foil, and stored at -80°C freezer until cryostat sectioning. Nanoparticle localization studies employed fluorescent light (FITC channel) using the Olympus BX51 fluorescence microscope (Olympus, Center Valley, PA) and the images were captured by the Nikon DS-Fi1 color digital microscope camera (Nikon, Melville, NY). Depth of nanoparticle penetration into the surface epithelium was qualitatively assessed using a 4-layer stratification system: basal 1/3, middle 1/3, superficial 1/3 of the epithelium, and stratum corneum (**Figure 7-4A** and **Figure 7-4B**).

7.3.7 Fluorescent Activated Cell Sorting Quantitative Assessment of Nanoparticle Internalization

Fluorescent activated cell sorting (FACS) analyses to quantitatively assess oral keratinocyte-nanoparticle membrane association and/or internalization were conducted at Ohio State's Analytical Cytometry Core. Cells were plated in serum free Dulbecco's Modified Eagle's Medium (GIBCO, ThermoFisher) and were incubated for 1 hour and 3 hours with fluorescent-labeled PLGA-chitosan JNP (1.5×10^4 cells + 1×10^9 nanoparticles). After incubation, the media was removed and the wells were vigorously washed twice with PBS. Cells were then dissociated with StemPro Accutase for 15-20 minutes, washed vigorously 3 times (PBS + 2%FBS "FACS buffer"), centrifuged at 420 ×g between washes, and the cell pellet re-suspended in FACS buffer, followed by nuclear staining with NucBlue Live Ready Probes 4',6-diamino-2-phenylindole,

dihydrochloride (DAPI) (ThermoFisher Scientific, Waltham, MA). FACS control samples included DAPI stained and unstained cells with and without non-fluorescent nanoparticles.

FACS analyses were conducted on a BD LSRFortessa™ cell analyzer (BD Biosciences, San Jose, CA) and employed forward and side scatter parameters to create a histogram with the log of fluorescent intensity on the horizontal and side scatter area (SSC-A) on the vertical axes, respectively. The population that concurrently expressed JNP fluorescence (488 nm) with DAPI-stained nuclei (405 nm) was identified as the JNP associated cell population.

7.3.8 Determination of Tocilizumab's Effects on Immunoreactivity of hsIL-6R

The capacity of JNP-released TCZ to perturb IL-6Rα immunoreactivity would confirm JNP-released TCZ retains functional activity. To establish a baseline for comparison, TCZ's ability to suppress immunoreactive IL-6Rα was evaluated via hL-6Rα alpha DuoSet ELISA, using the manufacturer's instructions. Conditioned medium from a pleural effusion transformed histiocytic cell line (U-937 cells), which generated high levels of soluble IL-6Rα (sIL-6R), was used in addition to IL-6Rα standards to assess TCZ's capacity to suppress IL-6Rα immunoreactivity.

Studies were also conducted, under the same conditions, on JNP-released TCZ to determine whether its functional activity was retained. The PLGA-chitosan JNP were stored at 4ºC for 2-8 days after collection. The supernatant was collected after serial centrifugation and protein concentration was measured with a micro-BCA analysis following the manufacturer's instructions. As the PLGA-chitosan JNP were not formulated with any other proteins, the protein concentration was extrapolated to represent the TCZ concentration of the PLGA-chitosan JNP supernatant. Suspension-cultured U-937 cells were seeded at 6×10^5 cells/well in 6 well plates in 1.2 mL of complete media (DMEM, 1% GlutaMax + 5 % FBS). Wells were treated with either 1.0 µg/mL of TCZ and 1.0 µg/mL of released-TCZ from PLGA-chitosan JNP. Control wells were also prepared

without treatment. The wells were incubated at 37ºC for 24 hours. Cell suspensions were then centrifuged (420 ×g for 5 minutes) and duplicate final cell counts were conducted with the average and used for cell density adjustment. The conditioned media were collected and used to determine the concentration of sIL-6Rα (Media). Then 500 µL of RIPA Lysis and Extraction Buffer 1x was added to each cell sample, which were subsequently triturated and placed on ice for 15 minutes. The samples were vortexed and centrifuged. The supernatant was collected and used for the analysis of IL-6Rα concentration of the cell lysate. Concentrations of sIL-6Rα (Media) and IL-6Rα (Cell lysate) produced by the U-937 cell line were obtained by performing the Human IL-6R alpha DuoSet ELISA, with results reported as pg/mL and adjusted to cell density. The concentrations were adjusted according to final cell density counted after the 24 h treatment time. Relative percentage decrease of sIL-6Rα (Media) compared to controls were calculated.

7.3.9 Proof of Concept In Vivo Chemoprevention Studies

To assess PLGA-chitosan JNP released TCZ function in vivo, a tumor regression model was used which entailed subcutaneous injection of an STR-validated, highly tumorigenic OSCC cell line, SCC2095sc. One million cells suspended in 100 µL Matrigel were subcutaneously injected into the flanks of nude mice. These studies entailed 3 experimental groups [drug-free JNP control (JNP), TCZ bolus injection, and TCZ-loaded JNP (JNP-TCZ)], n=9 mice per group, bilateral flank 2095sc injections. The mice and their tumor injection sites were monitored daily with measurements recorded (calipers length x width) every 3rd day. OSCC tumors developed in 90% of the 2095sc-Matrigel injection sites. Treatments (every 4th day, 3 total) were initiated on the 15th day after tumor cell injection and consisted of: JNP, JNP-TCZ (1.2 µg total TCZ release), and TCZ bolus (1.2 µg). JNP suspensions and TCZ stock drug dilution employed TCZ optimized buffer + 1% sucrose. Twenty seven days following tumor cell injection, final tumor measurements were

obtained and mice were sacrificed (CO_2 followed by cervical dislocation). Excised tumors were fixed in 10% neutral buffered formalin for 8 hours then transferred to PBS until histologic processing. A two-tailed t test was used to evaluate the impact of JNP on tumor clinical size while a Mann Whitney U test

7.3.10 Statistical Analysis

Data distribution, analyzed via a Shapiro Wilk normality test, was used to determine whether a parametric or nonparametric analysis was conducted (GraphPad Prism, San Diego, CA). The impact of TCZ to functionally impact IL-6R ELISA reactivity was evaluated by a Kruskal Wallis ANOVA followed by a Dunn's Multiple Comparison test. A 2-tailed t test was employed to evaluate the impact of PLGA-chitosan JNP on in vivo tumor growth while a Mann Whitney U test was used to assess the impact of delivery format on TCZ chemopreventive impact. Effects of treatment on histologic size were evaluated by one-way ANOVA, followed by a Tukey's post hoc test.

7.4 Results and Discussion

7.4.1 Design of Mucoadhesive and Mucopenetrating Janus Poly(lactide-co-glycolide)-chitosan Nanoparticles

Size, shape and material composition are well-established parameters in the design space for nanoparticle fabrication.[477] Our group developed and refined another nanoparticle parameter related to the controlled spatial distribution of matter via EHD co-jetting.[147] Notably, the presence of different materials in a single particle enables multifunctionality, i.e., augmentation of keratinocyte adherence, preservation of drug structure, capacity to deliver multiple agents.

The underlying mechanism responsible for trapping the foreign particulates is based on the formation of polyvalent adhesive interactions [478] through electrostatic interactions, van der Waals forces, hydrophobic forces, and hydrogen bonding.[479] Mucoadhesive polymers can enhance the retention time of the drug leading to improved drug penetration, localization and efficacy.[480] Cationic polymers such as chitosan, are one class of mucoadhesive polymers that interact with the negatively charged components on mucin fibers such as carboxyl or sulfate groups facilitating mucus adhesion.[478,480] Polycaprolactone nanoparticles, developed by a nanoprecipitation method, were loaded with curcumin by the nanoprecipitation method, followed by coating with the mucoadhesive polysaccharide chitosan via hydrogen bonding. The subsequent chitosan-coated nanoparticles' interaction with mucin, confirmed their application as mucoadhesive curcumin delivery platforms.[481] In addition, hydrophobic biomaterials such as PLGA can utilize hydrophobic interactions for mucous adhesion.[478] PLGA nanoparticles can also provide a controlled, sustained release drug profile that enhances therapeutic effects including against OSCC cells, and enhance drug transport and oral bioavailability in vivo.[482,483]

The dual adhesion capability to form multiple adhesion interactions such as electrostatic interaction and hydrophobic forces, however, presents a challenge for designing mucoadherent polymeric based drug delivery platforms.[478] Through the application of EHD co-jetting, however, we were able to present both hydrophobic polymer (PLGA) and cationic polymer (chitosan) side-by-side in one single particle (**Figure 7-1**). Here, the design of mucoadhesive JNP concurrently utilized multiple adhesion interactions in the particle. Each compartment of the JNP interacts with the mucus layer differently to allow formation of polyvalent adhesive interactions thus enhancing the mucoadhesive properties of the formulation.

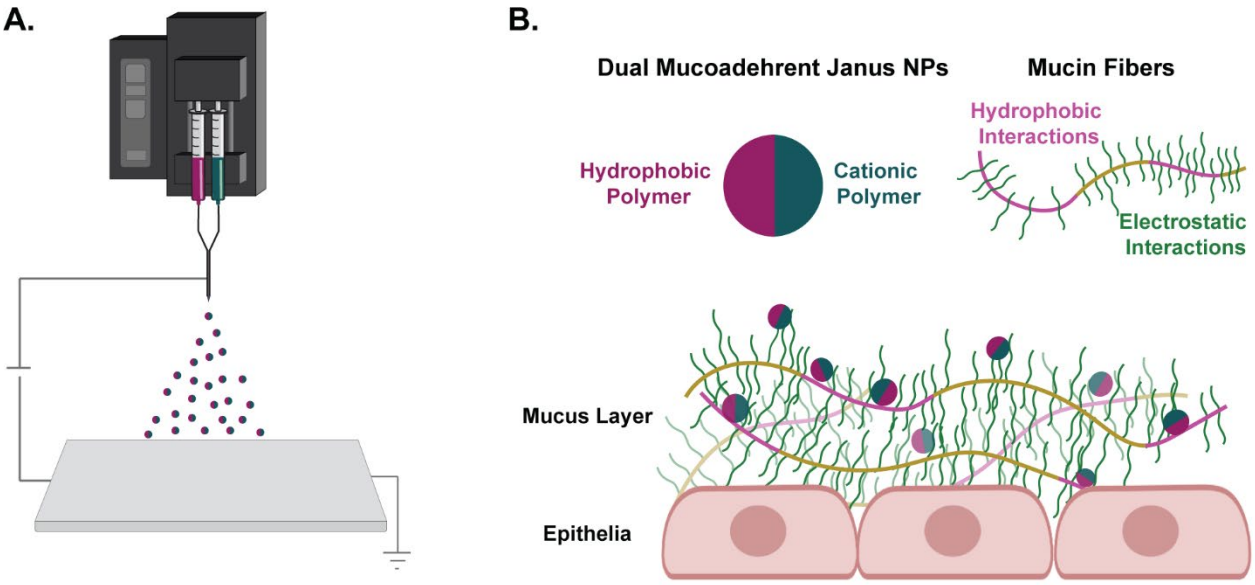

Figure 7-1. The Schematic design of dual mucoadhesive Janus PLGA-chitosan JNP via EHD co-jetting and their interactions with mucosal barrier

The transit time of mucoadhesive systems bound to mucin is determined by the physiological turnover time of the mucus layer.[478] Overcoming the mucus barrier and achieving longer retention time in the cell surface requires a nanoparticle formulation that can efficiently penetrate through the mucus barrier and accumulate in the underlying epithelium.[470,478] For the mucoadherent drug delivery formulation to be able to further penetrate through the mucus barrier, the surface charge of the system is known to play a major role.[484] Previous reports have shown that penetration through the mucosa can be improved effectively by neutral particles presenting high density of both positively and negatively charged groups on their surface.[484–487] This feature is incorporated into the design of PLGA-chitosan JNP by the presentation of positively charged chitosan compartment side-by-side of negatively charged PLGA compartment resulting in a net neutral surface charge.

PLGA-chitosan JNP were fabricated via EHD co-jetting as described. To achieve stable nanoparticles, the compartment comprised of chitosan was chemically crosslinked using a poly(ethylene glycol) diglycidyl ether (PEGDE) linker molecule. The morphology and size distribution of PLGA-chitosan JNP were obtained by SEM and further ImageJ analysis. (**Figure 7-2A** and **Figure 7-2C-F**). As shown in **Figure 7-2C-F** , the fabricated PLGA-chitosan JNP had an average diameter of 316 nm (Q1/Med./Q3 = 157/296/446) with PDI_{SEM} of 0.268, high circularity (Avg.=0.91, Q1/Med./Q3 = 0.88/0.95/1.00), relatively low anisotropy (Avg.=1.35, Q1/Med./Q3 = 1.09/1.20/1.47), and relatively high roundness (Avg.=0.78, Q1/Med./Q3 = 0.68/0.83/0.92) based on SEM analysis of as-jetted dry PLGA-chitosan JNP. The fabricated particles were collected and centrifuged to separate the JNP with the target size of 360 nm. The particles were analyzed with DLS to determine their size distribution and NTA to measure their concentration. (**Figure 7-2G**)

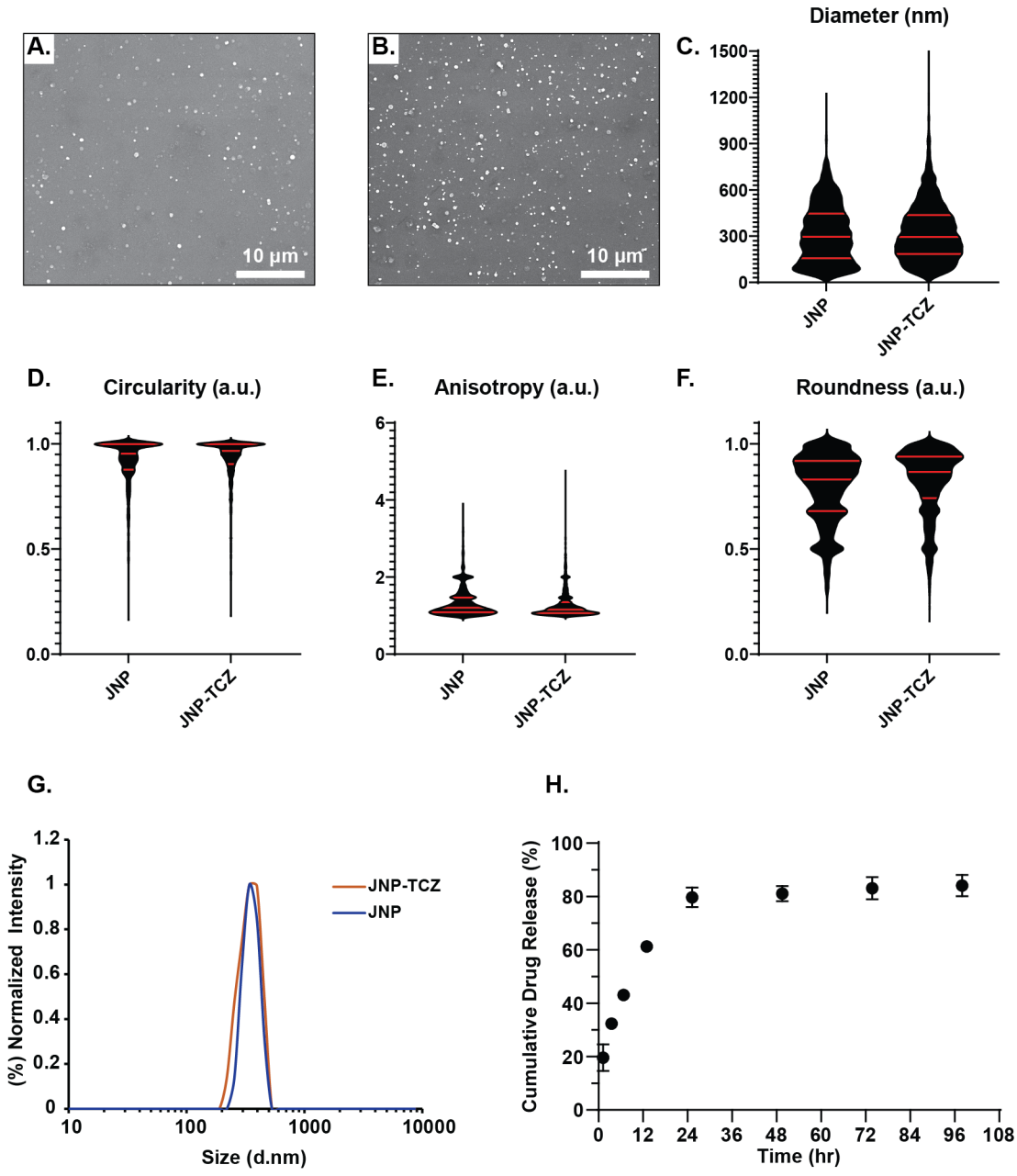

Figure 7-2. Characterization of PLGA-chitosan JNP and TCZ loaded PLGA-chitosan JNP (JNP-TCZ). SEM images of (A) PLGA-chitosan JNP, and (B) TCZ loaded PLGA-chitosan JNP. Scale bar is 10 µm. (C-F) Key geometric factors of PLGA-chitosan JNP and TCZ loaded PLGA-chitosan JNP based on SEM analysis. (G) Release kinetics of active TCZ from PLGA-chitosan JNP as measured by ELISA**.**

7.4.2 Janus Poly(lactide-co-glycolide)-chitosan Nanoparticles Preserved Immunoreactivity of Released Tocilizumab

A controlled release formulation for local delivery of the humanized monoclonal antibody that inhibits the IL-6 receptor, TCZ, was achieved by JNP. TCZ was loaded in the chitosan compartment due to solvent compatibility. To encapsulate TCZ in nanoparticles, the TCZ was mixed with the jetting formulation of the chitosan compartment. The TCZ-loaded PLGA-chitosan JNP were further characterized by SEM (**Figure 7-2B**) to study their size distribution and morphology (**Figure 7-2C-F**). The fabricated TCZ-loaded PLGA-chitosan JNP had an average diameter of 327 nm (Q1/Med./Q3 = 185/295/437) with PDI_{SEM} of 0.245. There was no significant difference between the size distribution of PLGA-chitosan JNP and TCZ-loaded PLGA-chitosan JNP. However, the circularity of TCZ-loaded PLGA-chitosan nanoparticles (Avg.=0.92, Q1/Med./Q3 = 0.90/0.97/1.00) was slightly higher than PLGA-chitosan JNP ($P < 0.05$). The TCZ-loaded PLGA-chitosan nanoparticles possessed higher roundness (Avg.=0.82, Q1/Med./Q3 = 0.74/0.87/0.94), and lower anisotropy (Avg.=1.29, Q1/Med./Q3 = 1.06/1.15/1.35) ($P < 0.0001$). DLS was used to determine the size distribution of collected particles after serial centrifugation to isolate the 360 nm size population (**Figure 7-2G**).

The release profile and immunoreactivity retention of TCZ from JNP were measured by TCZ mAb-based ELISA. The cumulative release over time showed that about 84% of the encapsulated TCZ was released after four days from PLGA-chitosan JNP. Being able to detect the released TCZ from JNP by TCZ mAb-based ELISA confirmed that PLGA-chitosan JNP formulation retained the immunoreactivity of TCZ after being encapsulated into nanoparticles (**Figure 7-2H**).

7.4.3 Human Oral Keratinocytes Readily Internalize Janus Nanoparticles

Confocal microscopy studies confirmed that both premalignant (Epi) and OSCC cell lines readily internalized the fluorescent-labeled PLGA-chitosan JNP (**Figure 7-3A-F**). In addition to the cytosolic location, some particles were observed strongly associated with external cell membranes. These experiments collectively demonstrated a positive correlation between incubation time and particle uptake with highest nanoparticle internalization at 18h. PLGA-chitosan JNP were taken up by both Epi and OSCC cell lines confirmed by colocalization of the fluorescent signals from actin filaments and JNP. The internalization of PLGA-chitosan JNP facilitates the intracellular delivery of TCZ.

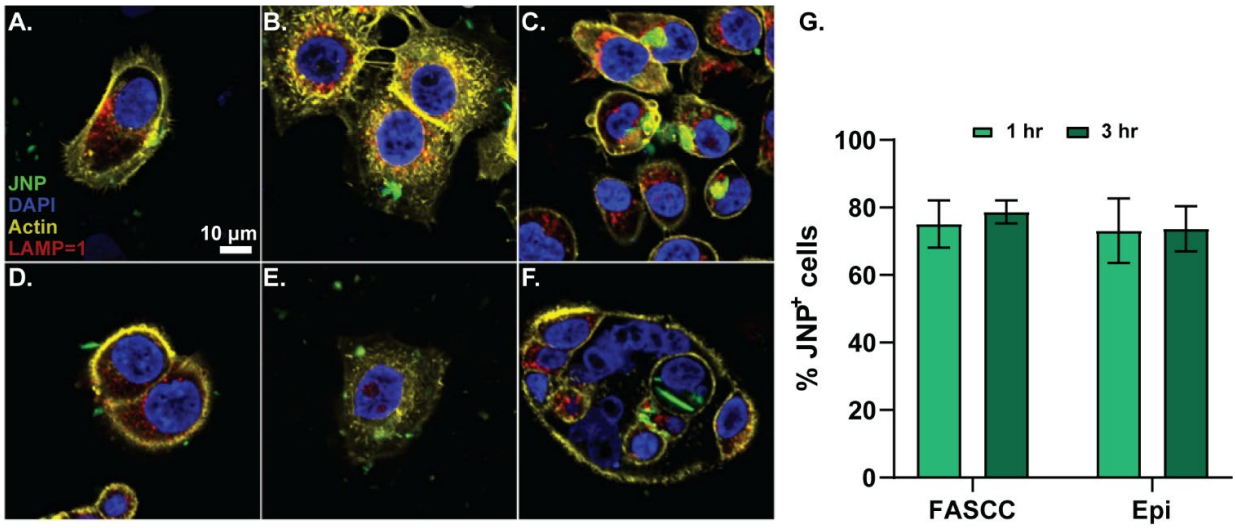

Figure 7-3. Qualitative and quantitative assessment of PLGA-chitosan JNP internalization by STR-validated human monolayer cultured human oral epithelial cell lines. For experiments using confocal microscopy, the cells were seeded at a density of 2.1×10^4 cells per µ-Slide VI0.4. Following complete attachment, the cells were incubated with 1×10^8 nanoparticles per well for (A,D) 1 hour, (B,E) 3 hours, and (C,F)18 hours followed by cell fixation. The uptake of JNP was evaluated in (A-C) E6/E7 transduced human oral keratinocytes, and (D-E) Fanconi Anemia OSCC cells. The fluorescent dyes indicate: Blue – Nucleus; Red – Lysosome; Yellow – Actin; Green – Nanoparticles. (40x oil objective, 4x zoom). **(**G) Quantitative assessment of proportion of cells associated with JNP was conducted by flow cytometry. Cells were seeded at 1.5×10^4 cells/well and incubated with 1 x 10^9 nanoparticles per well for 1 hour and 3 hours.

As prior studies from our labs demonstrated oral keratinocyte phagocytic capacities, these findings were positive, but not surprising.[488] Previous studies showed human oral keratinocytes' phenotypic plasticity encompasses "endotheliod" functions including phagocytosis of acetylated LDL.[488] In addition, proof of concept studies revealed monolayer human oral keratinocytes internalized FluoSphere model nanoparticles (210 nm).[489] Mechanistic studies by Sayedyahossein et al. identified a vital role for integrin-linked kinases, Rac1 activation and actin polymerization during skin keratinocyte phagocytosis.[490] All of these studies recapitulate an established keratinocyte physiologic function i.e., melanosome internalization/transfer from activated melanocytes to basal layer keratinocytes during tanning or reactive oral melanosis.[491]

7.4.4 Fluorescent Activated Cell Sorting Analyses Substantiate Confocal Studies and Demonstrate Janus Nanoparticle Internalization in the Majority of Exposed Keratinocytes

Confocal microscopy suggested that the internalization of PLGA-chitosan JNP by Epi and OSCC cell lines were increased with longer incubation time; however, to measure their uptake more quantitatively and determine the percentage of the cells interacting with nanoparticles, flow cytometry was performed for the 1-hour and 3-hour time points. Although the confocal experiments provided strong evidence regarding keratinocyte-nanoparticle associations, these data were qualitative in nature. The quantifiable, complementary FACS analyses revealed the majority of keratinocytes in both cell lines contained membrane-bound and internalized PLGA-chitosan JNP. The highest particle uptake, which was confirmed to be cell-associated via dual positive fluorescence for NucBlue Live (viable cell nuclei) with the 488 nm fluorophore (labeled PLGA-chitosan JNP) was noted in the Epi cell line (Highest uptake 96.1%). Both FA OSCC and Epi cells showed considerable high uptake (more than 70%) after 1 hour and 3 hours incubation with JNP (**Figure 7-3G)**. Appreciable PLGA-chitosan JNP uptake was noted at the shortest time point; after

a 1-hour incubation, 73% and 75% particle uptake was seen in the Epi and FA OSCC cells, respectively. Furthermore, these results were reproducible, with a variability of less than 18% between two separate experiments conducted with different passages, same cell line, and PLGA-chitosan JNP concentration. As the average unstimulated salivary flow rate varies between 0.3-0.4 mL/minute, rapid uptake of nanoparticles is essential for efficient topical treatment.[492]

These findings contrast with our previous FluoSphere results that showed the highest uptake of 18.4% (relative to U937 cells) in one OSCC cell line occurred at 24 h with no detectable particle uptake after 1 hour.[489] Although both particles were comparably sized, FluoSpheres and the PLGA-chitosan JNP displayed functional groups with both, negative and positive charges, on their respective surfaces. There were also distinct differences in composition, i.e., FluoSpheres (biotin labeled, fluorescein-loaded polystyrene nanoparticles) relative to PLGA-chitosan JNP. Polystyrene-associated cytotoxicity may be at least partially responsible for the observed reduced uptake of the FluoSphere model nanoparticles.[476] In contrast, PLGA nanoparticle encapsulation has been demonstrated to reduce cytotoxicity yet retain therapeutic effectiveness of chemotherapeutic drugs.[493]In addition, our prior studies evaluated only internalized nanoparticles, whereas current assays also included strongly-bound JNP at the membrane given the importance of this cellular location for TCZ's therapeutic action. Finally, as nanoparticle size affects particle uptake, our JNP (average size 360 nm) were likely internalized by a caveolae-mediated endocytosis.[494]

7.4.5 Janus Nanoparticles Demonstrate Surface Epithelial Penetration in Oral Mucosal Explants

Fluorescent-tagged nanoparticle studies revealed 76% of the mucosal explants (13/17) demonstrated particle penetration past the stratum corneum while 41% (7/17) contained

nanoparticles in the basilar third of the epithelium. Some of the explant tissues showed particle penetration into the superficial underlying connective tissue. Control specimens showed no fluorescent particles (**Figure 7-4**). The maximum depth of penetration for every tissue explant, demographics and other variables are reported in **Table 7-1**.

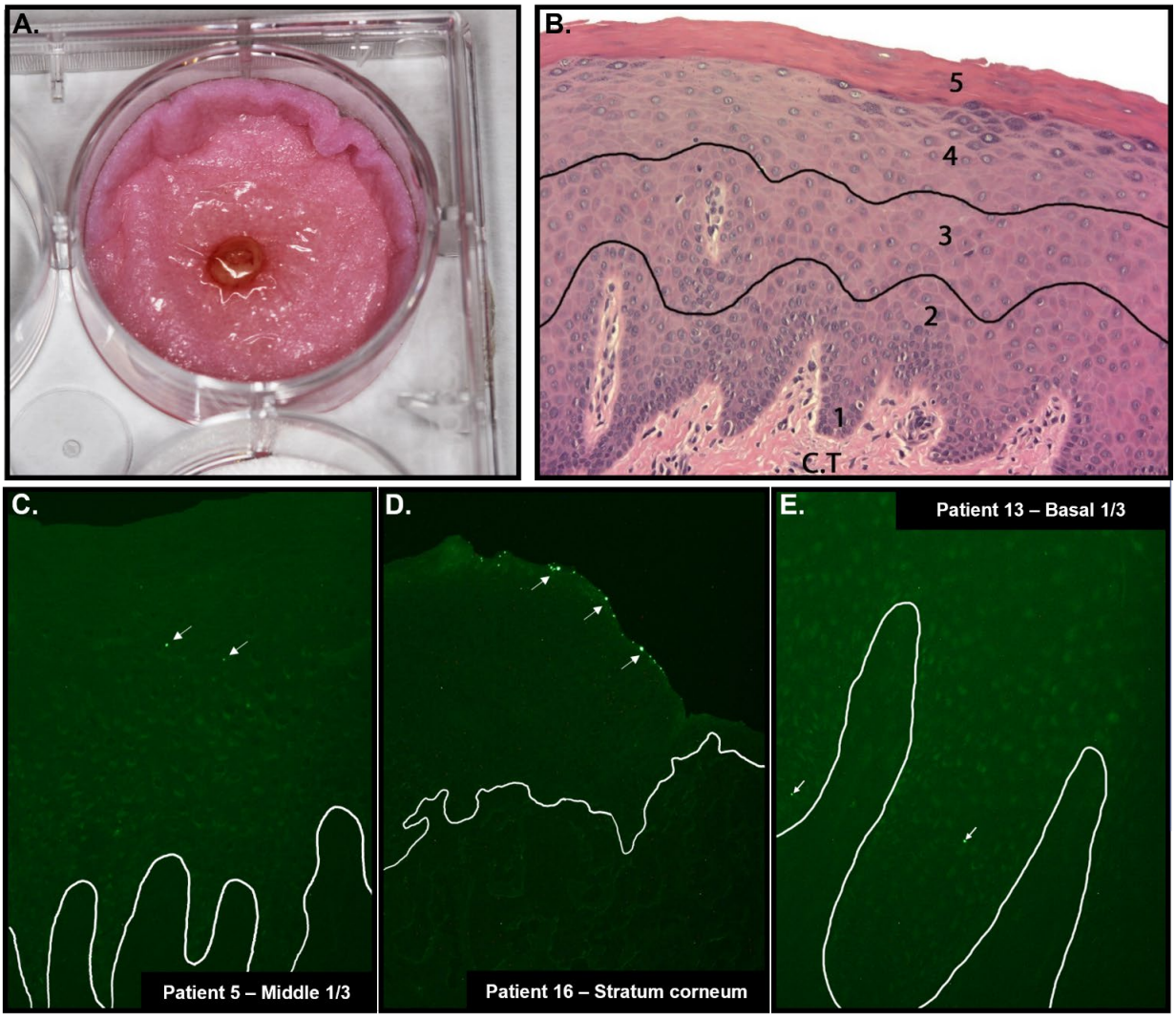

Figure 7-4. Nanoparticle penetration of clinically healthy oral gingival explants. (A) Human oral mucosal explants were obtained in accordance with our IRB approved human subjects protocol from patients undergoing an elective surgical procedure. For these studies, nanoparticle penetration under rigorous circumstances i.e., thick surface keratin was assessed. Depending on the tissue site and patients' social history and habits, keratinization varies throughout the mouth. Human gingiva, however, is routinely keratinized. Dental implant uncovering, which entails removal of the gingiva overlying the implant was the selected surgical procedure. (B) The depiction of the stratification system to assess the JNP penetration depth into the surface epithelium: (1) basal layer, (2) basal 1/3, (3) middle 1/3, (4) superficial 1/3 of the epithelium, and (5) stratum corneum. C.T.= connective tissue. (C-D) The fresh tissue explants were incubated with nanoparticle suspension placed overlying the surface keratin for 3 hours at 37 ºC, 5% CO_2. Immediately after incubation, the tissue explants were snap frozen in OCT medium using isopentane chilled with liquid nitrogen. Frozen sections were obtained on the unfixed tissue samples and the samples were analyzed under fluorescent light (FITC channel) using an Olympus BX51 microscope. Images were captured with the Nikon DS-Fi1 camera. The white arrows highlight some of the nanoparticles in the (C) middle 1/3, (D) stratum corneum, and (E) basal 1/3 of the epithelium whereas the white line shows the epithelium-connective tissue interface.

The keratinized human gingival explants used in these studies presented a nanoparticle delivery challenge. Our data, which demonstrated that JNP effectively migrate through keratinized gingival epithelium, show promise for the nonkeratinized, high OSCC risk sites such as floor of the mouth or ventral tongue. Not all explants showed the same depth of nanoparticle penetration; findings that likely reflect individual differences in transport mechanisms. JNP could have migrated via paracellular transport, which is a passive permeation process that enables small molecules to diffuse between keratinocytes, and/or energy dependent transcytosis.[495,496] Reports have also showed that chitosan can improve paracellular permeation by temporarily disrupting the tight junctions.[497,498] It is therefore probable that nanoparticle optimization combined with in vivo analyses in ATP-replete tissues will enhance nanoparticle transport to the targeted, proliferative epithelial cells.[496]

Table 7-1. Participant demographics, donor site, PLGA-chitosan JNP suspension volume applied to the explant and total nanoparticle quantity, time of incubation and maximum depth of penetration in the epithelium

Specimen	Age / Sex	Ethnicity	Smoking	Alcohol	Donor Site	Volume of suspension	Incubation time	Depth of penetration
1	72 F	Caucasian	Never-smoker	Non-drinker	Anterior maxilla	1 µL (3.79×10^7 NP)	3 h	Superficial 1/3
2	59 F	Caucasian	Never-smoker	Occasional drinker	Posterior right maxilla	1 µL (3.79×10^7 NP)	3 h	Stratum corneum
3a	61 F	African-American	Never-smoker	Occasional drinker	Posterior left maxilla	2 µL (7.58×10^7 NP)	2.5 h	Basal 1/3
3b					Posterior left maxilla	2 µL (7.58×10^7 NP)	2.5 h	Superficial 1/3
4	64 M	Caucasian	Former smoker	Occasional drinker	Posterior right mandible	4 µL (1.52×10^8 NP)	3 h	Basal 1/3
5	67 F	Caucasian	Former smoker	Occasional drinker	Posterior left maxilla	4 µL (1.52×10^8 NP)	3 h	Middle 1/3
6	60 F	Hispanic	Never-smoker	Non-drinker	Posterior left maxilla	2 µL (7.58×10^7 NP)	3 h	Stratum corneum
7	40 M	African-American	Never-smoker	Occasional drinker	Anterior maxilla	3 µL (1.13×10^8 NP)	3 h	Superficial 1/3
8	69 M	African-American	Former smoker	Occasional drinker	Posterior right maxilla	4 µL (1.52×10^8 NP)	3 h	Basal 1/3
9a	32 F	Caucasian	Never-smoker	Non-drinker	Posterior right maxilla	2 µL (7.58×10^7 NP)	3 h	Superficial 1/3
9b					Posterior left maxilla	4 µL (1.52×10^8 NP)		Basal 1/3
10	63 F	Caucasian	Former smoker	Occasional drinker	Anterior maxilla	4 µL (1.52×10^8 NP)	3 h	Basal 1/3
11	22 M	Caucasian	Never-smoker	Occasional drinker	Anterior maxilla	3 µL (1.13×10^8 NP)	3 h	Superficial 1/3
12a	38F	Caucasian	Never-smoker	Occasional drinker	Anterior maxilla	2 µL (7.58×10^7 NP)	3 h	Basal 1/3
12b					Anterior maxilla	2 µL (7.58×10^7 NP)	3 h	Basal 1/3
13	60 M	Caucasian	Never-smoker	Non-drinker	Posterior left maxilla	4 µL (1.52×10^8 NP)	3 h	Stratum corneum
14	84 M	Caucasian	Former smoker	Occasional drinker	Posterior right maxilla	2 µL (7.58×10^7 NP)	3 h	Stratum corneum

7.4.6 Interaction of Tocilizumab Released from Janus Nanoparticles on IL-6R ELISA Binding

Results from the sIL-6Rα ELISA revealed that both pharmaceutical dispensed TCZ and PLGA-chitosan JNP-released TCZ perturbed sIL-6Rα binding and therefore reduced sIL-6Rα detection. At a dose of 1 μg/mL, pharmaceutical dispensed TCZ demonstrated a 55% inhibition, while JNP-released TCZ showed 71% reduction of sIL-6 Rα in the U-937cells media. The IL-6Rα detection in the U-937 cells lysate was also reduced by 42% and 50% at 1 μg/mL of pharmaceutical dispensed TCZ and JNP-released TCZ, respectively (**Figure 7-5**). The observed favorable performance of PLGA-chitosan JNP-released TCZ relative to bolus drug delivery may reflect slight composition differences between the JNP supernatant and pharmaceutically dispensed TCZ. A dose of 1 μg/mL was selected as it is achievable through nanoparticle delivery and it has been shown in vitro to achieve nearly total inhibition of IL-6 binding to sIL-6Rα.[499] Absence of complete inhibition of sIL-6R may reflect binding at a different epitope on the capture antibody than where TCZ binds to sIL-6Rα. In addition, the ELISA capture antibody may overlap partially, but not completely with the TCZ-IL-6Rα complex. This premise is substantiated by preliminary competition assays performed in our lab showing that the maximum dose of TCZ (200 mg/mL) did not completely inhibit binding of the IL-6Rα standard supplied by the company to the capture antibody.

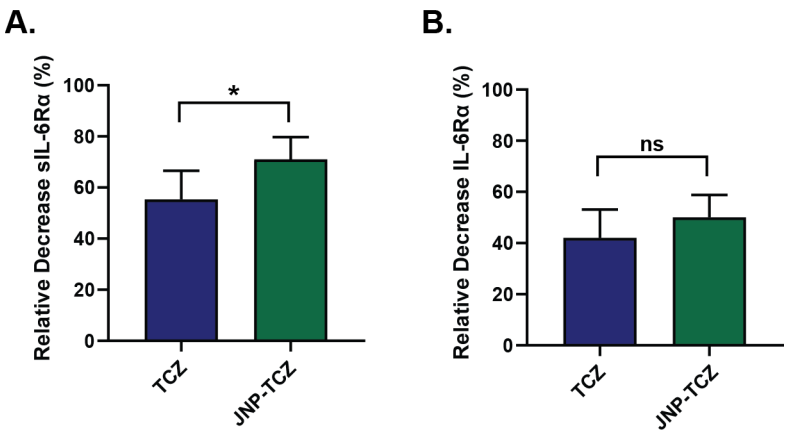

Figure 7-5. ELISA data showing the effects of the TCZ released from PLGA-chitosan JNP and pharmaceutically dispensed TCZ on sIL6R detection in (A) U-937 cells media and (B) U-937 cells lysate. *$P < 0.05$, non-paired, two-tailed t-test.

Average cell viability across assays with U-937 cells for treatment and control groups ranged between 89-94 %. Pharmaceutically dispensed TCZ as well as TCZ released from PLGA-chitosan JNP elicited a statistically significant decrease of sIL-6Rα detected by ELISA after 24h ($p < 0.02$), which confirmed the retention of functional activity of TCZ after encapsulation in PLGA-chitosan JNP.

7.4.7 Janus Nanoparticle-mediated TCZ Delivery Demonstrates Significant OSCC Tumor-Regressive Effects

OSCC tumor regression model was used to assess PLGA-chitosan JNP released TCZ function in vivo (**Figure 7-6A**). Clinical differences that corresponded to the presence/absence of TCZ were apparent in the OSCC tumors (**Figure 7-6B**). Groups that received TCZ were appreciably less erythematous; findings that are commensurate with TCZ's recognized anti-inflammatory properties (**Figure 7-6B**). Only when delivered from JNP did TCZ significantly reduce tumor size (**Figure 7-6C**). Notably, neither the presence of drug-free JNP nor bolus delivered TCZ suppressed tumor volume (**Figure 7-6C**).

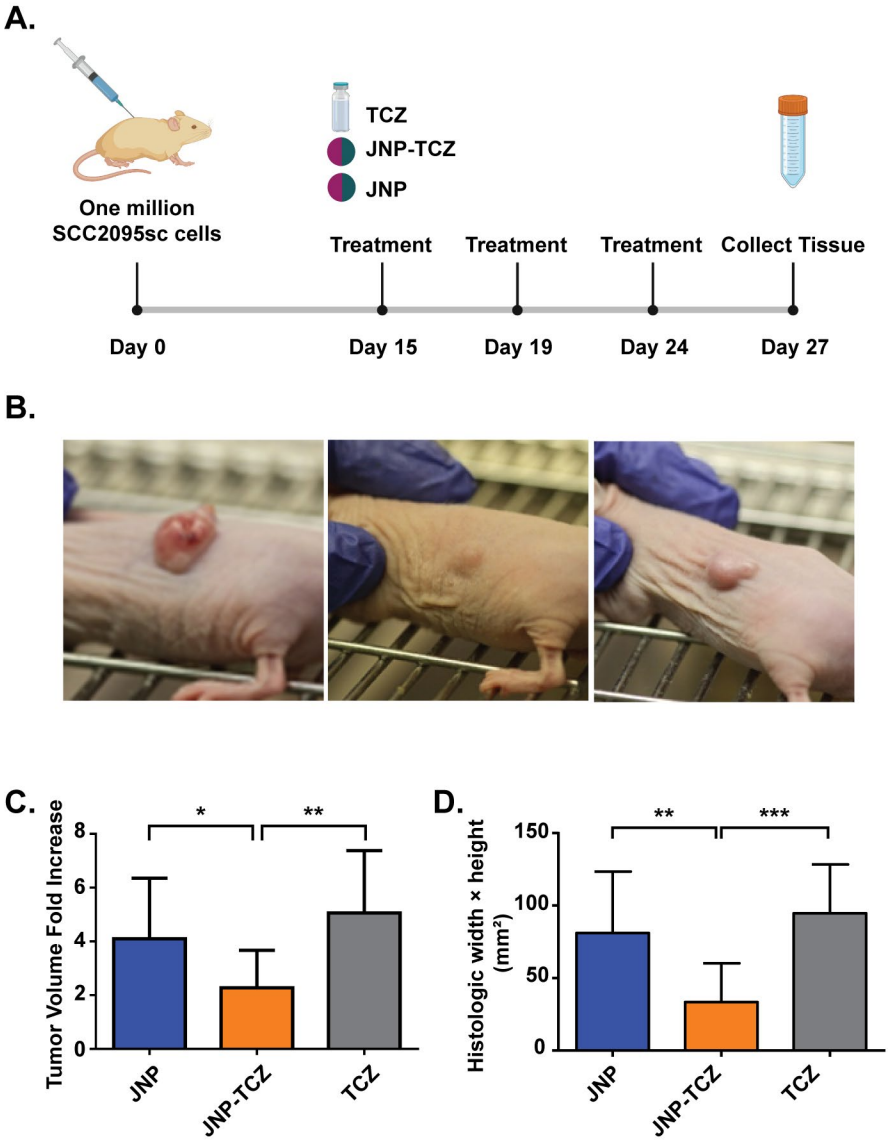

Figure 7-6. Effects of PLGA-chitosan JNP-mediated delivery of TCZ on OSCC tumor induction. (A) One million SCC2095sc cells, a highly tumorigenic oral squamous cell carcinoma (OSCC) cell line, suspended in 100 µL of Matrigel were subcutaneously injected into the flanks of nude mice. Three experimental groups (n=15) tumor injection sites for every group, drug-free JNP control (JNP), bolus TCZ delivery (1.2 µg/100µL TCZ optimized buffer every 4 days), TCZ-loaded JNP (JNP-TCZ) in TCZ optimized buffer (calculated to release 1.2 µg TCZ over 4 days). As per our reported protocol,[482] tumor treatment began at day 15, with the animals sacrificed at day 27. (B-D) Clinical assessment of JNP-TCZ chemopreventive efficacy using an in vivo OSCC tumor regression model. Tumor size (width x length) was assessed with calipers every 3 days. Tumor depth (caliper measurement) was recorded after tumor excision. (B) Differences in the OSCC cell explants tumors were clinically apparent. The tumors that arose in the TCZ-free mice were appreciably more erythematous, multinodular, and often had an ulcerated surface. In contrast, tumors of groups that received TCZ in either delivery format were less erythematous and not ulcerated. (C) Based on previous investigations, untreated tumor explants enter a very rapid growth

phase at approximately day 15 after implantation, at which point we initiated treatment in these studies. Based on the rate of tumor growth findings, comparisons of the effects of JNP and route of TCZ delivery, respectively, were conducted. With regard to the effects of JNP on tumor final size, tumors that arose in JNP-TCZ treated mice were significantly smaller relative to JNP controls. In addition, the route of TCZ delivery had a significant impact as tumors from JNP-TCZ treated mice were significantly smaller relative to bolus TCZ delivery (for JNP n=12, for JNP-TCZ n=11, for TCZ bolus n=13). (E) Microscopic assessment of JNP-TCZ chemopreventive efficacy using an in vivo OSCC tumor regression model. Excised tumors were formalin-fixed for 8 hours, transferred to PBS and then hemisected at the broadest central portion prior to histopathology processing. Microscopic measurements of greatest solid tumor width and height were obtained from hematoxylin and eosin stained tumor central sections. These data reveal that the solid tumor dimensions of the JNP-TCZ mice were significantly smaller relative to tumors in the control JNP and TCZ bolus treated animals (One-way ANOVA followed by Tukey's post hoc test, for JNP n=14, for JNP-TCZ n=11, for TCZ bolus n=12. A few tumors that contained large cystic spaces were not amenable to measurement.) $P < 0.05$ was considered statistically different ($*P < 0.05$, $**P < 0.01$, and $***P < 0.001$). $P > 0.05$ was considered not significant.

For accuracy, clinical measurements were restricted to tumors with discreet margins and a single tumor mass. Light microscopy, however, enabled assessment of all tumors including those not amenable to caliper measurement e.g., deep seated or multifocal. Similar to the clinical findings, microscopic measurements of JNP-TCZ treated tumors were also significantly smaller (**Figure 7-6D**). Interestingly, one of the OSCC tumors in the JNP-TCZ group had undergone regression and did not contain viable tumor tissue during microscopic assessment.

Our data demonstrated that JNP mediated TCZ delivery conveyed a local therapeutic advantage; findings that likely reflect several parameters. While subcutaneously injected TCZ displays an absorption half-life of 2-4 days in patients, dosing levels impact TCZ's elimination.[500] Notably, TCZ follows nonlinear kinetics, with increased dose prolonging the drug half-life. Because the TCZ dose administered to the nude mice was proportionately smaller (~50 fold) relative to the human subcutaneous dose, local drug clearance was likely more rapid. In contrast, due to JNP surface charge and capacity for target cell uptake, encapsulation likely sustained local TCZ levels, preserved drug activity, and augmented efficacy.

These studies employed a highly rigorous tumor-regression model that tested the efficacy of an agent intended for cancer prevention against an established OSCC tumor. It is therefore essential to place these findings in the context of future clinical applications. Even during the most challenging role i.e., tertiary chemoprevention, TCZ's growth and angiogenic inhibitory effects would likely convey greater impact during incipient tumor development.

7.5 Conclusions

Results from this study, which demonstrated TCZ stabilization and controlled release combined with excellent oral keratinocyte nanoparticle uptake and penetration of oral mucosal explants, confirm that engineered, mucoadhesive JNP represent a promising formulation for the local delivery of oral cancer chemopreventives. EHD co-jetting enabled imparting dissimilar properties in one nanocarrier delivery system. As premalignant OIN lesions often possess disruptions to multiple pathways and their microenvironment,[501,502] optimal chemoprevention strategies combine complementary agents for improved efficacy.[501,502] JNP' biphasic geometry, which enables simultaneous delivery of two chemically distinct chemopreventives, is ideal for this multi-agent chemopreventive approach.[147] We have identified a second chemopreventive, fenretinide, which functions in an additive fashion with TCZ.[466,503] Furthermore, incorporation of the JNP into a dispersing formulation such as a rinse would enable field coverage throughout the oral cavity.

Chapter 8
Conclusions and Future Directions

This dissertation describes nanoparticle-based targeted drug delivery platforms to surpass three major biological barriers, namely, (i) the immune system barrier, (ii) the blood-brain barrier, and (iii) the oral mucosal barrier. Synthetic protein-based and biopolymer-based nanoparticles were both engineered using a versatile particle fabrication technology, electrohydrodynamic (EHD) co-jetting for the development of a large toolbox of nanoparticles. In the case of SPNPs, single compartment nanoparticles with single proteins or blend of two or more proteins and multicompartment nanoparticles with independent proteins, each consisting of human serum albumin, bovine serum albumin, ovalbumin, lysozyme, hemoglobin, mucin, insulin, or transferrin has been achieved. The effects of various formulation parameters such as the protein composition, type of functional macromer, protein to macromer ratio, and solvent systems were investigated, ultimately allowing access to tailor-made SPNPs with appropriate physicochemical properties and biological responses suited to cross the desired barrier. Using a similar approach, biopolymer-based bicompartmental PLGA-chitosan nanoparticles were prepared to utilize their differential adhesion behavior to address the oral mucosal barrier. An appropriate nanoparticle-based system was consequently used to address the challenge of circumventing specific biological barriers.

To target the immune system barrier, ovalbumin nanoparticles from protein antigen with macromer to protein antigen ratios from 5 to 50% leading to the formation of nanoparticles from 200-500 nm

in size with elasticities of 40-800 KPa was used. Tuning these key defining parameters of the nanoparticles led to the improvement of immunological responses in terms of dendritic cells uptake, $CD8^+$ T cell activation, draining lymph nodes delivery, and antibody production. The enhanced antigen-specific cellular and humoral immune responses of the OVA SPNPs ultimately enhanced their overall anti-tumor response compared to solute antigen in a murine model of B16F10-OVA melanoma.

In order to cross the blood-brain barrier, the endogenous properties and functionalities of proteins were leveraged to design a suitable nanoparticle-based delivery platform. HSA SPNPs were prepared to exploit albumin capacity to bind to endothelial cell surface receptors such as albumin-binding glycoprotein (gp60) and mediate endothelium transcytosis. Further, to boost the local concentration of nanoparticles at the brain endothelium, RBC-hitchhiking of HSA SPNPs in combination with intracarotid artery injection was employed. This was successfully achieved by the surface modification of HSA SPNPs with IgG, thereby obtaining an enhanced binding to the RBCs without detrimental effects on the carrier cells. The benefits of HSA SPNPs were in addition in synergy with that of the vascular mobility and circulation of RBCs allowing for enhanced uptake of the nanoparticles in the brain. Subsequently, as envisioned, the intracarotid injection of the RBC hitchhiked HSA SPNPs showed 19-fold and 10-fold improvement in their delivery to the brain compared to the free HSA SPNPs in the inflamed and naive models, respectively. Once delivered to the brain via a novel RBC hitchhiking delivery platform, these tailored HSA SPNPs showed improved biodistribution, increased brain uptake with reduced clearance by the reticuloendothelial system. In yet another cellular hitchhiking platform to target the BBB, both polymeric (PS and PMMA) and protein-based (HSA and TF) nanoparticles of sizes 200 and 500 nm were loaded directly into monocytes as the carrier cell to evaluate and compare their uptake and migration

behavior. Although the uptake of SPNPs was lower than PMMA-based nanoparticles, the SPNPs-loaded monocytes showed a superior migration profile. The above results clearly showed that the use of SPNPs that are delivered by a cell-mediated approach to the brain is a versatile platform to be explored to cross the BBB for brain drug delivery.

Developing a novel method to target the oral mucosal barrier, nanoparticles with tailored compartmentalization were designed by EHD co-jetting to develop a drug delivery platform for intraoral field-coverage chemoprevention. Mucoadhesive bicompartmental PLGA-chitosan nanoparticles were designed with dual adhesion characteristics where each compartment leveraged a different mechanism for mucoadhesion. The bicompartmental design of nanoparticles was also foreseen for simultaneous co-delivery of two chemically distinct chemopreventives for further improved efficacy. The 360 nm PLGA-chitosan nanoparticles penetrated through human oral mucosal explants to the targeted basal cell epithelial layer and maintained the immunoreactivity and functional activity of the encapsulated biological chemopreventive agent tocilizumab. Bicompartmental nanoparticle-mediated delivery of tocilizumab conveyed a local therapeutic advantage as demonstrated by its significant oral squamous cell carcinoma tumor-regressive effects compared to that of bolus injections.

In conclusion, a rational combination of an engineered nanoparticle and a suitable delivery platform is needed to surpass organ-specific biological barriers to achieve an optimum delivery of therapeutics. Protein nanoparticles, multicompartmental nanoparticles, and cellular hitchhiking platforms are among the emerging trends in the field of nanomedicine to address the persisting targeted drug delivery challenges. Potential applications of these engineered nanoparticles can include immunotherapeutics, gene- and cell-based therapies, and dose-controlled delivery *via* the

tailoring formulation-function-response relationships. In the following sections, selected extensions of this dissertation research and specific outlooks are discussed briefly.

8.1 Toward Neutrophil-mediated Lung Targeting of SPNPs[4]

Acute lung inflammation is associated with severe morbidity, as seen in COVID-19 patients. Acute alveolar inflammation causes the clinical syndrome known as acute respiratory distress syndrome (ARDS), in which inflammation prevents the lungs from oxygenating the blood. Lung inflammation is accompanied or led by massive accumulation of neutrophils in pulmonary capillaries ("margination"). Neutrophils are "first responder" cells in acute inflammation, rapidly adhering and activating in large numbers in inflamed vessels and forming populations of "marginated" neutrophils along the vascular lumen.[504–510] Neutrophils can be activated by a variety of initiating factors, including pathogen- and damage-associated molecular patterns such as bacterial lipopolysaccharides (LPS).[511,512] After acute inflammatory insults, neutrophils marginate in most organs, but by far most avidly in the lung capillaries.[508,509,513–515] Targeted nanoparticle delivery to marginated neutrophils could provide an ARDS treatment with minimal side effects, but specific delivery to marginated neutrophils remains an open challenge. Antibodies against markers such as Ly6G have achieved targeting to neutrophils in mice, but also deplete

[4] The materials in this chapter has been adapted with minor modifications from the following articles:
Jacob W. Myerson*, Priyal N. Patel*, Nahal Habibi, Landis R. Walsh, Yi-Wei Lee, David C. Luther, Laura T. Ferguson, Michael H. Zaleski, Marco E. Zamora, Oscar A. Marcos-Contreras, Patrick M. Glassman, Ian Johnston, Elizabeth D. Hood, Tea Shuvaeva, Jason V. Gregory, Raisa Y. Kiseleva, Jia Nong, Kathryn M. Rubey, Colin F. Greineder, Samir Mitragotri, George S. Worthen, Vincent M. Rotello, Joerg Lahann, Vladimir R. Muzykantov, Jacob S. Brenner. Supramolecular Organization Predicts Protein Nanoparticle Delivery to Neutrophils for Acute Lung Inflammation Diagnosis and Treatment. *bioRxiv* **2020**, 2020.04.15.037564.
Jacob W. Myerson*, Priyal N. Patel*, Kathryn M. Rubey*, Marco E. Zamora, Michael H. Zaleski, Nahal Habibi, Landis R. Walsh, Yi-Wei Lee, David C. Luther, Laura T. Ferguson, Oscar A. Marcos-Contreras, Patrick M. Glassman, Liudmila L. Mazaleuskaya, Ian Johnston, Elizabeth D. Hood, Tea Shuvaeva, Jichuan Wu, Hong-Ying Zhang, Jason V. Gregory, Raisa Y. Kiseleva, Jia Nong, Tilo Grosser, Colin F. Greineder, Samir Mitragotri, George S. Worthen, Vincent M. Rotello, Joerg Lahann, Vladimir R. Muzykantov, Jacob S. Brenner. Supramolecular Organization Predicts Protein Nanoparticle Delivery to Neutrophils for Acute Lung Inflammation Diagnosis and Treatment. *Nature Nanotechnology* **2020,** accepted.

populations of circulating neutrophil.[516–519] Additionally, while Ly6G readily marks neutrophils in mice, there is no analogous specific and ubiquitous marker on human neutrophils.[516] Therefore, antibody targeting strategies have not been widely adopted for targeted drug delivery to these cells.[518] As another route to neutrophil targeting, two previous studies noted that activated neutrophils take up denatured and agglutinated bovine albumin.[520,521] Nanoparticle structural properties such as shape, size, and deformability can define unique targeting behaviors.[240,522–525] In collaboration with Professor Vladimir Muzykantov at the University of Pennsylvania, a diverse panel of nanoparticles was screened to determine the nanostructural properties that predict uptake in pulmonary marginated neutrophils during acute inflammation and therefore to target severely inflamed lungs. A library of nanoparticles was designed and an in vivo screen of biodistributions in naive mice and mice treated with lipopolysaccharides (LPS) was conducted. Bovine serum albumin (BSA), human serum albumin (HSA), chicken lysozyme, human transferrin, and human hemoglobin SPNPs were prepared by EHD jetting process as described in **Chapter 2** and **Chapter 3**. Briefly, protein solutions were prepared by dissolving the protein of interest at a 7.5% (w/v) concentration in a solvent mixture of ultrapure water and ethylene glycol with 4:1 (v/v) ratio. The homo-bifunctional amine-reactive crosslinker, O,O′-bis[2-(N-succinimidyl-succinylamino)ethyl]polyethylene glycol with molecular weight of 2kDa was mixed with the protein solution at 10% ($w/w_{protein}$). Protein nanoparticles were kept at 37°C for 7 days for completion of the crosslinking reaction. The as-prepared protein nanoparticles were collected in PBS buffer and their size distribution was analyzed using dynamic light scatting (**Figure 8-1**).

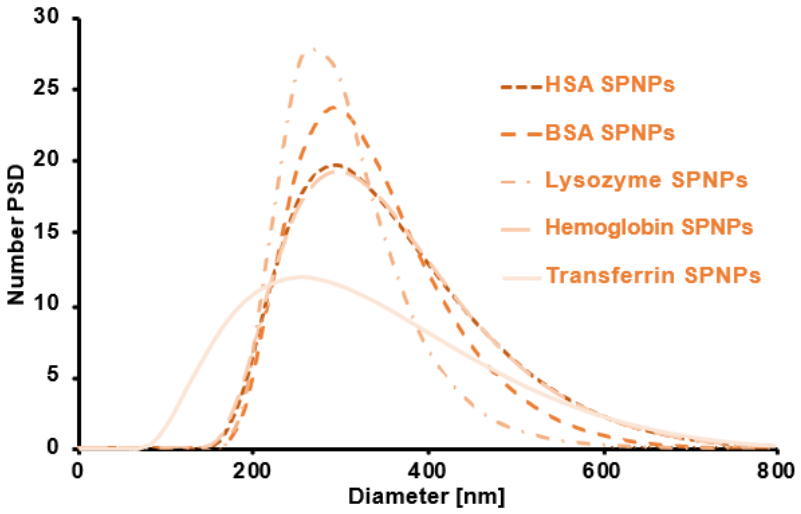

Crosslinked Protein Nanoparticles		
	Diameter	**PDI**
HSA SPNPs	318 ± 4 nm	0.14 ± 0.05
BSA SPNPs	317 ± 38 nm	0.17 ± 0.04
Lysozyme SPNPs	299 ±12 nm	0.06 ± 0.01
Hemoglobin SPNPs	328 ±16 nm	0.08 ± 0.01
Transferrin SPNPs	345 ±10 nm	0.12 ± 0.01

Figure 8-1. Dynamic light scattering characterization of SPNPs.

In order to identify nanostructural parameters that correlate with nanoparticle uptake in inflamed lungs, Professor Muzykantov's group conducted an in vivo screen of the library of nanoparticles. The screen was based on the developed procedure to inject radiolabeled nanoparticles into mice and measure their biodistributions, comparing pulmonary nanoparticle uptake in naïve and LPS-inflamed mice.

HSA SPNPs (317.8±3.6 nm diameter, 0.14±0.05 PDI, **Figure 8-1**) were administered in naïve and IV-LPS-injured mice. Neither SPNPs was functionalized with antibodies or other affinity tags. The protein component of each SPNPs was labeled with ^{125}I for tracing in biodistributions and assessed 30 minutes after IV administration of SPNPs. Specificity for LPS-injured lungs was recapitulated with HSA SPNPs. HSA SPNPs accumulated in naïve lungs at 6.34% injected dose

per gram organ weight (%ID/g), and in LPS-injured lungs at 87.62 %ID/g, accounting for a 14-fold increase in lung uptake after intravenous LPS insult (**Figure 8-2**).

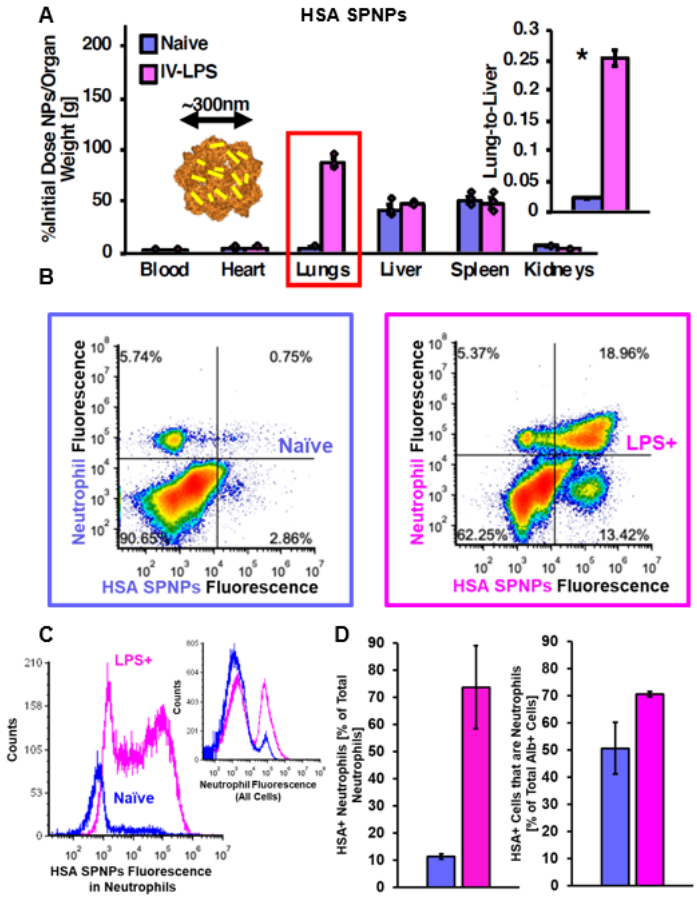

Figure 8-2. HSA SPNPs accumulate in marginated neutrophils in inflamed lungs. (A) Biodistributions of HSA SPNPs in naïve (n=3) and IV-LPS-injured (n=3) mice (red box = $P < 0.001$, * = $P < 0.01$). (B-D) Flow cytometric characterization of single cell suspensions prepared from naïve and IV-LPS-injured injured mouse lungs. (B) Vertical axis indicates Ly6G staining (APC signal) and horizontal axis indicates signal from fluorescent HSA SPNPs. (C) HSA SPNPs fluorescent signal from neutrophils in IV-LPS-injured mouse lungs (red/pink), compared to naïve lungs (blue) (inset: Flow cytometry data verifying increased neutrophil concentration in IV-LPS-injured mouse lungs (red/pink). (D) Fraction of neutrophils positive for HSA SPNPs in naïve (blue, n=3) or IV-LPS-injured (red/pink, n=3) lungs and fraction of HSA SPNPs-positive (pink, D) cells that are neutrophils (* = $P < 0.01$).

Single cell suspensions were prepared from lungs after administration of fluorescent HSA SPNPs. Flow cytometric analysis of cells prepared from lungs after nanoparticle administration enabled identification of cell types with which nanoparticles associated. Firstly, the total number of cells containing HSA SPNPs increased between naïve and LPS-injured lungs. In naïve control lungs, 4.4% of cells were positive for albumin NPs. In LPS-injured lungs, 31.3% of cells were positive for HSA SPNPs (**Figure 8-3A** and **Figure 8-3B**).

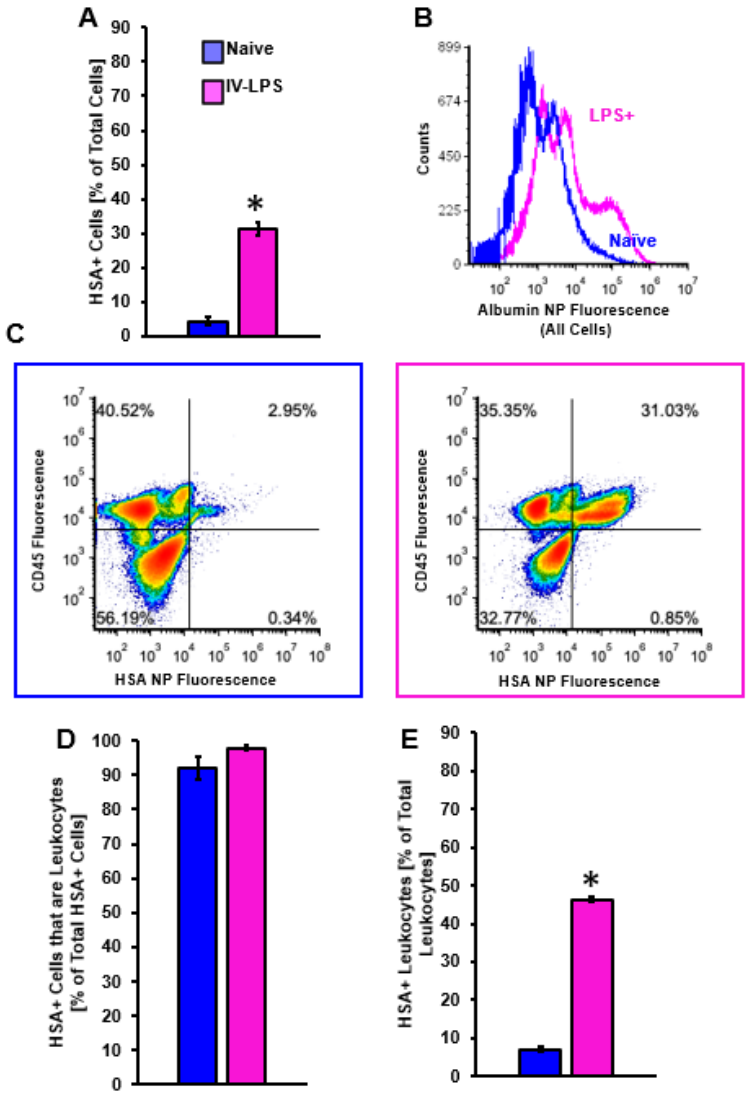

Figure 8-3. Flow cytometric characterization of HSA SPNPs uptake in leukocytes in naïve and inflamed lungs. (A) Fluorescence from Alexa Fluor 488-labeled HSA SPNPs was measured in single cell suspensions prepared from mouse lungs harvested after 30 minutes nanoparticle circulation. With gates set as depicted in **Figure 8-2B**, the number of cells positive for HSA SPNPs fluorescence increased between naïve and LPS-challenged lungs. (B) A population of high-fluorescence cells was detected in IV LPS-challenged lungs, but not naïve lungs. (C) Fluorescence generated by CD45 staining, distinguishing leukocytes in single cell suspensions, plotted against HSA SPNPs fluorescence in single cell suspensions prepared from naïve and IV LPS-challenged lungs. (D) With gates set by the quadrants delineated in (C), correlation between nanoparticle fluorescence and CD45 staining indicated the percentage of HSA SPNPs bearing cells that were leukocytes as >90% in both naïve and IV LPS-challenged lungs. (E) Similar analysis indicated that the fraction of leukocytes containing HSA SPNPs increased in LPS-challenged vs. naïve lungs (* = $P < 0.01$).

Ly6G stain for neutrophils indicated that the bulk of HSA SPNPs accumulation in LPS-injured lungs could be accounted for by uptake in neutrophils. In **Figure 8-2B**, counts above the horizontal threshold indicate neutrophils and counts to the right of the vertical threshold indicate cells containing HSA SPNPs. In IV-LPS-injured lungs, HSA SPNPs uptake was dominated by neutrophils (**Figure 8-2B**, upper right quadrants indicate nanoparticle-positive neutrophils). In LPS-injured lungs, the majority of neutrophils, 73.7% of cells, contained significant quantities of HSA SPNPs, compared to 11.4% in naïve lungs. Likewise, the majority of nanoparticle uptake in the lungs (70.6%) was accounted for by nanoparticle uptake in neutrophils(**Figure 8-2C** and **Figure 8-2D**).

For HSA SPNPs uptake not accounted for by neutrophils, CD45 staining indicated that the remaining nanoparticle uptake was attributable to other leukocytes. Co-localization of HSA SPNPs fluorescence with CD45 stain showed that 91.9% of HSA SPNPs uptake was localized to leukocytes in naïve lungs and 97.8% of HSA SPNPs uptake was localized to leukocytes in injured lungs (**Figure 8-3C** and **Figure 8-3D**).

Previous work has indicated that nanoparticles based on denatured albumin accumulate in neutrophils in inflamed lungs and at sites of acute vascular injury, whereas nanoparticles coated with native albumin do not.[520,521] Muzykantov group characterized HSA SPNPs with circular dichroism (CD) spectroscopy to compare secondary structure of proteins in the nanoparticles to secondary structure of the native component proteins **(Figure 8-4A)**. Identical CD spectra were recorded for HSA SPNPs vs. free HSA. Deconvolution of the CD spectra via neural network algorithm trained against a library of CD spectra for known structures verified that secondary structure composition of HSA was unchanged by incorporation of the proteins in the SPNPs.[526]

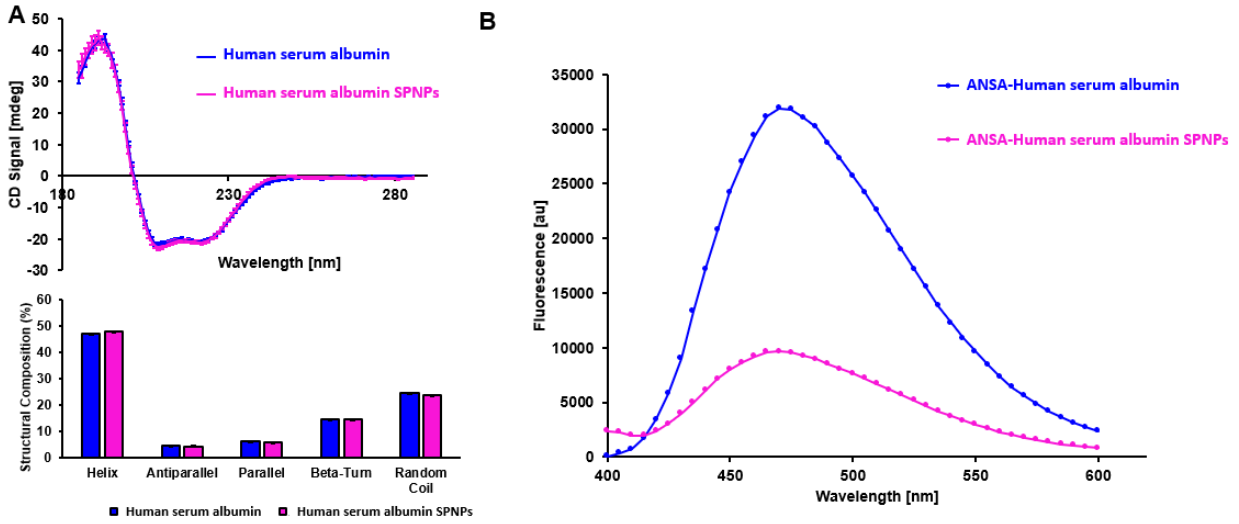

Figure 8-4. Circular dichroism spectroscopic characterization of protein secondary structure and ANSA characterization of hydrophobic domain accessibility for HSA SPNPs. (A) Circular dichroism spectra for HSA SPNPs and free HSA, with free HSA concentration set to match the concentration of HSA in the SPNPs. Inset: neural network deconvolution of CD spectra indicating no differences in secondary structure composition between isolated HSA and HSA in SPNPs. (B) 8-anilino-1-naphthalenesulfonic acid (ANSA) staining of HSA SPNPs and free HSA. Reduced ANSA fluorescence indicates lesser accessibility of hydrophobic domains in the SPNPs, compared to free HSA.

Free protein and SPNPs were also probed with 8-anilino-1-naphthalenesulfonic acid (ANSA), previously established as a tool for determining the extent to which hydrophobic domains are exposed on proteins.[527] Consistent with known structures of the two proteins, ANSA staining indicated substantial hydrophobic exposure on HSA (**Figure 8-4B**). HSA SPNPs had reduced hydrophobic accessibility compared with native HSA. Therefore, our data indicated that HSA was not denatured in HSA SPNPs, but the SPNPs presented a balance of hydrophobic and hydrophilic surfaces differing from the native proteins.

Expanding on data with HSA SPNPs, we varied the protein composition of SPNPs. BSA SPNPs (317.3±38.5 nm, PDI 0.17±0.04), human hemoglobin SPNPs (328.1±16.1 nm, PDI 0.08±0.01), human transferrin SPNPs (345.2±10.2 nm, PDI 0.12±0.004), and chicken lysozyme SPNPs

(298.6±12.4 nm, PDI 0.06±0.01) were traced in naïve and IV LPS-injured mice (**Figure 8-1** and **Figure 8-5**). With the exception of lysozyme SPNPs, all of the tested formulations had clear specificity for acutely inflamed lungs over naïve lungs. Lysozyme SPNPs accumulated in naïve lungs at a uniquely high concentration of 137.47 %ID/g, compared to 170.92 %ID/g in inflamed lungs. Degree of uptake in injured lungs, along with injured vs. naïve contrast, did vary with SPNPs composition. However, acute inflammatory injury resulted in a minimum three-fold increase in lung uptake for all examined SPNPs, excluding lysozyme SPNPs, which still accumulated in injured lungs at a high concentration (25.64% of initial dose).

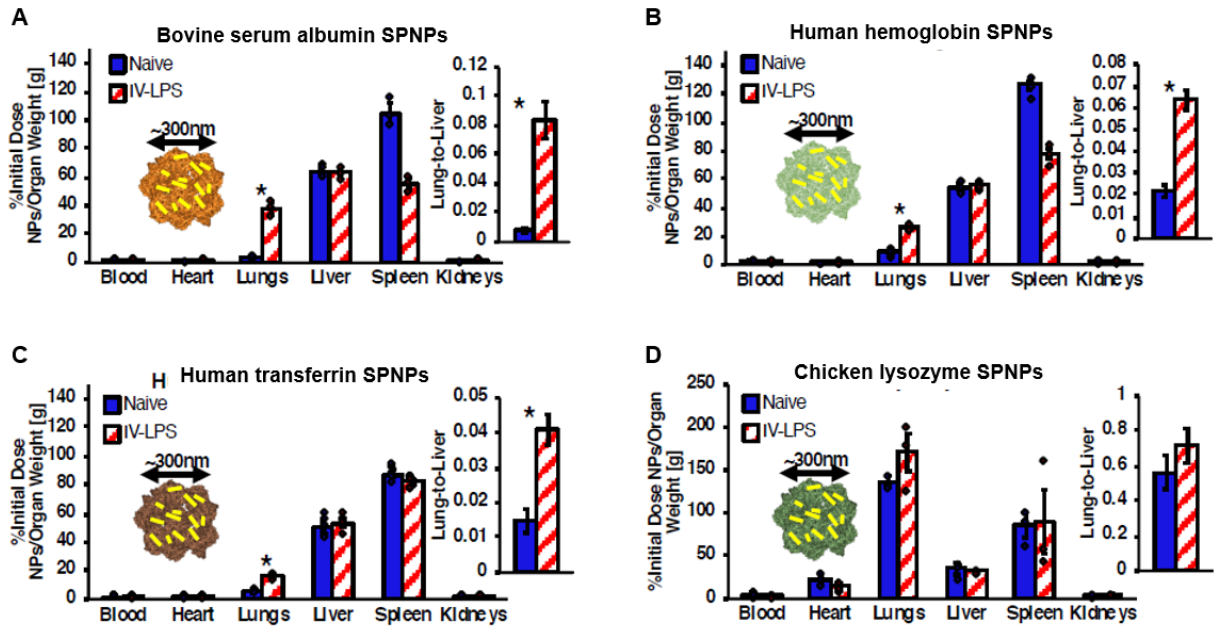

Figure 8-5. Biodistributions of compositional variants of SPNPs s in naïve and IV-LPS-injured mice. Different SPNPs were traced in naïve and intravenous LPS-challenged mice. LPS treatment enhanced pulmonary nanoparticle uptake for all SPNPs variants, except for lysozyme SPNPs. For lysozyme SPNPs, uptake in both injured and naïve lungs exceeded 20% of initial dose (* = $P <$ 0.001).

Muzykantov group employed adeno-associated virus, adenovirus, and horse spleen ferritin nanocages as examples of protein-based nanoparticles with highly symmetrical structure.[528–530] The ratios of lung uptake in LPS-challenged to naïve mice were 0.80, 1.01, and 1.15 respectively, for adeno-associated virus, adenovirus, and horse spleen ferritin nanocages indicating no enhancement of lung uptake following injury. For each of these highly ordered protein nanoparticles, IV LPS injury had no significant effect on biodistribution and levels of uptake in the injured lungs were minimal (<10 %ID/g). Therefore, highly ordered protein nanoparticles traced in our studies did not have tropism for the lungs after acute inflammatory injury.

In contrast to SPNPs, three particles (adenovirus, AAVs, and ferritin) characterized by highly symmetric arrangement of protein subunits into a protein superstructure[528–530] did not accumulate in the inflamed neutrophil-rich lungs. These three particles have evolved structures that lead to prolonged circulation or evasion of innate immunity in mammals.[531–534] It is conceivable that neutrophils more effectively recognize less patterned and more variable protein arrangements that may better parallel the wide variety of structures presented by the staggering diversity of microbes against which neutrophils defend.[515,535]

In conclusion, supramolecular organization in nanoparticle structure predicts nanoparticle uptake in pulmonary marginated neutrophils during acute inflammation. Specifically, nanoparticles with agglutinated protein (e.g., SPNPs) accumulate in marginated neutrophils, while protein nanoparticles with symmetric structure (e.g., viral capsids) were ignored by pulmonary neutrophils and had biodistributions unaffected by LPS injury. This work demonstrates that structure-dependent interactions with neutrophils can dramatically alter the biodistribution of nanoparticles, highlighting their significant potential in detecting and treating respiratory conditions arising from injury or infections. Future work may more deeply explore therapeutic effects of nanoparticles

with agglutinated protein in ARDS and other diseases in which neutrophils play key roles. This study also obviates future testing of supramolecular organization as a variable in in vivo behavior of nanoparticles, including screens of tropism for other pathologies and cell types. These studies could in turn guide engineering of new particles with intrinsic cell tropisms. These "targeting" behaviors, requiring no affinity moieties, may apply to a wide variety of nanomaterials. But our current findings with neutrophil tropism indicate that many protein-based and protein-coated nanoparticles could be untapped resources for treatment and diagnosis of devastating inflammatory disorders like ARDS.

8.2 Toward Exploiting Red Blood Cell-hitchhiking and Bicompartmental Nanoparticles for Lung Targeting

Lung cancer is the second most prevalent cancer and the leading cause of cancer death.[457,536] According to the National Cancer Institute, the most common site of metastasis for various primary cancers is the lung as it possesses a high vascular density.[537] This highlights the need for engineering optimal drug delivery platforms targeted to the lungs. While delivery of traditional nanoparticles to the target tissue is limited due to the series of biological barriers, including rapid clearance from circulation by the reticuloendothelial system, red blood cell (RBC) hitchhiking offers remarkable advantages for lung targeting of nanoparticles.[538–540]As elaborated in **Chapter 5**, RBCs, which naturally evolved to deliver cargo (oxygen and carbon dioxide) in the bloodstream, represent a nearly ideal carrier of nanoparticles for drug delivery within the vascular system.[6,153] The binding of nanoparticles to RBCs is considered the foundation of hitchhiking. Adhesion of nanoparticles to RBCs appears to be driven by a surface-wetting-like process where the extent of membrane spreading is determined by adhesion interactions.[153,541] Therefore, nanoparticles that bind well to RBCs generally tend to perform better in terms of extended circulation lifetime and

alterations in biodistributions.[153,541] The nanoparticles can leverage different mechanisms to bind to RBCs such as nonspecific binding (electrostatic, hydrogen bonding, van der Waals, and hydrophobic forces), or specific binding (ligand-receptor interactions or chemical conjugations).[6] However, simultaneous utilization of two different adhesion mechanisms in the nanoparticle design is hard-to-achieve by traditional nanoparticle systems. EHD co-jetting technique allows for engineering multicompartmental nanoparticles with dissimilar and orthogonal properties.[127,140] To leverage both electrostatic and hydrophobic interactions in the same nanoparticle system for binding to RBCs, bicompartmental PLGA-chitosan nanoparticles with a mostly similar design to nanoparticles described in **Chapter 7,** were exploited. The PLGA compartment interacts with RBCs through hydrophobic interactions, where the chitosan compartment binds through electrostatic interactions.

The next crucial step in the RBC-mediated delivery of nanoparticles is the transfer of nanoparticles to the vascular cells. When RBC-hitchhiked nanoparticles squeeze through capillaries, due to cell-cell interactions and shear forces, nanoparticles detach from RBCs and are deposited to vascular endothelium. The hemodynamic factors and the architecture of lung capillaries, as the first microvascular bed encountered by RBC-hitchhiked nanoparticles after intravenous injection, lead to high uptake of nanoparticles in the lungs.[542] Regarding the transfer of nanoparticles from RBCs to lung vasculature, PLGA-chitosan Janus nanoparticles (JNP) present yet another advantage in RBC-mediated lung targeting; the positively charged chitosan compartment can facilitate binding to the negatively charged glycocalyx of the endothelium to boost the transfer of nanoparticles from RBCs and enhance the lung deposition of nanoparticles.

Similar to the bicompartmental particles developed in **Chapter 7**, here PLGA-chitosan JNP were fabricated with the first compartment composed of 1.3% (w/v), 5:2 (w/w) glycol chitosan:

poly(ethylene glycol) diglycidyl ether in 1:1 v/v% ultrapure water: Ethylene glycol and the second compartment composed of 1% (w/v) PLGA in dimethylformamide. Acid-terminated PLGA (lactide:glycolide 50:50, 38-54 kg/mol) was used to allow for further surface modifications such as conjugation of lung targeting antibodies[543] to further enhance the lung uptake of nanoparticles. As shown in **Figure 8-6**, the fabricated PLGA-chitosan JNP had an average diameter of 294 nm (Q1/Med./Q3 = 165/265/375) with PDI_{SEM} of 0.232, high circularity (Avg.=0.91, Q1/Med./Q3 = 0.89/0.95/1.00), relatively low anisotropy (Avg.=1.34, Q1/Med./Q3 = 1.10/1.21/1.44), and relatively high roundness (Avg.=0.79, Q1/Med./Q3 = 0.69/0.82/0.91) based on SEM analysis of as-jetted dry particles. Once fully hydrated, the PLGA-chitosan JNP possessed an average diameter of 360 nm based on the size distribution as measured by DLS. The nanoparticles had an average zeta potential of -5.5 mV.

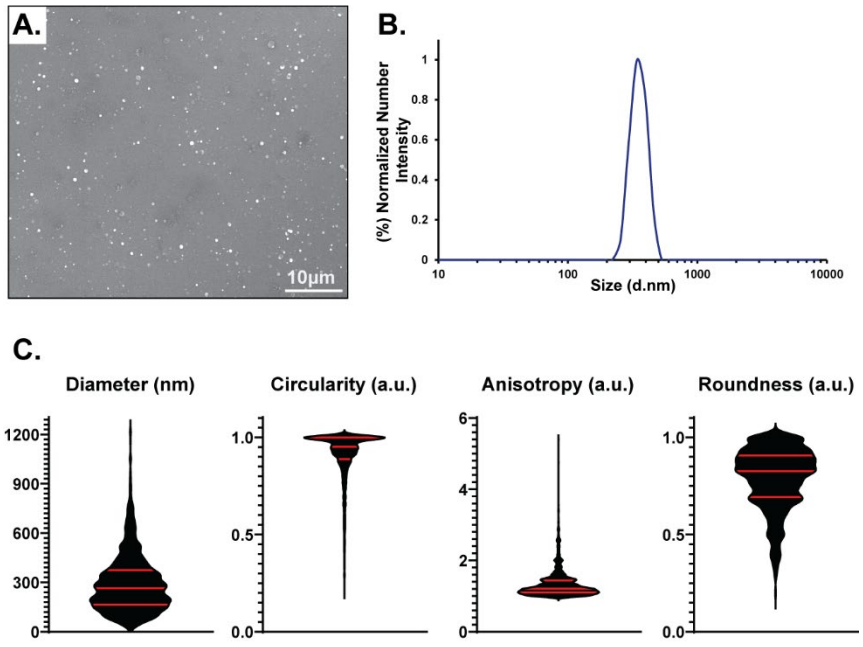

Figure 8-6. Characterization of bicompartmental PLGA-chitosan JNP. (A) SEM image of PLGA-chitosan JNP. Scale bar is 10 µm. (B) DLS size distribution of PLGA-chitosan JNP. (C) Key geometric factor analysis of PLGA-chitosan JNP based on their SEM images.

To bind PLGA-chitosan JNP to RBCs, as described in **Chapter 5**, whole blood from BALB/c male mice was collected in EDTA coated tubes and centrifuged to remove plasma as well as platelets and white blood cells. Isolated erythrocytes (RBCs) were extensively washed three times with Dulbecco's phosphate-buffered saline (DPBS) three times. Fluorescently labeled PLGA-chitosan JNP were briefly sonicated and then incubated with murine RBCs at RBC:JNP ratios of 1:5, 1:10, 1:25, and 1:200 for 1 hour under constant rotation at room temperature in DPBS or 55% murine serum. Nanoparticles were washed with ice-cold DPBS three times to remove unattached PLGA-chitosan JNP prior to experiments. The RBC-hitchhiked PLGA-chitosan JNP were then analyzed using flow cytometry to confirm their binding. As shown in **Figure 8-7A**, without any further surface modification, at RBC:JNP ratios of 1:5, 1:10, 1:25, and 1:200, 22%, 25%, 21%, and 15% of RBCs were associated with PLGA-chitosan JNP, respectively. The percentages of RBCs associated with PLGA-chitosan JNP at different RBC:JNP ratios were not statistically significant different. As the next step, to characterize the effects of PLGA-chitosan JNP on RBCs, agglutination, phosphatidylserine exposure, and osmotic fragility assays were conducted. Briefly, the agglutination assay was performed on freshly obtained RBCs. RBCs and RBCs-JNP suspensions (at 1% hematocrit) were dispensed into 96-well U-bottom plates and visually accessed for agglutination after 2 hours at room temperature after RBC and RBCs-JNP suspension had fully sedimented. Carboxylated polystyrene beads were used as a positive control. As shown in **Figure 8-7B**, the binding of PLGA-chitosan JNP onto RBCs did not induce agglutination even at higher RBC:JNP ratios of 1:200. To further investigate whether the binding of PLGA-chitosan JNP onto RBCs induced mechanisms of RBC removal, the amount of phosphatidylserine on the surface of RBCs was investigated. The exposure of phosphatidylserine serves as a signal for eryptosis and removal from blood circulation.[381,382] To perform phosphatidylserine exposure assay, washed

naive RBCs and RBCs-JNP suspensions at 10% hematocrit were incubated at room temperature with fluorescent annexin V Alexa Fluor 488 in buffer containing 2mM $CaCl_2$ for 15 min. After incubation, they were analyzed for the exposure of phosphatidylserine using flow cytometry. Carboxylated polystyrene beads were used as a control. **Figure 8-7C** shows that the PLGA-chitosan JNP did not cause phosphatidylserine exposure on RBCs even at the highest RBC:JNP ratio. The percentage of RBCs expressing phosphatidylserine after PLGA-chitosan JNP at various RBC:JNP ratios were very comparable to naïve RBCs. To determine whether adsorption of PLGA-chitosan JNP onto RBCs induces RBCs sensitivity, osmotic fragility assay was performed on freshly obtained RBCs and RBCs-JNP suspensions (**Figure 8-7D**). Briefly, isolated RBC and RBCs-JNP suspensions were placed in various salt concentrations, from 0 mM to 150 mM at 37°C, at a final concentration of 1% hematocrit. Suspensions were immediately centrifuged, and absorbance of supernatant was read at 540mm by plate reader. RBCs suspension in water was used as 100% lysis. Hemolysis curves as a function of concentration of NaCl are shown in (**Figure 8-7D**); Left or right shifts of the curves indicate increase and decrease in RBCs sensitivity/stability, respectively. Binding of PLGA-chitosan JNP to RBCs at a higher loading ratio of 1:200 (RBC:JNP) slightly aggravated hemolysis at a final hematocrit of 1% under normal isotonic conditions. Unlike other nanoparticles such as lysozyme- dextran nanogels which did not cause any detectable lysis[381] or nanoparticles such as carboxylated polystyrene nanoparticles that induced lysis,[381,382] the adsorption of PLGA-chitosan JNP seemed to make the RBCs more resistant to lysis in hypotonic NaCl solutions (from ~75 to 30mM NaCl). This resistance might be due that PLGA-chitosan JNP bound onto RBCs stronger compared to the other nanoparticles. Noteworthy, the levels of hemolysis at isotonic solutions compared to naïve RBCs would probably be lower at other loading ratios of PLGA-chitosan JNP lower than 1:200 (e.g., 1:25, RBC:JNP).

Furthermore, adverse changes in RBCs such as increased sensitivity may result from their isolation at 1% hematocrit concentration (compared to ~45% as normal hematocrit level) and presence of serum and plasma.

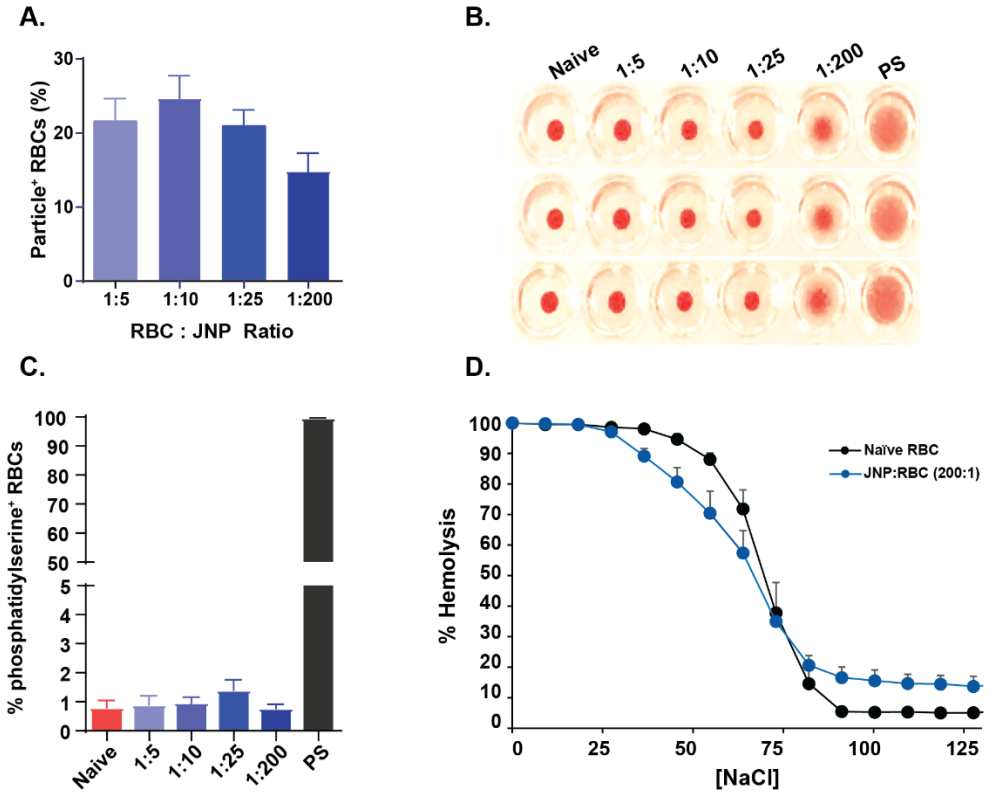

Figure 8-7. Binding of PLGA-chitosan JNP onto RBCs at various RBC:JNP ratios and characterization of their effects on RBCs. (A) Percentage of RBCs associated with PLGA-chitosan particles at RBC:JNP ratios of 1:5, 1:10, 1:25, 1:200. Assessment of potential adverse and sensitizing effects of the surface adsorbed PLGA-chitosan JNP on RBCs. (B) RBC agglutination to PLGA-chitosan JNP at various RBC:JNP ratios. (C) Measurement of phosphatidylserine exposure on RBCs based on the binding of Annexin V-Alexa Fluor 488 to phosphatidylserine at various RBC:JNP ratios. (D) Osmotic fragility of naïve RBCs and RBCs with adsorbed PLGA-chitosan JNP at RBC:JNP ratio of 1:200.

After confirming that the binding of PLGA-chitosan JNP onto RBCs does not induce adverse effects on carrier cells, their lung targeting capacity was analyzed. Male BALB/c mice were administered intravenously with either free PLGA-chitosan JNP or RBC hitchhiked PLGA-

chitosan JNP at a loading ratio of 1:200 (RBC:JNP). Animals were sacrificed at 5 minutes after injection. Heart, lung, liver, spleen, kidneys, and brain were harvested, and the far-red fluorescence signal was imaged using Perkin Elmer IVIS small animal imaging system and quantified by livingImage software. As expected, strong signal intensities were observed 5 minutes after administrated in the liver. However, there was a significant signal increase in the lung with RBC-hitchhiked PLGA-chitosan JNP (16 times higher) compared to their free PLGA-chitosan JNP counterpart, indicating high lung uptake. Furthermore, there was nearly a 13-fold increase in the lung-to-liver ratio of RBC hitchhiked PLGA-chitosan JNP compared to free JNP (**Figure 8-8**).

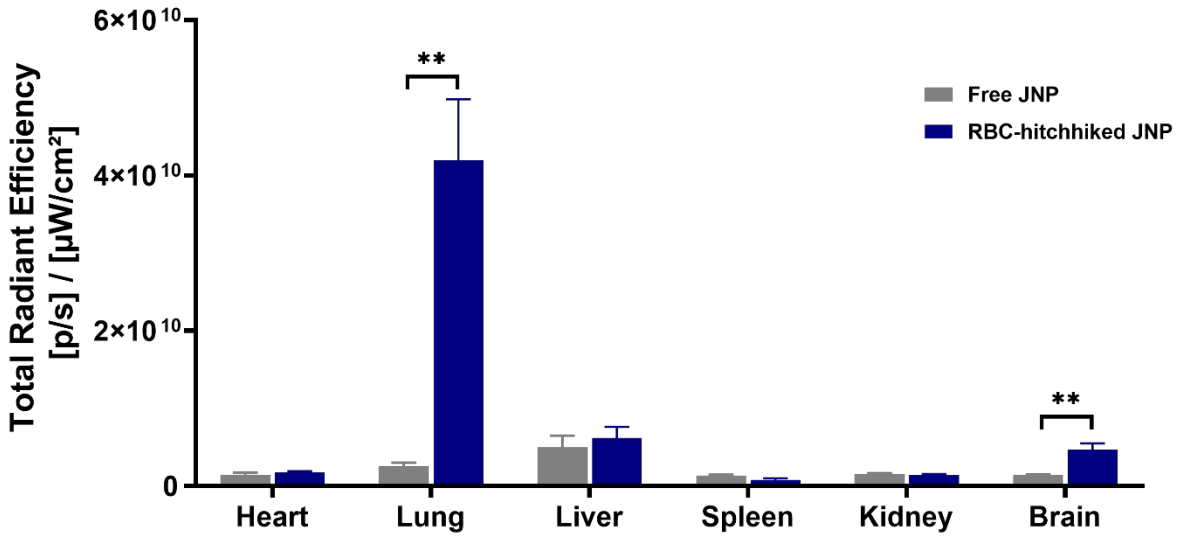

Figure 8-8. Biodistribution of fluorescently labeled free or RBC-hitchhiked PLGA-chitosan JNP 5 minutes after intravenous administration.

Surprisingly, minimal signals were detected in the spleen for free PLGA-chitosan JNP. Minimal signals were detected in the blood as well, suggesting immediate desorption of PLGA-chitosan JNP from RBCs in the lung capillaries. It is unclear whether any cells in the lung took up the PLGA-chitosan JNP since animals were not perfused. As expected, minimal signals were detected in the heart and kidney. Surprisingly, there was a signal increase in the brain with hitchhiked

PLGA-chitosan JNP. It is unclear how quickly over time, signals in the lungs would gradually decrease. It is plausible that PLGA-chitosan JNP may remain in the lungs longer than other RBC delivered nanoparticles due to its positive charge interacting with lung endothelium, giving it more time to being taken up by cells. This highlights the potential of RBC-hitchhiked PLGA-chitosan JNP as a lung targeting drug delivery platform. Unlike most nanoparticles, RBC-hitchhiked PLGA-chitosan JNP achieved high lung accumulation without any affinity moieties.

It is important to note that, only selected organs were harvested for nanoparticle uptake analysis. Other organs, such as small intestine, cecum, colon as well as site of injection (tail) were not collected. Moreover, free PLGA-chitosan JNP could have adhered to endothelial cells covering the vascular lumen through electrostatic interactions.

The RBC-hitchhiked PLGA-chitosan JNP demonstrate a promising lung targeting drug delivery platform. In future studies, each compartment of PLGA-chitosan JNP can be independently used to encapsulate therapeutics with different physicochemical properties with tunable release profiles and/or imaging modalities. The surface of each compartment in the particles present different chemical moieties enabling selective surface modifications using orthogonal chemistries. Combination of bicompartmental nanoparticles and carrier features of RBCs provided by cellular hitchhiking afford a potential drug delivery platform for targeting various lung conditions such as cancer, respiratory distress syndrome, pulmonary hypertension and pulmonary embolism, and respiratory infections.

8.3 Outlook

Delivering therapeutic cargos to target cells to achieve maximal therapeutic efficacy with minimal side effects is the fundamental concept of drug delivery. The work presented in this dissertation provides a concrete foundation for the design, fabrication, and engineering of protein and biopolymer-based nanoparticles to cross biological barriers and achieve high levels of specificity for the targeted tissue. The design space for the fabrication of novel protein-based nanoparticles via EHD co-jetting can be expanded further venturing into new proteins to altering the morphologies and physicochemical properties of existing ones. This can be envisioned to be performed at three different levels starting from the composition to the surface and ultimately the cargo. At the composition level, with the recombinant protein technologies providing access to protein building blocks, EHD co-jetting can be employed for the design and development of custom-made protein nanoparticles with precisely engineered functions. At the surface chemistry level, EHD co-jetting allows for the preparation of particles composing chemically variable compartments that consequently enable orthogonal surface chemistries on individual compartments leading to dual or multi-targeting capabilities for nanoparticles. As an example, bicompartmental nanoparticles can be engineered to exploit both cell-mediated and targeting ligand-mediated transport simultaneously for accumulation at the target site; the surface of one compartment can be modified with circulatory cells-specific targeting ligands while the other compartment with targeting moieties that are specific for the target tissue. Subsequently, this strategy also allows for conjugating nanoparticles onto circulatory cells for cellular hitchhiking in vivo, rather than loading them onto cells ex-vivo. At the cargo level, recent trends show an increased interest in the drugs landscape focusing on biological drugs such as nucleotides, antibodies, and recombinant proteins. It is therefore vital that the design of nanoparticles also

incorporate creative strategies to sequentially negotiate the intracellular barriers such as the cell membrane and endocytosis in target cells, endosomal escape, diffusion through cytoplasm, and eventually the nuclear membrane for entry into the nucleus, if required. An extension of EHD co-jetting engineered multicompartmental nanoparticles can be independently equipping the compartments to address the intracellular barriers, incorporate multiple biological cargos, and provide imaging modalities simultaneously.

Permutation and combination of multifunctional and multicompartmental nanoparticles can be prepared by EHD co-jetting to access a broad range of novel therapeutics to address both intra- and extracellular barriers otherwise unavailable through other platforms. In lieu of the complexity of nanoparticle–cell interactions and the sequential presence of extracellular and intracellular biological barriers, the next generation of clinically translatable nanotherapeutics must ideally combine superior nanoparticles with the body's natural delivery vehicles and transport mechanisms to substantially increase the positive patient outcomes.

Appendix B
SEM Analysis via ImageJ/FIJI

The material in this section has been adapted with minor modifications from the following article: Nahal Habibi, Ava Mauser, Jeffery E. Raymond, Joerg Lahann. Systematic Studies into Monodisperse Synthetic Protein Nanoparticles. *In Preparation.*

SEM images are collected as lossless TIFF files. The images are then opened with ImageJ (or FIJI, a distribution of ImageJ with plugins that are biased towards life scientists) and the software is initialized to have a known scale for the image (typically a pixel/distance or a distance/pixel ratio). With the scale set, all extraneous regions of the image are cropped, and the histogram of the resultant image is observed. If the intensity counts do not span the scale afforded by the bit depth of the image, a rescaling is advised in order to provide the best possible intensity thresholding later. While this process can be performed at multiple bit depths, it is recommended that the image be converted to 8-bit (0 to 255 intensity scale) after rescaling. This process, depending on the expertise of the microscopist, may result in a gapped intensity histogram due to rescaling. If this is the case, it may be useful to perform a 'gentle' gaussian smoothing operation utilizing filter math in ImageJ - a standard deviation size of 0.5 pixels is recommended here. Once these processing steps have been undertaken, thresholding the image into a binary dataset can be conducted. Utilizing a live time histogram of the image (with both log and linear counts expressed), thresholding should occur somewhere near the intensity associated with the first local minima after the background peak. The precise intensity selected should be informed by comparison to the

original image for sensibility. If the original image exhibited particles that were touching or overlapped, it may be necessary to utilize the binary watershed tool to separate features. It may also be necessary to utilize manual separation of particles. With this said, depending on the statistics of your system or the average space around features, these steps may be of low value. For example, an n = 40 may require the steps and an n = 800 may not. Particle analysis is then undertaken utilizing size (area) and shape (circularity) to exclude background features that can clearly be excluded from the data set. Typically, this will mean excluding small clusters of pixels that are associated with substrate maxima or background features that are very large/unrelated to the materials. Depending on the sample, it may be prudent to collect two or more size ranges with different exclusionary parameters in each. After comparing your binary, original, and particle analysis images for meaningful discrepancies, the resultant data set should then be saved. The last phase of the ImageJ analysis is to generate binned histogram data for the attributes of interest. This can be done with automated binning or, as is done in this study, one can dictate the range and bin size in order to aid in data presentation and analysis. Alternately, individual data can be utilized for generating non-linear bins of various sizes for direct comparison to DLS data. One strategy for linear binning is to set the start of bins at the halfway point between the center of mass for each bin. A way to do this is setting the binning start points for nanoparticles at the 5's (5, 15, 25, etc.) with bins that are 10 nm wide. This will generate a data set where, for example, the 45 nm bin represents 45-55 and can be assigned to 50 nm in the histogram/ distribution data set. For non-linear binning, utilizing bins with boundaries that rest at the half-way point provides a reasonable approximation of the DLS data.

Data Processing via Opensource Spreadsheet Software

In order to obtain results that will allow comparison of the data from imaging with DLS-based PDI results for the systems, histograms and individuals data can be used to calculate volume-based values in order to generate a calculated SEM-based PDI value (denoted here as PDI_{SEM}) and to present an intensity-based analog (iSEM) for comparison to intensity-based DLS. iSEM distributions, which were calculated from nSEM × $(d/2)^3$ and then normalized. This was done to provide dry particle (as manufactured) analysis that is comparable to the nDLS and iDLS results (as used in solution after post-processing). The entirety of the analysis for this step is done utilizing an open source or free-to-use spreadsheet or statistical software (OfficeLibre Calc, Gnumeric, Google Sheets, etc.). Here, we chose OfficeLibre Calc. [1] The initial calculation is one in which each bin is assigned an arbitrary mass based on calculation of a volume. [2] This mass is used to calculate a Mz-based diameter (comparable to the diameter expressed in DLS), [3] which is then used in conjunction with the standard deviation of the individuals data to generate PDI_{SEM}. [4] For conversion of the number-based SEM histogram into an intensity based distribution can be achieved by simpler means; simply multiply the nSEM bins by an arbitrary scaling factor of the bin radius cubed, then normalize or convert to a population percentage.

(1) $$m_{bin}\,(a.u.) = 1\,\frac{a.u.}{nm^3} \times \frac{4\pi}{3} \times (\frac{d_{bin}}{2})^3$$

(2) $$d_z(nm) = 2 \times (\frac{3}{4\pi} \times \frac{\sum m_{bin}^3 n_{bin}}{\sum m_{bin}^2 n_{bin}})^{1/3}$$

(3) $$SEM\ PDI^* = \frac{SD_{individuals}}{d_z}$$

(4) (a) $n_{bin_i} = n_{bin_n} \times (\frac{d_{bin_n}}{2})^3$;

(b) $percent\ n_{bin_i} = \frac{n_{bin_i}}{\sum n_{bin_i}} \times 100$;

(c) $normalized\ n_{bin_i} = \frac{n_{bin_i}}{\max\ (all\ n_{bin_i})}$

Use of PDI_{SEM}, just like conventional DLS-based PDI values, is not a substitute for assessment of individuals or size distribution histograms. With this said, it (along with semilog data of the distribution histogram for the individuals) can be readily used to rapidly communicate the changes observed in ensemble when transitioning from a dry state system to a solution-based suspended state system. Additionally, by knowing the ensemble effects on the key geometric parameter (diameter), one may be able to begin to better assess solution-based performance in cells, tissue, and/or organisms. This is possible through use of the secondary geometric parameters (anisotropy, minor axis diameter, circularity/roundness, etc.) when comparing systems that are otherwise similar in diameter. Using the SEM data, it is also possible to generate both intensity average DLS data and number average DLS data by using logarithmic binning and estimated mass correction. This can be done to better understand the changes in distribution on suspension of a system or, as is often the case, compare sample preparation and suspension methods. The various expression of diameter population that are now present for a given study are appropriate for statistical (t-test, IQR, ANOVA, etc.) and qualitative comparison. This is also true for the secondary geometric factors.

Two-dimensional Analysis

The individual data for geometric parameters allow for conventional statistics related to similarity. However, from a formulations perspective, it is useful to be able to both qualitatively and quantitatively differentiate between the impact of constituents on overall geometric character for blended SPNPs. To address this, one can assess comparisons of diameter to the other geometric attributes (min. diameter, anisotropy, circularity, and roundness). Taking the linear regressions of these paired x-y data sets, one can construct an arbitrary scoring factor (here, 0-10) depicting the extent of the similarity to the monospecies SPNPs. This scoring factor is a convolution of the relative agreement of the blended regression slope and the agreement of the regression strength ($<r^2>$) when compared to the monospecies SPNPs. This is done by treating the slope of the blend regression as a linear combination of the slopes of the constituent regressions, scaling based on the extent of agreement between the strengths of the regressions.

Image Analysis Example

Data Files

The image file used for this tutorial is provided with this supporting information so that the reader might work through the process themselves. Result files and rendered data images are also provided.

Initialization of Scale/Resolution

After opening the image file in ImageJ, establish scale calibration through the use of the line tool then

`↳ Analyze ↳ Set Scale`

in order to state the known distance on your image. Zooming in on an existing scalebar in the image can help. If all of the images you intend to assess are of the same magnification, resolution, and aspect ratio then you may save time by selecting this as a global scale setting.

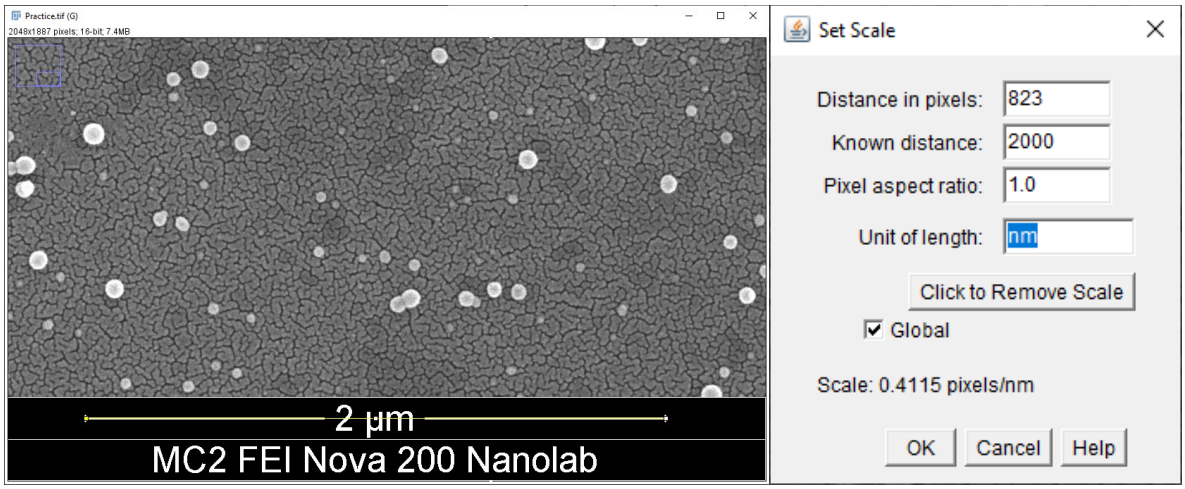

Figure A-1. Setting Scale.

Your metadata in the file may include the scale or automatically import your scale. If the scale is included but not automatically imported, you may enter it manually. Here, you could place 0.4115 in the 'distance in pixels' and 1 in 'known distance' to get the same scale settings. If your scale imports directly and correctly, then you can ignore these steps. Sometimes the scale that imports is not correct (units, scale, etc.) – when this occurs you will need to perform the steps above. It is also useful to stop here to assess whether or not you have an appropriate degree of resolution for the features that will be relevant to the study. Here, we know that centrifugation of the system will remove particles with diameters <20 nm prior to use, and that filtration will remove particles with diameters >1000 nm. Assuming that our smallest features of interest are actually items in the 20 nm x 20 nm size range, we would like to know that we have a minimum of 10 pixels per feature/particle. Here, we have about 2.5 nm per pixel in x and in y (ca. 5 nm^2). This means that our smallest particles of interest will have somewhere between 50-100 pixels associated with them certainly enough to differentiate from background noise/speckles later in the process.

Crop/Duplicate/Adjust

The next step is to crop your image to preclude any of the system level information (if present). Using the box tool, select the region with your features, right-click within the box, and select duplicate. After duplicating the field of view (FOV) you have an interest in, auto-contrast the selection. This is done by

↳ `Image` ↳ `Adjust` ↳ `Brightness/Contrast`

and then selecting 'Auto' from the pop-up (which will set the minimum and maxima such that 0.3% of the pixels are set to min or max, respectively) followed by 'Apply'.

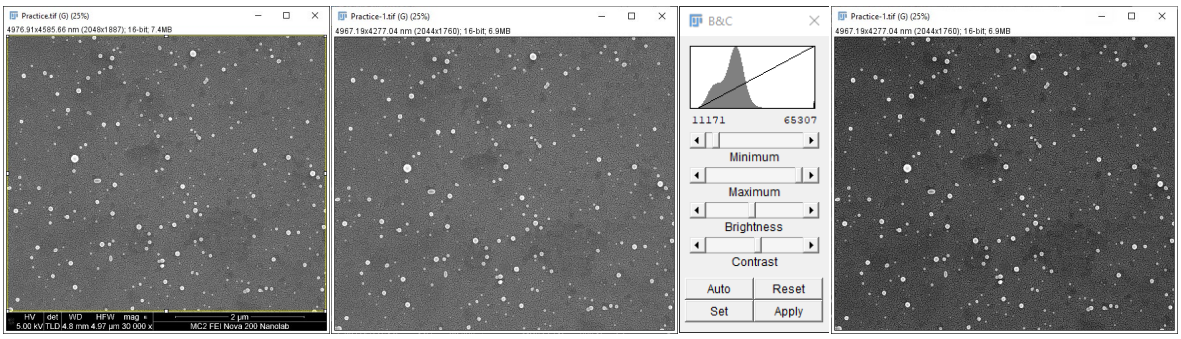

Figure A-2. Crop to Duplicate to Contrast.

Convert to 8-bit and Gaussian Blur

Once appropriate contrast has been obtained, convert the image to an 8-bit image through

↳ `Image` ↳ `Type` ↳ `8-bit`

as this will make thresholding easier. Proceed to perform a gaussian averaging function (Gaussian Blur in ImageJ) using

↳ `Process` ↳ `Filters` ↳ `Gaussian Blur`

with a setpoint of 0.50 pixels. Briefly, the impact of this setting is that the blur sigma relates to an averaging function that is much like a typical gaussian curve. That is to say, by setting the radius for a single sigma to half of a pixel, each pixel will return a value that is ~65% based on its original

value, ~30% based on the neighboring pixel values, and ~4% based on the next ring of pixels. By inspection in **Figure A-3,** it becomes clear that this provides several benefits. When observing the particles, it is clear that the overall geometry is not overtly impacted by this math and that 'maxed' out pixels become muted. When observing the background, it can be seen that possible bright outliers get muted into the rest of the background. This has two effects: [1] during thresholding, the likelihood of a false positive for the identification of a particle goes down and [2] the likelihood of artificially inflating the size of the particles decreases (since the likelihood of bright background features near the particle goes down).

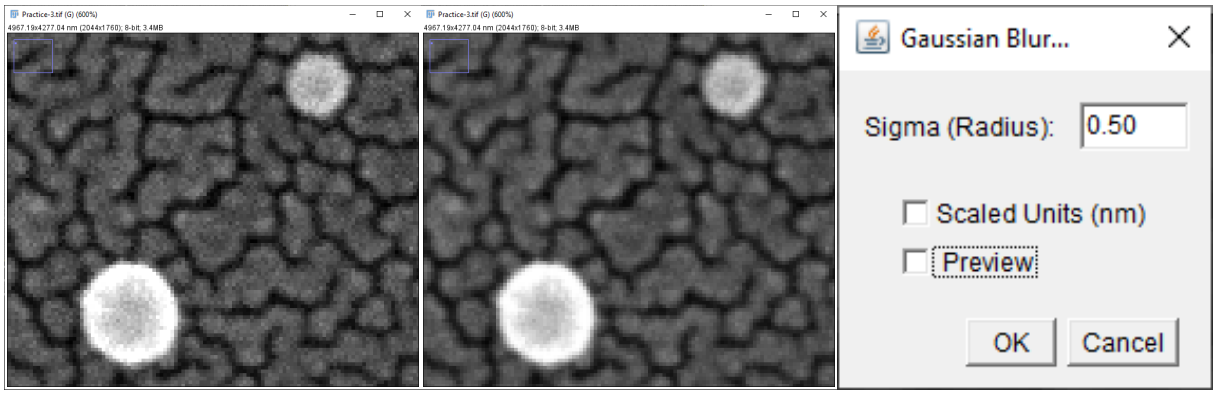

Figure A-3. Effects of gaussian blur with S = 0.5 pixels.

Taken in total, this step decreases the likelihood of a need for manual processing to occur during the analytical phase of the process.

Thresholding, Binary Image Creation, and Binary Clean Up

Despite the irregular crazing of dark and darker regions in the substrate, as well as an observation of darker patches, the steps taken up until now should be sufficient to make thresholding the system relatively straight forward. While multiple tutorials exist online for this component of particle analysis, this method of preparation and threshold selection takes some of the guesswork out of the process - and can lead to lower rates of analysis variation. In order to threshold the image,

which is to say create a binary image with 255 intensity indicating ‘feature’ and 0 intensity indicating ‘no feature’. First, we should take a moment to look at the histogram of the image as it stands. A histogram of the image can be accessed with Ctrl+H or through

↳ `Analyze` ↳ `Histogram`

and then select the ‘Live’ and ‘Log’ buttons. This will allow you to assess the major intensity regions easily, which will aid in your initial estimate for thresholding.

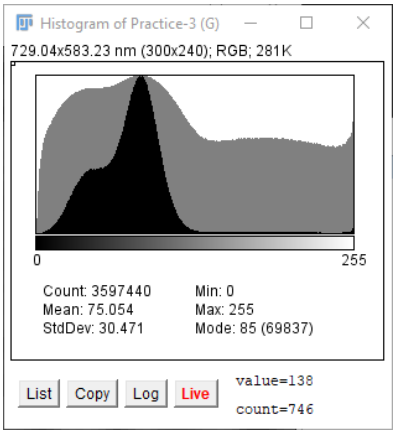

Figure A-4. Histogram assessment.

Here, four primary feature intensity distributions can be observed by looking for the inflection midpoint on the log-scale projection of the histogram. The first starts at 0 and goes to ca. 54; it can be assigned to the dark crack-like background features. The second region ranges from 54 to 138 and can be assigned to the lighter regions of the background. The third and fourth set of features can be assigned to the particles (beginning about 138) and the exceptionally bright features on those particles (beginning at 247, which are typical artifacts of low charge dispersion in organic/polymer/biomaterial-based particles). Taken in total, it makes sense to select 138 as an initial set point for the identification of features in thresholding. Keeping the histogram up, open the thresholding tool (Ctrl + Shift + T) by

↳ `Image` ↳ `Adjust` ↳ `Threshold`.

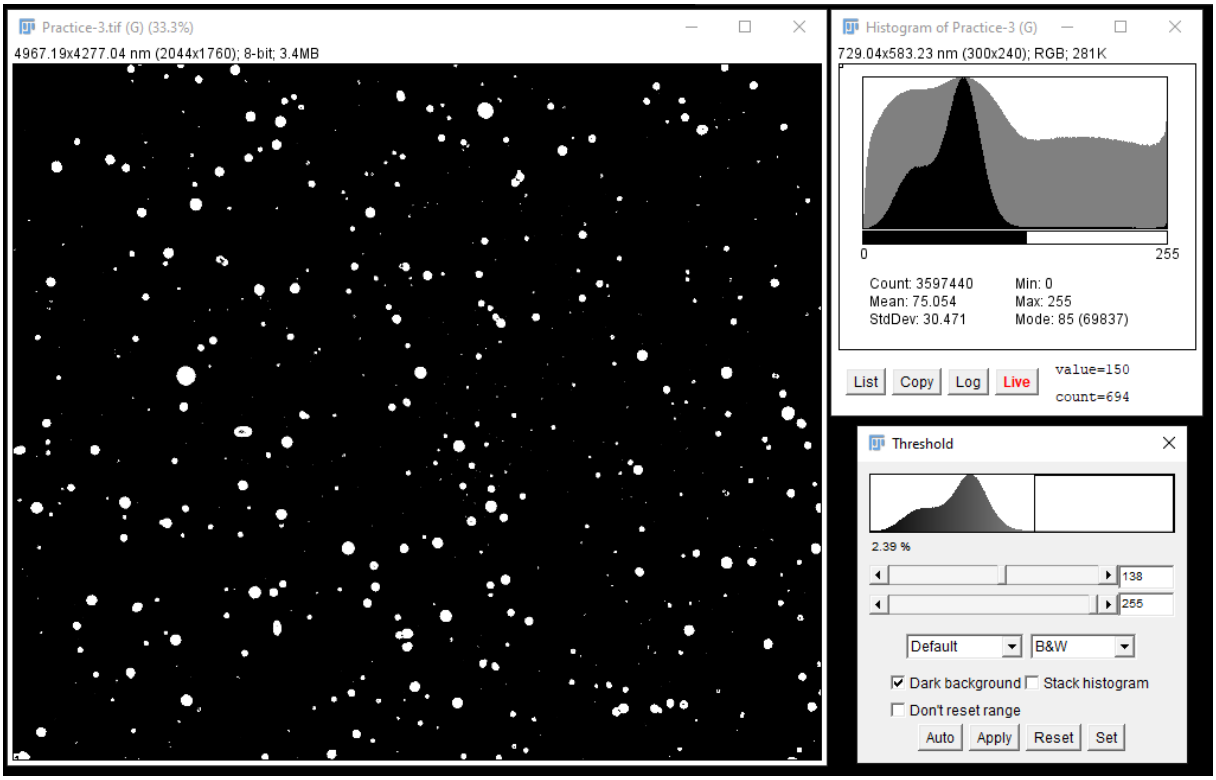

Figure A-5. Work area for thresholding.

Automatically, the software will try to give you a threshold that is on the cusp of the first two (primary) feature histograms – effectively trying to threshold in between dark background and darker background. Since we have already looked at our histogram, we know that the initial setting is not appropriate. Adjust the top sliding bar above in the Threshold window to 138. Take the time to inspect above or below that value. You will notice that the particles you have outlined start to lose some area if you go much higher than that (obvious by 155) and that noise starts to show up when you go much lower (obvious by 125). By inspection, sliding the bar back and forth, you should be able to see in the binary image the range where the primary features remain of a constant size. For the purposes of this demonstration, we will accept our initial value of 138 and proceed. Pressing 'apply' on the threshold will render the current image into a binary image. Duplicate the

non-thresholded frame if you desire to save the image of that step separately. With the binary image selected, there are four options for image clean-up that can be undertaken.

Fill Holes: The 'fill holes' operation is relatively straight forward. It can be accessed by ↳`Process` ↳ `Binary` ↳ `Fill Holes`.

Performing this operation will result in all voids (black pixels) that are entirely surrounded by feature (white pixels) to be overwritten as features. This is especially helpful in SEM imaging, where edge intensities may be higher due to charge dispersion limitations at the edge of features. If inclined to carry this method over to fluorescence imaging, it is possible that surface labelled materials (or cells) may also require this operation for different reasons (high edge label density, improved quantum yield at the edge of the feature, etc.). Either way, for this demonstration, we can observe gaps in some of the features and the fill holes operation should be performed.

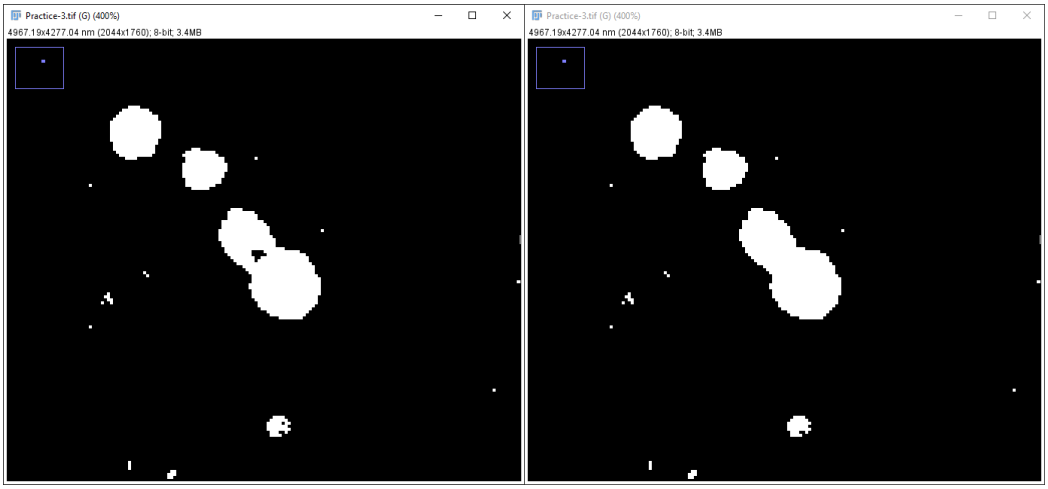

Figure A-6. Zoomed Binary feature before and after Fill Holes**.**

Despeckle: In an attempt to find the 'sweet spot' between over-thresholding (and shrinking our features) or under-thresholding (and including some outlying background points), a choice of where to threshold has to be made. From a practical sense, lost feature pixels cannot be readily re-

captured and background pixels can be cleaned up. Therefore, it is better to deal with the latter scenario and use built-in functionality to clean up the rogue background pixels. ImageJ has a built-in processing step, called 'Despeckle' that is designed to filter out static-like (random and semi-random) noise and remove it on a single pixel basis. It does so in a fashion similar to image clean up of static in analog to discrete or discrete to analog transitions in other types of data. This results in feature smoothing to a small degree, but that result does not substantially impact final results; It often results in pixel shifting without overt pixel removal from the larger features – assuming that the initial pixel count per feature threshold mentioned earlier was met at the resolution used. Activate this clean up by

↳`Process` ↳ `Noise` ↳ `Despeckle`.

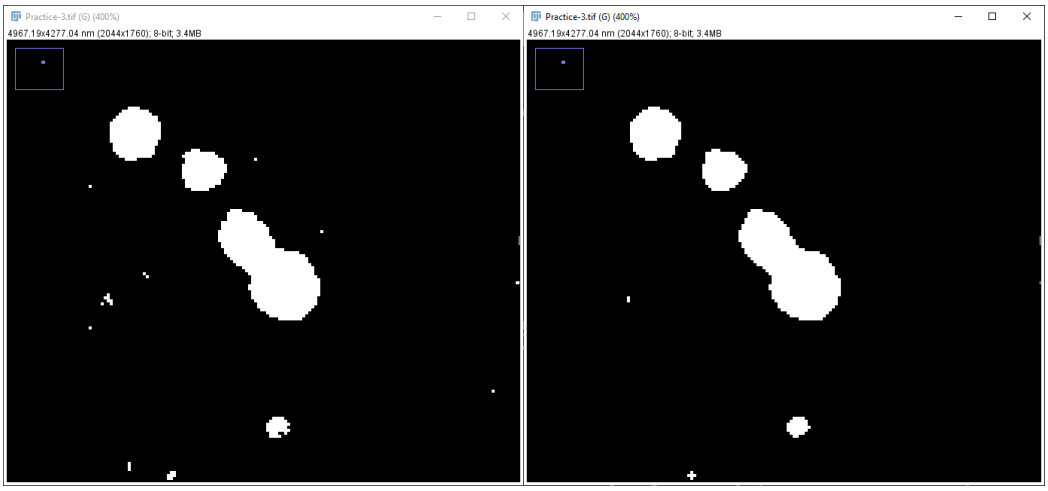

Figure A-7. Zoomed comparison of before and after Despeckle operation.

Watershed: In every image there is a chance for feature overlap/merger, due to most features existing in three dimensions and/or having the ability of boundaries to intermingle. The ability to proceed wisely when assessing a 2D representation of a 3D system is strongly tied to your knowledge of the system. In this case, experience has taught that many of the smaller clusters (two

or three particles overlapped) appear to dissociate into individual particles during processing. This means that, for this sample, it is appropriate to split these features. An automated mechanism exists in ImageJ and can be applied by

`↳Process ↳ Binary ↳ Watershed.`

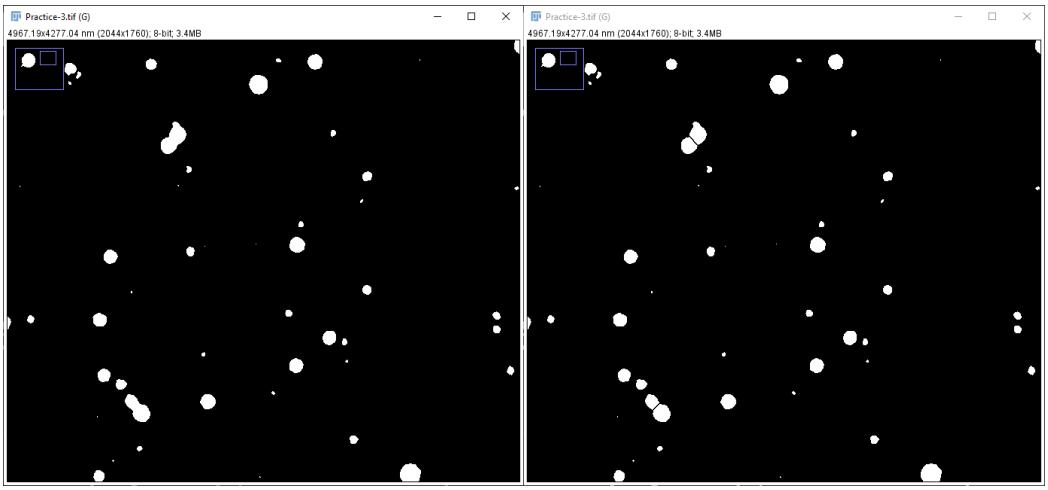

Figure A-8. Zoomed comparison of before and after Watershed operation.

Direct Manipulation: If all attempts to threshold, control noise, avoid background, and retain accurate feature structures result in unacceptable feature separation - manual manipulation may be appropriate. Examples include comparison with the original image and determination that the watershed tool has failed to identify some breaks in the features or that the tool has created breaks in inappropriate areas. Under those circumstances it may be appropriate to utilize the pencil or line tool to add or delete features. However, the authors would strongly suggest that you consider the value of such actions ("will it matter statistically?"), the difficulty of doing it routinely for multiple data sets ("is the gain worth it?"), and if it will compromise repeatability due to irregularities in application ("will different researchers get different results?"). Here, inspection of the watershed

binary does not show extensive deviation from the particles observed in the original image at a level that would justify this action.

Particle Analysis and Data Inspection

Before analyzing the particles, the results to measure must be selected. In

`↳Analyze ↳ Set Measurements`

one can select the parameters to output as results for the analysis. Some of the options are very application specific, and some of the options will include superfluous information. In **Figure A-9** the configuration needed for this work is presented (providing key parameters like Feret's diameter, circularity, perimeter, roundness, anisotropy, and minor/major axis diameters). After selecting the appropriate results to measure, and with the binary image selected, perform particle analysis by

`↳Analyze ↳ Analyze Particles…`

The Analyze Particles menu allows for several areas of control over feature selection. Here, we have already stated that features of less than 400 nm^2 are not important to the final system and that large particles (1000000 nm^2) will also be removed. Therefore, the first mechanism for control of feature selection is the area of the features – which is set to the range of 400-1000000. The second way to control collection is through circularity. Circularity is 4π*(area/$perimeter^2$) and can be thought of as an approximation of circle-like shape. Extremely non-regular shapes often generate very high perimeters and can sometimes be excluded with this filter. For this demonstration, a range of 0.2 to 1 is used. The final control at this stage is determining if exclusion of features on the edge is appropriate. Here, since fractions of particles would skew results, 'Exclude on Edges' is selected. Finally, presentation of a resulting image where results can be visually inspected or presented is often useful. Several options exist in the drop down, but here we will use 'outlines'. The outline output is useful because it provides numbered outlines that correspond to the output

data, allowing the assessment of individual features for sensibility or the removal of ‘bad’ features on a by-line basis from the results when a known artifact is present. After executing the analysis, a results page will present. Save these results as a csv file.

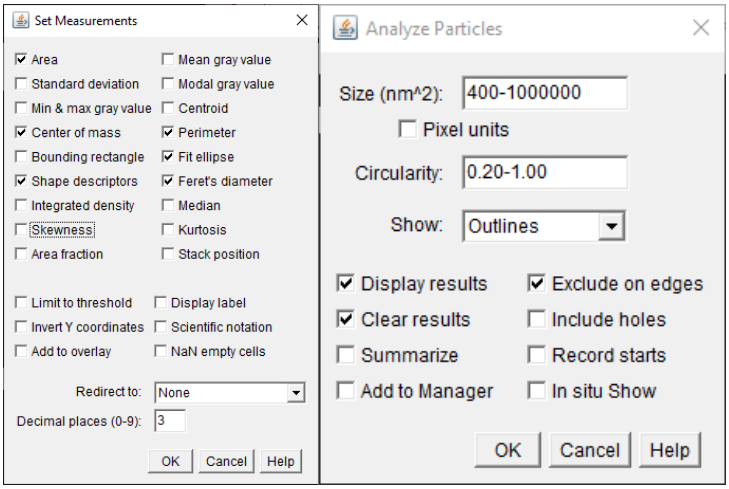

Figure A-9. Measurement and analysis settings.

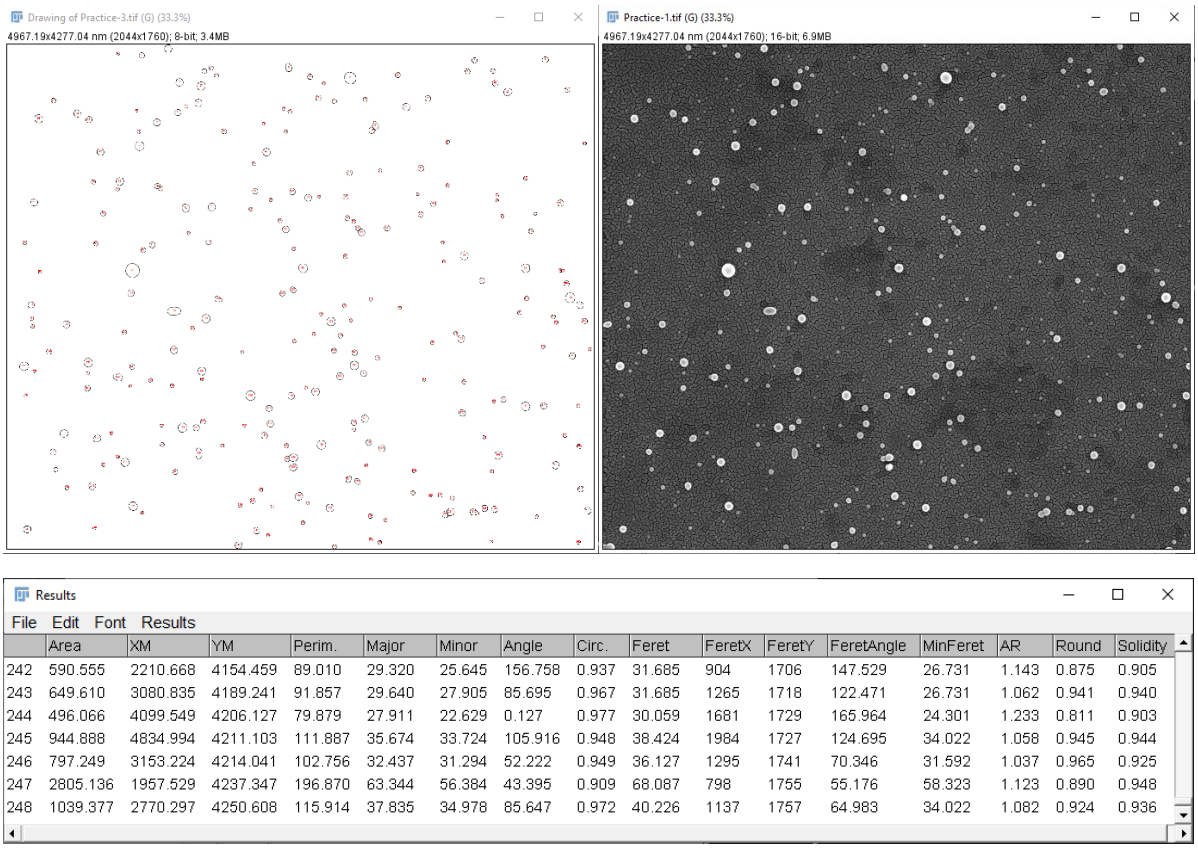

	Area	XM	YM	Perim.	Major	Minor	Angle	Circ.	Feret	FeretX	FeretY	FeretAngle	MinFeret	AR	Round	Solidity
242	590.555	2210.668	4154.459	89.010	29.320	25.645	156.758	0.937	31.685	904	1706	147.529	26.731	1.143	0.875	0.905
243	649.610	3080.835	4189.241	91.857	29.640	27.905	85.695	0.967	31.685	1265	1718	122.471	26.731	1.062	0.941	0.940
244	496.066	4099.549	4206.127	79.879	27.911	22.629	0.127	0.977	30.059	1681	1729	165.964	24.301	1.233	0.811	0.903
245	944.888	4834.994	4211.103	111.887	35.674	33.724	105.916	0.948	38.424	1984	1727	124.695	34.022	1.058	0.945	0.944
246	797.249	3153.224	4214.041	102.756	32.437	31.294	52.222	0.949	36.127	1295	1741	70.346	31.592	1.037	0.965	0.925
247	2805.136	1957.529	4237.347	196.870	63.344	56.384	43.395	0.909	68.087	798	1755	55.176	58.323	1.123	0.890	0.948
248	1039.377	2770.297	4250.608	115.914	37.835	34.978	85.647	0.972	40.226	1137	1757	64.983	34.022	1.082	0.924	0.936

Figure A-10. Outline image, pre-binary image, example of results.

Briefly, the results are presented in the units of calibration and can be interpreted as follows:

1. [blank]: Index number
2. Area: Area in units squared
3. XM: Location of center of mass, X-axis in units from upper left corner
4. YM: Location of center of mass, Y-axis in units from upper left corner
5. Perim: Length of perimeter in units
6. Major: Length along the primary axis of best fit ellipse
7. Minor: Length along the secondary axis of best fit ellipse
8. Angle: Angle of the primary axis of best fit ellipse

9. Circ.: Circularity as presented previously in this section
10. Feret: Feret's Diameter. This is the effective diameter of the feature as used throughout this work and can be taken as the maximum caliper distance about the feature. Often just referred to as the Diameter.
11. FeretX: X-axis starting point of Feret's Diameter.
12. FeretY: Y-axis starting point of Feret's Diameter.
13. Feret Angle: Angle of Feret's Diameter.
14. MinFeret: The diameter of the feature taken as the minimum caliper distance about the feature. Often just referred to as the Minimum Diameter.
15. AR: Aspect Ratio. Defined as AR = Major/Minor. Can be referred to anisotropy.
16. Roundness: An aspect ratio-corrected alternative to Circularity. Defined as Roundness = $4(\text{Area}/\pi)/\text{Major}^2$.
17. Solidity: The area of the feature divided by the calculated area if all concave regions on the edge were filled.

A reduced number of parameters is often appropriate for assessing nanoparticles based on application and the purpose of the study. Here, the systems being studied are currently being utilized in biological studies for nanomedicine applications, so the researchers are concerned with factors like uptake, toxicity, latency, degradation rate, clearance rate, etc. Given that particle size (diameter), particle anisotropy, minimum diameter, and circularity/roundness are of interest – it is possible to do some analysis (not related to DLS results) directly from ImageJ. While it is beyond the scope of this work to provide a review of why these factors might impact bioactivity,

distributions and graphs for these parameters as retrieved from ImageJ utilizing the following fields in the results window:

↳Results ↳ Distribution

↳Results ↳ Plot

The distribution window allows for auto-binning or specified binning of histograms for each property. The plot window allows for graphing of properties against one another for inspection. In the presented data 'easy to interpret binning' is used with bin sizes that are set to scales that are easy to digest (factors of 1, 2, 5, or 10). Often, one round of auto-binning to observe your range and shape can lead to good decisions around manually selected binning parameters. Using the List button in the diameter histogram data window, a list of bins and counts will be presented. Save that list as a csv file. For this work, our statistics are derived from setting the histogram distribution settings such that each bin starts and ends on the 5s, with a 10 nm bin width. It is important to remember that the list data for the histogram shows start-of-bin and not center-of-bin. Depending on how a study defines outliers or exceptional events, any of these plots might allow for rapid *ad hoc* assessment of the results before moving on to the next phase of analysis in the project – hopefully saving time and simplifying the analysis process overall.

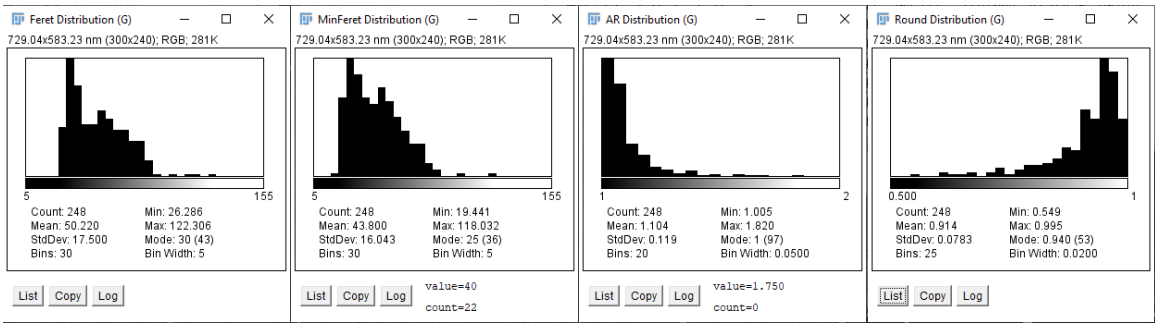

Figure A-11. Diameter, Minimum Diameter, Anisotropy and Roundness.

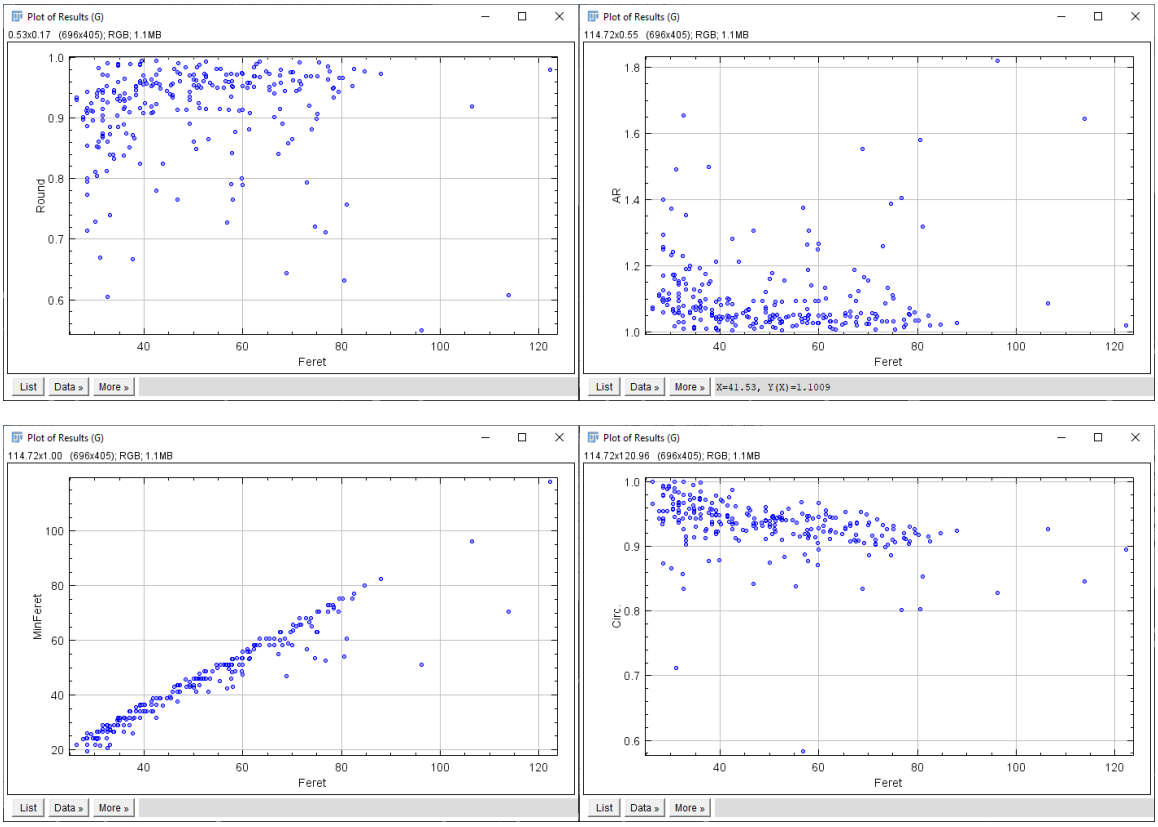

Figure A-12. Diameter versus Roundness, Anisotropy, Minimum Diameter, and Circularity.

OfficeLibre Calc

Multiple commercial software packages exist that are capable of calculations, data manipulation, spread sheet functionality, low-level statistical analysis, and graphing of data in various formats. However, in keeping with the premise of this walkthrough, an open source/access software package has been selected: OfficeLibre Calc. For users that operate in a Linux environment, the authors would also recommend Gnumeric as an alternative. All operations described in this portion are presented in the associated ods file provided with this work. The authors encourage others to use it as a template or starting point for their own work.

Import and Summary Statistics

Open the saved results file in OfficeLibre Calc and agree to the native import detection. If summary statistics are needed, performing those now may make sense. The Summary Statistics tab of the spreadsheet includes calculations for common summary statistics. Note that it is simpler from an interface standpoint to acquire histograms of the distribution of values directly from ImageJ (see previous). However, this file may also be a good place to insert those binned values.

2.5.2.2. SEM-based PDI (PDI_{SEM})

A method for approximating the PDI presented in DLS data when using the SEM data is presented in the main manuscript. While all attempts to estimate 3D intensity-based spectral data from 2D imaging data will fall short of an "apples to apples"-type comparison, it is often valuable to attempt the effort. To that effect, the first step of this method is to import the diameter histogram data from earlier. The next step is to convert the bin start values to center-of-bin values. For each bin center value, calculate an arbitrary mass (M*) using the diameter as a basis for the calculation. Here, we simply use the equation for the volume of a sphere. In the next column, calculate M* times the number of counts in the bin (MN*). In the next two columns calculate M* squared times the number of counts in the bin (MMN*) and M* cubed times the number of counts in the bin (MMMN*). Though it is not needed to be effective, it is worthwhile to appreciate the importance of having analogs to MW, MW^2, and MW^3 when dealing in volume and mass distributions. Calculate the following ratios: number ratio = sum(MN*)/sum(N), weight ratio = sum(MMN*)/sum(MN*), and z ratio = sum(MMMN*)/ sum(MMN*). Again, while not critical to this application, it is worthwhile to note that these ratios correspond to calculation of the number, weight, and z average molecular weights in an arbitrary mass space. Lastly convert, these arbitrary weights back into diameters (Dn*, Dw*, and Dz*) by treating them like arbitrary volumes and then solving for the diameter using the volume equation for a sphere. The final result for this section is obtained by dividing the standard deviation (from the summary statistics) of the diameter and by

the Dz* value, resulting in a PDI_{SEM} that can be used when comparing SEM results to DLS results. It should be noted that your Dn* and average diameter from the residuals should be reasonably close to one another. If a large deviation occurs, then this typically means that the bins are not evenly populated (with some bins being populated by lower numbers for a negative deviation of Dn*, and some bins being populated by higher numbers for a positive deviation of Dn*). As the number of images processed and compiled into your data set (combining both individuals data and binned data) increase, Dn* and the average diameter of individuals should approach unity. Lastly, it should be noted that Dw* and Dz* can also be valuable comparison numbers in a few other ways: [1] the relationship between Dn*/Dw*/Dz* is not entirely unlike using mean/median/mode distribution descriptors, [2] the bins can be changed to align with Dw* or Dz* derived value for each bin to align better with distributions obtained from methods that bias toward weight or volume determinations of size, and [3] may assist efforts to understand size exclusion techniques or processing techniques that have variable effects based on mass, density, and/or volume per particle.

2D Geometric Analysis and Scoring

Direct comparison (qualitative) of the relationship between two distributions through inspection of 2D scatter plots is capable of providing some insights. It is also appropriate to assess a regression (linear or otherwise) if there is a basis for such a comparison. Similarities in the characteristics of the regression may reveal how secondary geometric factors may trend with size, specifically for a blended formulation ("AB"). Taken one step further, same strategy can be applied to materials made only from the formulation components ("A" and "B"). This strategy is provided in the supporting .ODS documentation using individuals data as the basis. Linear regressions are performed for diameter vs. roundness for a blended (AB) sample and two mono-species (A and B). Additionally, an arbitrary scoring mechanism is used to assess the degree to which each

component (A or B) appears to contribute to the relationship observed in the blended system. While not perfect, the score presented here will return a number between 0 and 10. A possible interpretation of this score:

Score	Interpretation
0	no basis for impact
>0, ≤1	minor impact
>1, ≤5	moderate impact
>5, ≤10	major impact

The score is calculated as follows for a linear regression model: [1] the slope of the linear regression best fit lines are obtained, [2] the total range of the three slopes are converted to a 0-1 scale, [3] closeness on that scale is calculated, providing a value of 0-1, [4] the $<r^2>$ relative percent difference for each constituent is subtracted from 1 (expressed as a decimal) is calculated, and [5] the results of 3. and 4. are multiplied together and then multiplied by 10. Equations for this process are presented below for the calculation of a similarity score for sample A's closeness in feature trends to sample AB, as compared with sample B.

(5) $$Slope\ Closeness_{A,AB} = 1 - \frac{|m_A - m_{AB}|}{\max[m_A, m_B, m_{AB}] - \min[m_A, m_B, m_{AB}]}$$

(6) $$Relative\ Strength_{<r_A^2>,<r_{AB}^2>} = 1 - \frac{|<r_A^2> - <r_{AB}^2>|}{((<r_A^2> + <r_{AB}^2>)/2)}$$

(7) $$Score_{A,AB} = Slope\ Closeness_{A,AB} \times Relative\ Strength_{<r_A^2>,<r_{AB}^2>} \times 10$$

Data and fitting from the tutorial data sets presented in **Figure A-13** below.

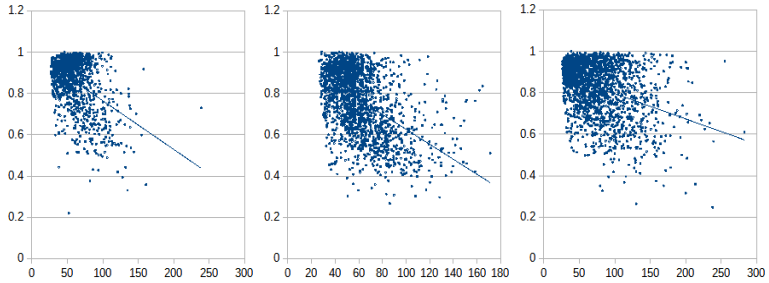

Figure A-13. Diameter-Roundness. Sample AB (left), sample A (center), and sample B (right). $Score_{A,AB}$ = 3.5 (moderate impact) and $Score_{B,AB}$ = 3.3 (moderate impact).

References

[1] E. Blanco, H. Shen, M. Ferrari, *Nat. Biotechnol.* **2015**, *33*, 941.

[2] N. Bertrand, J. Leroux, *J. Control. Release* **2012**, *161*, 152.

[3] T. Sun, Y. S. Zhang, B. Pang, D. C. Hyun, M. Yang, Y. Xia, *Angew. Chemie - Int. Ed.* **2014**, *53*, 12320.

[4] D. Peer, J. M. Karp, S. Hong, O. C. Farokhzad, R. Margalit, R. Langer, *Nat. Nanotechnol.* **2007**, *2*, 751.

[5] R. K. Upadhyay, *Biomed Res. Int.* **2014**, *2014*, 869269.

[6] N. Habibi, D. F. Quevedo, J. V. Gregory, J. Lahann, *Wiley Interdiscip. Rev. Nanomedicine Nanobiotechnology* **2020**, *12*, e1625.

[7] P. Ehrlich, *Proc. R. Soc. London* **1900**, *66*, 424.

[8] K. Strebhardt, A. Ullrich, *Nat. Rev. Cancer* **2008**, *8*, 473.

[9] O. C. Farokhzad, R. Langer, *ACS Nano* **2009**, *3*, 16.

[10] A. C. Anselmo, S. Mitragotri, *Bioeng. Transl. Med.* **2019**, *4*, e10143.

[11] D. Kim, K. Shin, S. G. Kwon, T. Hyeon, *Adv. Mater.* **2018**, *30*, 1802309.

[12] D. Peer, J. M. Karp, S. Hong, O. C. Farokhzad, R. Margalit, R. Langer, *Nat. Nanotechnol.* **2007**, *2*, 751.

[13] H. Ragelle, F. Danhier, V. Préat, R. Langer, D. G. Anderson, *Expert Opin. Drug Deliv.* **2017**, *14*, 851.

[14] M. J. Mitchell, M. M. Billingsley, R. M. Haley, M. E. Wechsler, N. A. Peppas, R. Langer,

Nat. Rev. Drug Discov. **2021**, *20*, 101.

[15] A. Z. Wang, R. Langer, O. C. Farokhzad, *Annu. Rev. Med.* **2012**, *63*, 185.

[16] J. Hrkach, R. Langer, *Drug Deliv. Transl. Res.* **2020**, *10*, 567.

[17] J. K. Patra, G. Das, L. F. Fraceto, E. V. R. Campos, M. del P. Rodriguez-Torres, L. S. Acosta-Torres, L. A. Diaz-Torres, R. Grillo, M. K. Swamy, S. Sharma, S. Habtemariam, H.-S. Shin, *J. Nanobiotechnology* **2018**, *16*, 71.

[18] F. Alexis, E. M. Pridgen, R. Langer, O. C. Farokhzad, in *Handb. Exp. Pharmacol.* (Ed.: M. Schäfer-Korting), Springer Berlin Heidelberg, Berlin, Heidelberg, **2010**, pp. 55–86.

[19] S. M. Moghimi, A. C. Hunter, J. C. Murray, *Pharmacol. Rev.* **2001**, *53*, 283.

[20] N. Kamaly, B. Yameen, J. Wu, O. C. Farokhzad, *Chem. Rev.* **2016**, *116*, 2602.

[21] K. Khalid, X. Tan, H. F. Mohd Zaid, Y. Tao, C. Lye Chew, D.-T. Chu, M. K. Lam, Y.-C. Ho, J. W. Lim, L. Chin Wei, *Bioengineered* **2020**, *11*, 328.

[22] N. Vol, M. Peptone, *Nature* **1976**, *263*, 797.

[23] A. L. Klibanov, K. Maruyama, V. P. Torchilin, L. Huang, *FEBS Lett.* **1990**, *268*, 235.

[24] Y. Barenholz, *J. Control. Release* **2012**, *160*, 117.

[25] D. Bobo, K. J. Robinson, J. Islam, K. J. Thurecht, S. R. Corrie, *Pharm. Res.* **2016**, *33*, 2373.

[26] S. Barua, S. Mitragotri, *Nano Today* **2014**, *9*, 223.

[27] A. C. Anselmo, S. Mitragotri, *J. Control. Release* **2014**, *190*, 531.

[28] V. Agrahari, V. Agrahari, A. K. Mitra, *Expert Opin. Drug Deliv.* **2017**, *14*, 285.

[29] Stefan Willhelm, Anthony J. Tavares, Qin Dai, Seiichi Ohta, Julie Audet, Harold F. Dvorak, Warren C.W. Chan, *Nat. Rev. Mater.* **2016**, *1*, 16014.

[30] H. Zou, Z. Wang, M. Feng, *J. Control. Release* **2015**, *214*, 121.

[31] Z. Zhao, A. Ukidve, J. Kim, S. Mitragotri, *Cell* **2020**, *181*, 151.

[32] S. Mitragotri, P. A. Burke, R. Langer, *Nat. Rev. Drug Discov.* **2014**, *13*, 655.

[33] L. Claesson-Welsh, E. Dejana, D. M. McDonald, *Trends Mol. Med.* **2021**, *27*, 314.

[34] J. Leal, H. D. C. Smyth, D. Ghosh, *Int. J. Pharm.* **2017**, *532*, 555.

[35] H. C. Zierden, A. Josyula, R. L. Shapiro, H. T. Hsueh, J. Hanes, L. M. Ensign, *Trends Mol. Med.* **2021**, *27*, 436.

[36] S. P. Bandi, S. Bhatnagar, V. V. K. Venuganti, *Acta Biomater.* **2021**, *119*, 13.

[37] J. S. Crater, R. L. Carrier, *Macromol. Biosci.* **2010**, *10*, 1473.

[38] T. L. Carlson, J. Y. Lock, R. L. Carrier, *Annu. Rev. Biomed. Eng.* **2018**, *20*, 197.

[39] J. das Neves, B. Sarmento, *Adv. Drug Deliv. Rev.* **2018**, *124*, 1.

[40] K. I. Cupic, J. J. Rennick, A. P. R. Johnston, G. K. Such, *Nanomedicine* **2018**, *14*, 215.

[41] L. I. Selby, C. M. Cortez-Jugo, G. K. Such, A. P. R. Johnston, *WIREs Nanomedicine and Nanobiotechnology* **2017**, *9*, e1452.

[42] H. Zou, Z. Wang, M. Feng, *J. Control. Release* **2015**, *214*, 121.

[43] K. B. Shepard, D. A. Christie, C. L. Sosa, C. B. Arnold, R. D. Priestley, *Appl. Phys. Lett.* **2015**, *106*, 093104.

[44] L. Palanikumar, M. T. Jeena, K. Kim, J. Y. Oh, C. Kim, M. H. Park, J. H. Ryu, *Sci. Rep.* **2017**, *7*, 1.

[45] A. B. Pawar, I. Kretzschmar, *Langmuir* **2009**, *25*, 9057.

[46] D. Varadharajan, H. Turgut, J. Lahann, H. Yabu, G. Delaittre, *Adv. Funct. Mater.* **2018**, *28*, 1.

[47] S. Rahmani, S. Saha, H. Durmaz, A. Donini, A. C. Misra, J. Yoon, J. Lahann, *Angew. Chemie - Int. Ed.* **2014**, *53*, 2332.

[48] Z. Nie, W. Li, M. Seo, S. Xu, E. Kumacheva, *J. Am. Chem. Soc.* **2006**, *128*, 9408.

[49] L. Hong, S. Jiang, S. Granick, *Langmuir* **2006**, *22*, 9495.

[50] B. V. N. Paunov, O. J. Cayre, *Adv. Mater.* **2004**, *16*, 788.

[51] J. Zhang, J. Jin, H. Zhao, *Langmuir* **2009**, *25*, 6431.

[52] Y. K. Takahara, S. Ikeda, S. Ishino, K. Tachi, K. Ikeue, T. Sakata, T. Hasegawa, H. Mori, M. Matsumura, B. Ohtani, *J. Am. Chem. Soc.* **2005**, *127*, 6271.

[53] L. Petit, J. P. Manaud, C. Mingotaud, S. Ravaine, E. Duguet, *Mater. Lett.* **2001**, *51*, 478.

[54] S. G. Jang, D. G. Choi, C. J. Heo, S. Y. Lee, S. M. Yang, *Adv. Mater.* **2008**, *20*, 4862.

[55] Y. P. Zhao, D. X. Ye, G. C. Wang, T. M. Lu, *Nano Lett.* **2002**, *2*, 351.

[56] G. Nikravan, V. Haddadi-asl, M. Salami-kalajahi, *Colloids Surfaces B Biointerfaces* **2018**, *165*, 1.

[57] Y. Liang, J. H. Jordahl, H. Ding, X. Deng, J. Lahann, *Chem. Vap. Depos.* **2015**, *21*, 288.

[58] A. M. Yake, C. E. Snyder, D. Velegol, *Langmuir* **2007**, *23*, 9069.

[59] B. C. Geiger, S. Wang, R. F. Padera, A. J. Grodzinsky, P. T. Hammond, *Sci. Transl. Med.* **2018**, *10*, eaat8800.

[60] A. M. Yake, A. S. Zahr, H. A. Jerri, M. V. Pishko, D. Velegol, *Biomacromolecules* **2007**, *8*, 1958.

[61] S. Rahmani, C. H. Villa, A. F. Dishman, M. E. Grabowski, D. C. Pan, H. Durmaz, A. C. Misra, L. Colón-Meléndez, M. J. Solomon, V. R. Muzykantov, J. Lahann, *J. Drug Target.* **2015**, *23*, 750.

[62] V. Lopez, M. Rocio Villegas, V. Rodriguez, G. Villaverde, D. Lozano, A. Baeza, M. Vallet-Regi, *Appl. Mater. Interfaces* **2017**, *9*, 26697.

[63] A. Shimoda, S. Sawada, A. Kano, A. Maruyama, M. Winnik, K. Akiyoshi, *Colloids Surfaces B Biointerfaces* **2012**, *99*, 38.

[64] J. Song, B. Wu, Z. Zhou, G. Zhu, Y. Liu, Z. Yang, L. Lin, G. Yu, F. Zhang, G. Zhang, H. Duan, G. D. Stucky, X. Chen, *Angew. Chemie - Int. Ed.* **2017**, *56*, 8110.

[65] N. Castro, D. Constantin, P. Davidson, B. Abécassis, *Soft Matter* **2016**, *12*, 9666.

[66] S. W. Morton, M. J. Lee, Z. J. Deng, E. C. Dreaden, E. Siouve, K. E. Shopsowitz, N. J. Shah, M. B. Yaffe, P. T. Hammond, M. L. Mcmaster, S. Y. Kristinsson, I. Turesson, M. Bjorkholm, O. Landgren, S. W. Morton, M. J. Lee, Z. J. Deng, E. C. Dreaden, E. Siouve, K. E. Shopsowitz, N. J. Shah, M. B. Yaffe, P. T. Hammond, *Sci. Signal.* **2014**, *7*, ra44.

[67] T. L. Reddy, K. R. Garikapati, S. G. Reddy, B. V. S. Reddy, J. S. Yadav, U. Bhadra, M. P. Bhadra, *Sci. Rep.* **2016**, *6*, 1.

[68] R. Kuai, C. Subramanian, P. T. White, B. N. Timmermann, J. J. Moon, M. S. Cohen, A. Schwendeman, *Int. J. Nanomedicine* **2017**, *12*, 6581.

[69] Y. Guo, W. Yuan, B. Yu, R. Kuai, W. Hu, E. E. Morin, M. T. Garcia-Barrio, J. Zhang, J. J. Moon, A. Schwendeman, Y. Eugene Chen, *EBioMedicine* **2018**, *28*, 225.

[70] K. P. Yuet, D. K. Hwang, R. Haghogooie, P. S. Doyle, *Langmuir* **2010**, *26*, 4281.

[71] K. Roh, D. C. Martin, J. Lahann, *Nat. Mater.* **2005**, *4*, 759.

[72] S. Hwang, K.-H. Roh, D. W. Lim, G. Wang, C. Uher, J. Lahann, *Phys. Chem. Chem. Phys.* **2010**, *12*, 11894.

[73] Y. Wang, Y. Zhang, B. Wang, Y. Cao, Q. Yu, T. Yin, *J. Nanoparticle Res.* **2013**, *15*, 1726.

[74] Y. Cao, B. Wang, Y. Wang, D. Lou, *J. Pharm. Sci.* **2014**, *103*, 3205.

[75] A. R. it. C. Duarte, B. Ünal, J. F. Mano, R. L. Reis, K. F. Jensen, *Langmuir* **2014**, *30*, 12391.

[76] C. Cha, J. Oh, K. Kim, Y. Qiu, M. Joh, S. R. Shin, X. Wang, G. Camci-Unal, K. T. Wan, R. Liao, A. Khademhosseini, *Biomacromolecules* **2014**, *15*, 283.

[77] K. H. Roh, D. C. Martin, J. Lahann, *J. Am. Chem. Soc.* **2006**, *128*, 6796.

[78] R. Nahire, M. K. Haldar, S. Paul, A. Mergoum, A. H. Ambre, K. S. Katti, K. N. Gange, D. K. Srivastava, K. Sarkar, S. Mallik, *Biomacromolecules* **2013**, *14*, 841.

[79] Z. J. Deng, S. W. Morton, E. Ben-Akiva, E. C. Dreaden, K. E. Shopsowitz, P. T. Hammond, *ACS Nano* **2013**, *7*, 9571.

[80] Y. Liu, B. Huang, J. Zhu, K. Feng, Y. Yuan, C. Liu, *RSC Adv.* **2018**, *8*, 40598.

[81] N. K. Devaraj, E. J. Keliher, G. M. Thurber, M. Nahrendorf, *Bioconjug. Chem.* **2009**, *20*, 397.

[82] C. H. Reynolds, N. Annan, K. Beshah, J. H. Huber, S. H. Shaber, R. E. Lenkinski, J. A. Wortman, *J. Am. Chem. Soc.* **2000**, *122*, 8940.

[83] Y. Liu, Z. Chen, C. Liu, D. Yu, Z. Lu, N. Zhang, *Biomaterials* **2011**, *32*, 5167.

[84] M. S. Strozyk, D. J. de Aberasturi, J. V Gregory, M. Brust, J. Lahann, L. M. Liz-Marzán, *Adv. Funct. Mater.* **2017**, *27*, 1.

[85] S. Hwang, J. Lahann, *Macromol. Rapid Commun.* **2012**, *33*, 1178.

[86] S. Rahmani, A. M. Ross, T. H. Park, H. Durmaz, A. F. Dishman, D. M. Prieskorn, N. Jones, R. A. Altschuler, J. Lahann, *Adv. Healthc. Mater.* **2016**, *5*, 94.

[87] A. H. Gröschel, A. Walther, T. I. Löbling, F. H. Schacher, H. Schmalz, A. H. E. Müller, *Nature* **2013**, *503*, 247.

[88] A. MaHam, Z. Tang, H. Wu, J. Wang, Y. Lin, *Small* **2009**, *5*, 1706.

[89] E. N. Hoogenboezem, C. L. Duvall, *Adv. Drug Deliv. Rev.* **2018**, *130*, 73.

[90] S. Hong, D. W. Choi, H. N. Kim, C. G. Park, W. Lee, H. H. Park, *Pharmaceutics* **2020**, *12*, 1.

[91] W. Lohcharoenkal, L. Wang, Y. C. Chen, Y. Rojanasakul, *Biomed Res. Int.* **2014**, *2014*, 1.

[92] I. Casanova, U. Unzueta, I. Arroyo-Solera, M. V. Céspedes, A. Villaverde, R. Mangues, E.

Vazquez, *Curr. Opin. Pharmacol.* **2019**, *47*, 1.

[93] A. O. Elzoghby, W. M. Samy, N. A. Elgindy, *J. Control. Release* **2012**, *157*, 168.

[94] A. Jain, S. K. Singh, S. K. Arya, S. C. Kundu, S. Kapoor, *ACS Biomater. Sci. Eng.* **2018**, *4*, 3939.

[95] L. P. Herrera Estrada, J. A. Champion, *Biomater. Sci.* **2015**, *3*, 787.

[96] D. Diaz, A. Care, A. Sunna, *Genes (Basel).* **2018**, *9*, 370.

[97] A. K. Singla, A. Garg, D. Aggarwal, *Int. J. Pharm.* **2002**, *235*, 179.

[98] N. Desai, *Drug Deliv. Rep.* **2010**, *505*, 1.

[99] L. Q. Thao, C. Lee, B. Kim, S. Lee, T. H. Kim, J. O. Kim, E. S. Lee, K. T. Oh, H. G. Choi, S. D. Yoo, Y. S. Youn, *Colloids Surfaces B Biointerfaces* **2017**, *152*, 183.

[100] T. Maruyama, V. T. G. Chuang, J. Fang, R. Kinoshita, M. Otagiri, H. Maeda, H. Watanabe, T. Shimizu, Y. Ishima, K. Okuhira, H. Nakamura, T. Ishida, *Biomaterials* **2017**, *140*, 162.

[101] A. Sparreboom, C. D. Scripture, V. Trieu, P. Williams, T. De, A. Yang, B. Beals, W. D. Figg, M. Hawkins, N. Desai, *Clin. Cancer Res.* **2005**, *11*, 4136.

[102] H. B. Ruttala, Y. T. Ko, *Pharm. Res.* **2015**, *32*, 1002.

[103] N. P. Desai, *Nanoparticle Compositions of Albumin and Paclitaxel*, **2014**.

[104] L. H. Estrada, S. Chu, J. A. Champion, *J. Pharm. Sci.* **2014**, *103*, 1863.

[105] M. J. Hawkins, P. Soon-Shiong, N. Desai, *Adv. Drug Deliv. Rev.* **2008**, *60*, 876.

[106] Y. L. Tan, H. K. Ho, *Drug Discov. Today* **2018**, *23*, 1108.

[107] T. O. Yeates, Y. Liu, J. Laniado, *Curr. Opin. Struct. Biol.* **2016**, *39*, 134.

[108] R. Arai, *Biophys. Rev.* **2018**, *10*, 391.

[109] N. M. Molino, S. W. Wang, *Curr. Opin. Biotechnol.* **2014**, *28*, 75.

[110] S. J. Kaczmarczyk, K. Sitaraman, H. A. Young, S. H. Hughes, D. K. Chatterjee, *Proc. Natl.*

Acad. Sci. **2011**, *108*, 16998.

[111] Z. Zhen, W. Tang, H. Chen, X. Lin, T. Todd, G. Wang, T. Cowger, X. Chen, J. Xie, *ACS Nano* **2013**, *7*, 4830.

[112] N. Kawakami, H. Kondo, Y. Matsuzawa, K. Hayasaka, E. Nasu, K. Sasahara, R. Arai, K. Miyamoto, *Angew. Chemie - Int. Ed.* **2018**, *57*, 12400.

[113] D. M. Ecker, S. D. Jones, H. L. Levine, *MAbs* **2015**, *7*, 9.

[114] C. Weber, C. Coester, J. Kreuter, K. Langer, *Int. J. Pharm.* **2000**, *194*, 91.

[115] B. Von Storp, A. Engel, A. Boeker, M. Ploeger, K. Langer, *J. Microencapsul.* **2012**, *29*, 138.

[116] K. Langer, M. G. Anhorn, I. Steinhauser, S. Dreis, D. Celebi, N. Schrickel, S. Faust, V. Vogel, *Int. J. Pharm.* **2008**, *347*, 109.

[117] S. Dreis, F. Rothweiler, M. Michaelis, J. Cinatl, J. Kreuter, K. Langer, *Int. J. Pharm.* **2007**, *341*, 207.

[118] L. P. Herrera Estrada, J. A. Champion, *Biomater. Sci.* **2015**, *3*, 787.

[119] M. Fathi, F. Donsi, D. J. McClements, *Compr. Rev. Food Sci. Food Saf.* **2018**, *17*, 920.

[120] S. Shao, X. Shen, M. Guo, *Int. J. Food Sci. Technol.* **2018**, *53*, 2205.

[121] T. Z. Chang, S. S. Stadmiller, E. Staskevicius, J. A. Champion, *Biomater. Sci.* **2017**, *5*, 223.

[122] A. N. Tsoras, J. A. Champion, *Bioconjug. Chem.* **2018**, *29*, 776.

[123] L. Deng, T. Mohan, T. Z. Chang, G. X. Gonzalez, Y. Wang, Y. M. Kwon, S. M. Kang, R. W. Compans, J. A. Champion, B. Z. Wang, *Nat. Commun.* **2018**, *9*, 1.

[124] W. Fiers, M. De Filette, K. El Bakkouri, B. Schepens, K. Roose, M. Schotsaert, A. Birkett, X. Saelens, *Vaccine* **2009**, *27*, 6280.

[125] C. B. Turley, R. E. Rupp, C. Johnson, D. N. Taylor, J. Wolfson, L. Tussey, U. Kavita, L.

Stanberry, A. Shaw, *Vaccine* **2011**, *29*, 5145.

[126] T. Z. Chang, L. Deng, B.-Z. Wang, J. A. Champion, *PLoS One* **2018**, *13*, e0202300.

[127] K.-H. Roh, D. C. Martin, J. Lahann, *Nat. Mater.* **2005**, *4*, 759.

[128] S. Rahmani, S. Saha, H. Durmaz, A. Donini, A. C. Misra, J. Yoon, J. Lahann, *Angew. Chemie - Int. Ed.* **2014**, *53*, 2332.

[129] J. R. Mauck, S. K. Yadav, J. M. Sadler, J. J. La Scala, G. R. Palmese, K. M. Schmalbach, J. F. Stanzione III, *Macromol. Chem. Phys.* **2017**, *218*, 1700013.

[130] T. H. Park, T. W. Eyster, J. M. Lumley, S. Hwang, K. J. Lee, A. Misra, S. Rahmani, J. Lahann, *Small* **2013**, *9*, 3051.

[131] A. C. Misra, S. Bhaskar, N. Clay, J. Lahann, *Adv. Mater.* **2012**, *24*, 3850.

[132] J. V Gregory, D. R. Vogus, A. Barajas, M. A. Cadena, S. Mitragotri, J. Lahann, *Adv. Healthc. Mater.* **2020**, *9*, 1.

[133] A. C. Misra, J. Lahann, *Adv. Healthc. Mater.* **2018**, *7*, 1.

[134] M. Á. Fernández-rodríguez, S. Rahmani, C. K. J. Yu, M. Á. Rodríguez-valverde, M. Á. Cabrerizo-vílchez, C. A. Michel, J. Lahann, R. Hidalgo-álvarez, *Colloids Surfaces A Physicochem. Eng. Asp.* **2018**, *536*, 259.

[135] A. M. Ross, S. Rahmani, D. M. Prieskorn, A. F. Dishman, J. M. Miller, J. Lahann, R. A. Altschuler, *J. Biomed. Mater. Res. Part A* **2016**, *104*, 1510.

[136] S. Rahmani, S. Ashraf, R. Hartmann, A. F. Dishman, M. V. Zyuzin, C. K. J. Yu, W. J. Parak, J. Lahann, *Bioeng. Transl. Med.* **2016**, *1*, 82.

[137] S. Rahmani, C. H. Villa, A. F. Dishman, M. E. Grabowski, D. C. Pan, H. Durmaz, A. C. Misra, L. Colón-Meléndez, M. J. Solomon, V. R. Muzykantov, J. Lahann, *J. Drug Target.* **2015**, *23*, 750.

[138] A. C. Misra, K. E. Luker, H. Durmaz, G. D. Luker, J. Lahann, *Biomacromolecules* **2015**, *16*, 2412.

[139] E. Sokolovskaya, S. Rahmani, A. C. Misra, S. Bräse, J. Lahann, *ACS Appl. Mater. Interfaces* **2015**, *7*, 9744.

[140] J. Lahann, *Small* **2011**, *7*, 1149.

[141] S. Rahmani, J. Lahann, *MRS Bull.* **2014**, *39*, 251.

[142] R. T. Collins, J. J. Jones, M. T. Harris, O. A. Basaran, *Nat. Phys.* **2008**, *4*, 149.

[143] S. J. Gaskell, *J. Mass Spectrom.* **1997**, *32*, 677.

[144] L. Peltonen, H. Valo, R. Kolakovic, T. Laaksonen, J. Hirvonen, *Expert Opin. Drug Deliv.* **2010**, *7*, 705.

[145] M. Cloupeau, B. Prunet-Foch, *J. Electrostat.* **1989**, *22*, 135.

[146] S. Rahmani, T. Park, A. Frances, J. Lahann, *J. Control. Release* **2013**, *172*, 239.

[147] K. H. Roh, D. C. Martin, J. Lahann, *Nat. Mater.* **2005**, *4*, 759.

[148] A. C. Misra, S. Bhaskar, N. Clay, J. Lahann, *Adv. Mater.* **2012**, *24*, 3850.

[149] J. Lahann, *Small* **2011**, *7*, 1149.

[150] S. Bhaskar, K. M. Pollock, M. Yoshida, J. Lahann, *Small* **2010**, *6*, 404.

[151] S. Rahmani, S. Ashraf, R. Hartmann, A. F. Dishman, M. V Zyuzin, C. K. J. Yu, W. J. Parak, J. Lahann, *Bioeng. Transl. Med.* **2016**, *1*, 82.

[152] M. Ayer, H. Klok, *J. Control. Release* **2017**, *259*, 92.

[153] J. S. Brenner, S. Mitragotri, V. R. Muzykantov, *Annu. Rev. Biomed. Eng.* **2021**, *23*, 225.

[154] N. Doshi, A. J. Swiston, J. B. Gilbert, M. L. Alcaraz, R. E. Cohen, M. F. Rubner, S. Mitragotri, *Adv. Mater.* **2011**, *23*, H105.

[155] R. Mooney, Y. Weng, E. Garcia, S. Bhojane, L. Smith-Powell, S. U. Kim, A. J. Annala, K.

S. Aboody, J. M. Berlin, *J. Control. Release* **2014**, *191*, 82.

[156] V. R. Muzykantov, *Expert Opin. Drug Deliv.* **2010**, *7*, 403.

[157] G. Tomaiuolo, *Biomicrofluidics* **2014**, *8*, 1.

[158] L. Pang, C. Zhang, J. Qin, L. Han, R. Li, C. Hong, H. He, J. Wang, *Drug Deliv.* **2017**, *24*, 83.

[159] Z. Wu, T. Li, J. Li, W. Gao, T. Xu, C. Christianson, W. Gao, M. Galarnyk, Q. He, L. Zhang, J. Wang, *ACS Nano* **2014**, *8*, 12041.

[160] C. H. Villa, J. Seghatchian, V. Muzykantov, *Transfus. Apher. Sci.* **2016**, *55*, 275.

[161] C. H. Villa, D. B. Cines, D. L. Siegel, V. Muzykantov, *Transfus. Med. Rev.* **2017**, *31*, 26.

[162] E. Chambers, S. Mitragotri, *Exp. Biol. Med.* **2007**, *232*, 958.

[163] C. H. Villa, A. C. Anselmo, S. Mitragotri, V. Muzykantov, *Adv. Drug Deliv. Rev.* **2016**, *106*, 88.

[164] E. Chambers, S. Mitragotri, *J. Control. Release* **2004**, *100*, 111.

[165] A. C. Anselmo, V. Gupta, B. J. Zern, D. Pan, M. Zakrewsky, V. Muzykantov, S. Mitragotri, *ACS Nano* **2013**, *7*, 11129.

[166] J. S. Brenner, D. C. Pan, J. W. Myerson, O. A. Marcos-Contreras, C. H. Villa, P. Patel, H. Hekierski, S. Chatterjee, J. Q. Tao, H. Parhiz, K. Bhamidipati, T. G. Uhler, E. D. Hood, R. Y. Kiseleva, V. S. Shuvaev, T. Shuvaeva, M. Khoshnejad, I. Johnston, J. V. Gregory, J. Lahann, T. Wang, E. Cantu, W. M. Armstead, S. Mitragotri, V. Muzykantov, *Nat. Commun.* **2018**, *9*, 1.

[167] A. C. Anselmo, S. Kumar, V. Gupta, A. M. Pearce, A. Ragusa, V. Muzykantov, S. Mitragotri, *Biomaterials* **2015**, *68*, 1.

[168] S. I. Grivennikov, F. R. Greten, M. Karin, *Cell* **2010**, *140*, 883.

[169] P. Sahdev, L. J. Ochyl, J. J. Moon, *Pharm. Res.* **2014**, *31*, 2563.

[170] S. Nourshargh, R. Alon, *Immunity* **2014**, *41*, 694.

[171] S. Gordon, P. R. Taylor, *Nat. Rev. Immunol.* **2005**, *5*, 953.

[172] C. Murdoch, A. Giannoudis, C. E. Lewis, *Blood* **2004**, *104*, 2224.

[173] C. Lewis, C. Murdoch, *Am. J. Pathol.* **2005**, *167*, 627.

[174] M. A. Evans, P. J. Huang, Y. Iwamoto, K. N. Ibsen, E. M. Chan, Y. Hitomi, P. C. Ford, S. Mitragotri, *Chem. Sci.* **2018**, *9*, 3729.

[175] T. L. Moore, D. Hauser, T. Gruber, B. Rothen-Rutishauser, M. Lattuada, A. Petri-Fink, R. Lyck, *ACS Appl. Mater. Interfaces* **2017**, *9*, 18501.

[176] J. Si, S. Shao, Y. Shen, K. Wang, *Small* **2016**, 5108.

[177] J. Choi, H. Kim, E. Jin, J. Jung, J. Park, H. Chung, J. Seong, J. Shin, H. Joo, S. Yeol, S. Jeong, E. Kyung, *Biomaterials* **2012**, *33*, 4195.

[178] E. V Batrakova, H. E. Gendelman, A. V Kabanov, *Expert Opin. Drug Deliv.* **2011**, *8*, 415.

[179] E. V Batrakova, S. Li, A. D. Reynolds, R. L. Mosley, T. K. Bronich, A. V Kabanov, H. E. Gendelman, *Bioconjug. Chem.* **2007**, *18*, 1498.

[180] S. K. Baek, A. R. Makkouk, T. Krasieva, C. H. Sun, S. J. Madsen, H. Hirschberg, *J. Neurooncol.* **2011**, *104*, 439.

[181] S. J. Madsen, C. Christie, S. J. Hong, A. Trinidad, Q. Peng, F. A. Uzal, H. Hirschberg, *Lasers Med. Sci.* **2015**, *30*, 1357.

[182] A. J. Swiston, C. Cheng, S. H. Um, D. J. Irvine, R. E. Cohen, M. F. Rubner, *Nano Lett.* **2008**, *8*, 4446.

[183] A. J. Swiston, J. B. Gilbert, D. J. Irvine, R. E. Cohen, M. F. Rubner, *Biomacromolecules* **2010**, *11*, 1826.

[184] N. L. Klyachko, R. Polak, M. J. Haney, Y. Zhao, R. J. Gomes Neto, M. C. Hill, A. V. Kabanov, R. E. Cohen, M. F. Rubner, E. V. Batrakova, *Biomaterials* **2017**, *140*, 79.

[185] S. L. Deshmane, S. Kremlev, S. Amini, B. E. Sawaya, *J. Interf. Cytokine Res.* **2009**, *29*, 313.

[186] A. C. Anselmo, J. B. Gilbert, S. Kumar, V. Gupta, R. E. Cohen, M. F. Rubner, S. Mitragotri, *J. Control. Release* **2015**, *199*, 29.

[187] B. Huang, W. D. Abraham, Y. Zheng, S. C. Bustamante López, S. S. Luo, D. J. Irvine, *Sci. Transl. Med.* **2015**, *7*, 291ra94.

[188] L. Wayteck, H. Dewitte, L. De Backer, K. Breckpot, J. Demeester, S. C. De Smedt, K. Raemdonck, *Biomaterials* **2016**, *77*, 243.

[189] N. P. Restifo, M. E. Dudley, S. A. Rosenberg, *Nat. Rev. Immunol.* **2012**, *12*, 269.

[190] M. T. Stephan, J. J. Moon, S. H. Um, A. Bersthteyn, D. J. Irvine, *Nat. Med.* **2010**, *16*, 1035.

[191] L. A. L. Fliervoet, E. Mastrobattista, *Adv. Drug Deliv. Rev.* **2016**, *106*, 63.

[192] S. Tan, T. Wu, D. Zhang, Z. Zhang, *Theranostics* **2015**, *5*, 863.

[193] M. Mimeault, R. Hauke, S. K. Batra, *Clin. Pharmacol. Ther.* **2007**, *82*, 252.

[194] M. F. Corsten, K. Shah, *Lancet Oncol.* **2008**, *9*, 376.

[195] X. Huang, F. Zhang, H. Wang, G. Niu, K. Y. Choi, M. Swierczewska, G. Zhang, H. Gao, Z. Wang, L. Zhu, H. S. Choi, S. Lee, X. Chen, *Biomaterials* **2013**, *34*, 1772.

[196] L. Li, Y. Guan, H. Liu, N. Hao, T. Liu, X. Meng, C. Fu, Y. Li, Q. Qu, Y. Zhang, S. Ji, L. Chen, D. Chen, F. Tang, *ACS Nano* **2011**, *5*, 7462.

[197] M. Roger, A. Clavreul, M. C. Venier-Julienne, C. Passirani, L. Sindji, P. Schiller, C. Montero-Menei, P. Menei, *Biomaterials* **2010**, *31*, 8393.

[198] R. Mooney, L. Roma, D. Zhao, D. Van Haute, E. Garcia, S. U. Kim, A. J. Annala, K. S.

Aboody, J. M. Berlin, *ACS Nano* **2014**, *8*, 12450.

[199] S. Ding, C. P. O'Banion, J. G. Welfare, D. S. Lawrence, *Cell Chem. Biol.* **2018**, *25*, 648.

[200] A. C. Anselmo, S. Mitragotri, *J. Control. Release* **2014**, *190*, 531.

[201] B. Singh, S. Mitragotri, *Biotechnol. Adv.* **2020**, *42*, 1.

[202] J. Shi, P. W. Kantoff, R. Wooster, O. C. Farokhzad, *Nat. Rev. Cancer* **2017**, *17*, 20.

[203] S. Senapati, A. K. Mahanta, S. Kumar, P. Maiti, *Signal Transduct. Target. Ther.* **2018**, *3*, 1.

[204] Y. Xin, M. Yin, L. Zhao, F. Meng, L. Luo, *Cancer Biol. Med.* **2017**, *14*, 228.

[205] H. Ragelle, F. Danhier, V. Préat, R. Langer, D. G. Anderson, *Expert Opin. Drug Deliv.* **2017**, *14*, 851.

[206] E. Blanco, H. Shen, M. Ferrari, *Nat. Biotechnol.* **2015**, *33*, 941.

[207] K. A. Gawde, S. Sau, K. Tatiparti, S. K. Kashaw, M. Mehrmohammadi, A. S. Azmi, A. K. Iyer, *Colloids Surfaces B Biointerfaces* **2018**, *167*, 8.

[208] L. Deng, T. Mohan, T. Z. Chang, G. X. Gonzalez, Y. Wang, Y. M. Kwon, S. M. Kang, R. W. Compans, J. A. Champion, B. Z. Wang, *Nat. Commun.* **2018**, *9*, 1.

[209] Z. Guo, F. Wang, Y. Di, L. Yao, X. Yu, D. Fu, J. Li, C. Jin, *Int. J. Nanomedicine* **2018**, *13*, 4869.

[210] J. Chen, X. Yi, K. Yang, P. Ning, L. Tian, G. Wang, Q. Chen, Z. Liu, *Theranostics* **2017**, *7*, 614.

[211] C. Weber, C. Coester, J. Kreuter, K. Langer, *Int. J. Pharm.* **2000**, *194*, 91.

[212] X. Yu, X. Gou, P. Wu, L. Han, D. Tian, F. Du, Z. Chen, F. Liu, G. Deng, A. T. Chen, C. Ma, J. Liu, S. M. Hashmi, X. Guo, X. Wang, H. Zhao, X. Liu, X. Zhu, K. Sheth, Q. Chen, L. Fan, J. Zhou, *Adv. Mater.* **2018**, *30*, 1705383.

[213] M. a Socinski, I. Bondarenko, N. a Karaseva, A. M. Makhson, I. Vynnychenko, I. Okamoto,

J. K. Hon, V. Hirsh, P. Bhar, H. Zhang, J. L. Iglesias, M. F. Renschler, *J. Clin. Oncol.* **2012**, *30*, 2055.

[214] U. S. Food & Drug Administration, "ABRAXANE® for Injectable Suspension (paclitaxel protein-bound particles for injectable suspension)," can be found under http://www.accessdata.fda.gov/drugsatfda_docs/label/2009/021660s022lbl.pdf, **2013**.

[215] S. Rahmani, S. Saha, H. Durmaz, A. Donini, A. C. Misra, J. Yoon, J. Lahann, *Angew. Chemie - Int. Ed.* **2014**, *53*, 2332.

[216] A. C. Misra, K. E. Luker, H. Durmaz, G. D. Luker, J. Lahann, *Biomacromolecules* **2015**, *16*, 2412.

[217] J. Yoon, T. W. Eyster, A. C. Misra, J. Lahann, *Adv. Mater.* **2015**, *27*, 4509.

[218] N. J. Greenfield, *Nat. Protoc.* **2007**, *1*, 2876.

[219] N. G. James, A. B. Mason, *Anal. Biochem.* **2008**, *378*, 202.

[220] N. Sreerama, R. W. Woody, *Anal. Biochem.* **2000**, *287*, 252.

[221] N. Sreerama, R. W. Woody, *Anal. Biochem.* **1993**, *209*, 32.

[222] S. W. Provencher, J. Glöckner, *Biochemistry* **1981**, *20*, 33.

[223] L. A. Compton, W. C. Johnson, *Anal. Biochem.* **1986**, *155*, 155.

[224] L. Whitmore, B. A. Wallace, *Biopolymers* **2008**, *89*, 392.

[225] S. Bhaskar, K. M. Pollock, M. Yoshida, J. Lahann, *Small* **2010**, *6*, 404.

[226] G. I. Taylor, *Proc. R. Soc. London. Ser. A. Math. Phys. Sci.* **1964**, *280*, 383.

[227] I. Migneault, C. Dartiguenave, M. J. Bertrand, K. C. Waldron, *Biotechniques* **2004**, *37*, 790.

[228] J. F. Povey, C. M. Smales, S. J. Hassard, M. J. Howard, *J. Struct. Biol.* **2007**, *157*, 329.

[229] S. Fleischer, A. Shapira, O. Regev, N. Nseir, E. Zussman, T. Dvir, *Biotechnol. Bioeng.* **2014**, *111*, 1246.

[230] K. Ulbrich, T. Hekmatara, E. Herbert, J. Kreuter, *Eur. J. Pharm. Biopharm.* **2009**, *71*, 251.

[231] G. Sharma, A. R. Sharma, J. S. Nam, G. P. C. Doss, S. S. Lee, C. Chakraborty, *J. Nanobiotechnology* **2015**, *13*, 1.

[232] H. Sakai, *J. Funct. Biomater.* **2017**, *8*, 10.

[233] V. L. Hughey, E. A. Johnson, *Appl. Environ. Microbiol.* **1987**, *53*, 2165.

[234] X. Guo, Y. Cheng, X. Zhao, Y. Luo, J. Chen, W. E. Yuan, *J. Nanobiotechnology* **2018**, *16*, 1.

[235] J. V. Gregory, P. Kadiyala, R. Doherty, M. Cadena, S. Habeel, E. Ruoslahti, P. R. Lowenstein, M. G. Castro, J. Lahann, *bioRxiv* **2019**, 862581.

[236] R. K. Sajja, S. Prasad, L. Cucullo, *Fluids Barriers CNS* **2014**, *11*, 8.

[237] N. Habibi, S. Christau, L. J. Ochyl, Z. Fan, A. Hassani Najafabadi, M. Kuehnhammer, M. Zhang, M. Helgeson, R. von Klitzing, J. J. Moon, J. Lahann, *Adv. Ther.* **2020**, *3*, 2000100.

[238] W. J. Gradishar, *Expert Opin. Pharmacother.* **2006**, *7*, 1041.

[239] Y. Jang, W. T. Choi, W. T. Heller, Z. Ke, E. R. Wright, J. A. Champion, *Small* **2017**, *13*, 1700399.

[240] S. Mitragotri, J. Lahann, *Nat. Mater.* **2009**, *8*, 15.

[241] E. N. Hoogenboezem, C. L. Duvall, *Adv. Drug Deliv. Rev.* **2018**, *130*, 73.

[242] D. Sleep, *Expert Opin. Drug Deliv.* **2015**, *12*, 793.

[243] T. E. Stinchcombe, *Nanomedicine* **2007**, *2*, 415.

[244] D. A. Yardley, *J. Control. Release* **2013**, *170*, 365.

[245] G. Pillai, *SOJ Pharm. Pharm. Sci.* **2014**, *1*, 1.

[246] C. M. Dawidczyk, C. Kim, J. H. Park, L. M. Russell, K. H. Lee, M. G. Pomper, P. C. Searson, *J. Control. Release* **2014**, *187*, 133.

[247] K. C. Liu, Y. Yeo, *Arch. Pharm. Res.* **2014**, *37*, 16.

[248] S. Bae, K. Ma, T. H. Kim, E. S. Lee, K. T. Oh, E. S. Park, K. C. Lee, Y. S. Youn, *Biomaterials* **2012**, *33*, 1536.

[249] D. Zhao, X. Zhao, Y. Zu, J. Li, Y. Zhang, R. Jiang, Z. Zhang, *Int. J. Nanomedicine* **2010**, *5*, 669.

[250] A. O. Elzoghby, W. M. Samy, N. A. Elgindy, *J. Control. Release* **2012**, *161*, 38.

[251] D. F. Quevedo, N. Habibi, J. V. Gregory, Y. Hernandez, T. D. Brown, R. Miki, B. N. Plummer, S. Rahmani, J. E. Raymond, S. Mitragotri, J. Lahann, *Macromol. Rapid Commun.* **2020**, *41*, 2000425.

[252] "Peptide calculator," can be found under https://www.bachem.com/knowledge-center/peptide-calculator/.

[253] A. O. Elzoghby, W. M. Samy, N. A. Elgindy, *J. Control. Release* **2012**, *161*, 38.

[254] M. Joshi, M. Nagarsenkar, B. Prabhakar, *J. Drug Deliv. Sci. Technol.* **2020**, *56*, 101529.

[255] P. T. Gomme, K. B. McCann, *Drug Discov. Today* **2005**, *10*, 267.

[256] A. G. HOVANESSIAN, Z. L. AWDEH, *Eur. J. Biochem.* **1976**, *68*, 333.

[257] F. J. J. Fogg, D. A. Hutton, K. Jumel, J. P. Pearson, S. E. Harding, A. Allen, *Biochem. J.* **1996**, *316*, 937.

[258] V. J. Schömig, B. T. Käsdorf, C. Scholz, K. Bidmon, O. Lieleg, S. Berensmeier, *RSC Adv.* **2016**, *6*, 44932.

[259] A. Curnutt, K. Smith, E. Darrow, K. B. Walters, *Sci. Rep.* **2020**, *10*, 21.

[260] Y. Zhao, G. Chen, Z. Meng, G. Gong, W. Zhao, K. Wang, T. Liu, *Drug Deliv.* **2019**, *26*, 717.

[261] S. Devineau, K. I. Inoue, R. Kusaka, S. H. Urashima, S. Nihonyanagi, D. Baigl, A.

Tsuneshige, T. Tahara, *Phys. Chem. Chem. Phys.* **2017**, *19*, 10292.

[262] R. Mo, T. Jiang, J. Di, W. Tai, Z. Gu, *Chem. Soc. Rev.* **2014**, *43*, 3595.

[263] F. Kivlehan, Y. H. Lanyon, D. W. M. Arrigan, *Langmuir* **2008**, *24*, 9876.

[264] Y. Takashimizu, M. Iiyoshi, *Prog. Earth Planet. Sci.* **2016**, *3*, 1.

[265] S. J. Blott, K. Pye, *Sedimentology* **2008**, *55*, 31.

[266] I. Cruz-Matías, D. Ayala, D. Hiller, S. Gutsch, M. Zacharias, S. Estradé, F. Peiró, *J. Comput. Sci.* **2019**, *30*, 28.

[267] J. J. Moon, B. Huang, D. J. Irvine, *Adv. Mater.* **2012**, *24*, 3724.

[268] D. J. Irvine, M. A. Swartz, G. L. Szeto, *Nat. Mater.* **2013**, *12*, 978.

[269] M. S. Goldberg, *Cell* **2015**, *161*, 201.

[270] P. Sahdev, L. J. Ochyl, J. J. Moon, *Pharm. Res.* **2014**, *31*, 2563.

[271] C. J. M. Melief, S. H. van der Burg, *Nat. Rev. Cancer* **2008**, *8*, 351.

[272] Y. Hailemichael, Z. Dai, N. Jaffarzad, Y. Ye, M. A. Medina, X.-F. Huang, S. M. Dorta-Estremera, N. R. Greeley, G. Nitti, W. Peng, C. Liu, Y. Lou, Z. Wang, W. Ma, B. Rabinovich, R. T. Sowell, K. S. Schluns, R. E. Davis, P. Hwu, W. W. Overwijk, *Nat. Med.* **2013**, *19*, 465.

[273] Y. Fan, J. J. Moon, *Vaccines* **2015**, *3*, 662.

[274] I. Sagiv-Barfi, D. K. Czerwinski, S. Levy, I. S. Alam, A. T. Mayer, S. S. Gambhir, R. Levy, *Sci. Transl. Med.* **2018**, *10*, eaan4488.

[275] N. M. Molino, M. Neek, J. A. Tucker, E. L. Nelson, S.-W. Wang, *Biomaterials* **2016**, *86*, 83.

[276] L. Seth, K. M. Bingham Ferlez, S. A. Kaba, D. M. Musser, S. Emadi, G. R. Matyas, Z. Beck, C. R. Alving, P. Burkhard, D. E. Lanar, *Vaccine* **2017**, *35*, 5448.

[277] H. Liu, K. D. Moynihan, Y. Zheng, G. L. Szeto, A. V Li, B. Huang, D. S. Van Egeren, C. Park, D. J. Irvine, *Nature* **2014**, *507*, 519.

[278] R. A. Rosalia, L. J. Cruz, S. van Duikeren, A. T. Tromp, A. L. Silva, W. Jiskoot, T. de Gruijl, C. L??wik, J. Oostendorp, S. H. van der Burg, F. Ossendorp, *Biomaterials* **2015**, *40*, 88.

[279] Y.-C. Chiu, J. M. Gammon, J. I. Andorko, L. H. Tostanoski, C. M. Jewell, *ACS Biomater. Sci. Eng.* **2015**, *1*, 1200.

[280] P. H. Lizotte, A. M. Wen, M. R. Sheen, J. Fields, P. Rojanasopondist, N. F. Steinmetz, S. Fiering, *Nat. Nanotechnol.* **2016**, *11*, 295.

[281] R. Kuai, L. J. Ochyl, K. S. Bahjat, A. Schwendeman, J. J. Moon, *Nat. Mater.* **2017**, *16*, 489.

[282] B. Choi, H. Moon, S. J. Hong, C. Shin, Y. Do, S. Ryu, S. Kang, *ACS Nano* **2016**, *10*, 7339.

[283] S. T. Reddy, A. J. van der Vlies, E. Simeoni, V. Angeli, G. J. Randolph, C. P. O'Neil, L. K. Lee, M. A. Swartz, J. A. Hubbell, *Nat. Biotechnol.* **2007**, *25*, 1159.

[284] J. J. Moon, H. Suh, A. Bershteyn, M. T. Stephan, H. Liu, B. Huang, M. Sohail, S. Luo, S. Ho Um, H. Khant, J. T. Goodwin, J. Ramos, W. Chiu, D. J. Irvine, *Nat. Mater.* **2011**, *10*, 243.

[285] I.-H. Lee, H.-K. Kwon, S. An, D. Kim, S. Kim, M. K. Yu, J.-H. Lee, T.-S. Lee, S.-H. Im, S. Jon, *Angew. Chemie Int. Ed.* **2012**, *51*, 8800.

[286] A. V Li, J. J. Moon, W. Abraham, H. Suh, J. Elkhader, M. A. Seidman, M. Yen, E.-J. Im, M. H. Foley, D. H. Barouch, D. J. Irvine, *Sci. Transl. Med.* **2013**, *5*, 204ra130 LP.

[287] L. Jeanbart, M. Ballester, A. de Titta, P. Corthésy, P. Romero, J. A. Hubbell, M. A. Swartz, *Cancer Immunol. Res.* **2014**, *2*, 436 LP.

[288] Z. Xu, Y. Wang, L. Zhang, L. Huang, *ACS Nano* **2014**, *8*, 3636.

[289] A. E. Gregory, R. Titball, D. Williamson, *Front. Cell. Infect. Microbiol.* **2013**, *4*, 1.

[290] M. Singh, *Vaccine Adjuvants and Delivery Systems*, Wiley, **2006**.

[291] L. Liu, P. Ma, H. Wang, C. Zhang, H. Sun, C. Wang, C. Song, X. Leng, D. Kong, G. Ma, *J. Control. Release* **2016**, *225*, 230.

[292] V. Torchilin, *Drug Discov. Today Technol.* **2008**, *5*, e95.

[293] Y. Lu, W. Sun, Z. Gu, *J. Control. Release* **2014**, *194*, 1.

[294] E. A. Simone, T. D. Dziubla, F. Colon-Gonzalez, D. E. Discher, V. R. Muzykantov, *Biomacromolecules* **2007**, *8*, 3914.

[295] K. Dutta, D. Hu, B. Zhao, A. E. Ribbe, J. Zhuang, S. Thayumanavan, *J. Am. Chem. Soc.* **2017**, *139*, 5676.

[296] C. Cai, S. Mao, T. Kissel, *Asian J. Pharm. Sci.* **2016**, *11*, 64.

[297] S. D. Xiang, A. Scholzen, G. Minigo, C. David, V. Apostolopoulos, P. L. Mottram, M. Plebanski, *Methods* **2006**, *40*, 1.

[298] A. Stano, C. Nembrini, M. A. Swartz, J. A. Hubbell, E. Simeoni, *Vaccine* **2012**, *30*, 7541.

[299] P. L. Mottram, D. Leong, B. Crimeen-Irwin, S. Gloster, S. D. Xiang, J. Meanger, R. Ghildyal, N. Vardaxis, M. Plebanski, *Mol. Pharm.* **2007**, *4*, 73.

[300] S. Kumar, A. C. Anselmo, A. Banerjee, M. Zakrewsky, S. Mitragotri, *J. Control. Release* **2015**, *220*, 141.

[301] C. A. Vaine, M. K. Patel, J. Zhu, E. Lee, R. W. Finberg, R. C. Hayward, E. A. Kurt-Jones, *J. Immunol.* **2013**, *190*, 3525 LP.

[302] S. Neumann, K. Burkert, R. Kemp, T. Rades, P. Rod Dunbar, S. Hook, *Immunol. Cell Biol.* **2014**, *92*, 535.

[303] B. S. Zolnik, A. González-Fernández, N. Sadrieh, M. A. Dobrovolskaia, *Endocrinology*

2010, *151*, 458.

[304] M. Embgenbroich, S. Burgdorf, *Front. Immunol.* **2018**, *9*, 1643.

[305] O. P. Joffre, E. Segura, A. Savina, S. Amigorena, *Nat. Rev. Immunol.* **2012**, *12*, 557.

[306] B. Slütter, L. Plapied, V. Fievez, M. Alonso, Y. Schneider, E. Van Riet, W. Jiskoot, V. Préat, *J. Control. Release* **2009**, *138*, 113.

[307] L. J. Cruz, P. J. Tacken, I. S. Zeelenberg, M. Srinivas, F. Bonetto, B. Weigelin, C. Eich, I. J. de Vries, C. G. Figdor, *Mol. Pharm.* **2014**, *11*, 4299.

[308] S. Hirosue, I. C. Kourtis, A. J. van der Vlies, J. A. Hubbell, M. A. Swartz, *Vaccine* **2010**, *28*, 7897.

[309] J. T. Wilson, S. Keller, M. J. Manganiello, C. Cheng, C. C. Lee, C. Opara, A. Convertine, P. S. Stayton, *ACS Nano* **2013**, *7*, 3912.

[310] V. Hornung, F. Bauernfeind, A. Halle, E. O. Samstad, H. Kono, K. L. Rock, K. A. Fitzgerald, E. Latz, *Nat. Immunol.* **2008**, *9*, 847.

[311] H. Li, S. B. Willingham, J. P.-Y. Ting, F. Re, *J. Immunol.* **2008**, *181*, 17 LP.

[312] F. A. Sharp, D. Ruane, B. Claass, E. Creagh, J. Harris, P. Malyala, M. Singh, D. T. O'Hagan, V. Pétrilli, J. Tschopp, L. A. J. O'Neill, E. C. Lavelle, *Proc. Natl. Acad. Sci.* **2009**, *106*, 870 LP.

[313] L. Zhao, A. Seth, N. Wibowo, C. Zhao, N. Mitter, C. Yu, A. P. J. Middelberg, *Vaccine* **2014**, *32*, 327.

[314] M. Kanekiyo, C. J. Wei, H. M. Yassine, P. M. McTamney, J. C. Boyington, J. R. R. Whittle, S. S. Rao, W. P. Kong, L. Wang, G. J. Nabel, *Nature* **2013**, *499*, 102.

[315] L. Deng, T. Mohan, T. Z. Chang, G. X. Gonzalez, Y. Wang, Y.-M. Kwon, S.-M. Kang, R. W. Compans, J. A. Champion, B.-Z. Wang, *Nat. Commun.* **2018**, *9*, 1.

[316] T. Z. Chang, I. Diambou, J. R. Kim, B. Wang, J. A. Champion, *Bioeng. Transl. Med.* **2017**, *2*, 120.

[317] S. I. Lim, C. I. Lukianov, J. A. Champion, *J. Control. Release* **2017**, *249*, 1.

[318] G. S. Shukla, Y.-J. Sun, S. C. Pero, G. S. Sholler, D. N. Krag, *J. Immunol. Methods* **2018**, *460*, 51.

[319] D. M. Da Silva, D. V Pastrana, J. T. Schiller, W. M. Kast, *Virology* **2001**, *290*, 350.

[320] A. N. Tsoras, J. A. Champion, *Annu. Rev. Chem. Biomol. Eng.* **2019**, *10*, 337.

[321] X. Dong, J. Liang, A. Yang, C. Wang, D. Kong, F. Lv, *ACS Appl. Mater. Interfaces* **2018**, *10*, 21861.

[322] X. Dong, Z. Sun, J. Liang, H. Wang, D. Zhu, X. Leng, C. Wang, D. Kong, F. Lv, *Nanomedicine Nanotechnology, Biol. Med.* **2018**, *14*, 1087.

[323] Z. Sun, J. Liang, X. Dong, C. Wang, D. Kong, F. Lv, *ACS Appl. Mater. Interfaces* **2018**, *10*, 20315.

[324] K. T. Gause, Y. Yan, N. M. O'Brien-Simpson, J. Cui, J. C. Lenzo, E. C. Reynolds, F. Caruso, *Adv. Funct. Mater.* **2016**, *26*, 7526.

[325] K. T. Gause, Y. Yan, J. Cui, N. M. Obrien-Simpson, J. C. Lenzo, E. C. Reynolds, F. Caruso, *ACS Nano* **2015**, *9*, 2433.

[326] A. N. Tsoras, J. A. Champion, *Bioconjug. Chem.* **2018**, *29*, 776.

[327] T. Z. Chang, S. S. Stadmiller, E. Staskevicius, J. A. Champion, *Biomater. Sci.* **2017**, *5*, 223.

[328] A. Jaworek, A. T. Sobczyk, *J. Electrostat.* **2008**, *66*, 197.

[329] Y. Wu, J. A. MacKay, J. R. McDaniel, A. Chilkoti, R. L. Clark, *Biomacromolecules* **2009**, *10*, 19.

[330] A. Gomez, D. Bingham, L. De Juan, K. Tang, *J. Aerosol Sci.* **1998**, *29*, 561.

[331] A. Jaworek, *Powder Technol.* **2007**, *176*, 18.

[332] J. W. Myerson, P. N. Patel, N. Habibi, L. R. Walsh, Y. W. Lee, D. C. Luther, L. T. Ferguson, M. H. Zaleski, M. E. Zamora, O. A. Marcos-Contreras, P. M. Glassman, I. Johnston, E. D. Hood, T. Shuvaeva, J. V. Gregory, R. Y. Kiseleva, J. Nong, K. M. Rubey, C. F. Greineder, S. Mitragotri, G. S. Worthen, V. M. Rotello, J. Lahann, V. R. Muzykantov, J. S. Brenner, *bioRxiv* **2020**, 2020.04.15.037564.

[333] J. Hao, K. C. K. Cheng, L. G. Kruger, L. Larsson, J. V Sugai, J. Lahann, W. V Giannobile, *Adv. Mater.* **2016**, *28*, 3145.

[334] S. Kline, *J. Appl. Crystallogr.* **2006**, *39*, 895.

[335] M. B. Lutz, N. Kukutsch, A. L. J. Ogilvie, S. Rößner, F. Koch, N. Romani, G. Schuler, *J. Immunol. Methods* **1999**, *223*, 77.

[336] R. García, I. B. Recalde, J. E. Figueruelo, A. Campos, *Macromol. Chem. Phys.* **2001**, *202*, 3352.

[337] P. Malo de Molina, S. Lad, M. E. Helgeson, *Macromolecules* **2015**, *48*, 5402.

[338] G. Porod, *Kolloid-Zeitschrift* **1951**, *124*, 83.

[339] P. Debye, H. R. Anderson, H. Brumberger, *J. Appl. Phys.* **1957**, *28*, 679.

[340] A. L. Weisenhorn, M. Khorsandi, S. Kasas, V. Gotzos, H.-J. Butt, *Nanotechnology* **1993**, *4*, 106.

[341] S. Ohya, S. Kidoaki, T. Matsuda, *Biomaterials* **2005**, *26*, 3105.

[342] J. Cui, R. De Rose, J. P. Best, A. P. R. Johnston, S. Alcantara, K. Liang, G. K. Such, S. J. Kent, F. Caruso, *Adv. Mater.* **2013**, *25*, 3468.

[343] P. J. Flory, *Polymer* **1979**, *20*, 1317.

[344] X. Banquy, F. Suarez, A. Argaw, J.-M. Rabanel, P. Grutter, J.-F. Bouchard, P. Hildgen, S.

Giasson, *Soft Matter* **2009**, *5*, 3984.

[345] K. K. Tran, H. Shen, *Biomaterials* **2009**, *30*, 1356.

[346] J. M. Brewer, K. G. J. Pollock, L. Tetley, D. G. Russell, *J. Immunol.* **2004**, *173*, 6143 LP.

[347] T. Fifis, A. Gamvrellis, B. Crimeen-Irwin, G. A. Pietersz, J. Li, P. L. Mottram, I. F. C. McKenzie, M. Plebanski, *J. Immunol.* **2004**, *173*, 3148 LP.

[348] V. Manolova, A. Flace, M. Bauer, K. Schwarz, P. Saudan, M. F. Bachmann, *Eur. J. Immunol.* **2008**, *38*, 1404.

[349] H. Kim, D. Sehgal, T. A. Kucaba, D. M. Ferguson, T. S. Griffith, J. Panyam, *Nanoscale* **2018**, *10*, 20851.

[350] M. Jambhrunkar, Y. Yang, M. Yu, M. Zhang, P. L. Abbaraju, T. Ghosh, M. Kalantari, Y. Wang, N. A. J. McMillan, C. Yu, *Mater. Today Adv.* **2020**, *6*, 100069.

[351] H. A. F. M. Hassan, L. Smyth, J. T.-W. Wang, P. M. Costa, K. Ratnasothy, S. S. Diebold, G. Lombardi, K. T. Al-Jamal, *Biomaterials* **2016**, *104*, 310.

[352] S.-Y. Kim, S. Kim, J.-E. Kim, S. N. Lee, I. W. Shin, H. S. Shin, S. M. Jin, Y.-W. Noh, Y. J. Kang, Y. S. Kim, T. H. Kang, Y.-M. Park, Y. T. Lim, *ACS Nano* **2019**, *13*, 12671.

[353] S. Kos, A. Lopes, V. Preat, M. Cemazar, U. Lampreht Tratar, B. Ucakar, K. Vanvarenberg, G. Sersa, G. Vandermeulen, *PLoS One* **2019**, *14*, e0217762.

[354] V. K. Gribkoff, L. K. Kaczmarek, *Neuropharmacology* **2017**, *120*, 11.

[355] H. Dowden, J. Munro, *Nat. Rev. Drug Discov.* **2019**, *18*, 495.

[356] M. M. Patel, B. M. Patel, *CNS Drugs* **2017**, *31*, 109.

[357] S. Ding, A. I. Khan, X. Cai, Y. Song, Z. Lyu, D. Du, P. Dutta, Y. Lin, *Mater. Today* **2020**, *37*, 112.

[358] K. E. Sandoval, K. A. Witt, *Neurobiol. Dis.* **2008**, *32*, 200.

[359] Y. Chen, L. Liu, *Adv. Drug Deliv. Rev.* **2012**, *64*, 640.

[360] W. M. Pardridge, *NeuroRx* **2005**, *2*, 3.

[361] R. Pandit, L. Chen, J. Götz, *Adv. Drug Deliv. Rev.* **2020**, *165–166*, 1.

[362] C. D. Arvanitis, G. B. Ferraro, R. K. Jain, *Nat. Rev. Cancer* **2020**, *20*, 26.

[363] A. Burgess, K. Hynynen, *ACS Chem. Neurosci.* **2013**, *4*, 519.

[364] S. I. Rapoport, *Expert Opin. Investig. Drugs* **2001**, *10*, 1809.

[365] R. Hunt Bobo, D. W. Laske, A. Akbasak, P. F. Morrison, R. L. Dedrick, E. H. Oldfield, *Proc. Natl. Acad. Sci. U. S. A.* **1994**, *91*, 2076.

[366] L. P. Serwer, C. D. James, *Adv. Drug Deliv. Rev.* **2012**, *64*, 590.

[367] Y. Zhou, Z. Peng, E. S. Seven, R. M. Leblanc, *J. Control. Release* **2018**, *270*, 290.

[368] A. M. Mehta, A. M. Sonabend, J. N. Bruce, *Neurotherapeutics* **2017**, *14*, 358.

[369] D. Peer, J. M. Karp, S. Hong, O. C. Farokhzad, R. Margalit, R. Langer, *Nat. Nanotechnol.* **2007**, *2*, 751.

[370] T. D. Brown, N. Habibi, D. Wu, J. Lahann, S. Mitragotri, *ACS Biomater. Sci. Eng.* **2020**, *6*, 4916.

[371] V. Bhardwaj, A. Kaushik, Z. M. Khatib, M. Nair, A. J. McGoron, *Front. Pharmacol.* **2019**, *10*, 1.

[372] K. Ulbrich, T. Knobloch, J. Kreuter, *J. Drug Target.* **2011**, *19*, 125.

[373] D. T. Wiley, P. Webster, A. Gale, M. E. Davis, *Proc. Natl. Acad. Sci.* **2013**, *110*, 8662.

[374] A. C. Anselmo, S. Mitragotri, *J. Control. Release* **2014**, *190*, 531.

[375] A. C. Anselmo, S. Mitragotri, *J. Control. Release* **2014**, *190*, 531.

[376] T. L. Moore, D. Hauser, T. Gruber, B. Rothen-Rutishauser, M. Lattuada, A. Petri-Fink, R. Lyck, *ACS Appl. Mater. Interfaces* **2017**, *9*, 18501.

[377] S. J. Madsen, C. Christie, S. J. Hong, A. Trinidad, Q. Peng, F. A. Uzal, H. Hirschberg, *Lasers Med. Sci.* **2015**, *30*, 1357.

[378] N. L. Klyachko, R. Polak, M. J. Haney, Y. Zhao, R. J. Gomes, M. C. Hill, A. V Kabanov, R. E. Cohen, M. F. Rubner, E. V Batrakova, *Biomaterials* **2017**, *140*, 79.

[379] P. S. Jiang, C. F. Yu, C. Y. Yen, C. W. Woo, S. H. Lo, Y. K. Huang, J. H. Hong, C. S. Chiang, *PLoS One* **2015**, *10*, 1.

[380] G. Tomaiuolo, *Biomicrofluidics* **2014**, *8*, 1.

[381] D. C. Pan, J. W. Myerson, J. S. Brenner, P. N. Patel, A. C. Anselmo, S. Mitragotri, V. Muzykantov, *Sci. Rep.* **2018**, *8*, 1.

[382] D. Pan, O. Vargas-Morales, B. Zern, A. C. Anselmo, V. Gupta, M. Zakrewsky, S. Mitragotri, V. Muzykantov, *PLoS One* **2016**, *11*, 1.

[383] S. Alkabie, J. Basivireddy, L. Zhou, J. Roskams, P. Rieckmann, J. A. Quandt, *J. Neuroinflammation* **2016**, *13*, 1.

[384] A. Wunder, U. Müller-Ladner, E. H. K. Stelzer, J. Funk, E. Neumann, G. Stehle, T. Pap, H. Sinn, S. Gay, C. Fiehn, *J. Immunol.* **2003**, *170*, 4793.

[385] E. Neumann, E. Frei, D. Funk, M. D. Becker, H. H. Schrenk, U. Mller-Ladner, C. Fiehn, *Expert Opin. Drug Deliv.* **2010**, *7*, 915.

[386] A. M. Merlot, D. S. Kalinowski, Z. Kovacevic, P. J. Jansson, D. J. Lane, M. L. H. Huang, S. Sahni, D. R. Richardson, *Future Med. Chem.* **2015**, *7*, 553.

[387] T. Lin, P. Zhao, Y. Jiang, Y. Tang, H. Jin, Z. Pan, H. He, V. C. Yang, Y. Huang, *ACS Nano* **2016**, *10*, 9999.

[388] S. M. Vogel, R. D. Minshall, M. Pilipović, C. Tiruppathi, A. B. Malik, *Am. J. Physiol. - Lung Cell. Mol. Physiol.* **2001**, *281*, 1512.

[389] S. A. Rempel, W. A. Golembieski, S. Ge, N. Lemke, K. Elisevich, T. Mikkelsen, J. A. Gutiérrez, *J. Neuropathol. Exp. Neurol.* **1998**, *57*, 1112.

[390] P. Zhao, Y. Wang, A. Wu, Y. Rao, Y. Huang, *ChemBioChem* **2018**, *19*, 1796.

[391] O. A. Marcos-Contreras, J. S. Brenner, R. Y. Kiseleva, V. Zuluaga-Ramirez, C. F. Greineder, C. H. Villa, E. D. Hood, J. W. Myerson, S. Muro, Y. Persidsky, V. R. Muzykantov, *J. Control. Release* **2019**, *301*, 54.

[392] K.-H. Roh, D. C. Martin, J. Lahann, *Nat. Mater.* **2005**, *4*, 759.

[393] M. Á. Fernández-rodríguez, S. Rahmani, C. K. J. Yu, M. Á. Rodríguez-valverde, M. Á. Cabrerizo-vílchez, C. A. Michel, J. Lahann, R. Hidalgo-álvarez, *Colloids Surfaces A Physicochem. Eng. Asp.* **2018**, *536*, 259.

[394] S. Rahmani, S. Ashraf, R. Hartmann, A. F. Dishman, M. V Zyuzin, C. K. J. Yu, W. J. Parak, J. Lahann, *Bioeng. Transl. Med.* **2016**, *1*, 82.

[395] E. Sokolovskaya, S. Rahmani, A. C. Misra, S. Bräse, J. Lahann, *ACS Appl. Mater. Interfaces* **2015**, *7*, 9744.

[396] J. L. Ekaterina Sokolovskaya, Jaewon Yoon, Asish C. Misra, Stefan Bräse, *Macromol. Rapid Commun.* **2013**, *34*, 1554.

[397] J. S. Brenner, D. C. Pan, J. W. Myerson, O. A. Marcos-Contreras, C. H. Villa, P. Patel, H. Hekierski, S. Chatterjee, J. Q. Tao, H. Parhiz, K. Bhamidipati, T. G. Uhler, E. D. Hood, R. Y. Kiseleva, V. S. Shuvaev, T. Shuvaeva, M. Khoshnejad, I. Johnston, J. V Gregory, J. Lahann, T. Wang, E. Cantu, W. M. Armstead, S. Mitragotri, V. Muzykantov, *Nat. Commun.* **2018**, *9*, 1.

[398] A. M. Spiotta, J. Vargas, R. Turner, M. I. Chaudry, H. Battenhouse, A. S. Turk, *J. Neurointerv. Surg.* **2014**, *6*, 511 LP.

[399] M. Palaniswami, B. Yan, *Interv. Neurol.* **2015**, *4*, 18.

[400] V. L. Feigin, E. Nichols, T. Alam, M. S. Bannick, E. Beghi, N. Blake, W. J. Culpepper, E. R. Dorsey, A. Elbaz, R. G. Ellenbogen, J. L. Fisher, C. Fitzmaurice, G. Giussani, L. Glennie, S. L. James, C. O. Johnson, N. J. Kassebaum, G. Logroscino, B. Marin, W. C. Mountjoy-Venning, M. Nguyen, R. Ofori-Asenso, A. P. Patel, M. Piccininni, G. A. Roth, T. J. Steiner, L. J. Stovner, C. E. I. Szoeke, A. Theadom, S. E. Vollset, M. T. Wallin, C. Wright, J. R. Zunt, N. Abbasi, F. Abd-Allah, A. Abdelalim, I. Abdollahpour, V. Aboyans, H. N. Abraha, D. Acharya, A. A. Adamu, O. M. Adebayo, A. M. Adeoye, J. C. Adsuar, M. Afarideh, S. Agrawal, A. Ahmadi, M. B. Ahmed, A. N. Aichour, I. Aichour, M. T. E. Aichour, R. O. Akinyemi, N. Akseer, A. Al-Eyadhy, R. Al-Shahi Salman, F. Alahdab, K. A. Alene, S. M. Aljunid, K. Altirkawi, N. Alvis-Guzman, N. H. Anber, C. A. T. Antonio, J. Arabloo, O. Aremu, J. Ärnlöv, H. Asayesh, R. J. Asghar, H. T. Atalay, A. Awasthi, B. P. Ayala Quintanilla, T. B. Ayuk, A. Badawi, M. Banach, J. A. M. Banoub, M. A. Barboza, S. L. Barker-Collo, T. W. Bärnighausen, B. T. Baune, N. Bedi, M. Behzadifar, M. Behzadifar, Y. Béjot, B. B. Bekele, A. B. Belachew, D. A. Bennett, I. M. Bensenor, A. Berhane, M. Beuran, K. Bhattacharyya, Z. A. Bhutta, B. Biadgo, A. Bijani, N. Bililign, M. S. Bin Sayeed, C. K. Blazes, C. Brayne, Z. A. Butt, I. R. Campos-Nonato, C. Cantu-Brito, M. Car, R. Cárdenas, J. J. Carrero, F. Carvalho, C. A. Castañeda-Orjuela, F. Castro, F. Catalá-López, E. Cerin, Y. Chaiah, J. C. Chang, I. Chatziralli, P. P. C. Chiang, H. Christensen, D. J. Christopher, C. Cooper, P. A. Cortesi, V. M. Costa, M. H. Criqui, C. S. Crowe, A. A. M. Damasceno, A. Daryani, V. De la Cruz-Góngora, F. P. De La Hoz, D. De Leo, M. G. Degefa, G. T. Demoz, K. Deribe, S. D. Dharmaratne, D. Diaz, M. T. Dinberu, S. Djalalinia, D. T. Doku, M. Dubey, E. Dubljanin, E. E. Duken, D. Edvardsson, Z. El-Khatib, M. Endres,

A. Y. Endries, S. Eskandarieh, A. Esteghamati, S. Esteghamati, F. Farhadi, A. Faro, F. Farzadfar, M. H. Farzaei, B. Fatima, S. M. Fereshtehnejad, E. Fernandes, G. T. Feyissa, I. Filip, F. Fischer, T. Fukumoto, M. Ganji, F. G. Gankpe, M. A. Garcia-Gordillo, A. K. Gebre, T. G. Gebremichael, B. K. Gelaw, J. M. Geleijnse, D. Geremew, K. E. Gezae, M. Ghasemi-Kasman, M. Y. Gidey, P. S. Gill, T. K. Gill, E. V. Gnedovskaya, A. C. Goulart, A. Grada, G. Grosso, Y. Guo, R. Gupta, R. Gupta, J. A. Haagsma, T. B. Hagos, A. Haj-Mirzaian, A. Haj-Mirzaian, R. R. Hamadeh, S. Hamidi, G. J. Hankey, Y. Hao, J. M. Haro, H. Hassankhani, H. Y. Hassen, R. Havmoeller, S. I. Hay, M. I. Hegazy, B. Heidari, A. Henok, F. Heydarpour, C. L. Hoang, M. K. Hole, E. Homaie Rad, S. M. Hosseini, G. Hu, E. U. Igumbor, O. S. Ilesanmi, S. S. N. Irvani, S. M. S. Islam, M. Jakovljevic, M. Javanbakht, R. P. Jha, Y. B. Jobanputra, J. B. Jonas, J. J. Józwiak, M. Jürisson, A. Kahsay, R. Kalani, Y. Kalkonde, T. A. Kamil, T. Kanchan, M. Karami, A. Karch, N. Karimi, A. Kasaeian, T. D. Kassa, Z. Y. Kassa, A. Kaul, A. T. Kefale, P. N. Keiyoro, Y. S. Khader, M. A. Khafaie, I. A. Khalil, E. A. Khan, Y. H. Khang, H. Khazaie, A. A. Kiadaliri, D. N. Kiirithio, A. S. Kim, D. Kim, Y. E. Kim, Y. J. Kim, A. Kisa, Y. Kokubo, A. Koyanagi, R. V. Krishnamurthi, B. Kuate Defo, B. Kucuk Bicer, M. Kumar, B. Lacey, A. Lafranconi, V. C. Lansingh, A. Latifi, C. T. Leshargie, S. Li, Y. Liao, S. Linn, W. D. Lo, J. C. F. Lopez, S. Lorkowski, P. A. Lotufo, R. M. Lucas, R. Lunevicius, M. T. Mackay, N. B. Mahotra, M. Majdan, R. Majdzadeh, A. Majeed, R. Malekzadeh, D. C. Malta, N. Manafi, M. A. Mansournia, L. G. Mantovani, W. März, T. P. Mashamba-Thompson, B. B. Massenburg, K. K. V. Mate, C. McAlinden, J. J. McGrath, V. Mehta, T. Meier, H. G. Meles, A. Melese, P. T. N. Memiah, Z. A. Memish, W. Mendoza, D. T. Mengistu, G. Mengistu, A. Meretoja, T. J. Meretoja, T. Mestrovic, B. Miazgowski, T. Miazgowski, T. R. Miller, G. K. Mini, E. M. Mirrakhimov,

B. Moazen, B. Mohajer, N. Mohammad Gholi Mezerji, M. Mohammadi, M. Mohammadi-Khanaposhtani, R. Mohammadibakhsh, M. Mohammadnia-Afrouzi, S. Mohammed, F. Mohebi, A. H. Mokdad, L. Monasta, S. Mondello, Y. Moodley, M. Moosazadeh, G. Moradi, M. Moradi-Lakeh, M. Moradinazar, P. Moraga, I. Moreno Velásquez, S. D. Morrison, S. M. Mousavi, O. S. Muhammed, W. Muruet, K. I. Musa, G. Mustafa, M. Naderi, G. Nagel, A. Naheed, G. Naik, F. Najafi, V. Nangia, I. Negoi, R. I. Negoi, C. R. J. Newton, J. W. Ngunjiri, C. T. Nguyen, L. H. Nguyen, D. N. A. Ningrum, Y. L. Nirayo, M. R. Nixon, B. Norrving, J. J. Noubiap, M. Nourollahpour Shiadeh, P. S. Nyasulu, F. A. Ogbo, I. H. Oh, A. T. Olagunju, T. O. Olagunju, P. R. Olivares, O. E. Onwujekwe, E. Oren, M. O. Owolabi, M. P. A, A. H. Pakpour, W. H. Pan, S. Panda-Jonas, J. D. Pandian, S. K. Patel, D. M. Pereira, M. Petzold, J. D. Pillay, M. A. Piradov, G. V. Polanczyk, S. Polinder, M. J. Postma, R. Poulton, H. Poustchi, S. Prakash, V. Prakash, M. Qorbani, A. Radfar, A. Rafay, A. Rafiei, F. Rahim, V. Rahimi-Movaghar, M. Rahman, M. H. U. Rahman, M. A. Rahman, F. Rajati, U. Ram, A. Ranta, D. L. Rawaf, S. Rawaf, N. Reinig, C. Reis, A. M. N. Renzaho, S. Resnikoff, S. Rezaeian, M. S. Rezai, C. M. Rios González, N. L. S. Roberts, L. Roever, L. Ronfani, E. M. Roro, G. Roshandel, A. Rostami, P. Sabbagh, R. L. Sacco, P. S. Sachdev, B. Saddik, H. Safari, R. Safari-Faramani, S. Safi, S. Safiri, R. Sagar, R. Sahathevan, A. Sahebkar, M. A. Sahraian, P. Salamati, S. Salehi Zahabi, Y. Salimi, A. M. Samy, J. Sanabria, I. S. Santos, M. M. Santric Milicevic, N. Sarrafzadegan, B. Sartorius, S. Sarvi, B. Sathian, M. Satpathy, A. R. Sawant, M. Sawhney, I. J. C. Schneider, B. Schöttker, D. C. Schwebel, S. Seedat, S. G. Sepanlou, H. Shabaninejad, A. Shafieesabet, M. A. Shaikh, R. A. Shakir, M. Shams-Beyranvand, M. Shamsizadeh, M. Sharif, M. Sharif-Alhoseini, J. She, A. Sheikh, K. N. Sheth, M. Shigematsu, R. Shiri, R. Shirkoohi, I. Shiue, S. Siabani, T. J.

Siddiqi, I. D. Sigfusdottir, R. Sigurvinsdottir, D. H. Silberberg, J. P. Silva, D. G. A. Silveira, J. A. Singh, D. N. Sinha, E. Skiadaresi, M. Smith, B. H. Sobaih, S. Sobhani, M. Soofi, I. N. Soyiri, L. A. Sposato, D. J. Stein, M. B. Stein, M. A. Stokes, M. B. Sufiyan, B. L. Sykes, P. Sylaja, R. Tabarés-Seisdedos, B. J. Te Ao, A. Tehrani-Banihashemi, M. H. Temsah, O. Temsah, J. S. Thakur, A. G. Thrift, R. Topor-Madry, M. Tortajada-Girbés, M. R. Tovani-Palone, B. X. Tran, K. B. Tran, T. C. Truelsen, A. G. Tsadik, L. Tudor Car, K. N. Ukwaja, I. Ullah, M. S. Usman, O. A. Uthman, P. R. Valdez, T. J. Vasankari, R. Vasanthan, Y. Veisani, N. Venketasubramanian, F. S. Violante, V. Vlassov, K. Vosoughi, G. T. Vu, I. S. Vujcic, F. S. Wagnew, Y. Waheed, Y. P. Wang, E. Weiderpass, J. Weiss, H. A. Whiteford, T. Wijeratne, A. S. Winkler, C. S. Wiysonge, C. D. A. Wolfe, G. Xu, A. Yadollahpour, T. Yamada, Y. Yano, M. Yaseri, H. Yatsuya, E. M. Yimer, P. Yip, E. Yisma, N. Yonemoto, M. Yousefifard, C. Yu, Z. Zaidi, S. Bin Zaman, M. Zamani, H. Zandian, Z. Zare, Y. Zhang, S. Zodpey, M. Naghavi, C. J. L. Murray, T. Vos, *Lancet Neurol.* **2019**, *18*, 459.

[401] C. L. Gooch, E. Pracht, A. R. Borenstein, *Ann. Neurol.* **2017**, *81*, 479.

[402] S. Wohlfart, S. Gelperina, J. Kreuter, *J. Control. Release* **2012**, *161*, 264.

[403] X. Dong, *Theranostics* **2018**, *8*, 1481.

[404] H. I. Tong, W. Kang, Y. Shi, G. Zhou, Y. Lu, *Int. J. Pharm.* **2016**, *505*, 271.

[405] J. W. Kinney, S. M. Bemiller, A. S. Murtishaw, A. M. Leisgang, A. M. Salazar, B. T. Lamb, *Alzheimer's Dement. Transl. Res. Clin. Interv.* **2018**, *4*, 575.

[406] Q. Wang, Y. Liu, J. Zhou, *Transl. Neurodegener.* **2015**, *4*, 1.

[407] W. Poewe, K. Seppi, C. M. Tanner, G. M. Halliday, P. Brundin, J. Volkmann, A. E. Schrag, A. E. Lang, *Nat. Rev. Dis. Prim.* **2017**, *3*, 1.

[408] A. G. M. Mostofa, S. R. Punganuru, H. R. Madala, M. Al-Obaide, K. S. Srivenugopal,

Biomolecules **2017**, *7*, 1.

[409] R. Medzhitov, *Nature* **2008**, *454*, 428.

[410] L. E. Ibarra, L. Beaugé, N. Arias-Ramos, V. A. Rivarola, C. A. Chesta, P. López-Larrubia, R. E. Palacios, *Nanomedicine* **2020**, *15*, 1687.

[411] H.-I. Tong, W. Kang, P. M. C. Davy, Y. Shi, S. Sun, R. C. Allsopp, Y. Lu, *PLoS One* **2016**, *11*, e0154022.

[412] A. M. Brynskikh, Y. Zhao, R. L. Mosley, S. Li, M. D. Boska, N. L. Klyachko, A. V. Kabanov, H. E. Gendelman, E. V. Batrakova, *Nanomedicine* **2010**, *5*, 379.

[413] Y. Zhao, M. J. Haney, *J. Nanomed. Nanotechnol.* **2011**, *01*, 1.

[414] J. Hou, X. Yang, S. Li, Z. Cheng, Y. Wang, J. Zhao, C. Zhang, Y. Li, M. Luo, H. Ren, J. Liang, J. Wang, J. Wang, J. Qin, *Sci. Adv.* **2019**, *5*, 1.

[415] E. Afergan, H. Epstein, R. Dahan, N. Koroukhov, K. Rohekar, H. D. Danenberg, G. Golomb, *J. Control. Release* **2008**, *132*, 84.

[416] A. C. Anselmo, J. B. Gilbert, S. Kumar, V. Gupta, R. E. Cohen, M. F. Rubner, S. Mitragotri, *J. Control. Release* **2015**, *199*, 29.

[417] C. He, Y. Hu, L. Yin, C. Tang, C. Yin, *Biomaterials* **2010**, *31*, 3657.

[418] J. A. Champion, S. Mitragotri, *Proc. Natl. Acad. Sci. U. S. A.* **2006**, *103*, 4930.

[419] A. C. Anselmo, M. Zhang, S. Kumar, D. R. Vogus, S. Menegatti, M. E. Helgeson, S. Mitragotri, *ACS Nano* **2015**, *9*, 3169.

[420] S. L. Tao, M. W. Lubeley, T. A. Desai, *J. Control. Release* **2003**, *88*, 215.

[421] F. A. Khan, S. Akhtar, D. Almohazey, M. Alomari, S. A. Almofty, I. Badr, A. Elaissari, *Artif. Cells, Nanomedicine Biotechnol.* **2019**, *47*, 1533.

[422] A. Bettencourt, A. J. Almeida, *J. Microencapsul.* **2012**, *29*, 353.

[423] C. Elvira, A. Fanovich, M. Fernández, J. Fraile, J. San Román, C. Domingo, *J. Control. Release* **2004**, *99*, 231.

[424] A. Sahu, P. Solanki, S. Mitra, *Int. J. Nanomedicine* **2018**, *13*, 101.

[425] G.-B. B. Vianey, O.-G. B. Eli, F.-F. Guillermina, M.-A. Enrique, A.-C. Alejandra, J.-A. Laura, *Curr. Pharm. Des.* **2017**, *23*, 3415.

[426] B. Elsadek, F. Kratz, *J. Control. Release* **2012**, *157*, 4.

[427] K. B. Johnsen, A. Burkhart, F. Melander, P. J. Kempen, J. B. Vejlebo, P. Siupka, M. S. Nielsen, T. L. Andresen, T. Moos, *Sci. Rep.* **2017**, *7*, 1.

[428] K. B. Johnsen, M. Bak, F. Melander, M. S. Thomsen, A. Burkhart, P. J. Kempen, T. L. Andresen, T. Moos, *J. Control. Release* **2019**, *295*, 237.

[429] H. Soo Choi, W. Liu, P. Misra, E. Tanaka, J. P. Zimmer, B. Itty Ipe, M. G. Bawendi, J. V. Frangioni, *Nat. Biotechnol.* **2007**, *25*, 1165.

[430] P. Decuzzi, B. Godin, T. Tanaka, S. Y. Lee, C. Chiappini, X. Liu, M. Ferrari, *J. Control. Release* **2010**, *141*, 320.

[431] H. Epstein-Barash, D. Gutman, E. Markovsky, G. Mishan-Eisenberg, N. Koroukhov, J. Szebeni, G. Golomb, *J. Control. Release* **2010**, *146*, 182.

[432] R. Zein, W. Sharrouf, K. Selting, *J. Oncol.* **2020**, *2020*, 5194780.

[433] M. A. Lameijer, J. Tang, M. Nahrendorf, R. H. J. Beelen, W. J. M. Mulder, *Expert Rev. Mol. Diagn.* **2013**, *13*, 567.

[434] Y. Hui, X. Yi, D. Wibowo, G. Yang, A. P. J. Middelberg, H. Gao, C. X. Zhao, *Sci. Adv.* **2020**, *6*, 1.

[435] A. C. Anselmo, S. Mitragotri, *Adv. Drug Deliv. Rev.* **2017**, *108*, 51.

[436] R. Patro, G. Duggal, M. I. Love, R. A. Irizarry, C. Kingsford, *Nat. Methods* **2017**, *14*, 417.

[437] A. D. Yates, P. Achuthan, W. Akanni, J. Allen, J. Allen, J. Alvarez-Jarreta, M. R. Amode, I. M. Armean, A. G. Azov, R. Bennett, J. Bhai, K. Billis, S. Boddu, J. C. Marugán, C. Cummins, C. Davidson, K. Dodiya, R. Fatima, A. Gall, C. G. Giron, L. Gil, T. Grego, L. Haggerty, E. Haskell, T. Hourlier, O. G. Izuogu, S. H. Janacek, T. Juettemann, M. Kay, I. Lavidas, T. Le, D. Lemos, J. G. Martinez, T. Maurel, M. McDowall, A. McMahon, S. Mohanan, B. Moore, M. Nuhn, D. N. Oheh, A. Parker, A. Parton, M. Patricio, M. P. Sakthivel, A. I. Abdul Salam, B. M. Schmitt, H. Schuilenburg, D. Sheppard, M. Sycheva, M. Szuba, K. Taylor, A. Thormann, G. Threadgold, A. Vullo, B. Walts, A. Winterbottom, A. Zadissa, M. Chakiachvili, B. Flint, A. Frankish, S. E. Hunt, G. Iisley, M. Kostadima, N. Langridge, J. E. Loveland, F. J. Martin, J. Morales, J. M. Mudge, M. Muffato, E. Perry, M. Ruffier, S. J. Trevanion, F. Cunningham, K. L. Howe, D. R. Zerbino, P. Flicek, *Nucleic Acids Res.* **2020**, *48*, D682.

[438] M. I. Love, W. Huber, S. Anders, *Genome Biol.* **2014**, *15*, 550.

[439] M. V Kuleshov, M. R. Jones, A. D. Rouillard, N. F. Fernandez, Q. Duan, Z. Wang, S. Koplev, S. L. Jenkins, K. M. Jagodnik, A. Lachmann, M. G. McDermott, C. D. Monteiro, G. W. Gundersen, A. Ma'ayan, *Nucleic Acids Res.* **2016**, *44*, W90.

[440] E. V Batrakova, S. Li, A. D. Reynolds, R. L. Mosley, T. K. Bronich, A. V Kabanov, H. E. Gendelman, *Bioconjug. Chem.* **2007**, *18*, 1498.

[441] S. P. Ju, H. Y. Chen, C. W. Shih, *J. Nanoparticle Res.* **2018**, *20*, 1.

[442] A. Leal-Junior, A. Frizera, C. Marques, M. J. Pontes, *Opt. Fiber Technol.* **2018**, *43*, 106.

[443] B. J. Briscoe, L. Fiori, E. Pelillo, *J. Phys. D. Appl. Phys.* **1998**, *31*, 2395.

[444] S. Jeon, J. Clavadetscher, D. K. Lee, S. V. Chankeshwara, M. Bradley, W. S. Cho, *Nanomaterials* **2018**, *8*, 1.

[445] C. G. Rolli, T. Seufferlein, R. Kemkemer, J. P. Spatz, *PLoS One* **2010**, *5*, e8726.

[446] K. Ley, C. Laudanna, M. I. Cybulsky, S. Nourshargh, *Nat. Rev. Immunol.* **2007**, *7*, 678.

[447] A. Salas, M. Shimaoka, A. N. Kogan, C. Harwood, U. H. Von Andrian, T. A. Springer, *Immunity* **2004**, *20*, 393.

[448] B. C. Chesnutt, D. F. Smith, N. A. Raffler, M. L. Smith, E. J. White, K. Ley, *Microcirculation* **2006**, *13*, 99.

[449] N. S. Astrof, A. Salas, M. Shimaoka, J. F. Chen, T. A. Springer, *Biochemistry* **2006**, *45*, 15020.

[450] J. L. Dunne, C. M. Ballantyne, A. L. Beaudet, K. Ley, *Blood* **2002**, *99*, 336.

[451] J. L. Dunne, R. G. Collins, A. L. Beaudet, C. M. Ballantyne, K. Ley, *J. Immunol.* **2003**, *171*, 6105.

[452] R. Shamri, V. Grabovsky, J. M. Gauguet, S. Feigelson, E. Manevich, W. Kolanus, M. K. Robinson, D. E. Staunton, U. H. Von Andrian, R. Alon, *Nat. Immunol.* **2005**, *6*, 497.

[453] C. Giagulli, L. Ottoboni, E. Caveggion, B. Rossi, C. Lowell, G. Constantin, C. Laudanna, G. Berton, *J. Immunol.* **2006**, *177*, 604.

[454] A. R. Schenkel, Z. Mamdouh, W. A. Muller, *Nat. Immunol.* **2004**, *5*, 393.

[455] R. Gorina, R. Lyck, D. Vestweber, B. Engelhardt, *J. Immunol.* **2014**, *192*, 324.

[456] R. M. Starzyk, C. Rosenow, J. Frye, M. Leismann, E. Rodzinski, S. Putney, E. I. Tuomanen, *J. Infect. Dis.* **2000**, *181*, 181.

[457] American Cancer Society, **2021**.

[458] E. Alsahafi, K. Begg, I. Amelio, N. Raulf, P. Lucarelli, T. Sauter, M. Tavassoli, *Cell Death Dis.* **2019**, *10*, 1.

[459] J. H. Chang, C. C. Wu, K. S. P. Yuan, A. T. H. Wu, S. Y. Wu, *Oncotarget* **2017**, *8*, 55600.

[460] O. Kujan, R. J. Oliver, A. Khattab, S. A. Roberts, N. Thakker, P. Sloan, *Oral Oncol.* **2006**, *42*, 987.

[461] A. Dylawerska, W. Barczak, A. Wegner, W. Golusinski, W. M. Suchorska, *Med. Oncol.* **2017**, *34*, 1.

[462] J. V. Bagan, Y. Jimenez, J. M. Sanchis, R. Poveda, M. A. Milian, J. Murillo, C. Scully, *J. Oral Pathol. Med.* **2003**, *32*, 379.

[463] K. Shinagawa, S. Yanamoto, T. Naruse, A. Kawakita, K. Morishita, Y. Sakamoto, S. Rokutanda, M. Umeda, *Pathol. Oncol. Res.* **2017**, *23*, 425.

[464] V. Brailo, V. Vučićević-Boras, A. Cekić-Arambašin, I. Ž. Alajbeg, A. Milenović, J. Lukač, *Oral Oncol.* **2006**, *42*, 370.

[465] T. Dineshkumar, B. K. Ashwini, A. Rameshkumar, P. Rajashree, R. Ramya, K. Rajkumar, *Asian Pacific J. Cancer Prev.* **2016**, *17*, 4899.

[466] S. R. Mallery, D. Wang, B. Santiago, P. Pei, S. P. Schwendeman, K. Nieto, R. Spinney, M. Tong, G. Koutras, B. Han, A. Holpuch, J. Lang, *Cancer Prev. Res.* **2017**, *10*, 76.

[467] A. Holpuch, K. G. Desai, S. Schwendeman, S. Mallery, *J. Carcinog.* **2011**, *10*, 23.

[468] W. N. William, J. J. Lee, S. M. Lippman, J. W. Martin, N. Chakravarti, H. T. Tran, A. L. Sabichi, E. S. Kim, L. Feng, R. Lotan, V. A. Papadimitrakopoulou, *Cancer Prev. Res.* **2009**, *2*, 22.

[469] H. Wen, H. Jung, X. Li, *AAPS J.* **2015**, *17*, 1327.

[470] M. Liu, J. Zhang, W. Shan, Y. Huang, *Asian J. Pharm. Sci.* **2015**, *10*, 275.

[471] T. K. Fábián, P. Hermann, A. Beck, P. Fejérdy, G. Fábián, *Int. J. Mol. Sci.* **2012**, *13*, 4295.

[472] S. Behzadi, V. Serpooshan, W. Tao, M. A. Hamaly, M. Y. Alkawareek, E. C. Dreaden, D. Brown, A. M. Alkilany, O. C. Farokhzad, M. Mahmoudi, *Chem. Soc. Rev.* **2017**, *46*, 4218.

[473] H. Hillaireau, P. Couvreur, *Cell. Mol. Life Sci.* **2009**, *66*, 2873.

[474] K. Netsomboon, A. Bernkop-schnürch, *Eur. J. Pharm. Biopharm.* **2016**, *98*, 76.

[475] D. S. Kohane, J. Y. Tse, Y. Yeo, R. Padera, M. Shubina, R. Langer, *J. Biomed. Mater. Res. - Part A* **2006**, *77*, 351.

[476] B. Prietl, C. Meindl, E. Roblegg, T. R. Pieber, G. Lanzer, E. Fröhlich, *Cell Biol. Toxicol.* **2014**, *30*, 1.

[477] M. Caldorera-Moore, N. Guimard, L. Shi, K. Roy, *Expert Opin. Drug Deliv.* **2010**, *7*, 479.

[478] S. K. Lai, Y. Wang, J. Hanes, *Adv. Drug Deliv. Rev.* **2009**, *61*, 158.

[479] G. Ponchel, J. M. Irache, *Adv. Drug Deliv. Rev.* **1998**, *34*, 191.

[480] R. Hejazi, M. Amiji, *J. Control. Release* **2003**, *89*, 151.

[481] L. Mazzarino, C. Travelet, S. Ortega-Murillo, I. Otsuka, I. Pignot-Paintrand, E. Lemos-Senna, R. Borsali, *J. Colloid Interface Sci.* **2012**, *370*, 58.

[482] S. R. Mallery, D. Wang, B. Santiago, P. Pei, S. P. Schwendeman, K. Nieto, R. Spinney, M. Tong, G. Koutras, B. Han, A. Holpuch, J. Lang, *Cancer Prev. Res.* **2017**, *10*, 76.

[483] K. Nieto, P. Pei, D. Wang, S. R. Mallery, S. P. Schwendeman, *Int. J. Pharm.* **2018**, *538*, 48.

[484] F. Laffleur, F. Hintzen, G. Shahnaz, D. Rahmat, K. Leithner, A. Bernkop-Schnürch, *Nanomedicine* **2014**, *9*, 387.

[485] I. Pereira De Sousa, C. Steiner, M. Schmutzler, M. D. Wilcox, G. J. Veldhuis, J. P. Pearson, C. W. Huck, W. Salvenmoser, A. Bernkop-Schnürch, *Eur. J. Pharm. Biopharm.* **2015**, *97*, 273.

[486] G. Perera, M. Zipser, S. Bonengel, W. Salvenmoser, A. Bernkop-Schnürch, *Eur. J. Pharm. Biopharm.* **2015**, *97*, 250.

[487] S. Bonengel, F. Prüfert, G. Perera, J. Schauer, A. Bernkop-Schnürch, *Int. J. Pharm.* **2015**,

483, 19.

[488] M. Tong, B. B. Han, A. S. Holpuch, P. Pei, L. He, S. R. Mallery, *Exp. Cell Res.* **2013**, *319*, 1028.

[489] A. S. Holpuch, G. J. Hummel, M. Tong, G. A. Seghi, P. Pei, P. Ma, R. J. Mumper, S. R. Mallery, *Pharm. Res.* **2010**, *27*, 1224.

[490] S. Sayedyahossein, L. Nini, T. S. Irvine, L. Dagnino, *FASEB J.* **2012**, *26*, 4218.

[491] G. Cardinali, G. Bolasco, N. Aspite, G. Lucania, L. V. Lotti, M. R. Torrisi, M. Picardo, *J. Invest. Dermatol.* **2008**, *128*, 558.

[492] C. Dawes, *J. Am. Dent. Assoc.* **2008**, *139*, 18S.

[493] H. I. Hung, O. J. Klein, S. W. Peterson, S. R. Rokosh, S. Osseiran, N. H. Nowell, C. L. Evans, *Sci. Rep.* **2016**, *6*, 1.

[494] J. Rejman, V. Oberle, I. S. Zuhorn, D. Hoekstra, *Biochem. J.* **2004**, *377*, 159.

[495] C. M. Van Itallie, J. M. Anderson, *Annu. Rev. Physiol.* **2006**, *68*, 403.

[496] P. L. Tuma, A. L. Hubbard, *Physiol. Rev.* **2003**, *83*, 871.

[497] T. H. Yeh, L. W. Hsu, M. T. Tseng, P. L. Lee, K. Sonjae, Y. C. Ho, H. W. Sung, *Biomaterials* **2011**, *32*, 6164.

[498] J. Smith, E. Wood, M. Dornish, *Pharm. Res.* **2004**, *21*, 43.

[499] M. Mihara, K. Kasutani, M. Okazaki, A. Nakamura, S. Kawai, M. Sugimoto, Y. Matsumoto, Y. Ohsugi, *Int. Immunopharmacol.* **2005**, *5*, 1731.

[500] "Actemra (tocilizumab) injection,for intravenous or subcutaneous use," can be found under https://www.accessdata.fda.gov/drugsatfda_docs/label/2017/125276s114lbl.pdf.

[501] G. Pitiyage, W. M. Tilakaratne, M. Tavassoli, S. Warnakulasuriya, *J. Oral Pathol. Med.* **2009**, *38*, 737.

[502] R. Ai, Y. Tao, Y. Hao, L. Jiang, H. Dan, N. Ji, X. Zeng, Y. Zhou, Q. Chen, *Oncotarget* **2017**, *8*, 81617.

[503] S. R. Mallery, D. Wang, B. Santiago, P. Pei, C. Bissonnette, J. A. Jayawardena, S. P. Schwendeman, R. Spinney, J. Lang, *Mol. Cancer Ther.* **2019**, *18*, 2308.

[504] H. L. Wright, R. J. Moots, R. C. Bucknall, S. W. Edwards, *Rheumatology* **2010**, *49*, 1618.

[505] F. Sônego, F. V. e S. Castanheira, R. G. Ferreira, A. Kanashiro, C. A. V. G. Leite, D. C. Nascimento, D. F. Colón, V. de F. Borges, J. C. Alves-Filho, F. Q. Cunha, *Front. Immunol.* **2016**, *7*, 155.

[506] G. C. Jickling, D. Liu, B. P. Ander, B. Stamova, X. Zhan, F. R. Sharp, *J. Cereb. Blood Flow Metab.* **2015**, *35*, 888.

[507] J. Mehta, J. Dinerman, P. Mehta, T. G. Saldeen, D. Lawson, W. H. Donnelly, R. Wallin, *Circulation* **1989**, *79*, 549.

[508] J. Grommes, O. Soehnlein, *Mol. Med.* **2011**, *17*, 293.

[509] C. Summers, S. M. Rankin, A. M. Condliffe, N. Singh, A. M. Peters, E. R. Chilvers, *Trends Immunol.* **2010**, *31*, 318.

[510] M. H. Gee, K. H. Albertine, *Annu. Rev. Physiol.* **1993**, *55*, 227.

[511] T. N. Mayadas, X. Cullere, C. A. Lowell, *Annu. Rev. Pathol. Mech. Dis.* **2014**, *9*, 181.

[512] A. Mantovani, M. A. Cassatella, C. Costantini, S. Jaillon, *Nat. Rev. Immunol.* **2011**, *11*, 519.

[513] A. E. Williams, R. C. Chambers, *Am. J. Physiol. Cell. Mol. Physiol.* **2013**, *306*, L217.

[514] R. L. Zemans, M. A. Matthay, *Thorax* **2017**, *72*, 1 LP.

[515] C. Summers, N. R. Singh, J. F. White, I. M. Mackenzie, A. Johnston, C. Solanki, K. K. Balan, A. M. Peters, E. R. Chilvers, *Thorax* **2014**, *69*, 623 LP.

[516] P. Y. Lee, J.-X. Wang, E. Parisini, C. C. Dascher, P. A. Nigrovic, *J. Leukoc. Biol.* **2013**, *94*,

585.

[517] J. M. Daley, A. A. Thomay, M. D. Connolly, J. S. Reichner, J. E. Albina, *J. Leukoc. Biol.* **2008**, *83*, 64.

[518] N. Vij, T. Min, M. Bodas, A. Gorde, I. Roy, *Nanomedicine Nanotechnology, Biol. Med.* **2016**, *12*, 2415.

[519] M. Bartneck, J. Wang, *Front. Immunol.* **2019**, *10*, 2257.

[520] Z. Wang, J. Li, J. Cho, A. B. Malik, *Nat. Nanotechnol.* **2014**, *9*, 204.

[521] D. Chu, J. Gao, Z. Wang, *ACS Nano* **2015**, *9*, 11800.

[522] J. W. Myerson, A. C. Anselmo, Y. Liu, S. Mitragotri, D. M. Eckmann, V. R. Muzykantov, *Adv. Drug Deliv. Rev.* **2016**, *99*, 97.

[523] A. C. Anselmo, S. Mitragotri, *Adv. Drug Deliv. Rev.* **2017**, *108*, 51.

[524] M. J. Ernsting, M. Murakami, A. Roy, S.-D. Li, *J. Control. Release* **2013**, *172*, 782.

[525] A. C. Anselmo, S. Mitragotri, *J. Control. Release* **2014**, *190*, 531.

[526] G. Böhm, R. Muhr, R. Jaenicke, *Protein Eng. Des. Sel.* **1992**, *5*, 191.

[527] M. Bertsch, R. J. Kassner, *J. Proteome Res.* **2003**, *2*, 469.

[528] L. M. Drouin, M. Agbandje-McKenna, *Future Virol.* **2013**, *8*, 1183.

[529] G. R. Nemerow, P. L. Stewart, V. S. Reddy, *Curr. Opin. Virol.* **2012**, *2*, 115.

[530] N. Pontillo, F. Pane, L. Messori, A. Amoresano, A. Merlino, *Chem. Commun.* **2016**, *52*, 4136.

[531] J. Zhu, X. Huang, Y. Yang, *J. Clin. Invest.* **2009**, *119*, 2388.

[532] F. Mingozzi, H. Büning, *Front. Immunol.* **2015**, *6*, 120.

[533] R. Hendrickx, N. Stichling, J. Koelen, L. Kuryk, A. Lipiec, U. F. Greber, *Hum. Gene Ther.* **2014**, *25*, 265.

[534] W. Wang, M. A. Knovich, L. G. Coffman, F. M. Torti, S. V Torti, *Biochim. Biophys. Acta - Gen. Subj.* **2010**, *1800*, 760.

[535] B. G. Yipp, J. H. Kim, R. Lima, L. D. Zbytnuik, B. Petri, N. Swanlund, M. Ho, V. G. Szeto, T. Tak, L. Koenderman, P. Pickkers, A. T. J. Tool, T. W. Kuijpers, T. K. van den Berg, M. R. Looney, M. F. Krummel, P. Kubes, *Sci. Immunol.* **2017**, *2*, eaam8929.

[536] S. Mangal, W. Gao, T. Li, Q. (Tony) Zhou, *Acta Pharmacol. Sin.* **2017**, *38*, 782.

[537] "Metastatic Cancer: When Cancer Spreads - National Cancer Institute," can be found under https://www.cancer.gov/types/metastatic-cancer.

[538] A. C. Anselmo, V. Gupta, B. J. Zern, D. Pan, M. Zakrewsky, V. Muzykantov, **2013**, 11129.

[539] I. V Zelepukin, A. V Yaremenko, V. O. Shipunova, A. V Babenyshev, I. V Balalaeva, P. I. Nikitin, S. M. Deyev, M. P. Nikitin, *Nanoscale* **2019**, *11*, 1636.

[540] Z. Zhao, A. Ukidve, Y. Gao, J. Kim, S. Mitragotri, *Sci. Adv.* **2019**, *5*, eaax9250.

[541] E. Chambers, S. Mitragotri, *J. Control. Release* **2004**, *100*, 111.

[542] O. A. Marcos-Contreras, J. S. Brenner, R. Y. Kiseleva, V. Zuluaga-Ramirez, C. F. Greineder, C. H. Villa, E. D. Hood, J. W. Myerson, S. Muro, Y. Persidsky, V. R. Muzykantov, *J. Control. Release* **2019**, *301*, 54.

[543] A. C. Anselmo, S. Kumar, V. Gupta, A. M. Pearce, A. Ragusa, V. Muzykantov, S. Mitragotri, *Biomaterials* **2015**, *68*, 1.